

NAVAL POSTGRADUATE SCHOOL

Monterey, California



THESIS

**A NOVEL APPROACH FOR THE DEVELOPMENT AND
OPTIMIZATION OF STATE-OF-THE-ART
PHOTOVOLTAIC DEVICES USING SILVACO**

by

Panayiotis Michalopoulos

March 2002

Thesis Advisor:

Sherif Michael

Bret Michael

Second Reader:

Todd Weatherford

Approved for public release; distribution is unlimited.

THIS PAGE INTENTIONALLY LEFT BLANK

REPORT DOCUMENTATION PAGE			Form Approved OMB No. 0704-0188
Public reporting burden for this collection of information is estimated to average 1 hour per response, including the time for reviewing instruction, searching existing data sources, gathering and maintaining the data needed, and completing and reviewing the collection of information. Send comments regarding this burden estimate or any other aspect of this collection of information, including suggestions for reducing this burden, to Washington headquarters Services, Directorate for Information Operations and Reports, 1215 Jefferson Davis Highway, Suite 1204, Arlington, VA 22202-4302, and to the Office of Management and Budget, Paperwork Reduction Project (0704-0188) Washington DC 20503.			
1. AGENCY USE ONLY (Leave blank)	2. REPORT DATE March 2002	3. REPORT TYPE AND DATES COVERED Master's Thesis	
4. TITLE AND SUBTITLE: Title (Mix case letters) A Novel Approach for the Development and Optimization of State-of-the-Art Photovoltaic Devices Using Silvaco			5. FUNDING NUMBERS
6. AUTHOR(S) Panayiotis Michalopoulos			8. PERFORMING ORGANIZATION REPORT NUMBER
7. PERFORMING ORGANIZATION NAME(S) AND ADDRESS(ES) Naval Postgraduate School Monterey, CA 93943-5000			10. SPONSORING / MONITORING AGENCY REPORT NUMBER
9. SPONSORING / MONITORING AGENCY NAME(S) AND ADDRESS(ES) N/A			11. SUPPLEMENTARY NOTES The views expressed in this thesis are those of the author and do not reflect the official policy or position of the Department of Defense or the U.S. Government.
12a. DISTRIBUTION / AVAILABILITY STATEMENT Approved for public release; distribution is unlimited.			12b. DISTRIBUTION CODE
13. ABSTRACT (maximum 200 words) In this thesis, a new method for developing realistic simulation models of advanced solar cells is presented. Several electrical and optical properties of exotic materials, used in such designs, are researched and calculated. Additional software has been developed to facilitate and enhance the modeling process. Furthermore, specific models of an InGaP/GaAs and of an InGaP/GaAs/Ge multi-junction solar cells are prepared and are fully simulated. The major stages of the process are explained and the simulation results are compared to published experimental data. Finally, additional optimization is performed on the last state-of-the-art cell, to further improve its efficiency. The flexibility of the proposed methodology is demonstrated and example results are shown throughout the whole process.			
14. SUBJECT TERMS Solar cell, multijunction, simulation, model, development, Silvaco, Atlas, InGaP, GaAs, Ge			15. NUMBER OF PAGES 187
			16. PRICE CODE
17. SECURITY CLASSIFICATION OF REPORT Unclassified	18. SECURITY CLASSIFICATION OF THIS PAGE Unclassified	19. SECURITY CLASSIFICATION OF ABSTRACT Unclassified	20. LIMITATION OF ABSTRACT UL

NSN 7540-01-280-5500

Standard Form 298 (Rev. 2-89)
Prescribed by ANSI Std. Z39-18

THIS PAGE INTENTIONALLY LEFT BLANK

Approved for public release; distribution is unlimited.

**A NOVEL APPROACH FOR THE DEVELOPMENT AND OPTIMIZATION OF
STATE-OF-THE-ART PHOTOVOLTAIC DEVICES USING SILVACO**

Panayiotis Michalopoulos
Lieutenant, Hellenic Navy
B.S., Hellenic Naval Academy, 1993

Submitted in partial fulfillment of the
requirements for the degree of

**MASTER OF SCIENCE IN ELECTRICAL ENGINEERING
and
MASTER OF SCIENCE IN COMPUTER SCIENCE**

from the
**NAVAL POSTGRADUATE SCHOOL
March 2002**

Author: Panayiotis Michalopoulos

Approved by: Sherif Michael
Thesis Advisor

Bret Michael
Co-Advisor

Todd Weatherford
Second Reader

Christopher Eagle
Chairman Department of Computer Science

Jeffrey B. Knorr
Chairman Department of Electrical and Computer Engineering

THIS PAGE INTENTIONALLY LEFT BLANK

ABSTRACT

In this thesis, a new method for developing realistic simulation models of advanced solar cells is presented. Several electrical and optical properties of exotic materials, used in such designs, are researched and calculated. Additional software has been developed to facilitate and enhance the modeling process. Furthermore, specific models of an InGaP/GaAs and of an InGaP/GaAs/Ge multi-junction solar cells are prepared and are fully simulated. The major stages of the process are explained and the simulation results are compared to published experimental data. Finally, additional optimization is performed on the last state-of-the-art cell, to further improve its efficiency. The flexibility of the proposed methodology is demonstrated and example results are shown throughout the whole process.

THIS PAGE INTENTIONALLY LEFT BLANK

TABLE OF CONTENTS

I.	INTRODUCTION	1
A.	BACKGROUND.....	1
B.	OBJECTIVE.....	2
C.	RELATED WORK.....	3
D.	ORGANIZATION.....	3
II.	INTRODUCTION TO SEMICONDUCTORS	5
A.	BASIC PHYSICS.....	5
B.	CRYSTAL STRUCTURES.....	9
C.	CARRIERS.....	10
D.	FERMI LEVEL.....	15
E.	CARRIER TRANSPORT.....	19
F.	MOBILITY.....	20
G.	RECOMBINATION.....	22
H.	TUNNELING.....	25
III.	SEMICONDUCTOR JUNCTIONS	27
A.	P–N JUNCTION.....	27
1.	Formation.....	27
2.	Forward Bias.....	30
3.	Reverse Bias.....	32
4.	Breakdown.....	34
5.	Capacitance, Ohmic Losses and Overview.....	35
B.	M–S JUNCTION.....	36
C.	OHMIC CONTACT.....	39
D.	TUNNEL JUNCTION.....	40
E.	DIRECT AND INDIRECT TUNNELING.....	43
F.	HETEROJUNCTIONS.....	44
IV.	SOLAR CELLS	49
A.	SOLAR ENERGY.....	49
B.	OPTICAL PROPERTIES.....	51
C.	FUNDAMENTALS.....	54
D.	TEMPERATURE AND RADIATION EFFECTS.....	57
E.	CELL TYPES.....	58
F.	CONTACTS.....	60
G.	ARRAYS.....	62

V.	MULTIJUNCTION SOLAR CELLS	63
A.	BASICS.....	63
B.	MONOLITHIC MULTIJUNCTION CELLS	66
C.	CURRENT DEVELOPMENTS.....	67
VI.	SIMULATION SOFTWARE.....	71
A.	MODELING TODAY	71
B.	SILVACO.....	72
C.	WORKING WITH ATLAS	74
	1. Mesh.....	74
	2. Regions	75
	3. Electrodes	76
	4. Doping	76
	5. Material Properties	77
	6. Models.....	77
	7. Light.....	77
	8. Simulation Results	77
D.	SIMULATION SOURCE CODE.....	78
E.	EXCHANGING DATA WITH MATLAB.....	80
	1. Creating Silvaco input files.....	81
	2. Extracting results.....	81
VII.	MATERIAL PROPERTIES.....	85
A.	CURRENT STATUS	85
B.	SILVACO LIBRARY	86
C.	LATTICE MATCHING AND ALLOY PROPERTIES.....	87
D.	OTHER CALCULATIONS.....	88
E.	RESULTS	89
F.	MOBILITY VS DOPING.....	91
G.	OPTICAL PARAMETERS.....	93
VIII.	BUILDING A MULTIJUNCTION CELL	97
A.	THE PROCESS	97
B.	THE SIMPLE GaAs CELL	99
C.	IMPROVING THE CELL.....	102
D.	THE COMPLETE InGaP CELL.....	104
E.	THE TUNNEL JUNCTION	106
F.	THE InGaP/GaAs MECHANICALLY STACKED TANDEM CELL.....	107
G.	THE InGaP/GaAs DUAL MULTIJUNCTION CELL	110
H.	THE COMPLETE InGaP / GaAs CELL.....	112

IX. DEVELOPING AND OPTIMIZING A STATE-OF-THE-ART MULTIJUNCTION CELL	115
A. FIRST STAGE OF DEVELOPMENT	115
B. PARAMETRIC ANALYSIS AND OPTIMIZATION	120
C. FURTHER OPTIMIZATIONS	128
X. CONCLUSIONS AND RECOMMENDATIONS	129
A. RESULTS AND CONCLUSIONS	129
B. FURTHER OPTIMIZATIONS AND RECOMMENDATIONS	130
APPENDIX A. LIST OF SYMBOLS	131
APPENDIX B. GREEK ALPHABET	133
APPENDIX C. SOME PHYSICAL CONSTANTS	135
APPENDIX D. UNITS	135
APPENDIX E. MAGNITUDE PREFIXES	137
APPENDIX F. ATLAS SOURCE CODE	139
APPENDIX G. MATLAB SOURCE CODE	159
LIST OF REFERENCES	167
INITIAL DISTRIBUTION LIST	171

THIS PAGE INTENTIONALLY LEFT BLANK

ACKNOWLEDGMENTS

Many people have contributed to the completion of this thesis. I would first like to express my deep appreciation to my advisor Dr Sherif Michael for his continuous guidance and support, my co–advisor Dr Bret Michael and my second reader Dr Todd Weatherford for providing valuable insights, improving this work. I have also benefited from the significant advice of Dr Gamani Karunasiri. Additionally, I am grateful to the professors of the Naval Postgraduate School for their outstanding tutoring. They were always a source of inspiration.

Furthermore, I am thankful to my country, Hellas, and the Hellenic Navy for making this educational experience possible. I am indebted to my parents, Theofanis and Sofia, whose love, patience, excellent example, motivation and encouragement were always by my side, even from thousands of miles away. Finally, I would especially like to express my gratitude to my dear wife, Elpida, who was always loving, supporting and encouraging, even during my long hours of study.

EXECUTIVE SUMMARY

One of the major limiting factors in space missions and applications is the production of electric power. Even though a plethora of energy sources have been invented and are widely used in terrestrial applications, most of them are not practical for use in space applications: their large volume, weight and cooling requirements are only some of the forbidding reasons. An abundant, renewable, small, and lightweight power source has yet to be discovered.

The use of solar cells is currently the best solution to this energy problem. They are light, they require almost no maintenance and they are totally renewable. However, their efficiency is limited and that has resulted to the construction and deployment of solar arrays spanning many cubic meters. This alone is the cause of many problems of mostly mechanical nature, like stowage volume, aerodynamic drag and maneuverability.

Advances in semiconductor design and fabrication has lead to the development of tandem cells in complex monolithic structures called multijunction cells. Their high level of efficiency allows significant reduction in array sizes. Such an advance in the design of solar cells could open up new vistas for the design of spacecraft.

Although many analytical models of solar cells have been created and published, almost all research on the design of solar cells is currently conducted using experimentation. This is in part due to the lack of computer-based tools with a complete design environment and a full set of models to simulate all aspects of an advanced solar cell, except for the Silvaco Virtual Wafer Fabrication (VWF) suite of tools. Despite the capabilities of VWF, to date there are no published accounts of its use to develop multijunction solar cells.

In this thesis, a methodology is introduced for using VWF – and in particular Atlas within that suite of tools – to model advanced solar cells. It simplifies the process by abstracting fabrication details and focusing on the device itself. Additionally, the software developed to post-process the output of Atlas in another tool called Matlab, is discussed. This software was also used to adjust and calibrate parameter values for use by

Atlas in modeling advanced solar cells. Such parameters include electrical and optical properties of exotic materials, often used in high-end cells. As most of them remain to be studied by the photovoltaic community, their properties must be interpolated from the properties of their components. Due to the non-linearity involved, several bowing parameters are used in more complex interpolation functions.

As a first attempt to verify the correctness of this approach for designing advanced solar cells, an InGaP/GaAs cell is developed. The first step is to model and simulate a simple GaAs cell. Voltage, current, IV characteristic and frequency response results are collected and compared with published experimental values. Although the similarity observed is remarkable, several parameters were tuned to attain better accuracy. The improved model is simulated again and new results are obtained. This process is repeated until the desired level of accuracy is obtained. Additional layers (e.g. BSF, buffers, windows) are added to the basic device to create a more advanced structure. Each step is followed by a comparison and evaluation of results.

Using the same approach, an InGaP cell is formed. Both cells are then placed in a mechanically stacked configuration to investigate shadowing phenomena. An appropriate tunnel junction is also developed to electrically interconnect the two cells, resulting in a creation of a multijunction cell. The dimensions and structural characteristics used are identical to those in published cells. The fact that the results also match is a good indication of the validity of this methodology.

The final case study reported in this thesis is of a triple InGaP/GaAs/Ge multijunction cell. This structure is only vaguely described in the literature, therefore requiring some modeling decisions. Those are made based on the experience gained from previous steps in this research. The simulation results closely approximate published results from experimentation. Finally, an optimization process is used for determining the best combination of thicknesses of the three cells involved. The results obtained from the optimization process correspond to those obtained for the original design.

I. INTRODUCTION

A. BACKGROUND

We live in the age of space exploration and conquest. Deep space missions, space stations, shuttles and satellites are currently everyday news. As technology advances and space applications become more and more demanding, their requirement for more energy becomes imperative.

On the other hand, one of the most significant factors, in any kind of space mission, is weight. This is due in part to both technological limitations and cost considerations. With an average cost exceeding \$20,000 per pound and electric power systems (EPSs) constituting almost 30% of the total spacecraft's weight, the need for efficient and renewable power sources is crucial.

Solar cells outweigh all these energy sources due to their small weight and their relatively high power density. However, solar arrays are still very large and in some cases have a surface of more than 30m³. This causes many problems due to their increased stowage volume, aerodynamic drag, and radar cross-section. The ability to maneuver such a large array and the vibrations that accompany an operation like that are also limiting factors.

Advances in semiconductor design and fabrication are very rapid and everyday provide new ideas and means for improving cell performance. After the impressive evolution of the 1839's primitive Selenium to the currently most popular Silicon cell, cutting-edge technology has presented state-of-the-art triple and quadruple multijunction cells. These advances provided for a reduction of solar array size by a factor of two, while more recent developments are expected to achieve even greater reductions. Therefore, innovative solar cell design is of the utmost importance to the design of new spacecraft.

A number of significant publications fully describe various aspects of device characteristics and modeling. However, all of them were focused on very specific issues, lacking the breadth of a complete simulation tool.

Today, experts solely utilize the above analytic models. Despite their credibility, they only describe a small fraction of the phenomena that take place in a complex solar cell, providing very little insight into the characteristics of the final product. For this reason, current research on the development and optimization of solar cells relies primarily on the use of experimentation. However, in such experiments, many undesired factors are involved. Most of them have to do with the details of the fabrication process used. This may result in confusion and misleading conclusions. Other important side effects are the long time required to set up the experiments (e.g., fabrication, development of instrumentation) and the high cost associated with conducting experiments.

The Silvaco Software Package is a suite of integrated simulation and analysis tools for use in electronic design. One of its major components of this suite of tools is the Virtual Wafer Fabrication package (VWF). Within VWF, the ATLAS tool aids in the design and development of all types of semiconductor and VLSI devices, from simple bipolar transistors to EEPROMs. The phenomena modeled start from simple electrical conductivity and extend to such things as thermal analysis, radiation, and laser effects. A wide variety of detailed layer-growth processes and material properties (e.g. mobilities, recombination parameters, ionization coefficients, optical parameters) add to the fidelity of the simulation. However, no effort to utilize this powerful tool for the modeling of advanced solar cells has been reported in the literature by researchers or the manufacturers of solar cells.

B. OBJECTIVE

The research issues addressed in this thesis research are as follows: whether ATLAS can be successfully used for simulating complex solar cell structures, how to prepare the necessary infrastructure for such tasks, and how to simulate devices of different levels of complexity. In addressing the last issue, the results obtained via simulation, are compared with published experimental data.

C. RELATED WORK

As it was mentioned earlier, no published papers were found in conferences or journals about fully modeling and simulating all major aspects in the behavior of an advanced solar cell. This is the reason why this methodology is considered to be novel. However, interest in this area was seen by students at the Naval Postgraduate School. The most remarkable work exists in Ref. 30 and 34.

In Ref. 34, modeling of a simple one-junction cell, using Silvaco, was performed and its IV characteristic was produced. No other results were shown and no comparison to experimental data was presented.

In Ref. 30, dark-current analysis of solar cells was mainly performed. An indication of the usage of Silvaco for their simulation was also briefly provided. Within this, there was an attempt to simulate a triple MJ cell, but little results were presented and no comparison with experimental results was done.

D. ORGANIZATION

Chapters 2 and 3 are an introduction to semiconductor physics and basic electronic devices. The principles and major functional characteristics of both simple and advanced solar cells are explained in chapters 4 and 5. In chapter 6, a novel methodology for simulating state-of-the-art cells is introduced and is continued throughout chapter 7 with the research of material properties. They both form the basis of the following two chapters. In chapter 8, a dual multijunction cell is constructed, simulated and the results are verified against published experiments. The first part of chapter 9 simulates a cutting-edge cell and also verifies its results with published experiments. Finally, an optimization of this cell is performed in the second part of this chapter.

Chapter 10 concludes the thesis with a summary and recommendations for future work.

THIS PAGE INTENTIONALLY LEFT BLANK

II. INTRODUCTION TO SEMICONDUCTORS

This chapter contains introductory information about semiconductors and the physics surrounding their nature and functionality. It is addressed to students not very familiar with such concepts. Readers well versed in this area might rather go directly to Chapter 3 or 4.

A. BASIC PHYSICS

The various materials can be categorized according to their electrical properties as *conductors*, semiconductors and *insulators*. *Resistivity* ρ and its reciprocal *conductivity* σ are two of the most important electrical properties. Table 2.1 displays the resistivity and conductivity for various types of materials:

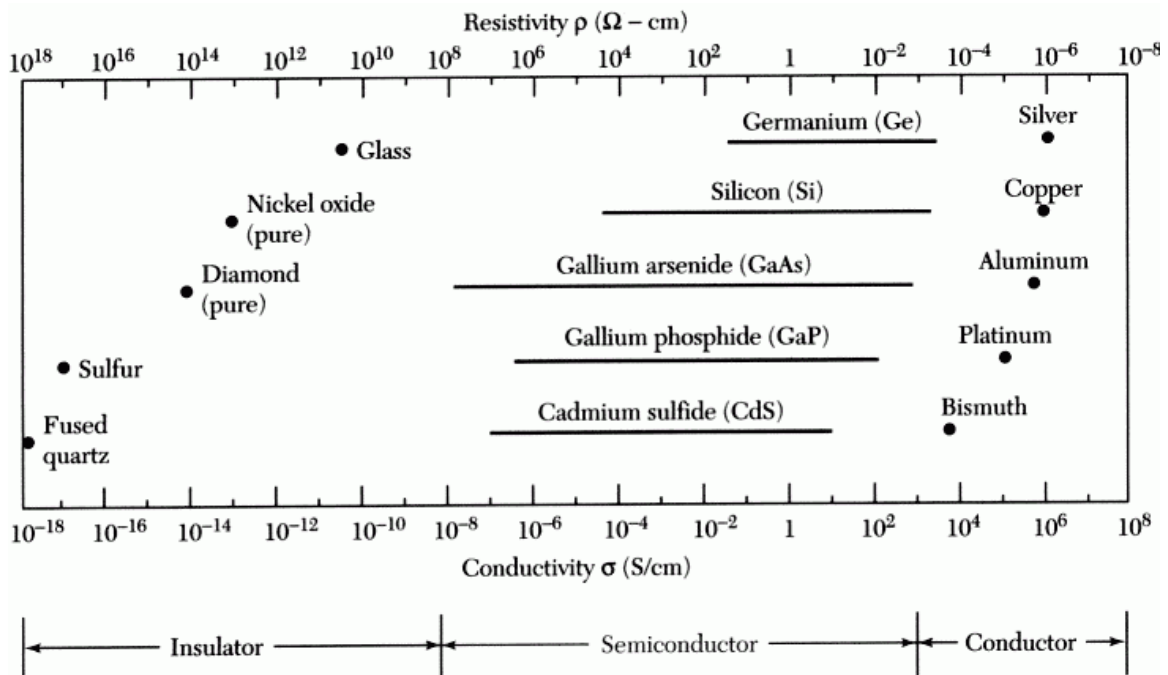


Table 2.1. Resistivity for various material types [from Ref. 1:p. 18].

It is well known that materials are comprised of atoms. Each atom has a nucleus and electrons revolving around it. The nucleus consists of protons and neutrons. The

attractive force between the positive charged protons and the negative charged electrons are responsible for holding this structure together.

According to *Niels Bohr*, electrons exist in specific orbits or shells around the nucleus, the outermost of which is called a *valence shell*. They can transition to a shell of higher (or lower) energy level by absorbing (or losing) energy, equal to the difference of the two levels (Figure 2.1). This energy can have the form of a photon or heat.

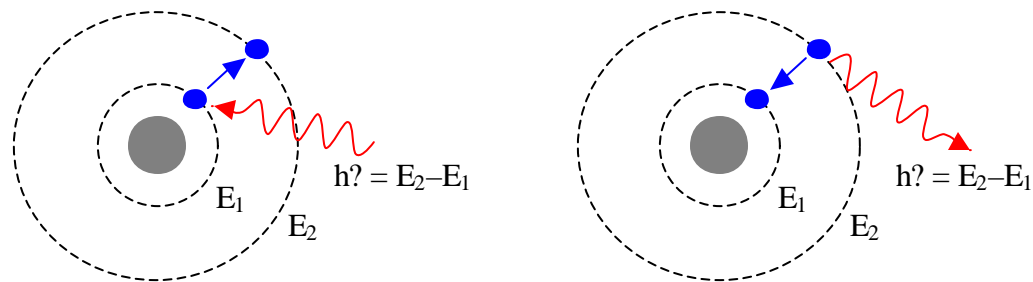


Figure 2.1. Transition of an electron from one shell to another.

Inside a material, however, things are a bit different. At 0°K all electrons are tightly held by their atoms and the material has zero conductivity. As temperature rises, heat increases the energies of valent electrons and some of them break free from their atoms. Those are called *free electrons*. Their number increases drastically with temperature. Free electrons are directly responsible for the electrical conductivity of a material and actually participate in current flow. Hence, as temperature increases, so does conductivity. This is true up to a certain temperature. Above that, there are no more electrons to become free and the conductivity stops to increase.

On the other hand, atoms *oscillate* due to heat. As temperature increases, this oscillation becomes larger. Free electrons moving in the material bounce on the oscillating atoms and reduce their speed. The larger the oscillation, the bigger the difficulty of movement for the free electrons. This way temperature decreases conductivity. The balance between the two factors is shown in Figure 2.2:

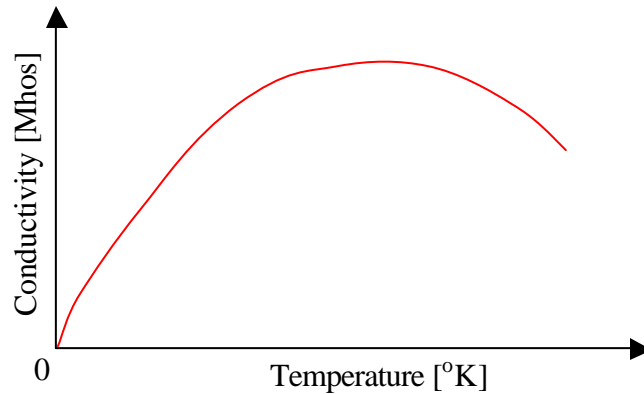


Figure 2.2. Conductivity vs. Temperature.

Free electrons are affected by electrostatic forces produced by nearby atoms. In order to achieve chemical stability, every atom requires a full valence shell. This is always done with eight electrons, except for the first shell, which only requires two. Elements with five or more valence electrons hold those tightly in their atoms and attract others in an attempt to reach a chemically stable state. The additional electrons will increase the negative charge of the atoms. These atoms now have an overall negative charge and are called *negative ions*. On the contrary, elements with three or less valence electrons allow them to escape, using one shell below as valent, again reaching a stable state. This loss will result in an excessive positive charge. These atoms are now called *positive ions*. The produced positive and negative ions are electrostatically attracted and an *ionic bond* is created. Elements with four valence electrons do not receive or offer any of them. Instead, they share them with other atoms. This way a *covalent bond* is created. Electrons existing in the inner shells require so much more energy to change energy level that they will not concern us.

Free electrons have higher energies and are said to exist in the *conduction band*. Electrons not freed from their atoms have lower energies and are said to exist in the *valence band*. Energies between the conduction and the valence bands form the *bandgap* E_g . Electrons can exist in the conduction or the valence band, but not in the bandgap. In conductors, the conduction and the valence bands overlap, thus there is no bandgap, as illustrated in Figure 2.3. For this reason, electrons can easily move from one band to the other. Finally, E_g tends to decrease with temperature.

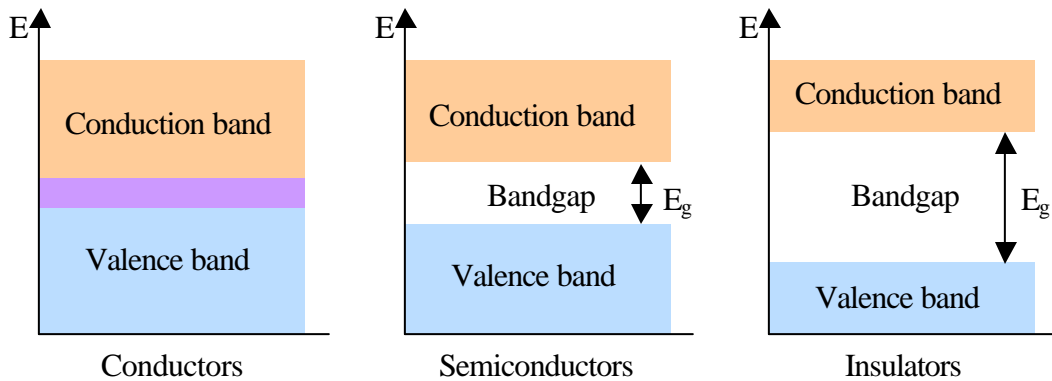


Figure 2.3. Energy bands in various material types.

The number of free electrons, and thus conductivity, can be increased by offering amounts of energy to them at least equal to the bandgap. Obviously conductors do not require any such energy. On the contrary, in order to reach noticeable conductivity levels, insulators require large amounts due to their large E_g . Semiconductors with much less energy reach levels almost as good as conductors.

While electrical systems use exclusively conductors and insulators, electronic systems are entirely based on semiconductors. That is because of their unique ability to behave as conductors and as insulators according to our needs. All diodes, transistors and thyristors are built using semiconductive materials. The most common semiconductors are silicon (Si) and Germanium (Ge) whose atomic structure is shown in Figure 2.5. Those are also called group IV materials due to the number of valent electrons. Additionally, *compound* semiconductors can also be used like Gallium Arsenide (GaAs) and Indium Phosphide (InP). Those are called group III–V materials. Other types may be II–VI like CdS and ZnO, IV–IV like SiC or IV–VI like PbS and PbTe. Most of them can be seen in the brief periodic table of Figure 2.4.

H																	He
Li	Be											B	C	N	O	F	Ne
Na	Mg											Al	Si	P	S	Cl	Ar
K	Ca	Sc	Ti	V	Cr	Mn	Fe	Co	Ni	Cu	Zn	Ga	Ge	As	Se	Br	Kr
Rb	Sr	Y	Zr	Nb	Mo	Tc	Ru	Rh	Pd	Ag	Cd	In	Sn	Sb	Te	I	Xe

Figure 2.4. Abbreviated Periodic Table of elements.

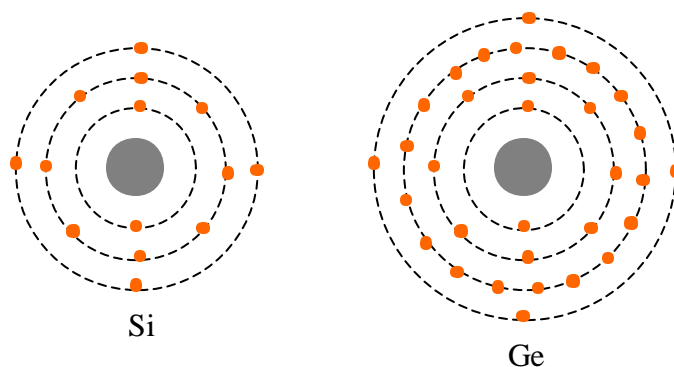


Figure 2.5. Atomic structure of Si and Ge.

B. CRYSTAL STRUCTURES

As mentioned earlier, electrostatic forces of neighboring atoms attract electrons and form ions, in their attempt to reach chemical stability. Electrostatic forces among these ions form symmetric *lattices* that are called *crystals*. One of the simplest crystals is that of O_2 and Ga, producing a simple *cubic* structure. Si and Ge form a more complex crystal called *cubic face centered* as shown in Figure 2.6. Each crystal structure is completely defined by a number called *lattice constant* α .

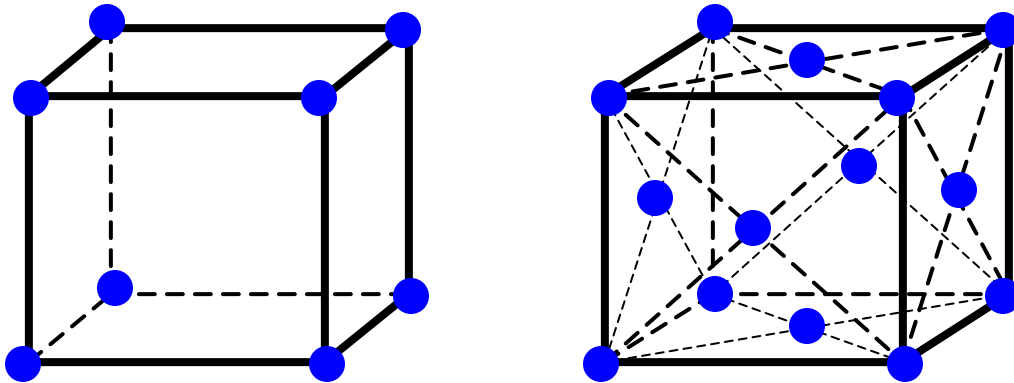


Figure 2.6. Examples of crystal structures.

The crystalline structure is necessary and very important in the production of wafers. Badly-matched structures may display unforeseen electrical behavior and very poor mechanical properties.

Production of crystalline materials in large sizes can be very expensive. Materials composed of very small crystals or grains are called *polycrystalline*. These have inferior properties than crystalline, but are much cheaper to produce. Materials with no crystal uniformity are called *amorphous* and their properties are far inferior, but they are very cheap. They are used where large areas of cheap semiconductive material is needed, such as displays, imagers and terrestrial solar cells etc.

C. CARRIERS

Another way to represent the structure of a semiconductor in two-dimensions is illustrated in Figure 2.7. In this, the valent electrons, being shared among atoms with covalent bonds, are clearly shown. Also shown is the charge of the nucleus (protons) related to those electrons. Since each atom has all four of its valent electrons, it is not electrically charged.

All electrons, initially, exist in the valence band. If an electron somehow absorbs enough energy to enter the conduction band, it breaks the covalent bond, leaves the crystalline structure and becomes free. The atom that owned that electron is now left with an excessive positive charge. This charge is called *hole*. It has a positive charge equal to

the absolute value of the electron's charge and is located where the free electron used to be. Both the free electron and the hole form a pair called *electron-hole pair* (EHP). The above described phenomenon is called *ionization* or *generation*. The production rate of EHP's is a strong function of temperature. On the other hand, electrons moving freely through the crystal tend to recombine with holes. This way EHP's disappear. This phenomenon is called *recombination* and its rate is proportional to the number of existing holes and free electrons. In thermal equilibrium the ionization and the recombination rate are equal keeping the number of EHP's constant.

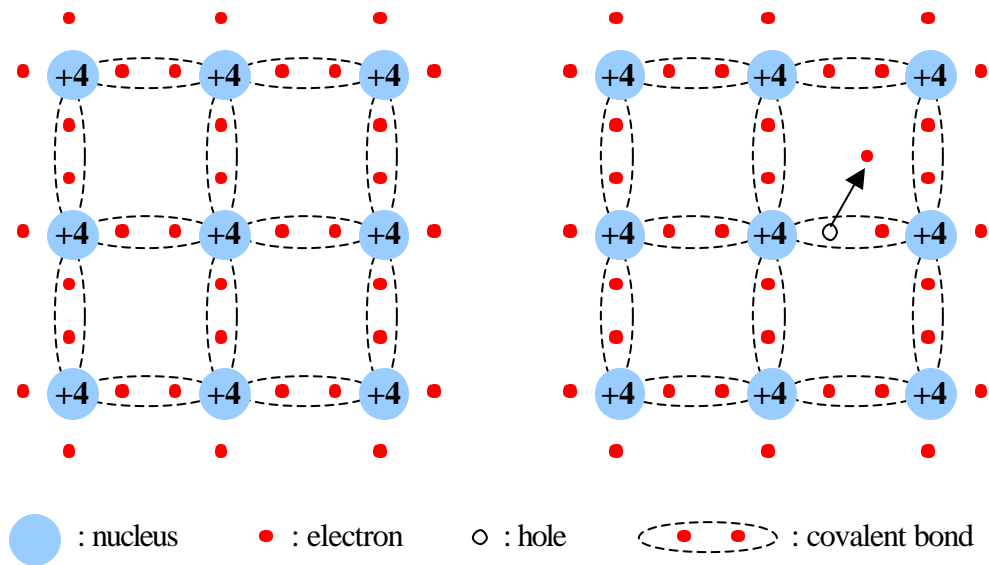


Figure 2.7. Structure of a semiconductor.

Pure semiconductor crystals, that do not contain any foreign atoms, are called *intrinsic*. In an intrinsic semiconductor at 0°K there are no EHP's. As temperature rises, however, the heat absorbed by the material will create a number of EHP's and the conductivity of the material will increase. Since EHP's are responsible for conductivity, they are called *intrinsic carriers*. Their number increases logarithmically. For Si, Ge and GaAs this is shown in Figure 2.8.

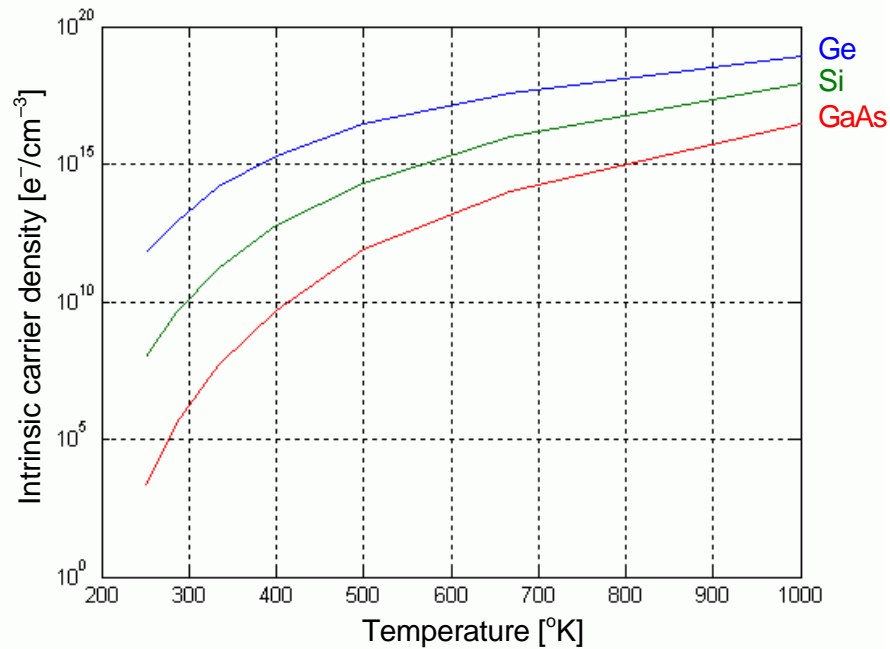


Figure 2.8. Intrinsic carrier density vs. Temperature [after Ref. 2:p. 19].

This number, although it seems large, is actually a very small percentage of the total atoms in the semiconductor. This is better shown in Table 2.2.

Semiconductor	atoms/cm ³	Intrinsic		
		carriers /cm ³	ratio	Bandgap [eV]
Ge	$4.42 \cdot 10^{22}$	$2.4 \cdot 10^{13}$	1 : $1.8 \cdot 10^9$	0.66
Si	$5 \cdot 10^{22}$	$1.45 \cdot 10^{10}$	1 : $3.4 \cdot 10^{12}$	1.12
GaAs	$4.42 \cdot 10^{22}$	$1.79 \cdot 10^6$	1 : $2.5 \cdot 10^{16}$	1.424

Table 2.2 Carrier concentration in intrinsic semiconductors at 300°K
[after Ref. 2:p. 850].

Elements other than semiconductors also have carriers. If an element has three or less electrons in the valence band, then its predominant carriers are holes and it is called an *acceptor*. Usually, acceptors have three valence electrons (*trivalent*). If an element has five or more valent electrons, then its predominant carriers are electrons and it is called a *donor*. Usually, donors have five valent electrons (*pentavalent*). The process of adding

impurities in an intrinsic semiconductor is called *doping*. This way the semiconductor becomes *extrinsic* and obtains new, very important electrical properties.

As a donor atom enters the crystal, it forms covalent bonds with the semiconductor atoms, but also has a number of electrons involved in no bonds with other atoms. Those are loosely held within the donor atom and become free electrons. Because of this excessive number of electron carriers, the material is called *n-type*. Any material can be used as a donor as long as its atom has more valent electrons than the semiconductor atom it replaces. N-type materials are said to have electrons as *majority carriers* and holes as *minority carriers*. On the contrary, acceptor atoms will not have enough valent electrons to share with neighboring semiconductor atoms and a hole will be created. As there is now an excessive number of holes, the material is called *p-type*. Any material can be used as an acceptor as long as its atom has less valent electrons than the semiconductor atom it replaces. P-type materials are said to have holes as majority carriers and electrons as minority carriers. Both types of semiconductors can be seen in Figure 2.9.

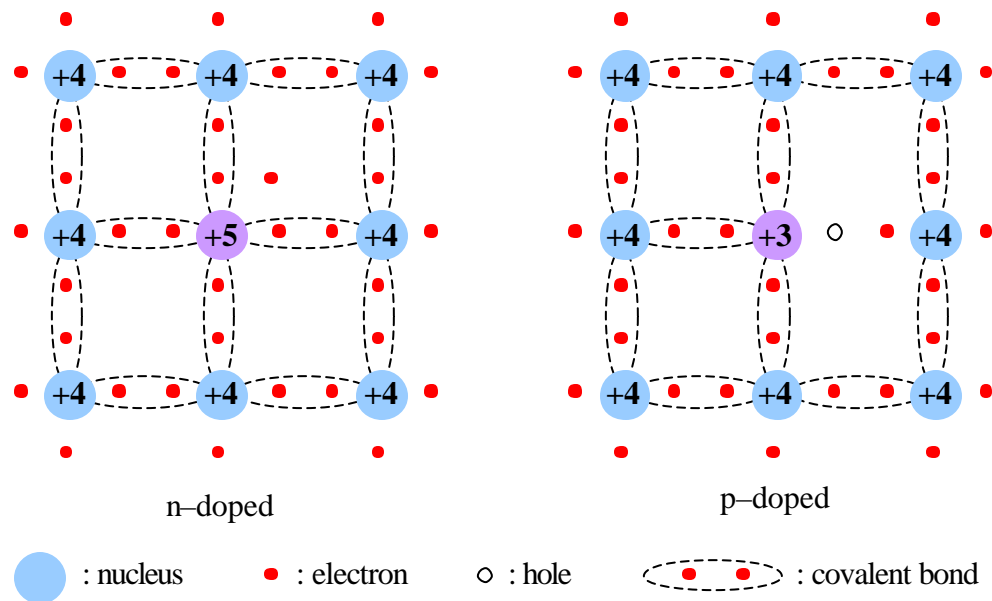


Figure 2.9. Structure of doped semiconductors.

The number of majority carriers is analogous to the doping in a material, while the number of minority carriers is analogous to temperature. Note that both p- and n-type

materials remain neutral. However, the effect of doping is great to the electrical properties of the material even at very small concentrations ($1 : 10^7$). Adding to the previous table, it is shown that the effect on the conductivity and the bandgap is significant:

Semicond.	atoms/cm ³	Intrinsic			Extrinsic		
		carriers /cm ³	ratio	E _g [eV]	carriers /cm ³	ratio	E _g [eV]
Ge	$4.42 \cdot 10^{22}$	$2.4 \cdot 10^{13}$	$1:1.8 \cdot 10^9$	0.66	$4.42 \cdot 10^{15}$	$1:10^7$	0.01
Si	$5 \cdot 10^{22}$	$1.45 \cdot 10^{10}$	$1:3.4 \cdot 10^{12}$	1.12	$5 \cdot 10^{15}$	$1:10^7$	0.05
GaAs	$4.42 \cdot 10^{22}$	$1.79 \cdot 10^6$	$1:2.5 \cdot 10^{16}$	1.424	$4.42 \cdot 10^{15}$	$1:10^7$	

Table 2.3 Carrier concentration in intrinsic and extrinsic semiconductors at 300°K
[after Ref. 2:p. 850].

In a material, the concentration of majority carriers (n_{n0} for electrons in n-type or p_{p0} for holes in p-type materials) is equal to the concentration of carriers created by the semiconductor plus the concentration of carriers created by the impurity. According to the above table this will be approximately equal to the concentration of impurity atoms (N_D for donor or N_A for acceptor).

On the other hand, the concentration of minority carriers (n_{p0} for electrons in p-type or p_{n0} for holes in n-type materials) times the concentration of majority carriers is constant ($p \cdot n = n_i^2$) in thermal equilibrium. According to the above:

	n-type	p-type
majority carriers	$n_{n0} \cong N_D$	$p_{p0} \cong N_A$
minority carriers	$p_{n0} \cong n_i^2 / N_D$	$n_{p0} \cong n_i^2 / N_A$
product $p \times n$	n_i^2	n_i^2

Table 2.4 Carrier concentration relations.

D. FERMIL LEVEL

All the above phenomena are described as very precise and distinct. However, in reality they are ruled by *Heisenberg's* principle of uncertainty. Thus, any reference to the direction, concentration, energy etc of electrons or holes should more precisely be done using probabilistic expressions.

In an intrinsic semiconductor at 0°K, all electrons have energies below a certain level called *Fermi level* E_F . As temperature rises and EHP's are created, electrons of energies higher than E_F appear, populating the conduction band. This is described in the *Fermi-Dirac distribution* function that is equal to:

$$f(E) = \frac{1}{1 + e^{(E-E_F)/kT}}$$

Where E is the electron energy, E_F is the Fermi level, k is Boltzmann's constant and T is the absolute temperature. A plot of $f(E)$ is shown in Figure 2.10.

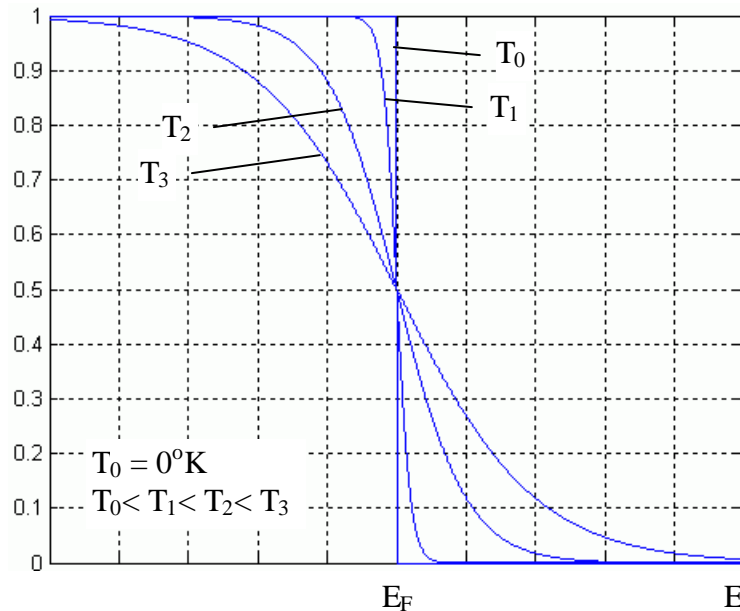


Figure 2.10. Fermi distribution.

As doping takes place, the carrier concentrations change and so do the populations on the various energy levels and the E_F . Dopants introduce more energy levels within the energy bands. This is shown in Figures 2.11 and 2.12.

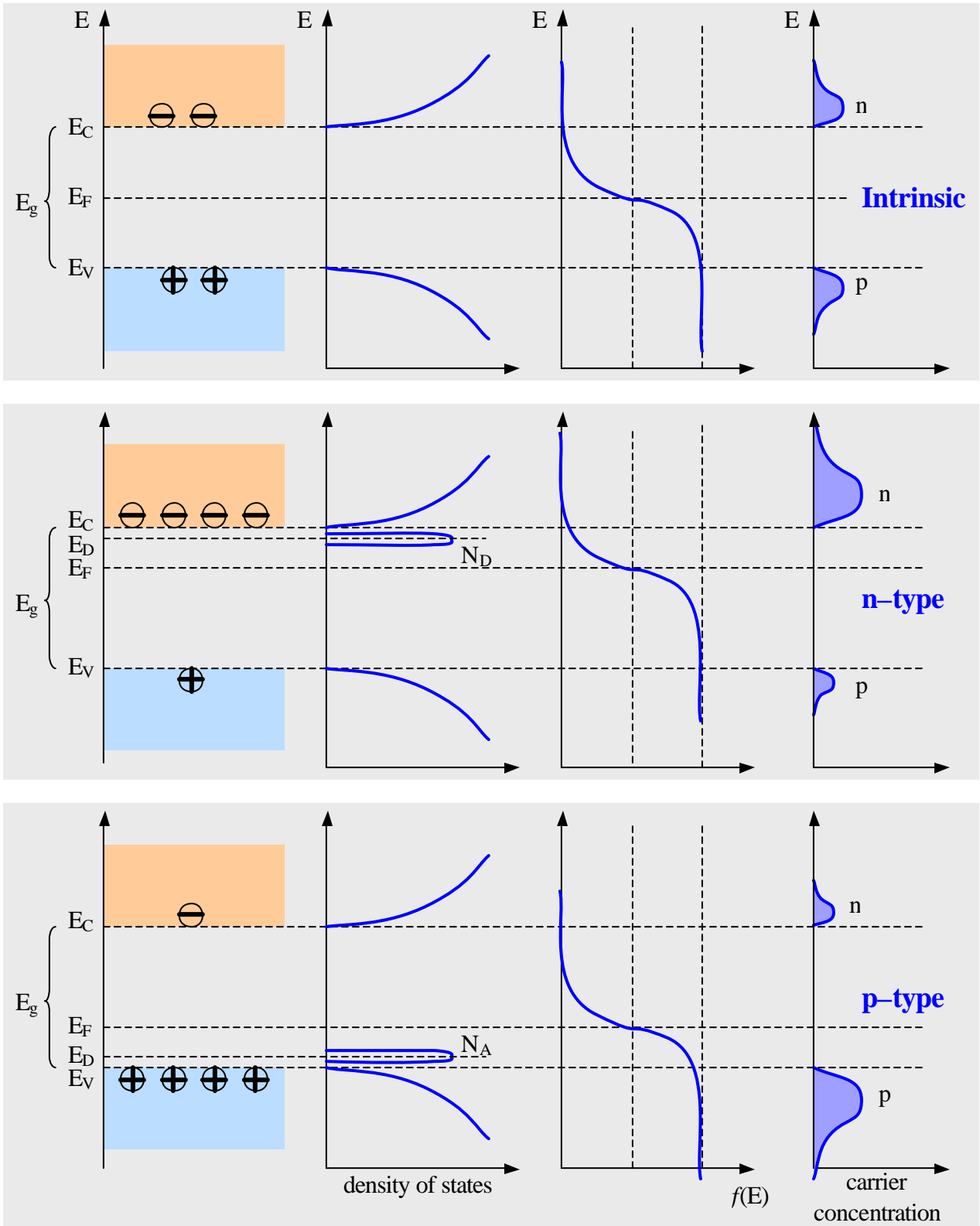


Figure 2.11. Band diagram, density of states, Fermi–Dirac distribution and carrier concentrations [after Ref. 2:p.23].

If a donor introduces energy levels close to the conduction band, then a very small amount of energy is needed to ionize its electrons to the conduction band. This is called *shallow donor*. Similarly, acceptors that introduce energy levels close to the valence band, require little energy to ionize its holes into the valence band. This is called *shallow acceptor*. Dopants away from their corresponding bands are called *deep dopants*. Some materials (like Si) can behave as donors or as acceptors depending on which site (Ga or As in GaAs) of the semiconductor they occupy. Other materials (like Cu and Au) have a very complicated behavior and introduce multiple energy levels. These are called *amphoteric*.

In reality, even the purest semiconductors contain a significant number of both donor and acceptor impurities. Their conductivity type is determined by the prevailing concentration of dopants, as the effect of one dopant is countered (compensated) by the effect of another. Even though all semiconductive materials fall into this category, the ones that contain significant amounts of both dopants are called *compensated semiconductors*. Compensation is used to counter the effects of “unwanted” impurities in a material.

If the concentrations of both dopants are very large and equal, the material is called *strongly compensated*. In spite of the fact that impurities are spread throughout the material, their distribution is not absolutely even. Therefore, energy fluctuations versus position are observed. In some cases, small portions of the conduction band exist below E_F (*electron droplets*) and in others, small portions of the valence band exist above E_F (*hole droplets*). This will introduce unique properties where the material behaves like an insulator containing conductive spots. Also, electrons with low energies and holes with high energies are trapped within the droplets and cannot move around the material like the rest of the carriers (Figure 2.13). As a result the material’s conductivity is affected.

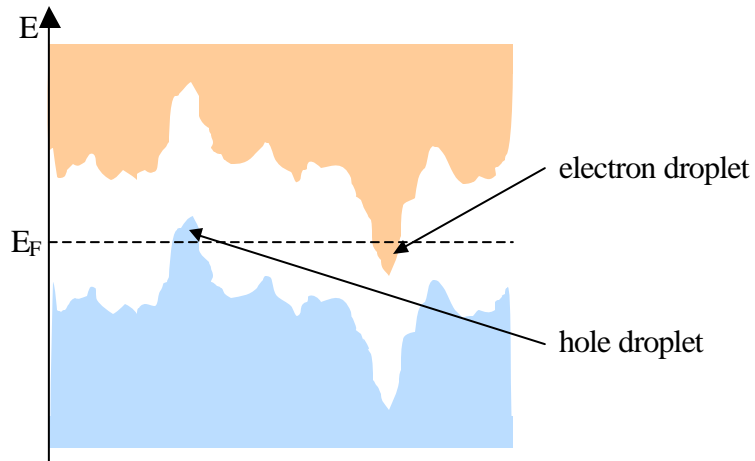


Figure 2.13. Strongly compensated material [after Ref. 3:p. 66].

E. CARRIER TRANSPORT

If there is a higher concentration of carriers in a part of a doped semiconductor, then those carriers will tend to diffuse, spreading evenly all over the material. This is analogous to a gas expanding evenly in a container. The current produced by this movement of carriers is called *diffusion current* (I_D) and is analogous to the majority carrier concentration and thus the doping. The carriers (holes) shown in the following example (Figure 2.14) move to the right, where their concentration is smaller, producing I_D . Note that if the carriers displayed were electrons, I_D would be reversed.

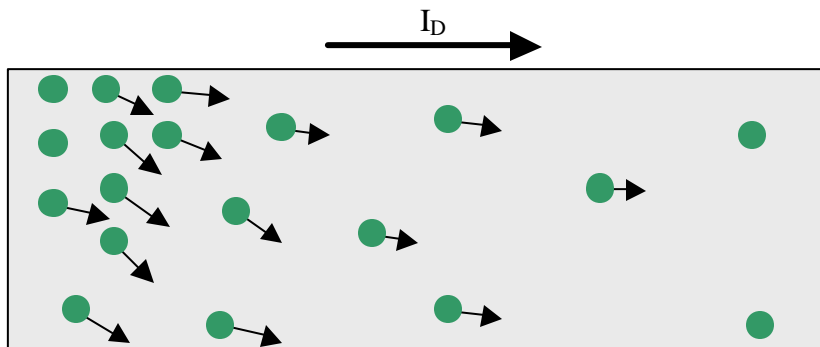


Figure 2.14. Diffusion current.

Current can also be produced by the movement of carriers by an external force, like an electric or a magnetic field. This will produce a current called *drift current* (I_S) and is analogous to the minority carrier concentration and thus the temperature. I_S will obviously be proportional to the intensity of the field, too. Again in the following example (Figure 2.15) the carriers displayed are holes.

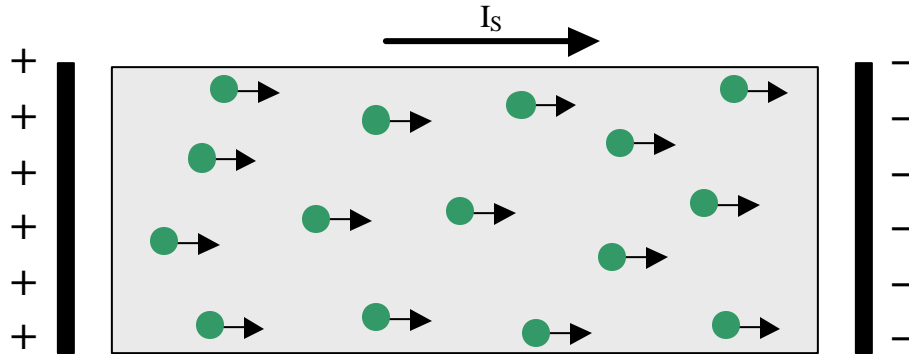


Figure 2.15. Drift current.

F. MOBILITY

We mentioned before that under thermal equilibrium, the population of energy levels is given by the Fermi–Dirac distribution. However, when an electric field is applied, or when light produces EHP’s etc, the material is not under equilibrium. In this case the equations of table 2.4 do not apply. Instead of the Fermi energy level E_F , the electron and hole *Quasi-Fermi* energy levels E_{Fp} , E_{Fn} must now be used. In equilibrium conditions we have $E_F = E_{Fn} = E_{Fp}$. The new distributions become:

$$f_n(E) = \frac{1}{1 + e^{(E - E_{Fn})/kT}}$$

$$f_p(E) = \frac{1}{1 + e^{(E - E_{Fp})/kT}}$$

In vacuum, an electron that exists inside an electric field will accelerate constantly. On the contrary, inside a material, the electron will originally accelerate, but as its speed increases it will collide more and more often with the atoms of the lattice.

Additionally, it will be affected by the charge of ionized impurities in the material. These collisions will decelerate it. Thus, the electron will soon stop accelerating and will reach a constant average speed called *drift speed*. The ratio of that speed to the applied field is called *mobility* μ . Mobility decreases with temperature and impurity concentration (Figure 2.16) due to the *carrier scattering* mentioned above.

Mobility is also reduced near the surface of the material due to surface or interface scattering mechanisms. In order to avoid this, a carrier density gradient can be created by varying the doping density in the semiconductor. Finally, mobility is analogous to the *permittivity* ϵ_s .

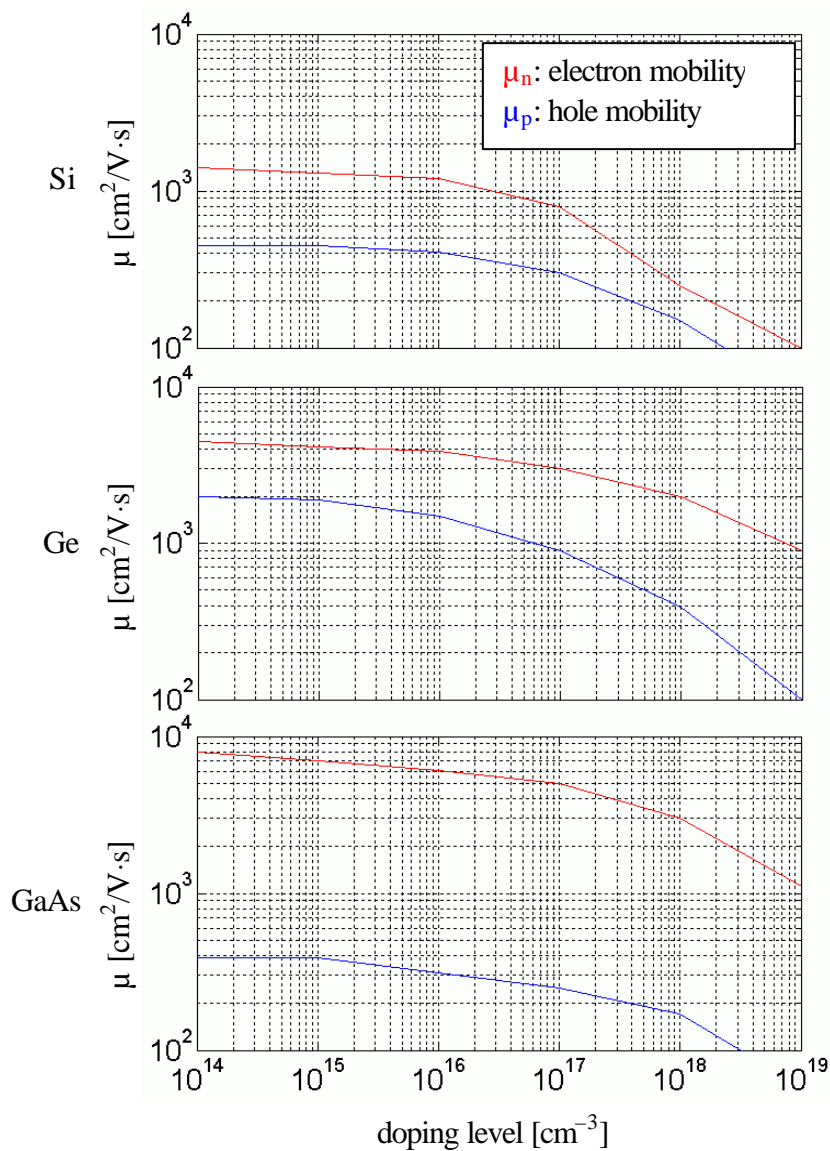


Figure 2.16. Mobility vs. doping level [after Ref. 2:p. 29].

G. RECOMBINATION

Energy–band levels vary as a function of the momentum of electrons. There are materials that have their minimum E_c and their maximum E_v at the same momentum k . Some of them are GaAs, InP etc and are called *direct*. All the others like Si, Ge etc are called *indirect*. In Figure 2.15, E-k diagrams of Ge, Si and GaAs are shown.

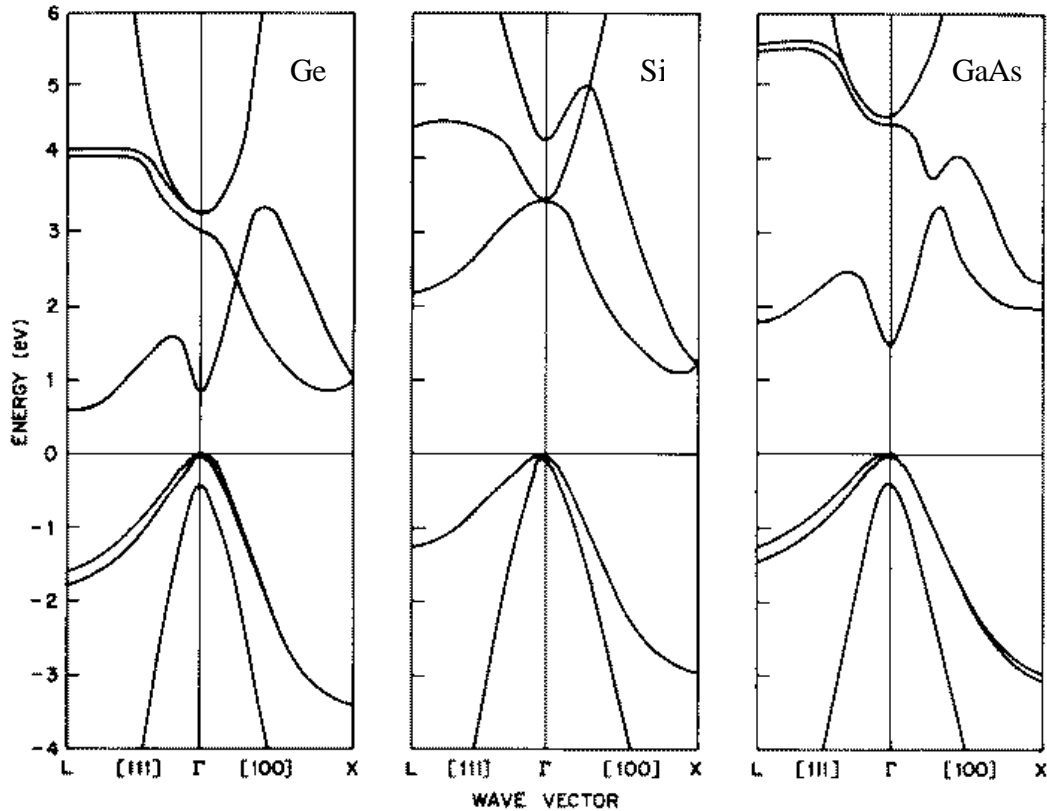


Figure 2.15. Energy–band structures vs. momentum of Ge, Si and GaAs
[after Ref. 2:p. 17].

A hole is actually a position in the lattice missing an electron. As seen in paragraph C, during recombination this empty space becomes occupied by some electron and so this particular EHP disappears. Thus, both electron and hole cease being carriers. During this phenomenon the electron transits into a state of lower energy. In order to do that it must release an energy quantum equal to the difference of its original and its final state. This can be done in three ways:

- emit a photon (radiative recombination)
- emit a phonon (non-radiative recombination)
- kinetically excite another electron (Auger recombination)

Recombination can be characterized as:

- band-to-band or direct recombination
- band-to-impurity, trap-assisted or indirect recombination
- surface recombination
- Auger recombination

Direct recombination is when an electron in the conduction band combines with a hole in the valence band, without change in the electron's momentum. This type of recombination occurs in direct materials such as Ge and GaAs. Since no momentum is required the recombination rate is the highest. The *lifetime* of a carrier is the reciprocal of its recombination rate, therefore in this case this lifetime is very short.

Indirect recombination occurs in indirect materials like Si. Impurities, structural defects of the lattice and interface phenomena can create energy levels inside the bandgap. Those are called *recombination centers* E_r . E_r is filled at equilibrium, however, an electron from there may jump down to the valence band combining with a hole. The energy $E_r - E_v$ emitted is usually offered to the lattice as heat. This way a hole is created in E_r . In a quite similar fashion, an electron from the conduction band may drop down to E_r occupying the hole and releasing energy $E_c - E_r$. Macroscopically, two carriers, a free electron and a hole, have recombined and energy $E_c - E_v$ has been released. The result is the same as direct recombination, but the process is different. This is also known as *Shockley-Read-Hall* (SRH) recombination. Direct and indirect recombination graphs can be seen in Figure 2.18.

As E_r approaches the middle of the bandgap, the recombination rate increases since the energy required for the completion of each step is less. Besides, more than one recombination center may exist in a material. Many of them can participate in an indirect recombination done in multiple steps. This is called *multiple-level recombination* (Figure

2.19). Since the energy required now for the completion of each step is even less, the recombination rate increases further.

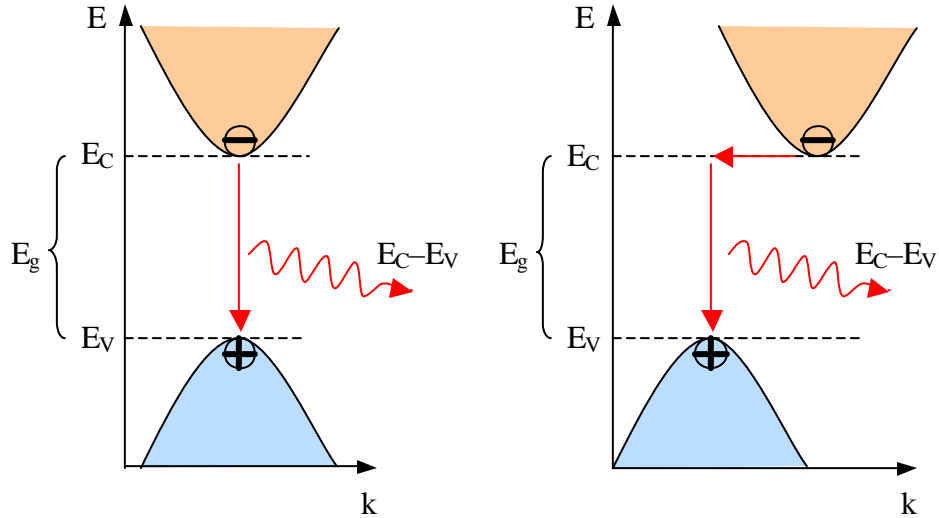


Figure 2.18. Direct and indirect recombination.

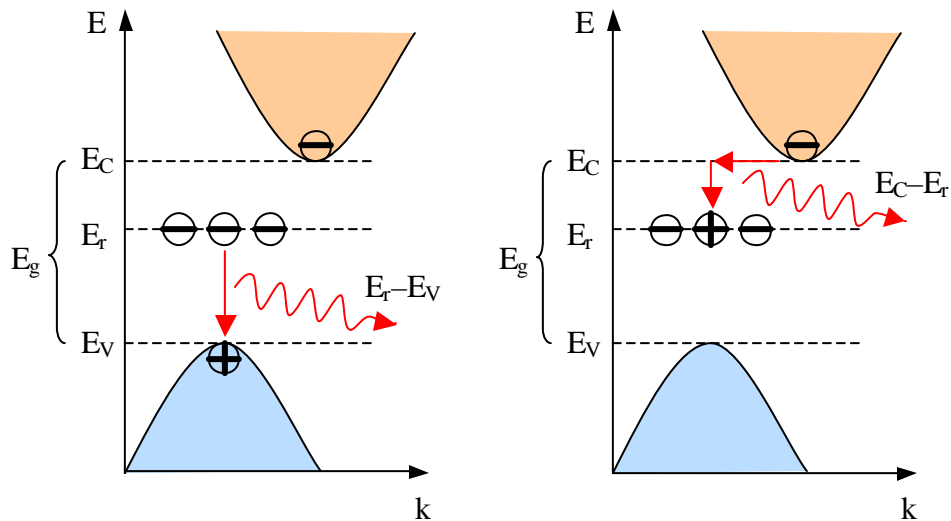


Figure 2.19. 2-level indirect recombination.

Sometimes when an electron moves from E_C to E_r or from E_r to E_V , it is thermally re-excited back to its original state. Since the phenomenon was not completed, recombination did not occur. This is called *temporary trapping* and E_r is called trapping

level E_t . The opposite phenomenon of recombination is the generation of carriers and is called *ionization*. This was discussed in paragraph A.

Surface recombination is due to the dangling bonds at the surface of a semiconductor. This abrupt discontinuity of the lattice introduces a large number of energy states called *surface states*. These serve as recombination centers and thus increase the recombination rate.

We have seen that during impact ionization an electron with high kinetic energy collides with a stationary one and produces an EHP. *Auger recombination* is observed at very highly doped materials and is exactly the opposite. The energy produced by the recombination of an EHP is given to a third carrier. Usually, this energy is later lost to the lattice as phonons.

H. TUNNELING

Assume two isolated semiconductive materials being brought very close to each other. Their band diagram would look like the one in Figure 2.20. According to conventional physics, carriers can move from one material to the other only by going over such energy barrier. This can only be done by obtaining equal or larger energy. On the contrary, quantum physics view the behavior of carriers as probability functions. Consequently, there is always a probability of a carrier going through the energy barrier without changing its energy as in Figure 2.21. *Tunneling* is a phenomenon tightly related to quantum theory. According to this, a carrier with low energy has a probability of jumping to the other side of an energy barrier without increasing its energy. The carrier does not go over the barrier, since that would require energy absorption, rather it goes through the energy barrier (is tunneled) and retains its original energy. This is a phenomenon with many applications in electronics and solar cells, as will be explained in later chapters.

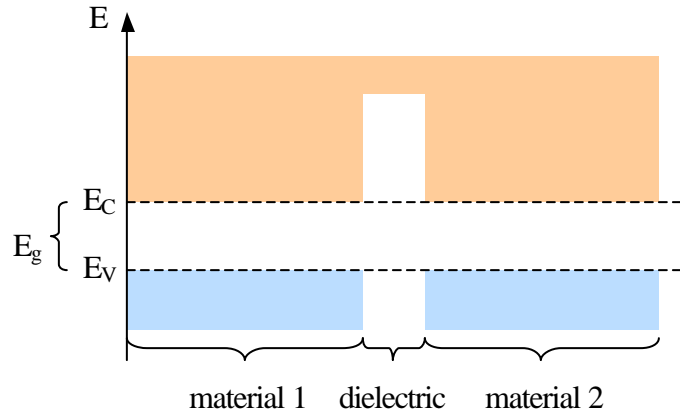


Figure 2.20. Band diagram of two close-by semiconductors.

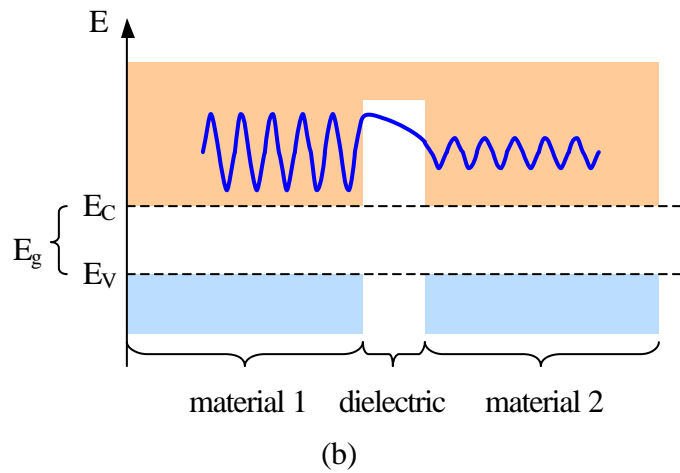
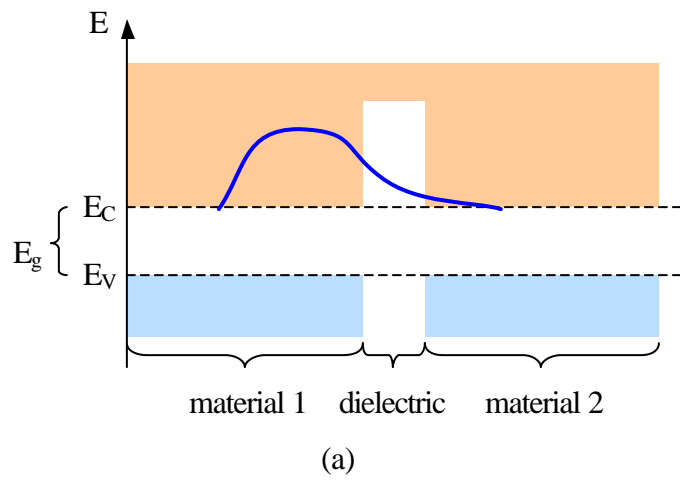


Figure 2.21. Tunneling (a) as probability, (b) as wave function.

III. SEMICONDUCTOR JUNCTIONS

A. P–N JUNCTION

The p–n junction was invented and explained by W. Shockley in “The theory of p–n Junctions in Semiconductors and p–n Junction Transistors” in 1949 [Ref. 2].

1. Formation

It is known that doped semiconductors at equilibrium have no charge and no diffusion current. Assume two such materials, one p–type and one n–type. If they are brought in contact with each other, a series of phenomena are observed.

First of all, holes (majority carriers) from the p–type will begin to diffuse into the n–type. Similarly, electrons from the n–type will begin to diffuse into the p–type. Both will contribute to the development of a large *diffusion current* I_D , which is obviously analogous to the number of majority carriers and thus the doping. During this process, holes diffusing across the junction into the n–type material, will recombine with the existing electrons and both carriers will disappear from the scene. Similarly, electrons diffusing across the junction into the p–type material will recombine with the existing holes and will, again, disappear. This carrier depletion will lead to the formation of an area near the junction where no carriers will be present. This area is called the *depletion region*.

At the same time, impurity atoms, in the depletion region, that have lost their carriers are either positively (donors) or negatively (acceptors) charged. Consequently, a negative charge will be built up at the p–doped side of the junction and a positive charge at its n–doped side. This, in turn, will form an electrostatic field that will oppose the diffusion of carriers. Also, minority carriers on each side will be forced by this field to their opposite ends creating a small *drift current* I_S due to thermal generation. This is obviously analogous to the number of minority carriers and thus the temperature. As time progresses, the charge build–up (and therefore the field and the depletion region)

becomes bigger and so does I_S , while I_D decreases. A steady state is reached when I_S becomes equal in magnitude to I_D .

A voltage differential V_0 of about 0.7V for Si or 0.1V for Ge is developed between the two materials with its negative side on the p-doped material. This is a *barrier voltage* that is responsible for the reduction of I_D . However, this voltage cannot be measured physically. If we attempt to attach electrodes on the materials to measure it, then another junction will be created between each electrode and the semiconductor. These will develop voltages equal, but opposite to the original. So, the total voltage and the external current will be zero. If that was not the case, then the p-n junction could be used as a power source producing electricity out of nothing. This would be against the *energy conservation principle*. A p-n junction is shown in Figure 3.1.

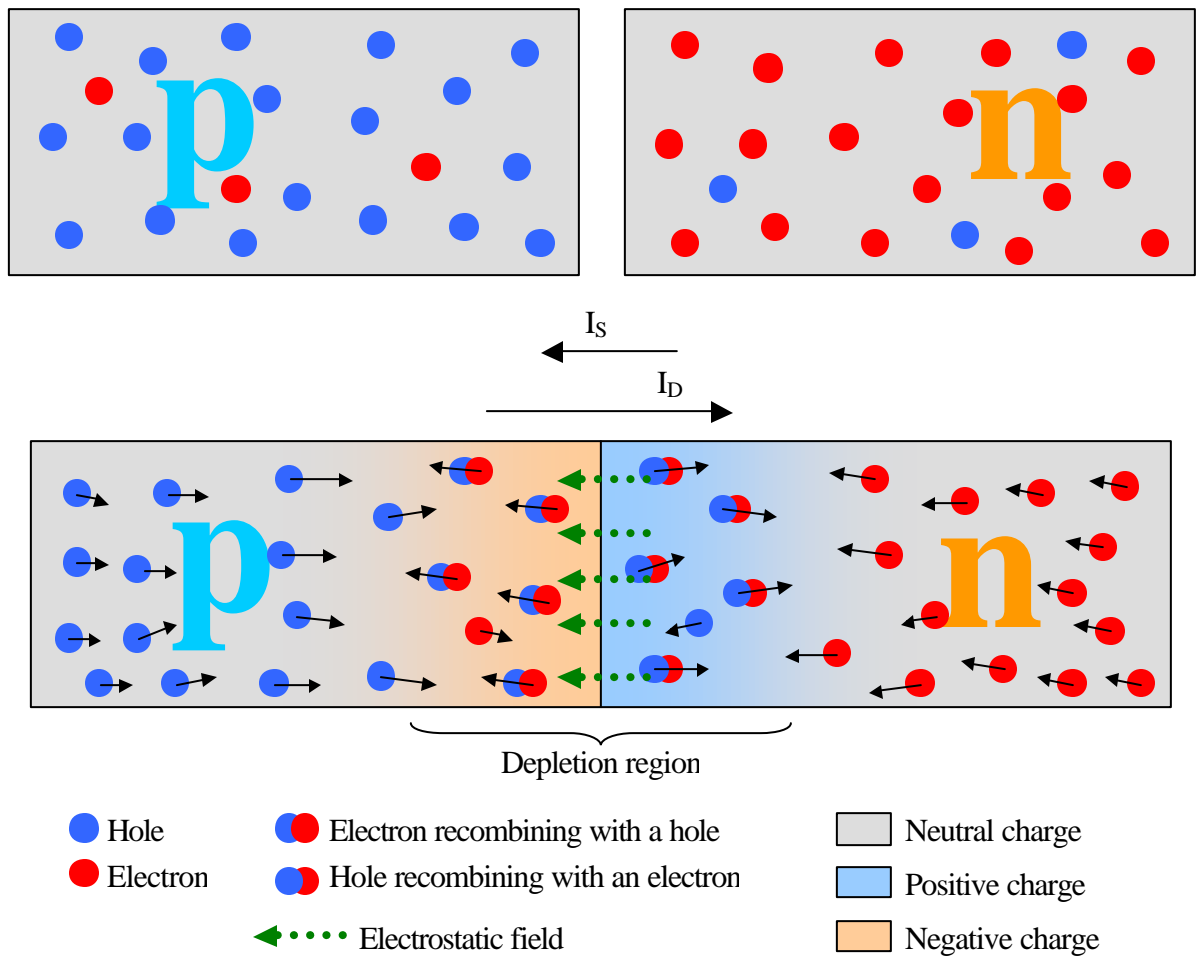


Figure 3.1. Schematic of p-n junction formation.

From an energy-level point of view, the p- and the n-type materials have different Fermi levels. As the two materials become connected, the exchange of carriers will equalize the Fermi levels. Also, a gradual interface is formed between the two conduction and valence energy levels, as shown in Figure 3.2.

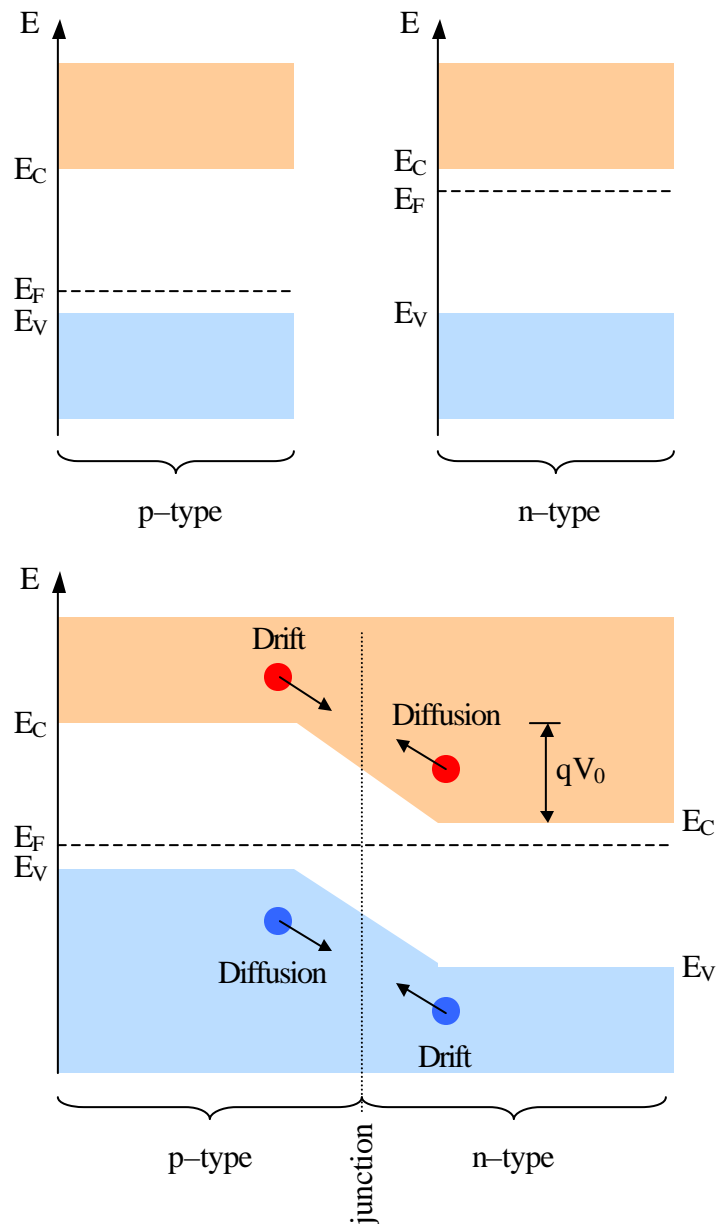


Figure 3.2. Band diagram of p-n junction formation.

2. Forward Bias

Assume that a voltage is applied externally to the junction as illustrated in figure 3.3. A large number of majority carriers will be constantly provided on both ends. These carriers will tend to diffuse towards their opposite ends. Additionally, the external voltage applied will force (*inject*) majority carriers to their opposite ends. In the process, they will neutralize the charge in the depletion region, narrowing it. Therefore, the barrier voltage across the junction becomes smaller and so I_D increases greatly. At the steady state, $I_D - I_S = I$ or $I \cong I_D$, which is very large. This is called *forward bias*. A representation is shown in Figure 3.3 and the band diagram in Figure 3.4.

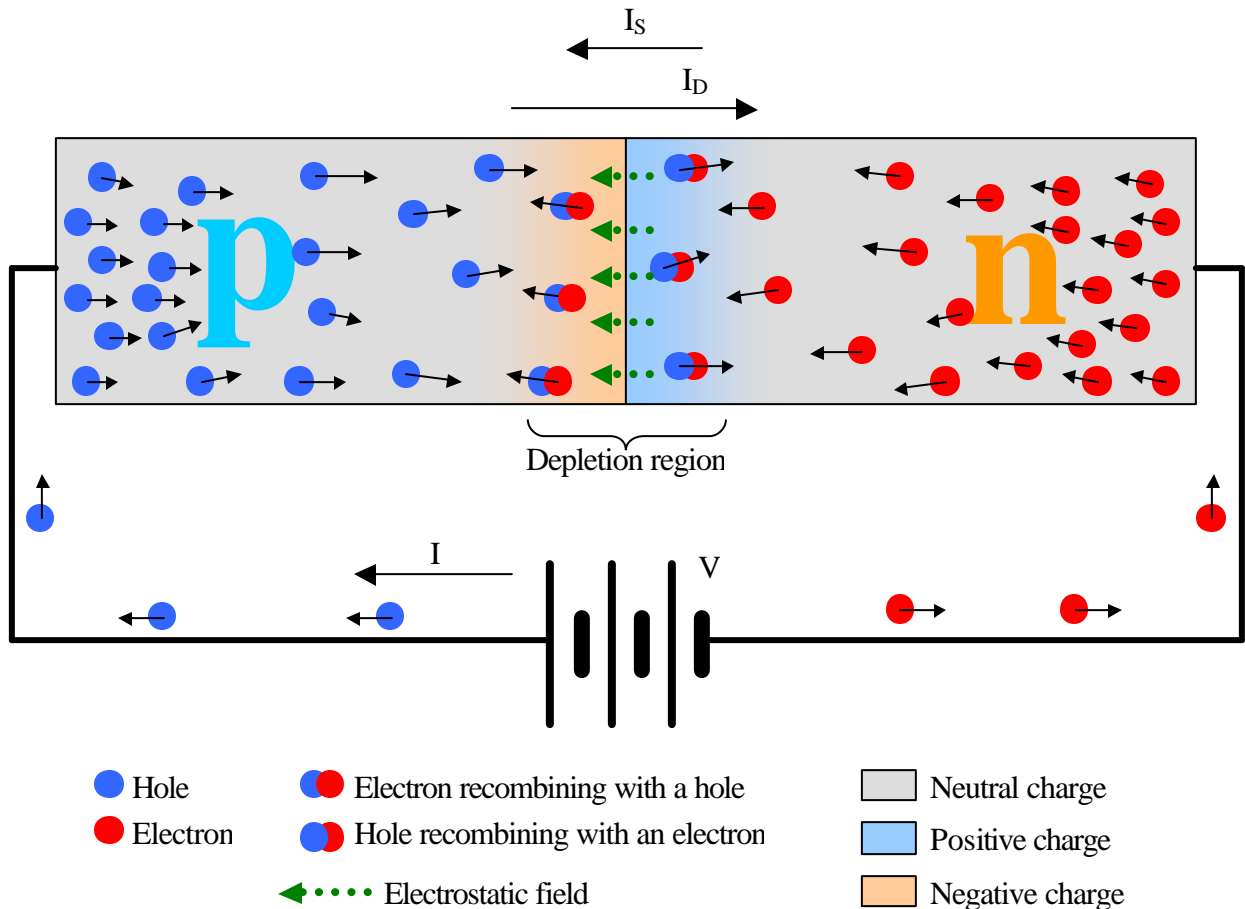


Figure 3.3. Schematic of a forward biased p–n junction.

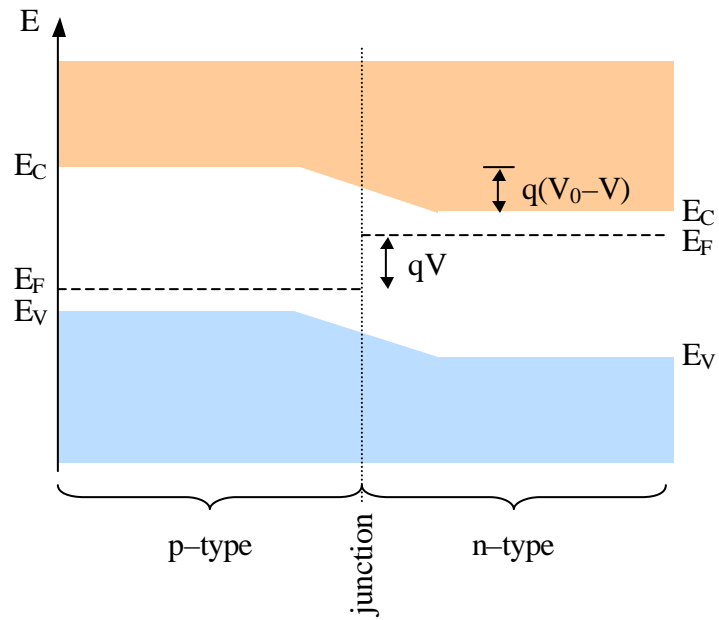


Figure 3.4. Band diagram of the forward biased p-n junction.

If we record the current I over the voltage V , we get the *characteristic curve* of the forward biased p-n junction. This looks like the one in Figure 3.5, where $V_D = V_0$ is equal to 0.7V for Si or 0.1V for Ge. Note that I increases greatly for only a small increase of V after V_D .

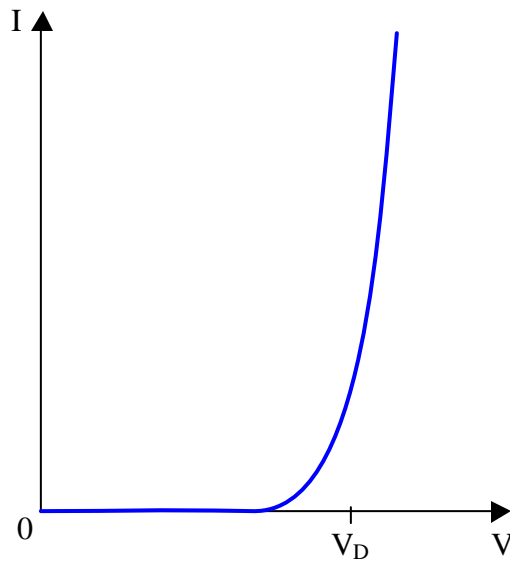


Figure 3.5. Characteristic curve of the forward biased p-n junction.

3. Reverse Bias

Assume now that voltage is applied externally to the junction in the opposite way, as shown in figure 3.6. In this case the external source will draw majority carriers from both sides and provide them with excessive minority carriers. This will increase the imbalance of charges near the junction, widening the depletion region, increasing the barrier voltage and therefore decreasing I_D . At the steady state $I_S - I_D = I$ or $I \cong I_S$ which is very small. This is called *reverse bias*. A representation is shown in Figure 3.6 and the band diagram in Figure 3.7.

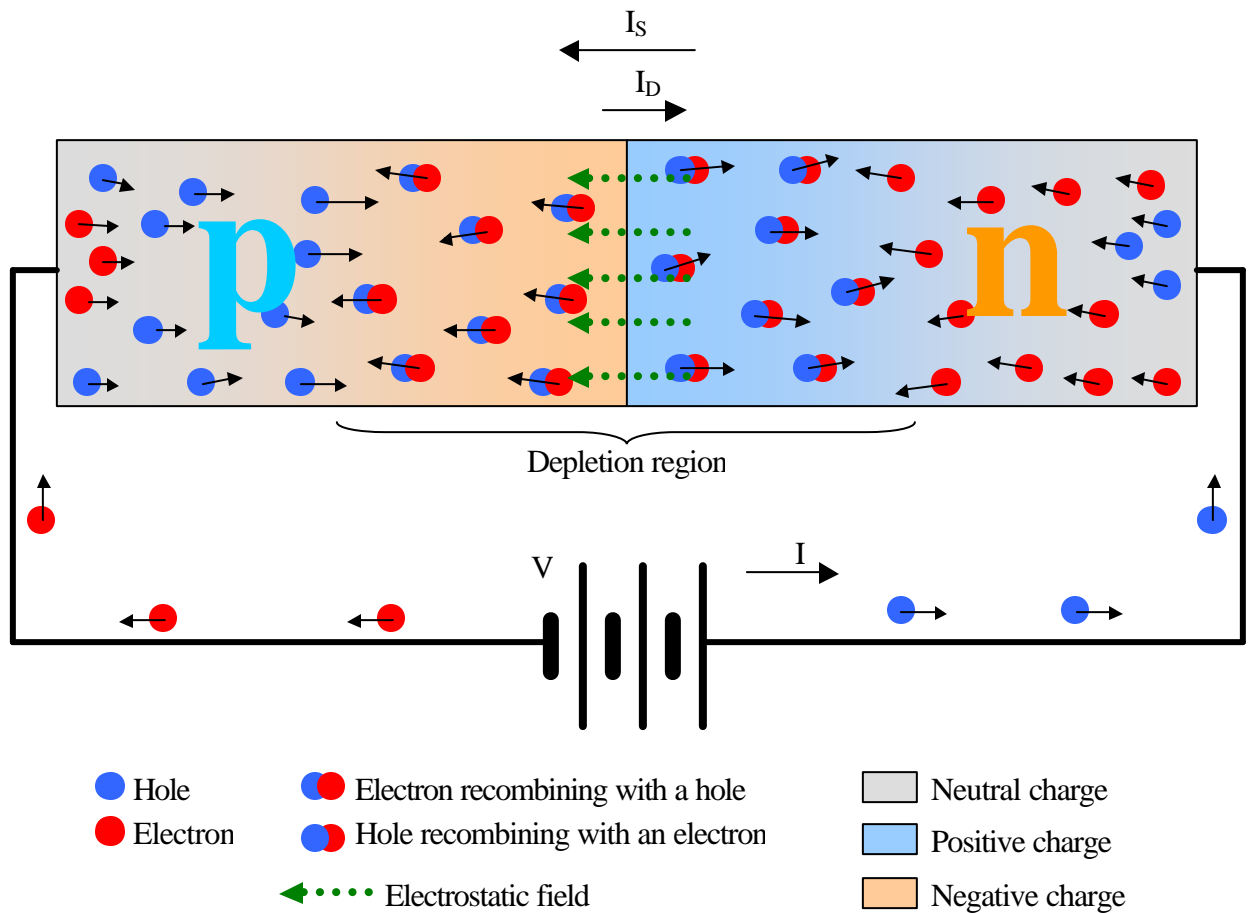


Figure 3.6. Schematic of a reverse biased p-n junction.

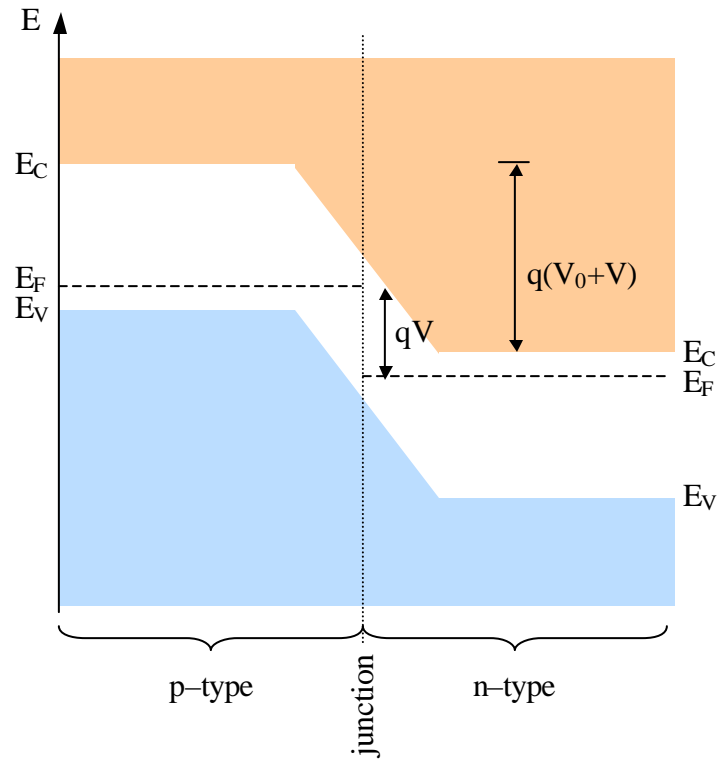


Figure 3.7. Band diagram of the reverse biased p-n junction.

The characteristic curve for the reverse biased p-n junction can be seen in Figure 3.8.

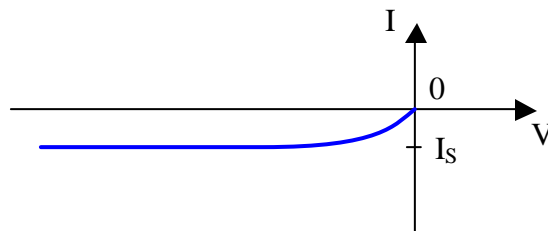


Figure 3.8. Characteristic curve of the reverse biased p-n junction.

4. Breakdown

Assume a reverse-biased p-n junction. It is explained that for any external voltage V the current I is small and approximately equal to I_s . However, if V increases above a certain threshold, the current suddenly becomes very large as if the junction was forward-biased. This threshold is called *breakdown voltage* V_Z . There are two phenomena that are responsible for this behavior. For instance in Si, if $V_Z < 5V$ then the predominant mechanism is the zener effect, if $V_Z > 7V$ it is the avalanche effect and if $5V < V_Z < 7V$ then either or both effects occur and contribute to the breakdown phenomenon.

In the *zener effect* (or *tunneling effect*), the electrostatic field in the depletion region is strong enough to break covalent bonds and generate EHP's. From an energy point of view, an electron is tunneled from the valence to the conduction band, penetrating through the bandgap. Due to the same field, created minority carriers will be swept to the opposite side. Thus, electrons will be forced to the n-doped and holes to the p-doped region. This exchange of minority carriers is so intense that creates a large current equal to I . With only small changes in V the current I varies greatly.

In the *avalanche effect* (or *avalanche multiplication*), the minority carriers that go through the depletion region have very large kinetic energy. As they collide with atoms they are able to break covalent bonds and create EHP's (impact ionization). This is also called *ionizing collision*. The new carriers created may have sufficient energy to repeat this phenomenon and create more EHP's. This continues in the form of an avalanche. Again, minority carriers are swept to their opposite sides and this creates a large current I with only small changes in V .

The avalanche effect is more sudden and abrupt than the zener effect. However, neither is destructive as long as the power dissipated is less than the maximum allowed by the physical characteristics of the device.

5. Capacitance, Ohmic Losses and Overview

The existence of charge in the depletion region also behaves like a capacitor. Since this charge is more when the junction is reverse-biased, its capacitance is also higher. There are many applications (ie tuning) that make use of this property. However, in most cases it is parasitic and designers try to eliminate it because it limits high-frequency operation.

Like every non-ideal material, p-n junctions have inherent ohmic resistances throughout all their mass. These are usually very small and most times negligible due to the high doping of the materials. However, this is still a factor when very small signals are applied.

Overall, the p-n junction has a characteristic that looks like the one in Figure 3.9:

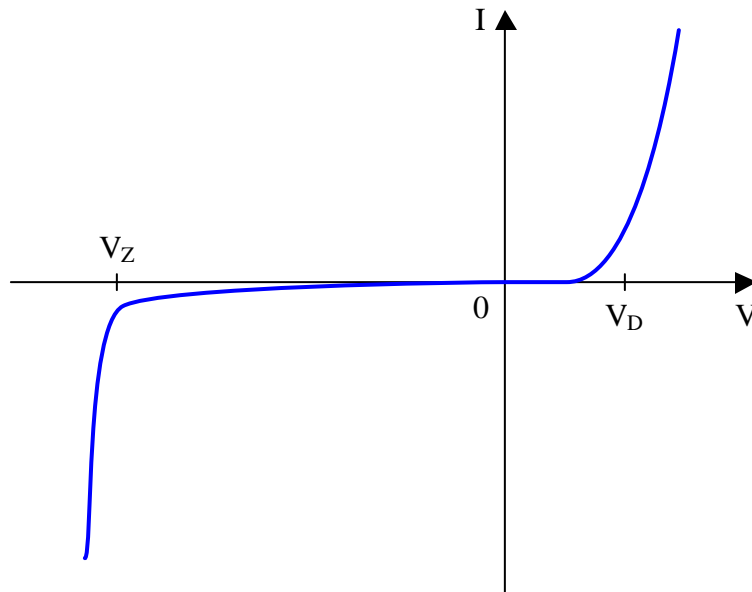


Figure 3.9. Characteristic curve of the p-n junction.

B. M–S JUNCTION

The first semiconductor device was actually the *metal–semiconductor junction* (M–S), which was invented by Braun as early as 1874. Its concept is simpler than the p–n junction explained before.

The energy difference between the Fermi level E_F and the energy level of the vacuum (*vacuum level*) is called the *work function*. When two materials make contact, at equilibrium, the Fermi levels become equalized. The work function of each material remains unchanged except near the junction. There, the vacuum levels become continuous with a gradual interface, thus affecting the work function. In our case, when a metal and a semiconductor make contact, their energy bands are shown below. Note the energy barrier formed which obstructs the exchange of carriers across the junction (Figure 3.10).

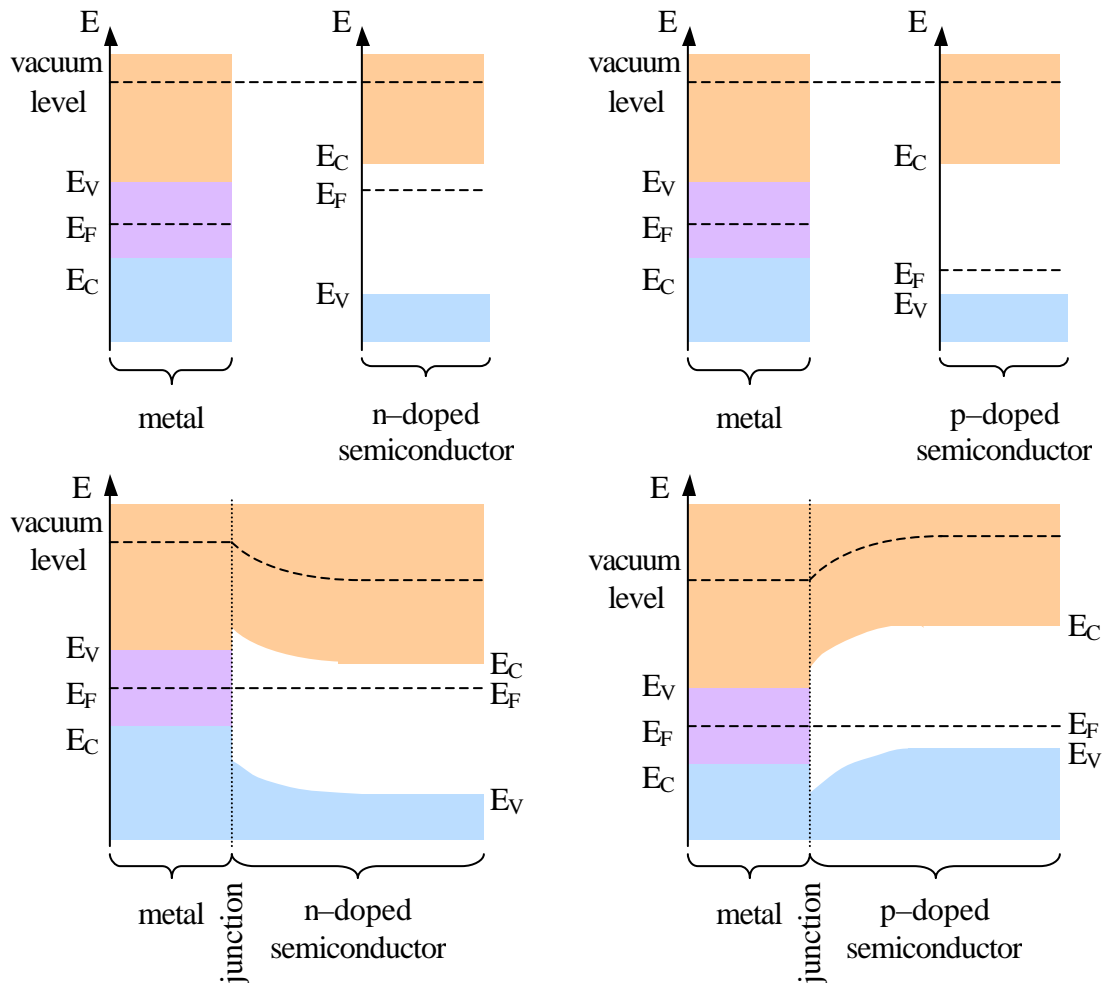


Figure 3.10. Band diagram of M–S junction formations.

If a voltage is applied to an M-S junction, the energy bands change levels. Assume a junction with n-doped semiconductor. If the potential of the metal is more positive than the potential of the semiconductor, then the barrier becomes smaller and electrons move from the semiconductor to the metal easier. This is an *ohmic junction*. On the contrary, if the potential of the metal becomes more negative, the barrier increases and electrons can no longer move from the semiconductor to the metal. This is a *rectifying junction*.

The same is also illustrated below using current densities. For the non-biased junction with n-doped semiconductor, the current densities in the metal and in the semiconductor are balanced. The current from the metal to the semiconductor (M→S) and the one from the semiconductor to the metal (S→M) are equal and so no total current is observed.

In ohmic mode, the semiconductor energy levels are raised. The M→S current remains the same since the barrier height is unchanged in that side. However, the barrier height becomes smaller on the semiconductor side and therefore, the S→M current largely increases and prevails over the M→S.

Similarly, in rectifying mode, the M→S current remains the same, but now the S→M current decreases and the total current observed is very small. Using the same reasoning, corresponding conclusions can be derived for a junction with p-doped semiconductor. All three cases are shown in Figure 3.11.

The general characteristic and use of the M-S junction is very similar to those of the p-n junction. Its big advantage, however, is the fact that its capacitance is much smaller – due to the absence of minority carriers – and that makes it ideal for high-frequency applications. The M-S junction is also called a Schottky junction.

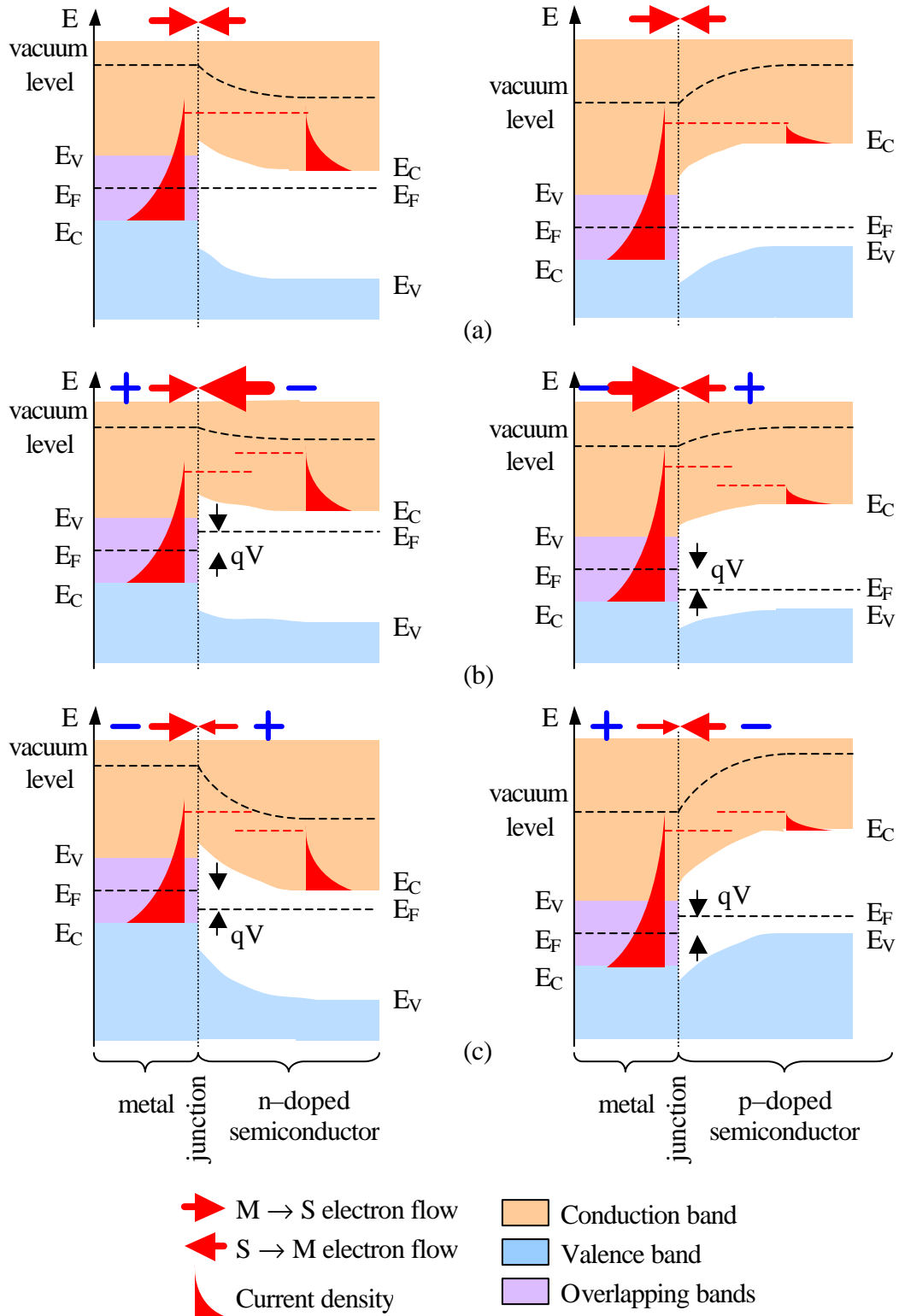


Figure 3.11. Band diagram and currents of: (a) non-biased, (b) forward-biased and (c) reverse-biased M-S junctions [after Ref. 1].

C. OHMIC CONTACT

If the interface region of an M-S junction is highly doped, then the barrier region developed is quite narrow. When any kind of bias is applied to the junction, electrons do not go over the barrier, instead, they are tunneled through it. This changes its behavior totally making it resemble a regular small ohmic resistance. This is called a *tunneling ohmic contact*. It is represented in Figure 3.12 and its characteristic can be seen in Figure 3.13.

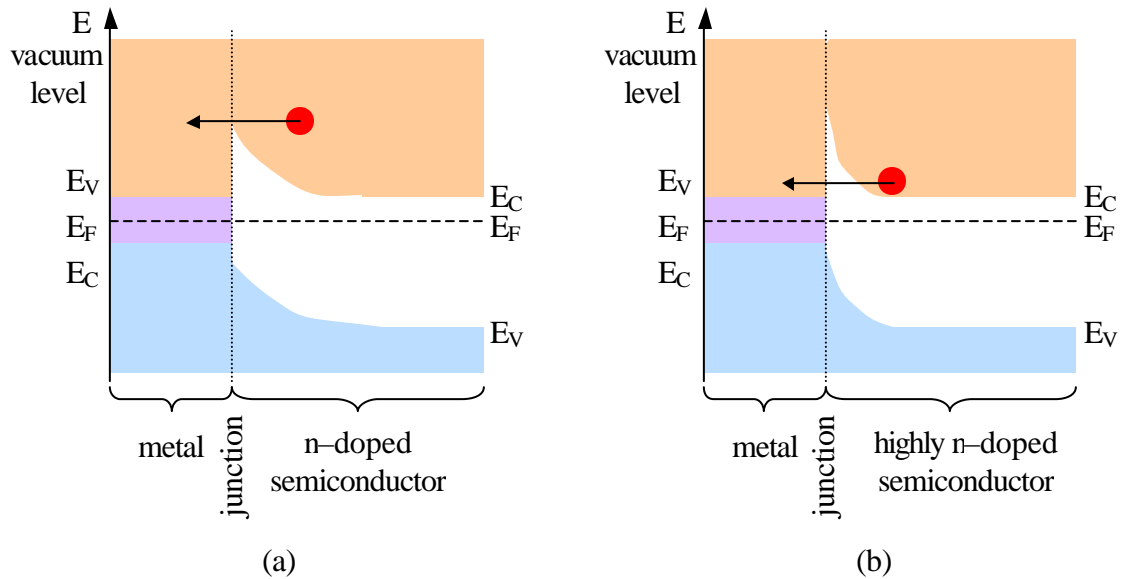


Figure 3.12. Band diagram of: (a) Schottky and (b) tunneling ohmic junction.

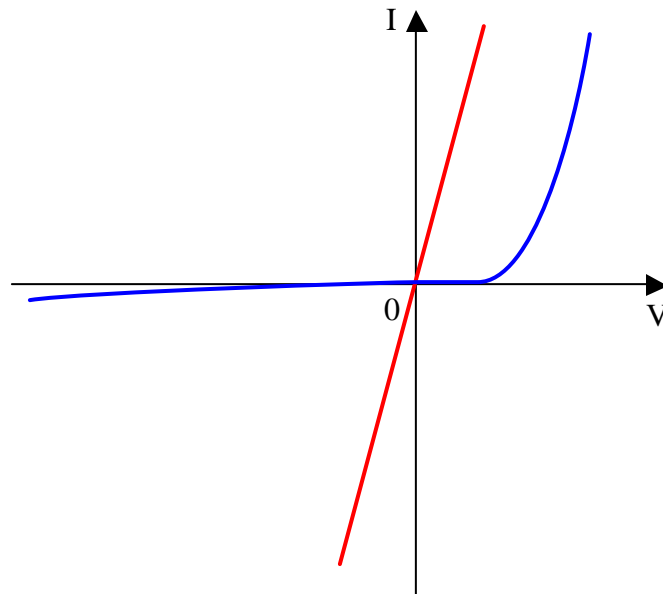


Figure 3.13. Characteristic curves of an ohmic (red) and a Schottky (blue) junction.

D. TUNNEL JUNCTION

The regular p–n junction as described earlier is built using lightly doped materials. The concentration of impurities is around $1:10^7$ atoms of semiconductor. In 1958, the Japanese scientist *Leo Esaki* created a p–n junction using highly doped materials with impurity concentration around $1000:10^7$ making them degenerate. The new junction develops a region of differential negative resistance, not seen in any other device. This is called *tunnel junction*.

As shown in the energy diagram of Figure 3.14, the Fermi levels exist within the bands themselves, due to the heavy doping. This creates a unique formation of the bands' interface around the junction. For the same reason, the depletion region is far narrower than this of a regular p–n junction. This enables electrons to be tunneled through the barrier, without any change in their energy, instead of going over it. This is called *band-to-band tunneling*. The tunneling phenomenon was explained in the previous chapter.

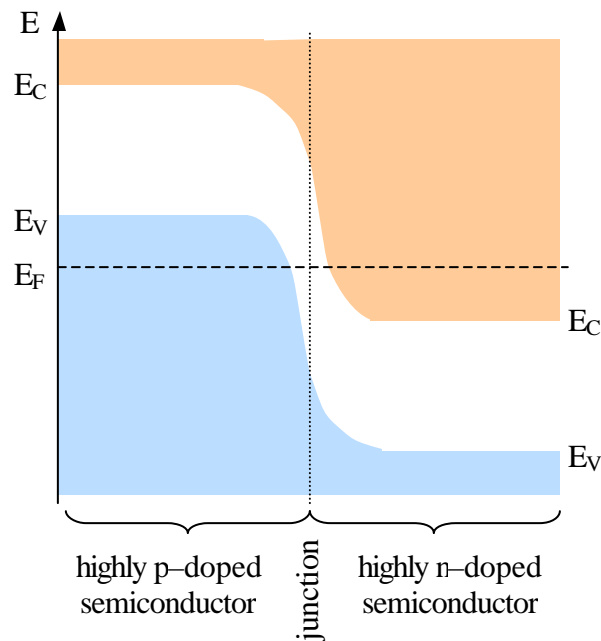


Figure 3.14. Band diagram of a tunnel junction.

In the characteristic I-V curve (Figure 3.15), the forward current is increasing to a peak I_p at V_p and then is decreasing to a smaller valley current I_v at V_v , only to increase again like a regular p-n junction. The region between V_p and V_v is that of negative resistance.

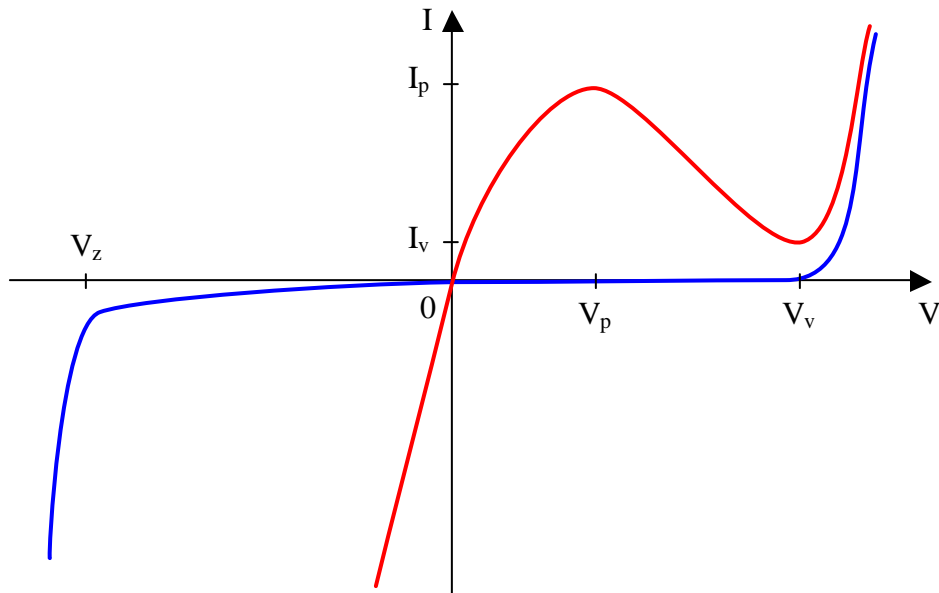


Figure 3.15. Characteristic curves of a tunnel (red) and a regular (blue) p-n junction.

From the carrier transport point of view the I-V curve is formed in the following way. When the junction is reverse-biased, tunneling of electrons from the p-side valence band to the n-side conduction band is observed (Figure 3.16a). If the bias is zero the electrons tunneled from the p- to the n- side are in balance with those tunneled the opposite direction and so no current is observed (Figure 3.16b). If forward bias is applied, electrons are tunneled from the n-side conduction band to the p-side valence band increasing the current (Figure 3.16c). As the bias increases, the common energy levels of the n-side conduction band and the p-side valence band are reduced and so the current decreases (Figure 3.16d). As the bias increases further, a point is reached when there are no more common energy levels and so tunneling can no longer occur. Electrons now flow from the n-side to the p-side conduction bands, absorbing energy and going over the barrier like a regular p-n junction (Figure 3.16e).

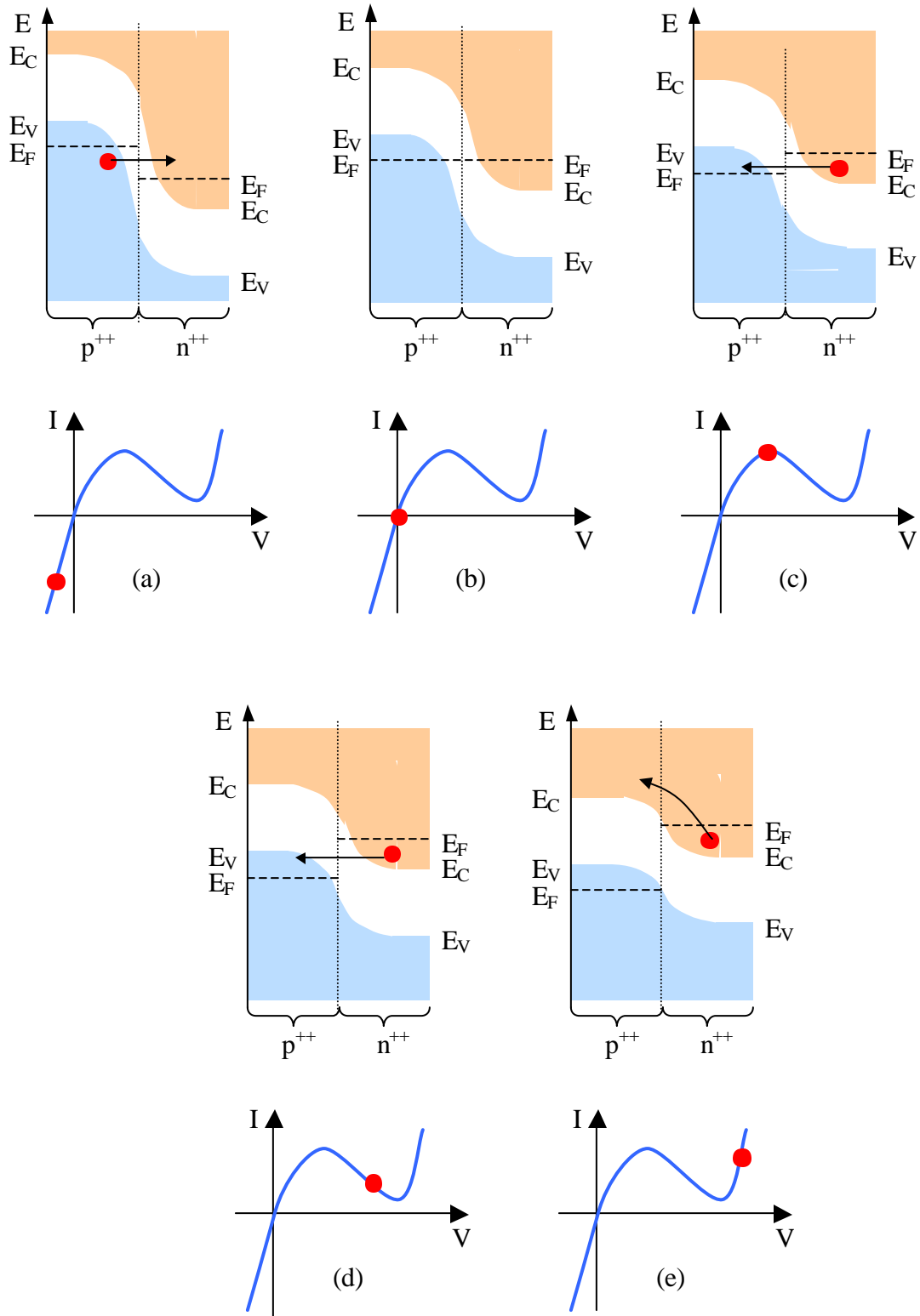


Figure 3.16. Tunnel junction energy diagrams for each section of the I–V curve [after Ref. 2:p. 518].

Characteristic curves of the so common Ge and GaAs are shown in Figure 3.17. Other ways to build tunneling junctions are by using *metal–insulator–semiconductor* or *metal–insulator–metal* technologies. Tunnel junctions have many applications in high frequency circuits as well as multijunction solar cells as explained in the next chapter.

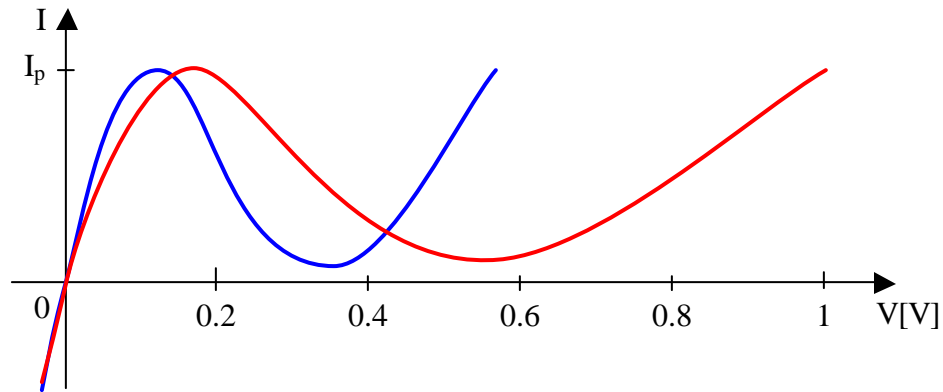


Figure 3.17. Characteristic curves of a Ge (blue) and a GaAs (blue) tunnel junction [after Ref. 2:p. 530].

E. DIRECT AND INDIRECT TUNNELING

In the previous chapter the direct and indirect materials were defined and their recombination differences were explained. Similar differences exist in tunneling, too. Electrons are tunneled from the minimum of the conduction band energy–momentum ($E-k$) curve to the maximum of the valence band $E-k$ curve. In *direct tunneling*, those two points have the same momentum. Direct tunneling occurs in direct bandgap materials, but also in indirect materials when the applied voltage is large enough to accelerate electrons sufficiently to transition between the bandgap at equal point of momentum.

When the minimum of the conduction band $E-k$ curve is not the same as the maximum of the valence band $E-k$ curve, the phenomenon is called *indirect tunneling*. This difference in momentum Δk is supplied by phonons or impurities. In *phonon–assisted* tunneling, the sum of the phonon energy plus the initial electron energy must equal the final electron energy after the tunneling.

$$E_e(\text{init}) + E_{\text{ph}} = E_e(\text{fin})$$

Similarly, the sum of the phonon momentum plus the initial electron momentum must equal the final electron momentum after the tunneling.

$$k_e(\text{init}) + k_{\text{ph}} = k_e(\text{fin})$$

This way, both energy and momentum are conserved.

Direct tunneling, when possible, has a larger probability of occurrence than indirect. Also, indirect tunneling with only one phonon is more probable than with several phonons (Figure 3.18).

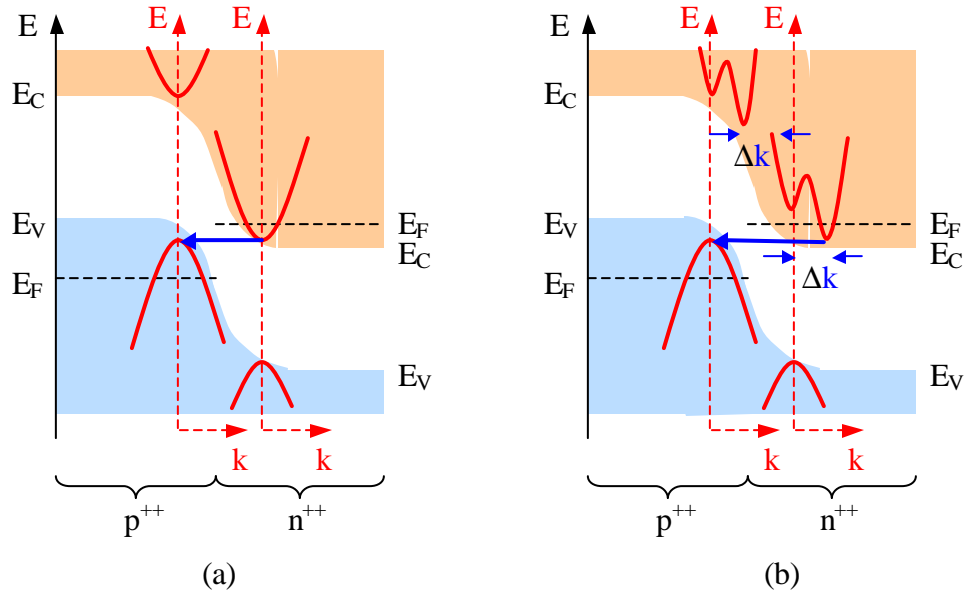


Figure 3.18. Direct (a) and indirect (b) tunneling [after Ref. 2:p. 519].

F. HETEROJUNCTIONS

A junction created by the same semiconductive material is called *homojunction*. As both sides of the junction have the same lattice constant, the crystal atoms form smooth chemical bonds in the interface area. Homojunctions of materials with the same type of conductivity (p- or n-type) are called *isotype* while those with a different one are called *anisotype*.

Junctions created using different materials are called *heterojunctions*. Since now the lattice constants do not match, the atoms create chemical bonds in the *heterointerface* by adjusting their positions. This creates strain and causes crystal dislocations and structure imperfections in depth. This will increase carrier scattering and hence decrease their mobility. Additionally, atoms with dangling bonds will form carrier traps acting as recombination centers, which will decrease carrier lifetime (Figure 3.19).

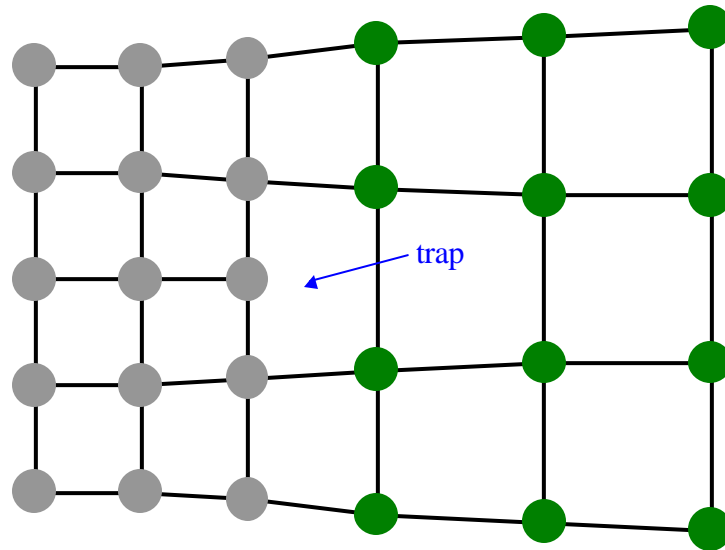


Figure 3.19. Crystal dislocation in heterojunction.

For this reason, materials with similar lattice constants are used, like GaAs with AlAs. The use of ternary compounds, like GaP + InP, is also recommended, as their proportion can adjust their lattice constant to the required levels. $(\text{GaP})_{0.51}(\text{InP})_{0.49} \equiv \text{Ga}_{0.51}\text{In}_{0.49}\text{P}$ is matched to GaAs.

Another way is to choose a substrate crystal plane that is slightly offset from a major crystal plane so that the distance between the atoms on the substrate surface approximates the distance between the atoms in the deposited film of another semiconductor material. This may also lead to a deflection of the dislocations, so that they are primarily located near the heterointerface [Ref. 3 p. 222].

From an energy point of view, the formation of the heterointerface uses the vacuum and Fermi energy levels in a way very similar to that of the M–S junction explained in paragraph B and is illustrated in Figure 3.20.

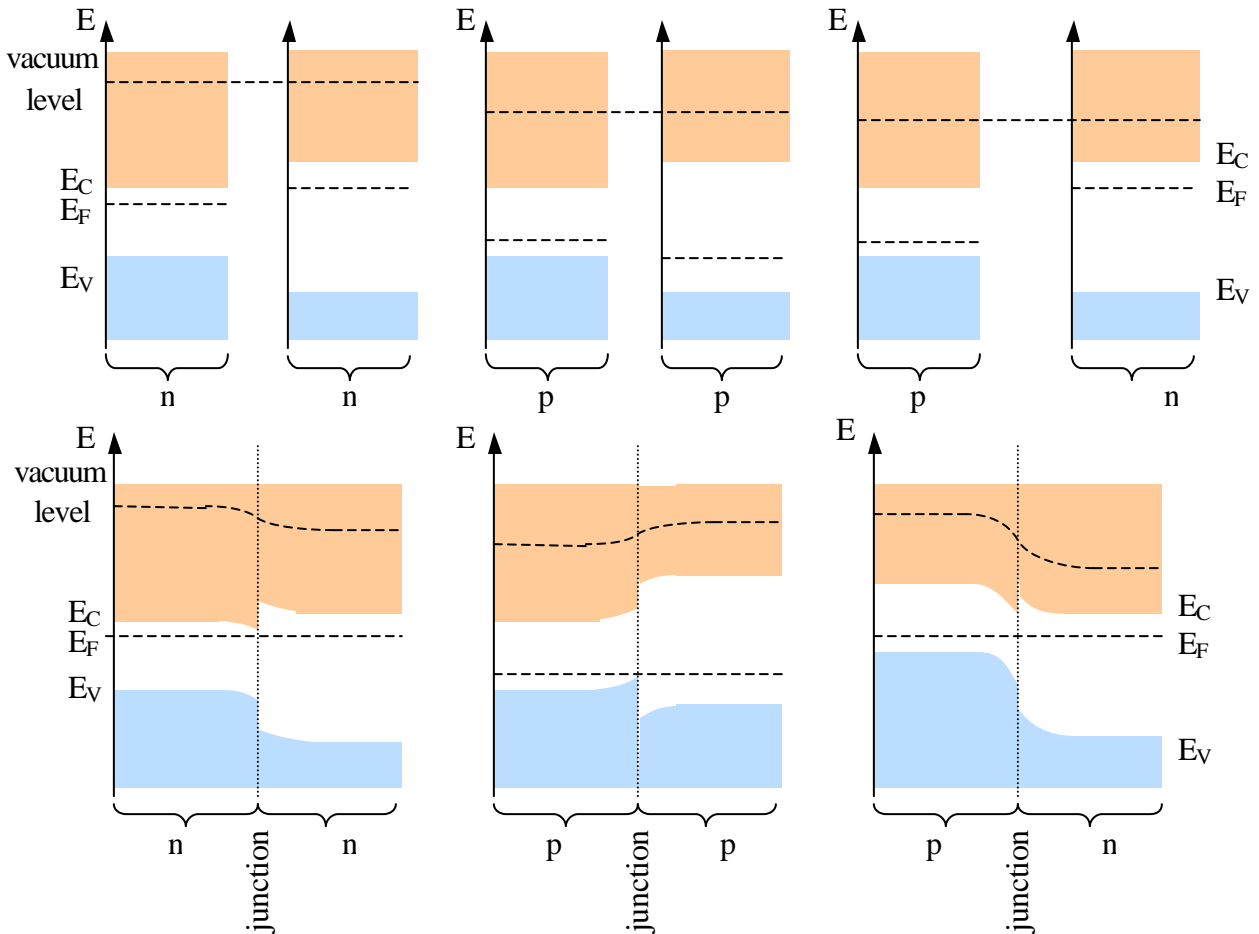


Figure 3.20. Band diagram of heterojunction formations.

The use of heterostructure films on porous Si has been proposed. The microscopic islands and grooves of the Si surface relieve the strains and reduce dislocations. Finally, the use of alternative, very thin layers, of the two materials is called *superlattice* and is known not only to reduce the formation of dislocations, but increase the carrier mobility of the device. For example, GaAs has a bandgap of 1.42eV and $\text{Al}_{0.3}\text{Ga}_{0.7}\text{As}$ has 1.72eV. Their difference is 0.3eV. The process used to produce such precisely thin layers is called *molecular beam epitaxy (MOCVD)*. The undoped structure will look like in figure 3.21a. Si can be used to dope the AlGaAs and make it n-type while the GaAs remains undoped.

This will raise the Fermi level and change the energy diagram like in figure 3.21b. Electrons from the donor (Si) in AlGaAs will move into the GaAs layers because of their lower energy conduction band. Now the donor atoms that would cause carrier scattering are separated from the carriers (Figure 3.21), hence the electron mobility in GaAs is increased. This increase is far greater than that of the bulk material and thus the carrier mobility is substantially improved.

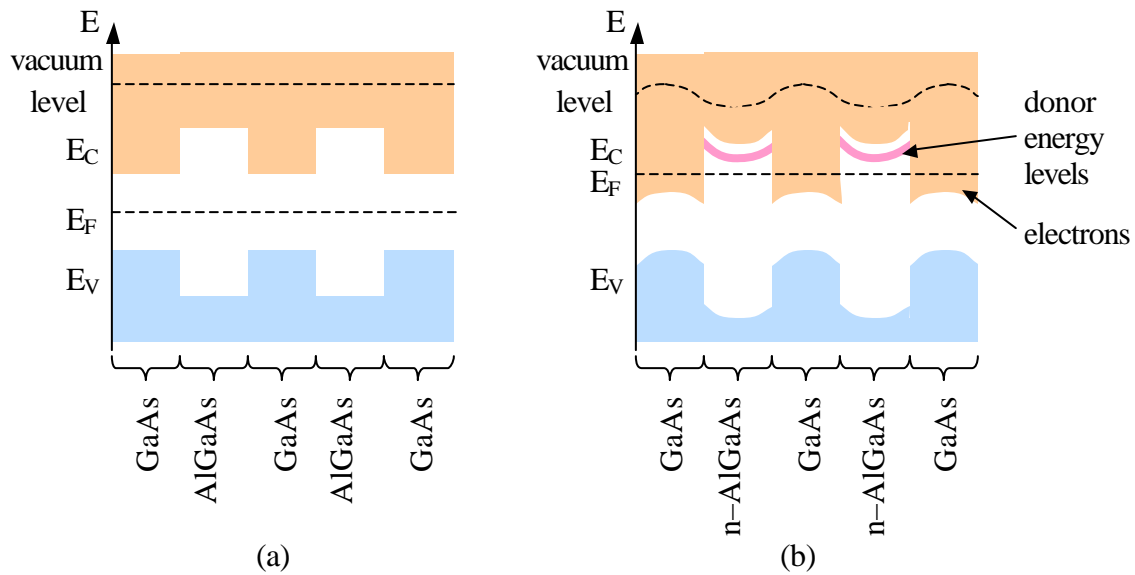


Figure 3.21. Band diagram of superlattice formation
(a) undoped and (b) AlGaAs doped [after Ref. 2:p.128].

Some heterojunction applications include photonic devices like photodetectors, photodiodes, semiconductor lasers and solar cells.

THIS PAGE INTENTIONALLY LEFT BLANK

IV. SOLAR CELLS

A. SOLAR ENERGY

The sun's very high temperature is due to the nuclear fusion reaction of hydrogen into helium. Every second, $6 \cdot 10^{11}$ Kg H_2 is converted to $4 \cdot 10^3$ Kg He. The difference in mass is called *mass loss*. It is converted into energy which, according to Einstein's relation $E=mc^2$, is equal to $4 \cdot 10^{20}$ J. This energy is emitted as electromagnetic radiation. Its wavelength spans the ultraviolet and infrared region (0.2 to $3\mu\text{m}$) [after Ref. 2:p. 791].

This energy arrives outside the earth's atmosphere with an intensity of 1365W/m^2 and a specific spectral distribution called *air mass zero* (AM0). As it approaches the surface, it is attenuated by infrared absorption due to water-vapor, ultraviolet absorption due to ozone and scattering due to airborne dust and aerosols. The various solar energy spectral distributions are specified in detail in the ISO standards, a brief summary of which is shown in the Table 4.1:

Height	Sun's position	Incident solar power [W/m^2]	Weather conditions	Spectral distribution
outside atmosphere	–	1365	–	AM0
surface	$\theta=90^\circ$ (zenith)	925	optimum	AM1
surface	$\theta=48^\circ$	963	USA average	AM1.5
surface	$\theta=60^\circ$	691	average	AM2

Table 4.1. Solar energy spectral distribution conditions [after Ref. 1, 2, 3, 4].

For space applications AM0 is used, while for terrestrial applications both AM1 and AM1.5 (most common) are used. Both are shown in Figure 4.1.

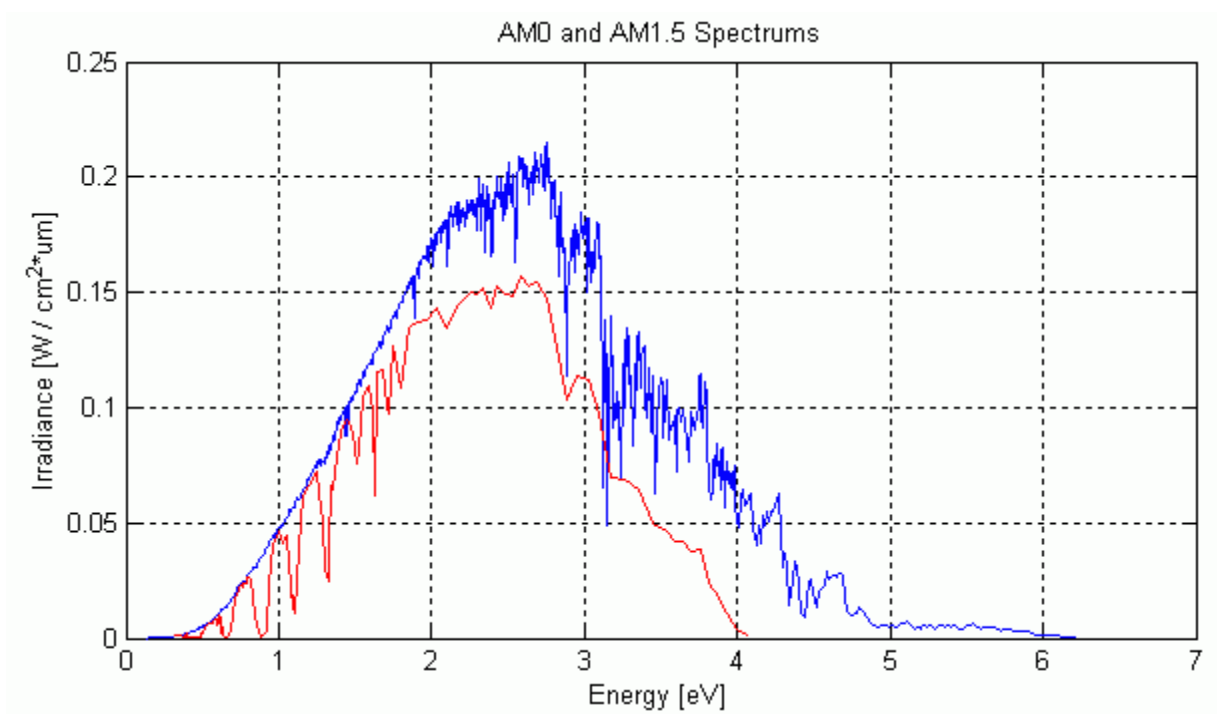
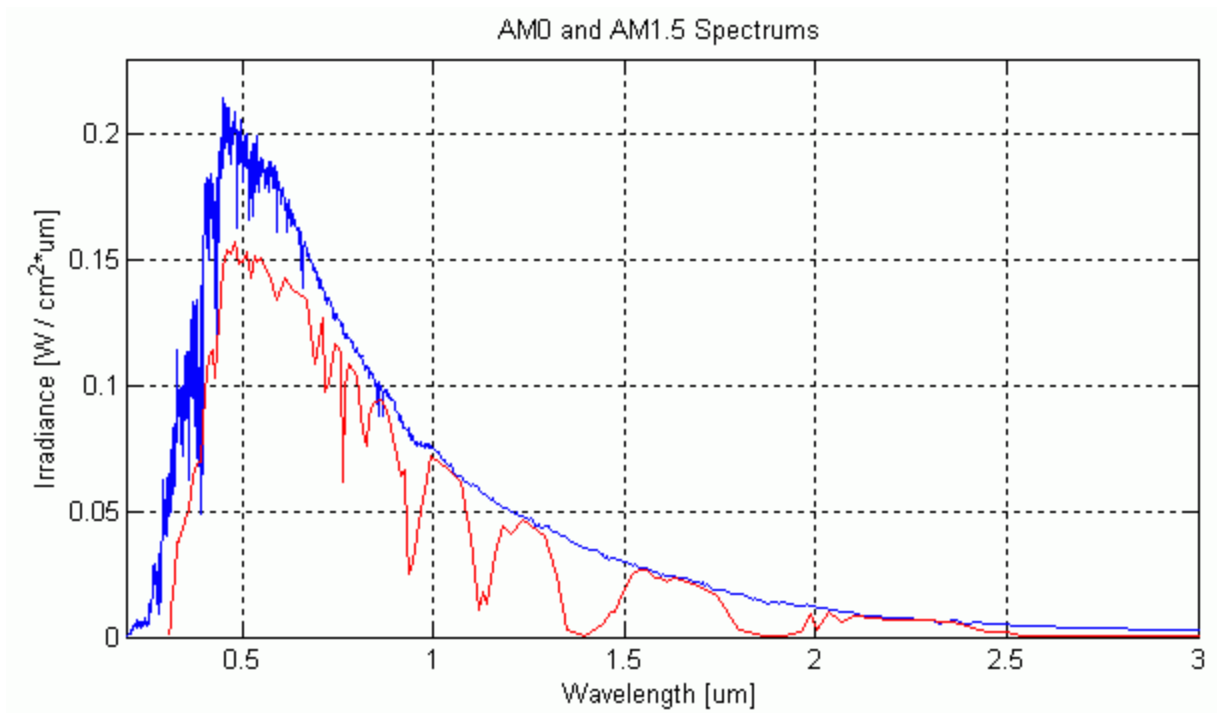


Figure 4.1. AM0 (blue) and AM1.5 (red) solar energy spectral distributions [data after Ref. 31].

B. OPTICAL PROPERTIES

A beam of light is shined at a semiconductor (incident beam) with a certain angle. If this angle is large enough, part of this electromagnetic energy will be reflected back by the semiconductor's surface with an equal angle (Snell's law). The rest of it will be refracted inside the material with a smaller angle (Figure 4.2). The ratio of the incident and the refractive angles is equal to the ratio of the speed of light outside and inside the material. This ratio is called *refraction index* n_r .

$$\frac{a_{\text{incident}}}{a_{\text{refractive}}} = \frac{c_{\text{outside}}}{c_{\text{inside}}} = n_r$$

From the energy refracted in the semiconductor again only a part is absorbed. The rest of it goes through and exits the material from its other side with an angle equal to the incident angle. The amount of energy absorbed is described by the *absorption index* χ . The complex index of refraction n_r^* is defined as:

$$n_r^* = n_r \times (1 - i\chi)$$

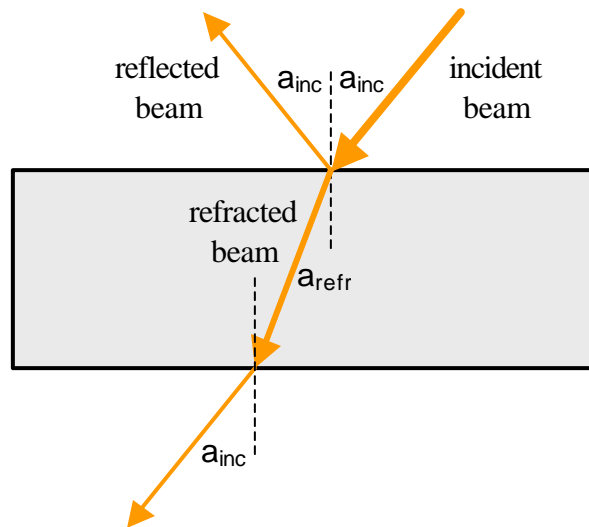


Figure 4.2. Path of light beam through semiconductor.

Another way to describe the optical properties of a material is the *dielectric function* ϵ . This is given by:

$$\mathbf{e} = \mathbf{e}_1 \pm i\mathbf{e}_2 = (n \pm ik)^2 \text{ from which } \mathbf{e}_1 = n^2 - k^2 \text{ and } \mathbf{e}_2 = 2nk$$

Finally, *reflectivity* R is given by:

$$R = \frac{(n-1)^2 + k^2}{(n+1)^2 + k^2}$$

The values of ϵ_1 , ϵ_2 , n and k vary according to the material and the wavelength of the light shined. For Si ϵ_1 and ϵ_2 can be seen in Figure 4.3.

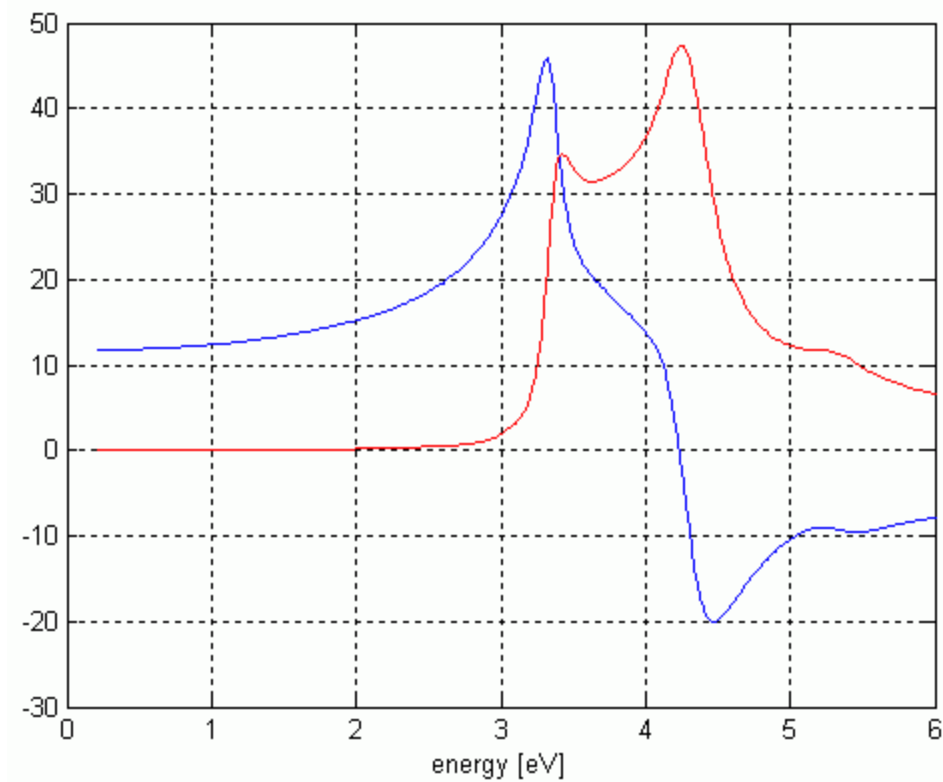


Figure 4.3. ϵ_1 (blue) and ϵ_2 (red) for Si [after Ref. 6].

It is obvious that the light that is reflected or not absorbed (passed through) contains energy that is lost for the solar cell. In order to increase absorption, the material's thickness is increased. However, the reduction of reflection is not that easy. The simplest method is the use of very thin layers of *anti-reflective coating* (ARC)

materials like MgF_2 and ZnS . More sophisticated and expensive methods involve the creation of *microgrooves* on the surface of the semiconductor. Light rays reflected from one groove hit another and finally enter the material. This is shown in Figures 4.4 and 4.5.

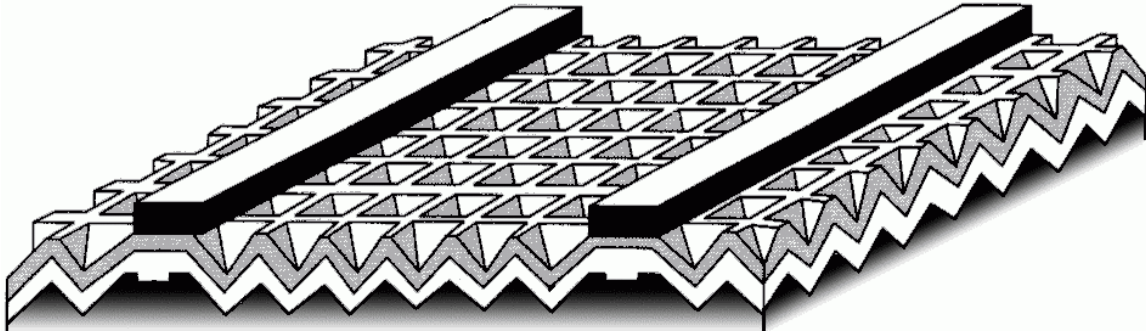


Figure 4.4. Surface with microgrooves [after Ref. 1:p. 326].

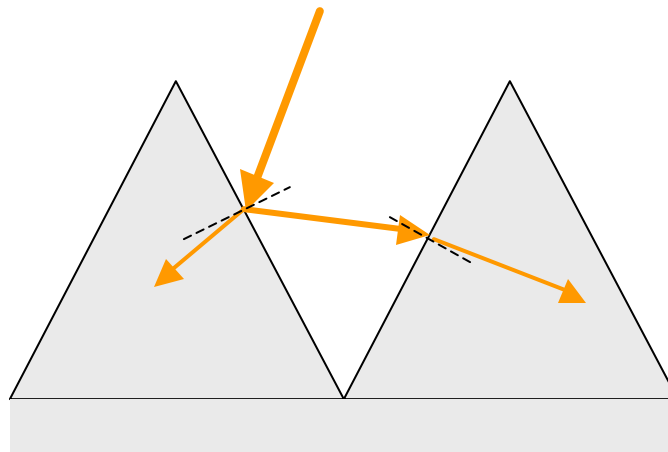


Figure 4.5. Light path in microgroove.

Still, not all photons entering a solar cell are used. A number of them just happen to go through it unaffected. A technique to reduce this number is using a very well shined metallic plate as the bottom contact of the cell. Photons not used are now reflected by it and re-enter the cell layers. This way, the probability of them not being used is reduced by half. An improvement of that introduces a thin oxide layer above the bottom contact to increase its reflectivity (Figure 4.6).

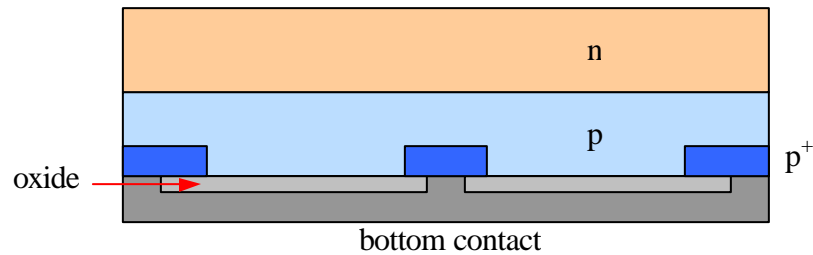


Figure 4.6. Improved reflective bottom contact.

The energy produced by a solar cell is directly proportional to the intensity of light shining on it. In order to increase this amount, various lens and mirror constructions (*concentrators*) are used. These are much cheaper than cells and can greatly reduce the total cost of produced energy, since less cells are now required. However, in space applications, their weight is very high and the cost related to it largely exceeds that of the cells. This restricts their use only to terrestrial applications.

C. FUNDAMENTALS

We have seen earlier that electrons can be excited with heat and that atoms can be ionized to produce EHP's. Another way to offer such energy to a material is photons (*photogeneration*), thus light. In a single type semiconductor this creation of carriers leads to an increase in conductivity.

In a p-n junction, however, those carriers will become separated (*carrier separation*) and minority carriers will be swept across the junction, due to the electrostatic field of the depletion region. This way, an excess of electrons (negative charge) will be observed in the n-type semiconductor and similarly, an excess of holes (positive charge) will be observed in the p-type. This excess of majority carriers will develop a voltage differential on the two sides of the device (figure 4.1). This voltage is quite large for the M-S junctions of the contacts to counter and therefore, can be easily measured. If a resistance is connected to the device, current (*photocurrent*) will flow. This phenomenon is called *photovoltaic*.

In order to create an EHP, a specific minimum quantum of energy is required. This is equal to the bandgap E_g of the semiconductor. A photon entering the cell with energy less than E_g will not be absorbed and will pass through it. A photon with energy equal to E_g is ideal for the creation of an EHP. Finally, a photon with larger energy will create an EHP offering energy equal to E_g and waste the remaining amount as heat to the lattice. Such heat, however, will deteriorate the electrical properties of the material.

As the amount of photons entering the material becomes larger, so does the number of generated EHPs. Hence, the photocurrent increases and the produced power increases, too. Unfortunately, a number of carriers recombine inside the material before they are collected at the contacts. This number becomes very large in semiconductors with significant amount of recombination centers. A schematic of a cell is shown in Figure 4.7.

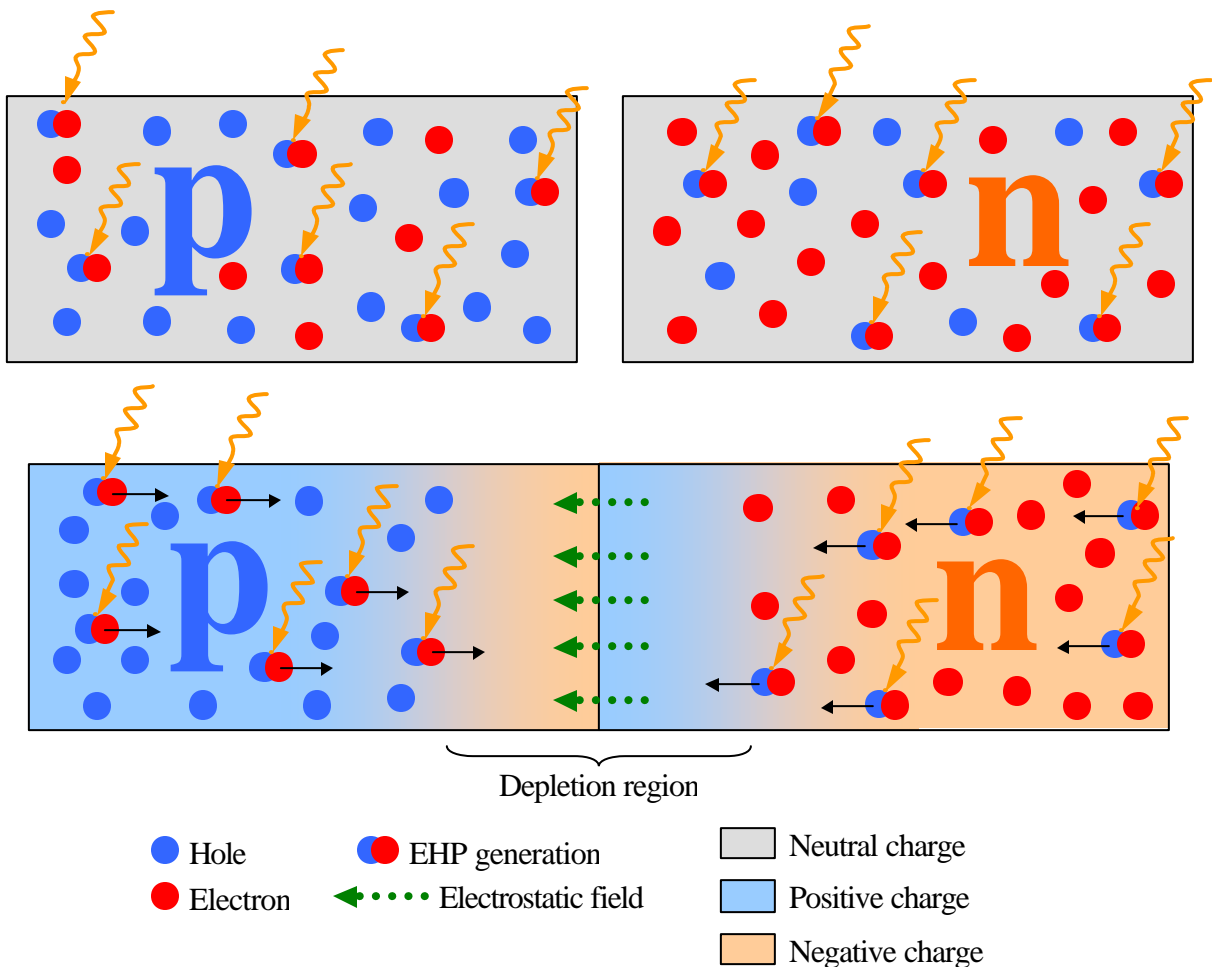


Figure 4.7. Schematic of a simple solar cell.

The derived I–V curve (*illuminated characteristic*) is illustrated in Figure 4.8a with the red line. It mainly exists in the 4th quadrant, which means that it produces energy. Note the similarity to the I–V shown in the same figure in blue. This is the characteristic in the absence of light and is called *dark current characteristic*. As a power supply, the illuminated characteristic can be presented inverted like in Figure 4.8b. V_{OC} is the open circuit voltage and I_{SC} is the short circuit current. The blue rectangle is called *maximum power rectangle* and corresponds to the values of V and I for which the power produced ($P=V \cdot I$) becomes maximum. The ratio of the maximum power rectangle to the V_{OC} – I_{SC} rectangle is called *fill factor* FF.

$$FF = \frac{S_{\text{maxpower}}}{S_{V_{OC}-I_{SC}}} = \frac{V_{\text{max}} \cdot I_{\text{max}}}{V_{OC} \cdot I_{SC}}$$

The *power conversion efficiency* η of the solar cell is the ratio of the maximum produced power P_{max} to the incident power P_{inc} of the light.

$$\eta = \frac{P_{\text{max}}}{P_{\text{inc}}} = \frac{FF \times V_{OC} \times I_{SC}}{P_{\text{inc}}}$$

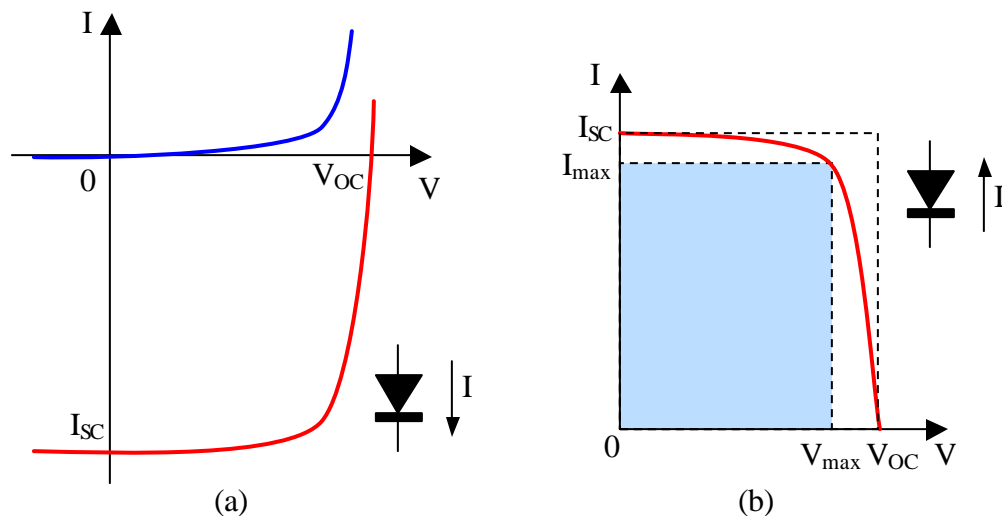


Figure 4.8. Dark (blue) and illuminated (red) characteristic curve of the solar cell.

If the light propagates towards the y -axis, then its intensity can be expressed by $F(y)$. The light absorption would then be $dF(y)/dy$. This leads to the following equation:

$$\frac{dF(y)}{dy} = -aF(y)$$

where a is called *absorption coefficient*. The distance $1/a$ is called *light penetration depth* and its relation to F is show in Figure 4.9:

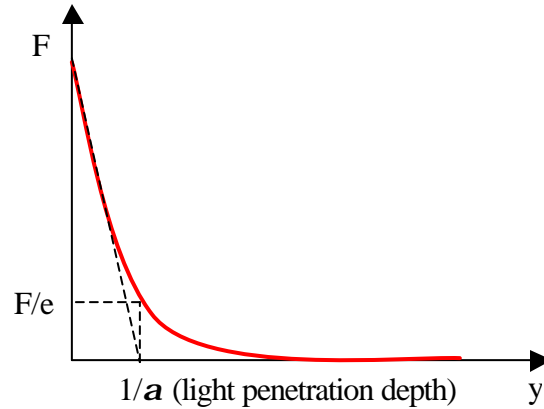


Figure 4.9. Light intensity F in semiconductor vs distance from surface y [Ref. 3].

D. TEMPERATURE AND RADIATION EFFECTS

The effects of temperature on the resistivity of materials were explained in previous chapters. In solar cells and in semiconductors in general, it was shown that a small increase in temperature facilitates EHP generation and hence is beneficial to the electrical properties of the materials. However, further rising of temperature causes an unwanted increase in their resistivity, drastically deteriorating their behavior.

In addition to that, the phenomenon of diffusion becomes more intense as temperature rises. This leads to an increase of I_{SC} . However, V_{OC} decreases exponentially with temperature, countering the benefit of the higher I_{SC} and further reducing the maximum power produced by the cell.

The knee of the cell's I - V curve also becomes more round (soft) with temperature. This way, the maximum power rectangle and the fill factor are decreased. It is obvious now that, overall, the efficiency of the cell is greatly reduced as temperature rises (Figure 4.10).

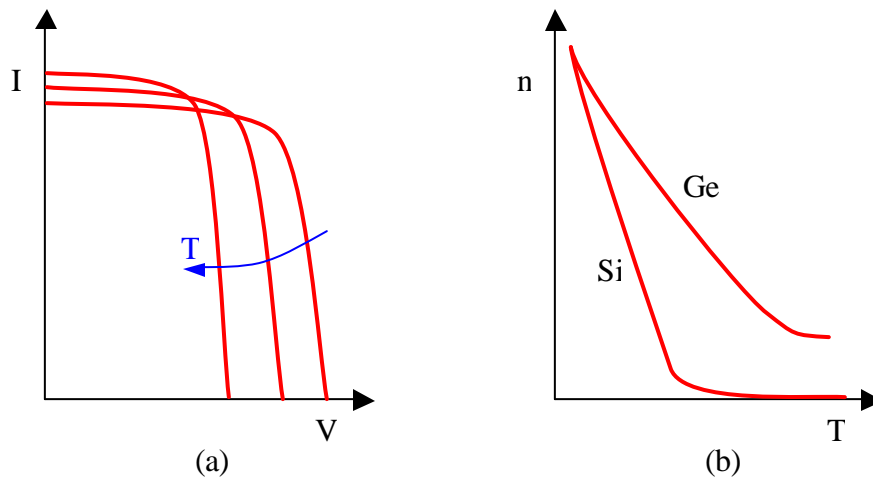


Figure 4.10. Effect of temperature on the I–V curve (a) and the normalized efficiency (b) of solar cells.

For space applications, radiation that exists outside the earth’s atmosphere can also have a significant effect on solar cells. High–energy particles, entering the cell, create imperfections in the lattice structure that act as recombination or trapping centers. This particle bombardment is continuous and thus, the cell output decreases with time. Various materials are affected differently by radiation. For example Si is more sensitive than Ge. Also, p–on–n cells are also more sensitive than n–on–p. In order to cope with this problem, several techniques are used. Introducing Li to the lattice is one of them. Li can diffuse to and combine with the created defects and so prevent the degradation of the cell. Another method is the placement of a thin cover (usually cerium–doped) in front of the cell to filter out some of the high–energy particles (Ref. 2).

E. CELL TYPES

Photovoltaic phenomena were first observed and studied by the French scientist *Henri Becquerel* in 1839. The first material used was *selenium* in 1877. Better understanding of the mechanics involved was provided by *Einstein* in 1905 and by *Schottky* in 1930. *Chapin*, *Pearson* and *Fuller* were the first to develop a Si solar cell, in 1954, with 6% efficiency. (ACREWeb, <http://acre.murdoch.edu.au>)

One way to categorize solar cells is by their substrate material. The most common materials used are Si, Ge and GaAs. Si is actually sand and so it is very cheap. It also has better efficiency than Ge or GaAs, but is more sensitive to radiation. Even though Ge and GaAs are not very efficient, their combination in a multijunction cell (discussed later) can produce much better results, but with a big increase in fabrication cost. Finally, Si is non-toxic and non-poisonous, in contradiction to GaAs. For all these reasons it is widely used for terrestrial applications while Ge and GaAs are more used for space applications.

According to the amount of material crystallization, a cell can be amorphous, polycrystalline or single-crystal. The easiest and cheapest method for creating solar cells is by using non-crystalline or amorphous semiconductors (Figure 4.11c). The problem with such materials is the existence of many dangling bonds that act as recombination centers. To cope with this problem, semiconductor-hydrogen alloys, with fairly large concentration of H₂, are used. H₂ tends to tie up those bonds and reduce the number of recombination centers. Si-H (α -Si), Ge-H and Si-C-H have been built and are used in cells. Maybe the most important advantage of this type is its combination with thin-film technology. This provides the ability to produce large-area cells, using small amounts of semiconductive material. It also allows their fabrication on various, even flexible, substrates (glass, plastic etc) at very low cost. Their efficiencies are not very high, reaching only up to 15%, therefore they are mostly used in commercial appliances and terrestrial applications.

Polycrystalline cells are produced from thin (approx 300 μ m) slices of semiconductive material that contains a number of large *crystallites* separated by *grain boundaries* (Figure 4.11b). This is done by pouring molten material into a cylindrical or rectangular mold and allowing it to set. A significant number of recombination centers exist on the borders of the crystallites. The fabrication cost is a little higher, but the efficiency of the cell is much better reaching 20%. Much of the cost increase is attributed to the material lost as sawdust during the slicing process.

Single crystal cells (Figure 4.11a) are produced from slices of a large (usually 6-8") single crystal ingot called *boule*. This ingot is grown by slowly lifting a small crystal over a highly-pure melt of the same semiconductive material. The wafer produced is an almost perfect lattice with very little impurities or defects. The efficiency of these cells is

the highest available reaching 25%, but the whole process of growing the crystal, added to the slicing loss, makes these cells very expensive. Single crystal cells are mostly used for space applications where the need for high-density and lightweight power sources is more important than fabrication cost.

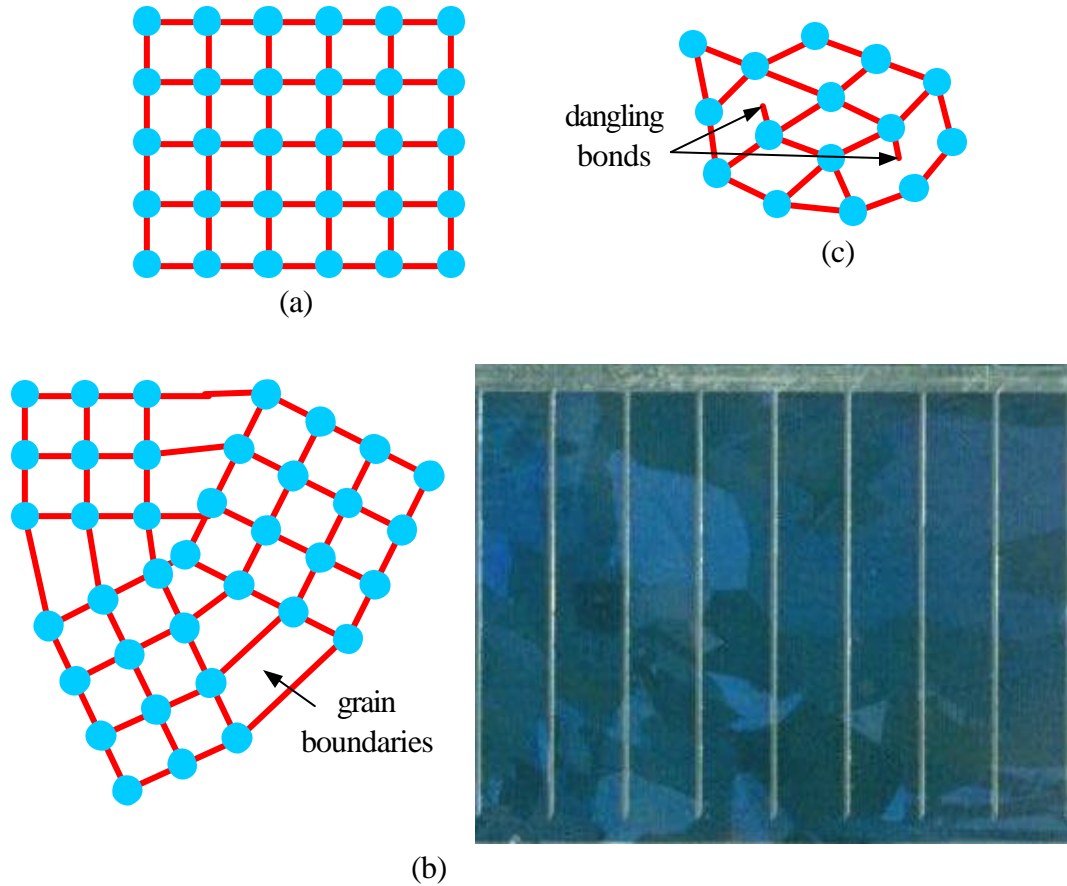


Figure 4.11. (a) Single-crystal, (b) polycrystalline and (c) amorphous material.

F. CONTACTS

Since the efficiency of all types of solar cells is not high, it is essential to minimize losses wherever possible. One area is the method used to collect the produced current. Electrical contacts may introduce junction voltages and ohmic resistances. In order to eliminate the first, layers of metal-semiconductor alloys on top of highly-doped semiconductive material are introduced between the contact and the cell. Ohmic resistance can be eliminated by using very low-resistivity metals like gold (Au).

The bottom contacts of a cell are easier to develop as the only additional consideration is that they have a good reflective surface, as seen in paragraph B. On the contrary, top contacts require more examination as they block photons from entering the cell (*shadowing effect*). For this reason, various grid structures have been developed. On one hand, these grids need to be thick enough for good conductivity and dense enough for collecting as much photogenerated carriers as possible. On the other hand, they need to be thin and sparse enough to avoid casting too much shadow on the cell. A very common compromise is a shadowing (or *shadow loss*) of 10% for single crystal cells. Some contact configurations can be seen in Figure 4.12.

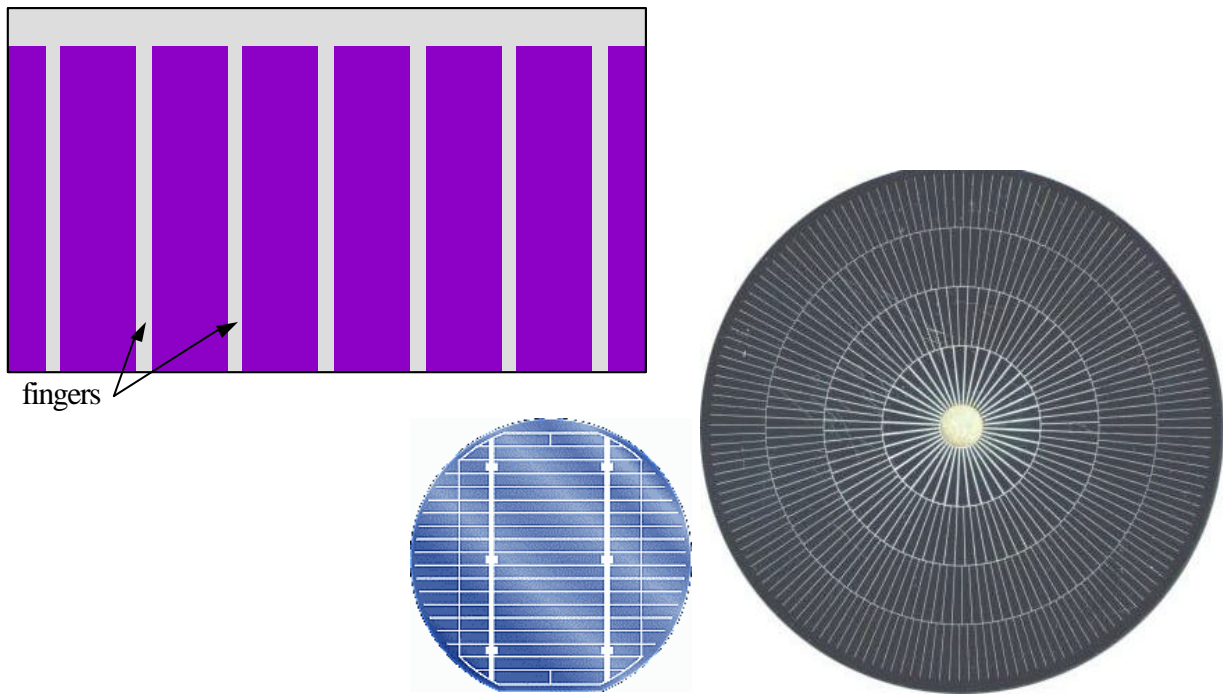


Figure 4.12. Collector grids.

However, amorphous cells would require a much more dense grid. This is due to the fact that their carriers display very small horizontal movement. Such a grid would cast too much shadow over the cell, making it unusable. For this reason transparent contacts, with smaller conductivity, have been developed. These are made by using a *transparent conducting oxide* (TCO) such as tin oxide (SnO_2). Amorphous cells are usually built the opposite way. First the TCO layer is created in the form of a glass

superstrate. All the cell layers are then built on it from top to bottom using thin–film technology. In the end, the bottom metal contact is added.

G. ARRAYS

As seen before, a cell usually has a V_{OS} less than 2V and a I_{SC} of a few mA providing a total power of 2–3Watts. In order to use solar cells in a wider range of applications, a number of cells is connected in series to increase the voltage and then in parallel to increase the current provided. Those constructions are called *modules*. Thin–film modules can be built directly, bypassing the single–cell stage. Furthermore, modules can be connected together to form much larger power *arrays* in the range of several MWatts (Figure 4.13).

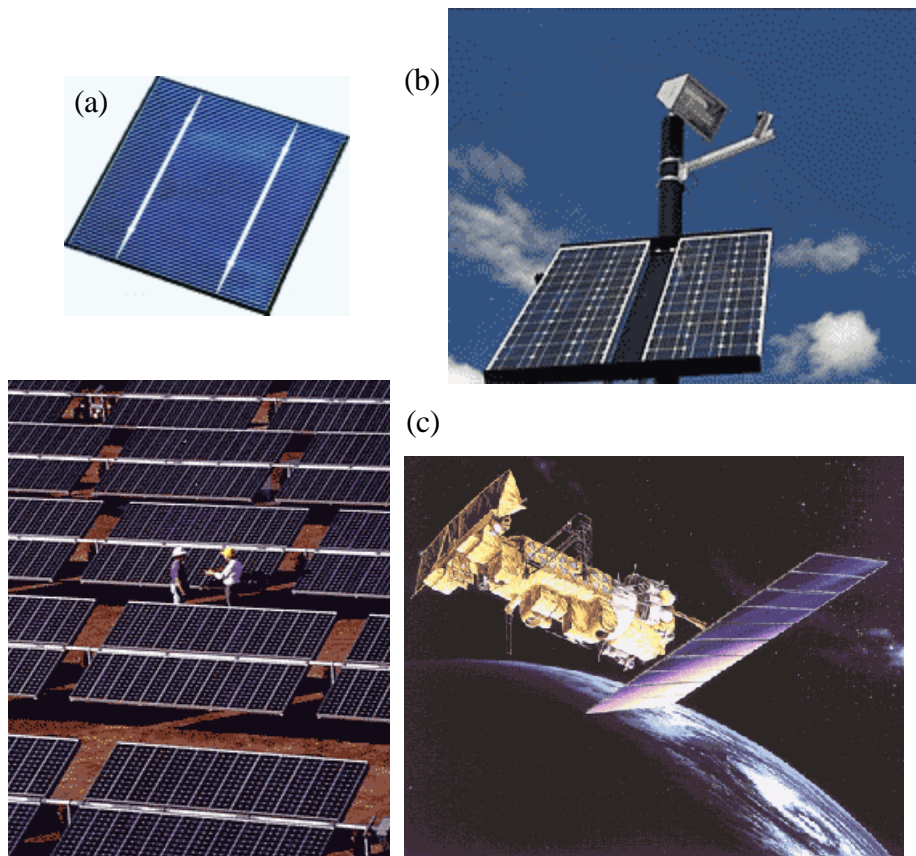


Figure 4.13. (a) Solar cell, (b) module and (c) array
[after Ref. 32].

V. MULTIJUNCTION SOLAR CELLS

A. BASICS

We have seen previously that a material can be ionized by photons with energies higher than its bandgap, or in other words with wavelengths lower than the wavelength corresponding to this bandgap. The equations connecting photon energy and wavelength are the following:

$$E = hf \quad \text{and} \quad c = \lambda f$$

where E is the photon energy, λ is its wavelength, f is its frequency, c is the speed of light and h is Planck's constant. Photons with energies lower than the bandgap go through the material unaffected and unused (Figure 5.1).

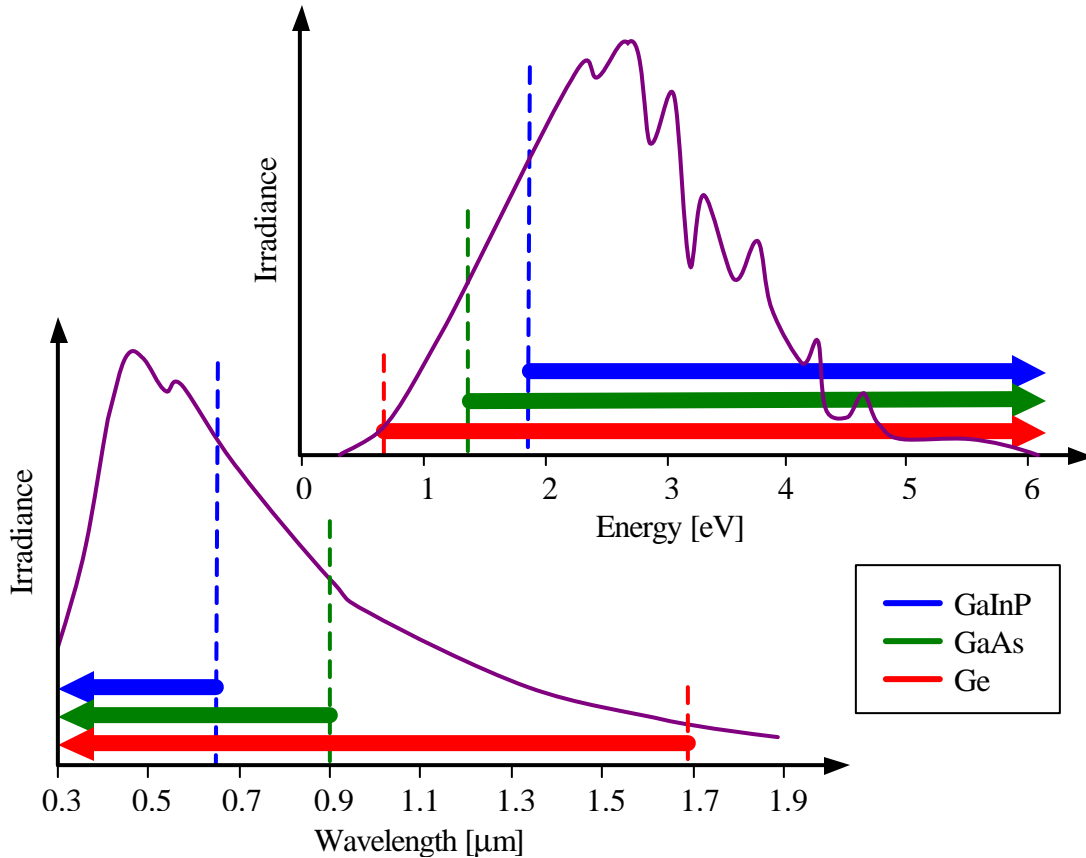


Figure 5.1. Absorption energies and wavelengths for Ge, GaAs and GaInP on AM0 spectrum.

This might lead to creating only Ge cells, since they can absorb most of the solar spectrum. Another reason that might lead to the same conclusion is shown in the I–V curves of the individual cells in Figure 5.2. Obviously, Ge cells produce much more current per cm^2 than others. However, its voltage is much smaller and so the power output per area unit of Ge is smaller than this of Si.

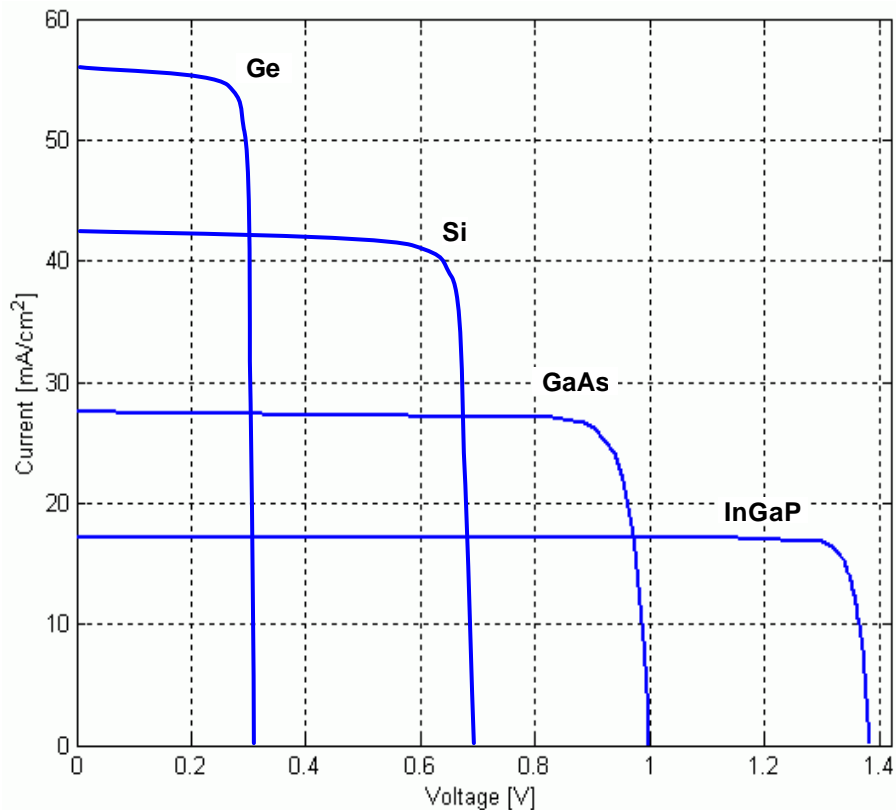


Figure 5.2. I–V curves for Si, Ge, GaAs and GaInP cells.

An optimal combination is the mechanical stacking of all these types (one over the other) and connected in series. This is called *tandem cell*. Cells with the higher bandgap are placed above cells with lower bandgap. This way, a cell will absorb the higher-energy photons and will produce electric power. At the same time, it will allow the lower-energy photons to pass through it. These will enter the next cell in line and so on... There is virtually no limitation to the number of cells stacked, as long as their bandgaps are different. In theory, the efficiency of such cell can reach 60%. The sum of the cells' individual spectrum responses produces the response of the tandem cell. This method is called *spectrum separation* (Figures 5.3 and 5.4).

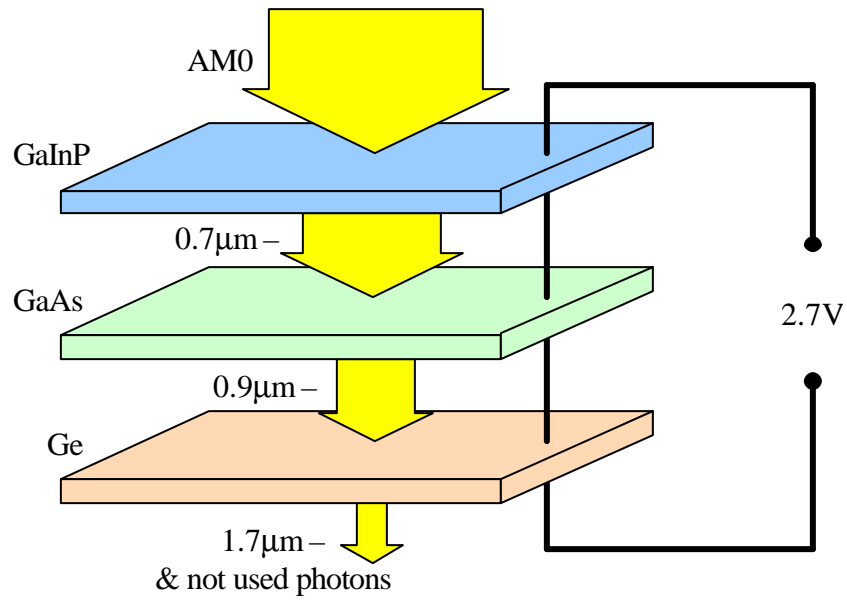


Figure 5.3. Tandem cells.

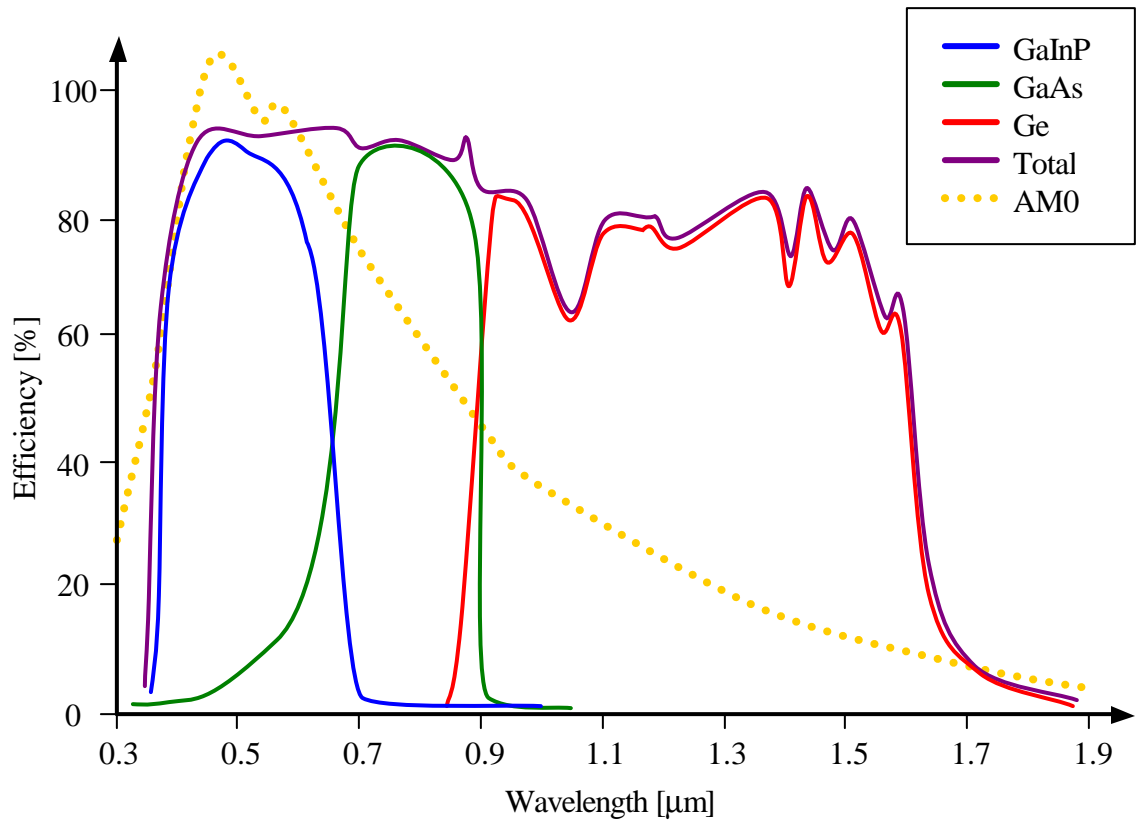


Figure 5.4. Spectrum separation [after Ref. 19].

B. MONOLITHIC MULTIJUNCTION CELLS

Mechanically stacked cells have a lot of additional volume and weight due to the stacking mechanisms used. This is a serious disadvantage for space applications. In addition, a significant amount of energy is lost due to reflection as light goes from one cell to the other. In an attempt to eliminate these problems, the *monolithic* tandem cells were created. In these cells, oxide layers are used to provide electrical insulation between cells. A number of internal contacts were also used to perform the in-series connection of cells. These contacts were also made external to provide valuable information of the individual cells (Figure 5.5).

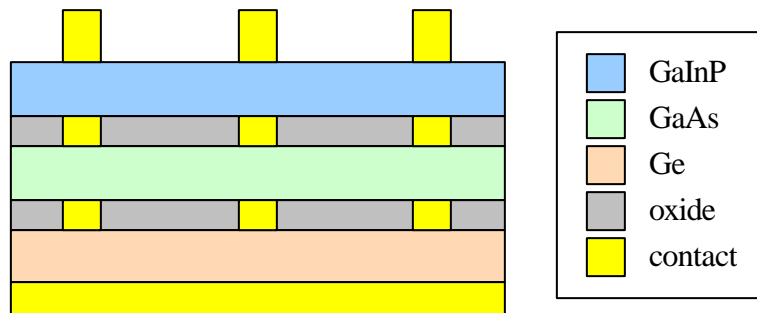


Figure 5.5. Monolithic tandem cell.

However, significant loss and shadowing led to the creation of what is now called monolithic *multijunction cell* (MJ cell). The problem with simply connecting cells together lies to the fact that new junctions would be created between cells. Those junctions would be reverse-biased and their depletion-region electrostatic field would oppose the flow of carriers towards the contacts. This would prevent the cell from producing any current.

Instead, specially prepared tunnel junctions can be used to solve this problem. A reverse-biased *tunnel junction* will conduct current the desirable way, due to the tunneling phenomenon explained in earlier chapters. The tunnel layers are always more heavily-doped than the cell layers. For this reason, intermediate junctions formed between the tunneling junctions and the cells will conduct current from the p to the p⁺ regions and from the n⁺ to the n regions. This will allow current flow instead of hindering it. Although the tunneling junction layers introduce considerable losses that affect the

overall efficiency of the cells, they are currently the most attractive technique for connecting cells (Figure 5.6).

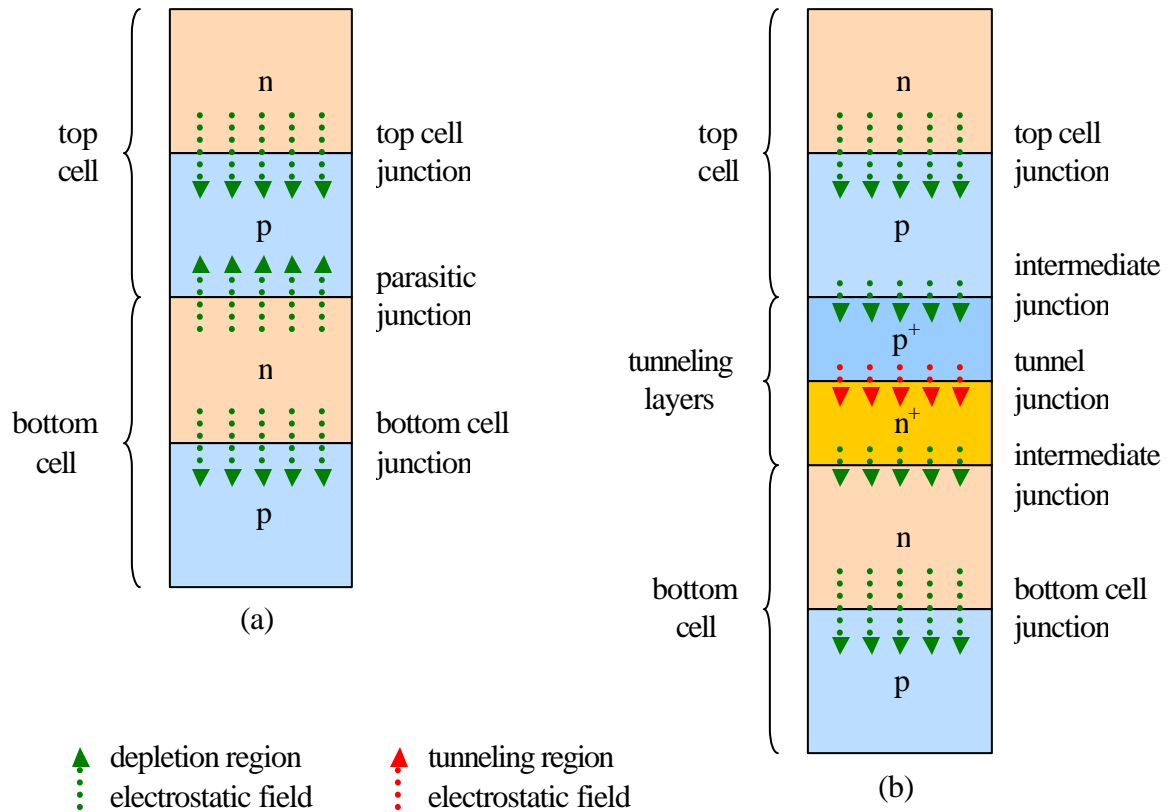


Figure 5.6. (a) Simple connection of cells and (b) connection using tunneling junction.

C. CURRENT DEVELOPMENTS

We have seen previously that layers of different materials, grown on top of each other, create dangling bonds that act as recombination centers. For this reason, the need for using lattice-matched layers is apparent. Unary semiconductors like Ge and binary like InP have fixed lattice constants and therefore cannot be matched directly. On the other hand, ternary like GaInP and quaternary like AlGaInP alloys can easily be constructed to have almost any desirable lattice constant.

When non-matching materials (i.e. unary and binary) are required to be placed in contact together, a method called *windowing* can be used. According to this, a thin layer

(window) of an alloy is grown between them to eliminate the unwanted surface recombination. The window creates a gradient that smoothes-out the lattice difference. Its bandgap is carefully selected to be higher than the bandgap of the cells below it. Additionally, with its small thickness, the window does not consume valuable photons.

As photogeneration takes place, minority carriers diffuse towards the junction of the cell. However, some of them tend to diffuse the opposite way, towards the back surface of the cell, introducing more losses. To avoid that, a thin highly-doped layer is placed right below the cell, creating an electrostatic field that will push minority carriers towards the junction. This is called *back surface field* (BSF). Thicker BSFs are often used above the substrate, forming what is called a *high-low junction*.

At this moment, the triple MJ cell (Figure 5.7) with the highest efficiency (29.3%) published is built by Spectrolab [Ref. 19]. It is built on a Ge substrate, which also acts as a base for the bottom cell. On top of it is the Ge emitter and an AlGaAs window. Two heavily-doped n and p GaAs layers follow, forming the tunnel junction between the bottom and the middle cell. On top of it is a GaInP BSF and then the GaAs middle cell with its GaInP window. Another GaAs tunnel junction follows and above that the AlGaInP BSF of the top cell, the top GaInP cell itself and its AlInP window. The surface of the cell is covered with an ARC to eliminate reflection. Below the contacts only, there is a GaAs layer. This is called *cap* and is used to facilitate current movement to the fingers. It also protects the underlying layers from being damaged when the contacts are heated during bonding. In following chapters we will model the parts of this configuration individually and then combine them to form the whole structure. The same company is also experimenting with a quadruple AlGaInP/GaAs/GaInNAs/Ge MJ cell with even higher efficiency.

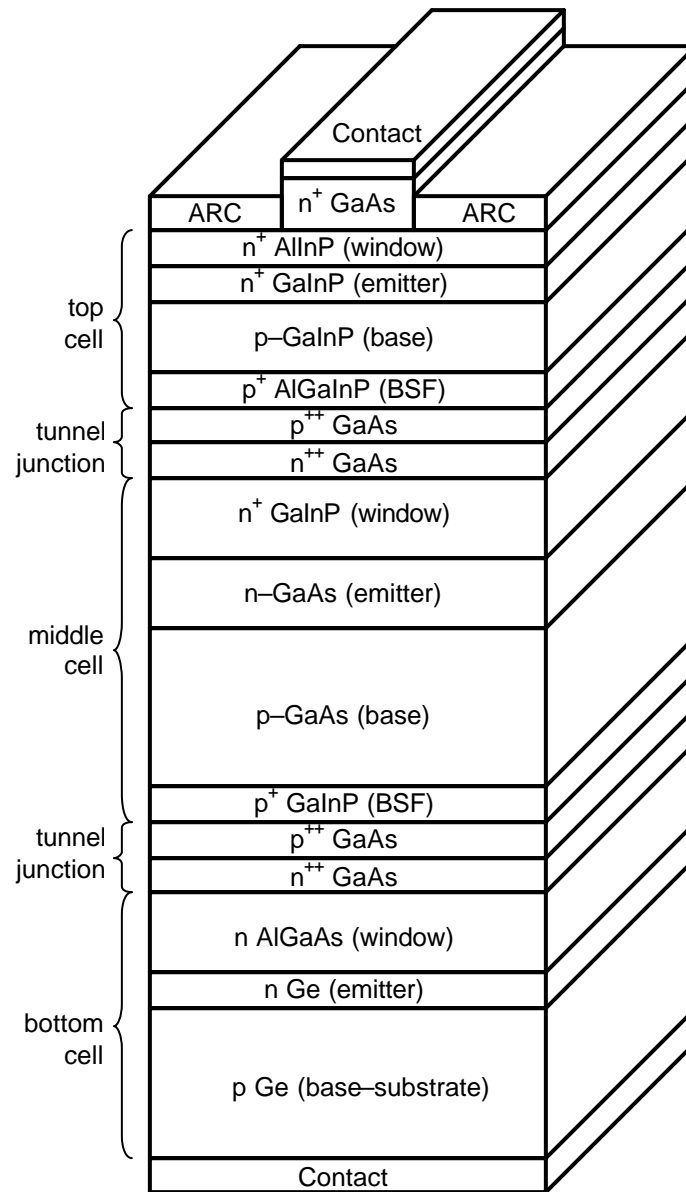


Figure 5.7. Spectrolab's triple MJ cell [after Ref. 19].

THIS PAGE INTENTIONALLY LEFT BLANK

VI. SIMULATION SOFTWARE

After a thorough review of the existing modeling and analysis tools, along with related publications, the suite of tools and reusable models developed by Silvaco [Ref. 14] was selected. In this chapter, the strategy and methodology, for modeling solar cells using Silvaco, is discussed. An overview is also given of the software that was developed or reused in order to enhance its functionality and to meet the modeling and simulation needs for researching advanced solar cells.

A. MODELING TODAY

There is a very large number of publications available that document the modeling of almost every aspect of solar cell function and behavior. These span from the macroscopic electrical to the microscopic molecular level and have very high accuracy and credibility.

However, they all address individual solar cell viewpoints, without providing a complete coverage of the complex combination of phenomena that actually take place. Thus, there is a need to select and use a large number of different models, in order to study an actual complete cell structure. An important consideration is the fact that not all of these models are compatible with each other. This makes their selection prone to errors, quite hard, and time consuming. In addition, each one exposes the researcher to many detailed parameters that usually create a lot of unnecessary confusion. All the above make complete simulation of advanced solar cells a forbidding task.

As a consequence, solar cell research today is conducted by actually fabricating cells and experimenting with them. Then, researchers theorize about the collected results. Although that methodology provides the most credible results, it may also lead to some confusion. The reason lies in the huge number of factors that always need to be considered, most of which are more relevant to the fabrication process used and not the cell itself. Therefore, many combinations of parameters need to be materialized like material types and characteristics, doping, dimensions, fabrication conditions and

processes. This is not only a time and personnel consuming task, but can also be expensive to carry out. The number of experiments, needed to answer questions, is also very large, due to the fact that experts are not allowed to focus on a certain issue. Instead, they need to consider and develop the design and the complete fabrication process of the cell under study. Additionally, in any kind of experiment there is always a number of unpredictable factors that may introduce deviation among results.

Extensive research, of the existing literature and COTs, revealed that no methodology, coping with these problems, currently exists. Small attempts were found to lack the breadth of a complete simulation tool. For this reason, they have not been adopted by the Photovoltaic community. In this thesis, a new method for developing a realistic model of any type of solar cell is presented.

B. SILVACO

Silvaco is a company that specializes in the creation of simulation software targeting almost every aspect of modern electronic design. In their TCAD suite of tools, the company provides modeling and simulation capabilities for simple Spice-type circuits all the way to detailed VLSI fabrication (Figure 6.1). User-friendly environments are used to facilitate design and a vast number of different modeling options. The tools provide for creating complex models and 3D structural views.

The phenomena modeled range from simple electrical conductivity to such things as thermal analysis, radiation and laser effects. A wide variety of detailed layer-growth processes and material properties (e.g. mobilities, recombination parameters, ionization coefficients, optical parameters) add to the accuracy of the simulation. However, to date there is no publicly available documentation of efforts by researchers or solar cell manufacturers to utilize this powerful tool for the modeling of advanced solar cells, but only of simple structures.

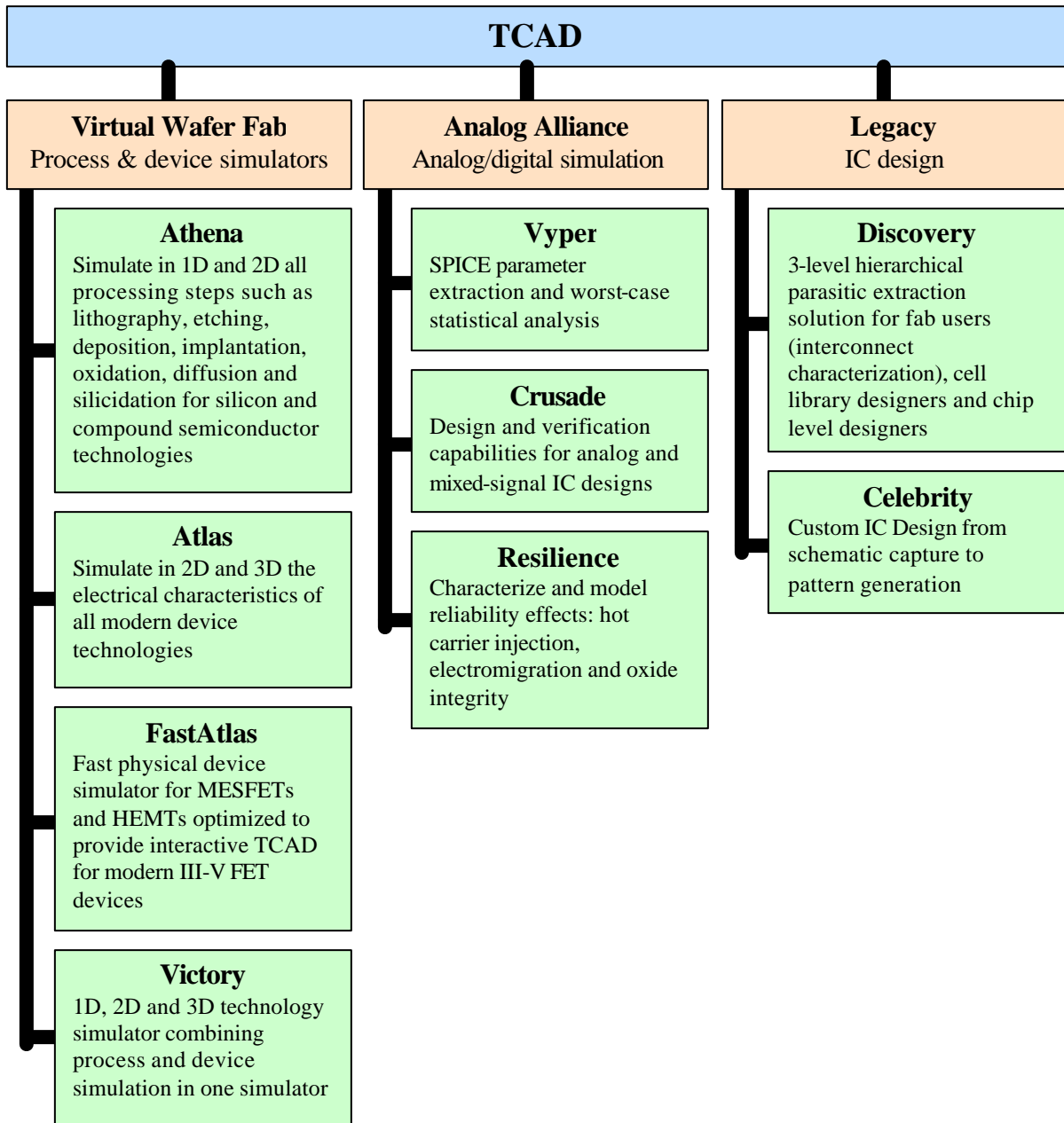


Figure 6.1. Silvaco's TCAD suite of tools [after Ref. 14].

For this purpose, Atlas is a good combination of sophisticated in-depth device analysis in 2D or 3D. In addition, it abstracts away all fabrication details, shifting the focus of the modeler to the actual design. Like the rest of TCAD applications, it is based on hundreds of widely accepted publications, verified for their accuracy and correctness

by numerous researchers. This variety provides for features such as the following and others [Ref. 10 p. 1.4]:

- DC, AC small-signal, and full time-dependency
- Drift-diffusion transport models
- Energy balance and Hydrodynamic transport models
- Lattice heating and heatsinks
- Graded and abrupt heterojunctions
- Optoelectronic interactions with general ray tracing
- Amorphous and polycrystalline materials
- General circuit environments
- Stimulated emission and radiation
- Fermi-Dirac and Boltzmann statistics
- Advanced mobility models
- Heavy doping effects
- Full acceptor and donor trap dynamics
- Ohmic, Schottky, and insulating contacts
- SRH, radiative, Auger, and surface recombination
- Impact ionization (local and non-local)
- Floating gates
- Band-to-band and Fowler-Nordheim tunneling
- Hot carrier injection
- Thermionic emission currents

C. WORKING WITH ATLAS

Atlas can accept structure description files from Athena and DevEdit, but also from its own command files. Since, for the purposes of this thesis, detailed process description is not required, the later is the more attractive choice. The development of the desired structure in Atlas is done using a declarative programming language. This is interpreted by the Atlas simulation engine to produce results. A brief walk-through of how a structure is built and simulated follows.

1. Mesh

The first thing that needs to be specified is the mesh on which the device will be constructed (Figure 6.2). This can be 2D or 3D and can be comprised of many different sections. Orthogonal and cylindrical coordinate systems are available. Several constant or variable densities can be specified, while scaling and automatic mesh relaxation can also

be used. This way, a number of minimum triangles is created; this determines the resolution of the simulation. The correct specification of the mesh is very important for the final accuracy of the results. If the number or density of triangles is not high enough in regions, such as junctions or material boundaries, the results of the simulation will be crude and possibly misleading. On the other hand, use of too many triangles will likely lead to significant and unnecessary increases in execution time.

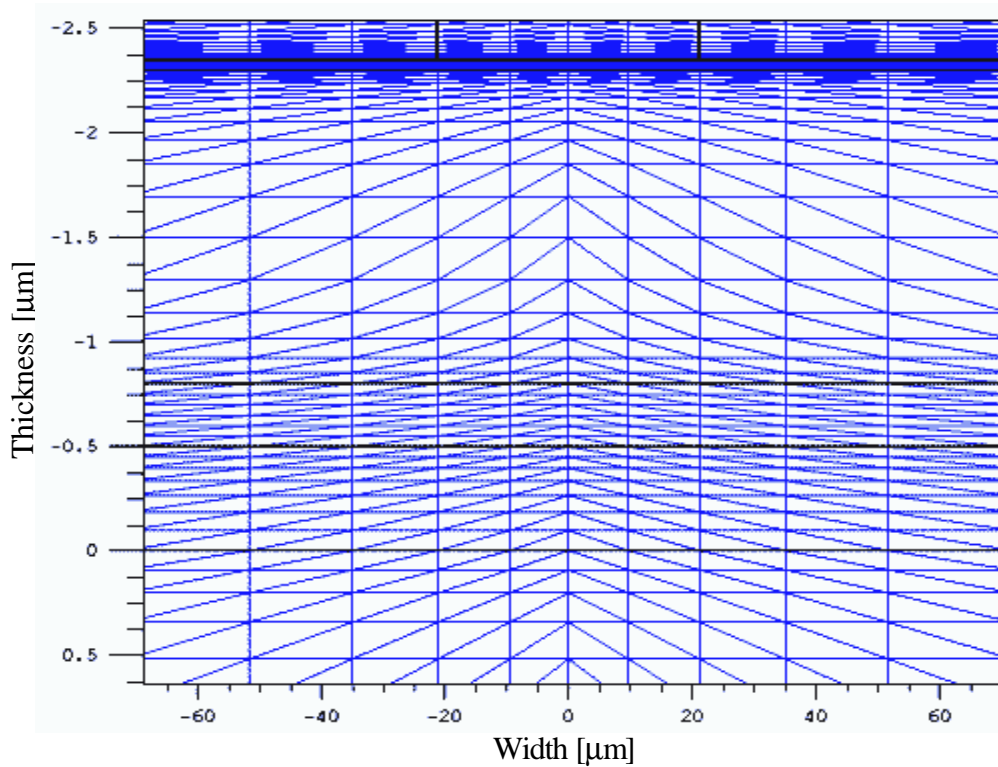


Figure 6.2. Typical mesh.

2. Regions

The material regions need to be specified next. Here, all parts of the grid are assigned to a specific material (Figure 6.3). This can be selected out of Silvaco's own library or can be custom-made by the user. In addition, heterojunction grading between materials can also be described.

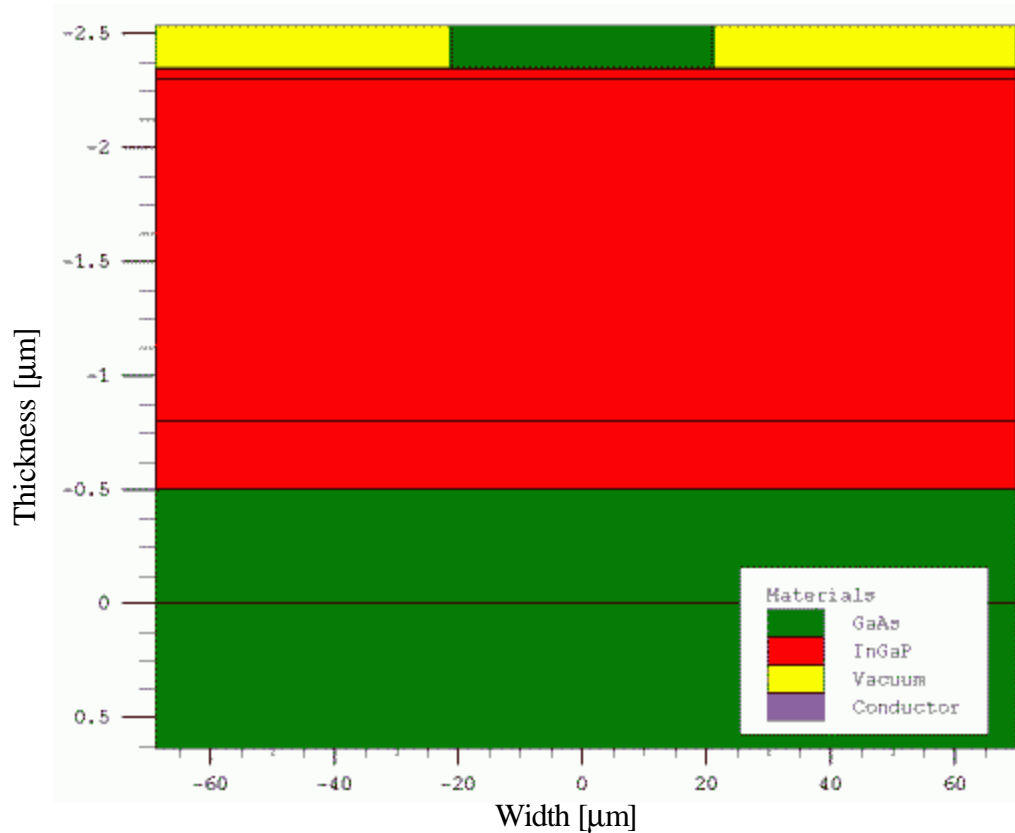


Figure 6.3. Regions specified.

3. Electrodes

To define the electrodes of the device, their position and size need to be entered. Additional information about their materials and workfunctions can be supplied if needed.

4. Doping

Each material can be doped by any dopant to the desired concentration. This can be done in a regular uniform way, in a linear or even a Gaussian distribution. Non-standard doping profiles can also be inputted from other TCAD programs or from custom ASCII files. More advanced doping can be used by using the built-in C interpreter. Automatic optimizations of the mesh according to doping can be performed afterwards.

5. Material Properties

Materials used throughout the simulation can be selected from a library that includes a number of common elements, compounds and alloys. These have their most important parameters already defined. However, in solar cells the use of exotic materials is not unusual. For such purposes, there is the ability to fully define already existing or brand new materials, down to their smallest detail. Such properties range from the essential bandgap and mobility all the way to laser absorption coefficients. Contact information and workfunctions can also be entered here.

6. Models

More than seventy models can be used to achieve better description of a full range of phenomena. Each model can be accompanied by a full set of its parameters, when these differ from the default. Again new models can be described using the C interpreter capability.

7. Light

When lighting is important for a device (like in solar cells), there is the ability to use a number of light sources and adjust their location, orientation and intensity. The spectrum of the light can be described in all the necessary detail. Polarization, reflectivity and raytrace are also among the simulator's features.

8. Simulation Results

Once everything is defined the user can take unbiased measurements, bias certain contacts, short others and take more measurements (Figure 6.4). This way I_{sc} , V_{oc} and other values can be read. Additionally, I-V curves and frequency responses may be obtained. From these, a variety of diagrams can be displayed using a program called TonyPlot. An additional feature is the ability to take measurements from any part of the device and see a 2D or 3D picture of various metrics such as carrier and current densities, photogeneration, potential and e-fields. These pictures are invaluable for the insights they offer.

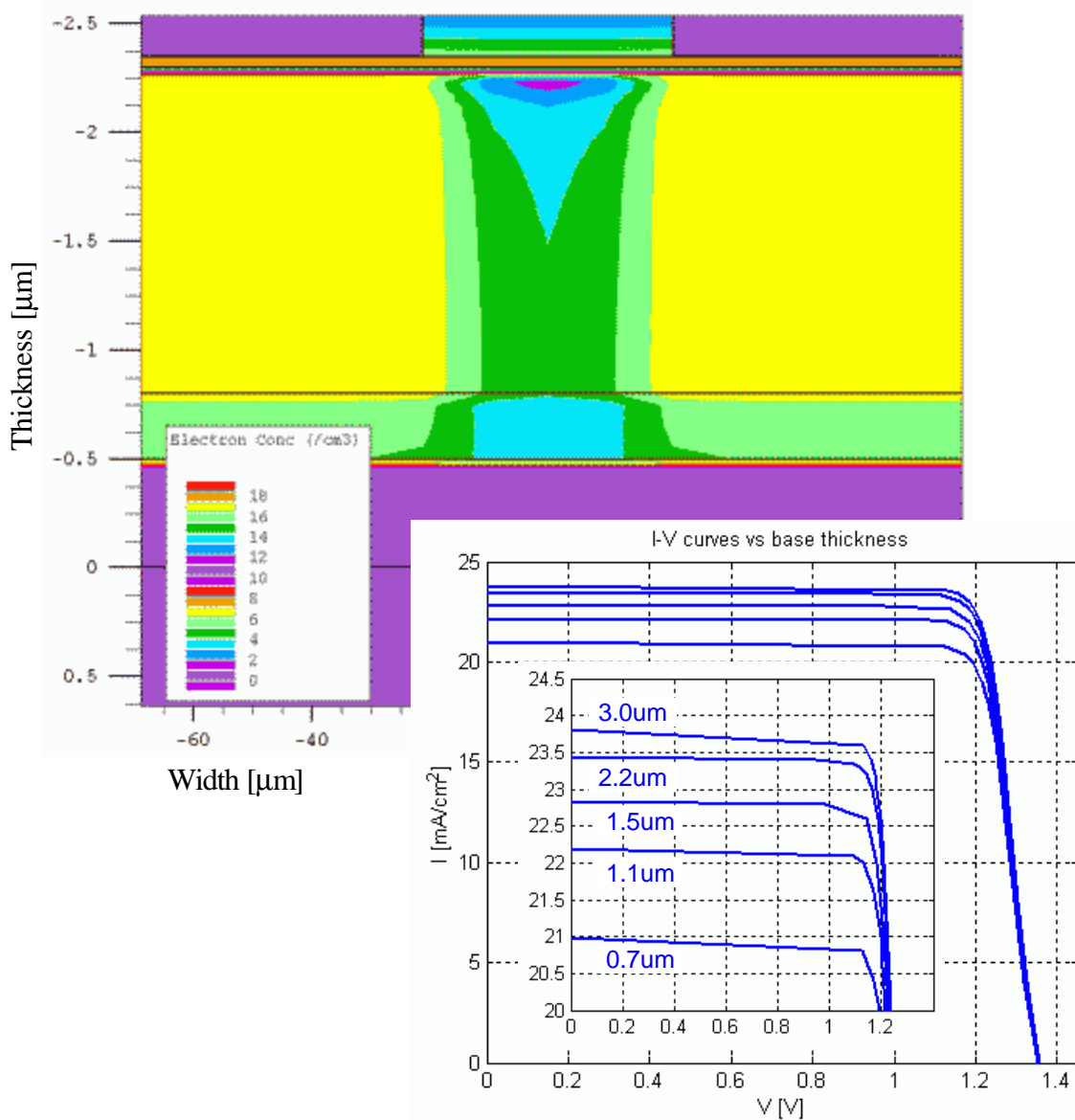


Figure 6.4. Electron concentration picture and I–V curves.

D. SIMULATION SOURCE CODE

The full set of source code used to program the simulations described in the following chapters can be found in Appendix F. In order to enhance understanding, aid further development by others and avoid unnecessary repetitions and confusion, the following scheme has been used to present the code. All the files contain main sections structured the same way:

```

go atlas
# Definition of constants
# Mesh
# X-Mesh
# Y-Mesh
# Regions
# Electrodes
# Doping
# Material properties
# Models
# Light beams
# Solving

```

Each commented section is filled using code from its corresponding subsections. For example for deriving the I_{SC} and V_{OC} of a simple GaAs cell, the code becomes:

```

go atlas
# Definition of constants
# Mesh
    mesh space.mult=1
# X-Mesh: surface=500 um2 = 1/200,000 cm2
    x.mesh loc=-250 spac=50
    x.mesh loc=0 spac=10
    x.mesh loc=250 spac=50
# Y-Mesh
    # Vacuum
    y.mesh loc=-0.1 spac=0.01
    # Emitter (0.1 um)
    y.mesh loc=0 spac=0.01
    # Base (3 um)
    y.mesh loc=3 spac=0.3
# Regions
    # Emitter
    region num=1 material=GaAs x.min=-250 x.max=250 y.min=-0.1 y.max=0
    # Base
    region num=2 material=GaAs x.min=-250 x.max=250 y.min=0 y.max=3
# Electrodes

```

```

    electrode name=cathode top
    electrode name=anode bottom
# Doping
    # Emitter
    doping uniform region=1 n.type conc=2e18
    # Base
    doping uniform region=2 p.type conc=1e17
# Material properties
    material TAUN=1e-7 TAUP=1e-7 COPT=1.5e-10 AUGN=8.3e-32 AUGP=1.8e-31
    # GaAs
    material material=GaAs EG300=1.42 PERMITTIVITY=13.1 AFFINITY=4.07
    material material=GaAs MUN=8800 MUP=400
    material material=GaAs NC300=4.7e17 NV300=7e18
    material material=GaAs index.file=GaAs.opt
# Models
    models BBT.KL
# Light beams
    beam num=1 x.origin=0 y.origin=-5 angle=90 \
        power.file=AM0silv.spec wavel.start=0.21 wavel.end=4 wavel.num=50
# Solving
    # Get Isc and Voc
    solve init
    solve b1=1
    contact name=cathode current
    solve icathode=0 b1=1

```

If now, the IV characteristic must be produced, only the “Solving” section needs to be changed with code from the corresponding subsection. This could very well be handled by using object-oriented programming. Unfortunately, VWF does not support such functionality. The scheme used here is an attempt to provide a substitute even though it is a primitive one.

E. EXCHANGING DATA WITH MATLAB

In spite of the functionality provided by TonyPlot, there is often the need to exchange data between TCAD and more flexible and general environments such as

Matlab. Since this functionality is not supported by the program, part of this thesis involved the development of several Matlab functions to provide this. The source code can be found in Appendix G.

1. Creating Silvaco input files

Before running a simulation, several input data must be provided to the program. One set of inputs consists of solar spectrum power files and material optical parameter files. *VEC2SPEC* creates the power file for any solar spectrum specified in its input. Using this function, power files for AM0, AM1.5 and AM2 were created.

Function name: VEC2SPEC

Input arguments: wavel: An array with the wavelengths to be saved.
int: An array with the corresponding intensities.
filename: The name of the file to be saved.

Output arguments: none

Syntax: VEC2SPEC(wavel, int, filename)

OPT2SILV creates n and k optical parameter files for various materials. This was used to produce files for all the materials used in this research (i.e. Ge, GaAs, GaP, InP etc).

Function name: OPT2SILV

Input arguments: filename: The name of the .mat file that contains the data.
t: The type of data. “e” for e1 and e2 vs. energy [eV] and “n” for n and k vs. wavelength [μm]

Output arguments: none

Syntax: OPT2SILV(filename, t)

2. Extracting results

All Silvaco numerical data may be saved at log files. These may contain totally different types of data. *DISPLOG* scans a log file and displays the types of its contents.

Function name: DISPLOG

Input arguments: filename: The name of the .log file to be read.

Output arguments: none

Syntax: DISPLOG(filename)

An example of its output is:

```
>> displog('GaAs-1-IV')
ATLAS
Electrodes:
  1. cathode
  2. anode
Values:
  1. Light Intensity beam 1
  2. Available photo current
  3. Source photo current
  4. Optical wavelength
  5. cathode Voltage
  6. cathode Int. Voltage
  7. cathode Current
  8. anode Voltage
  9. anode Int. Voltage
 10. anode Current
```

Various log files have a peculiar format. *PARSELOG* translates this and parses all existing data.

Function name: PARSELOG

Input arguments: filename: The name of the .log file to be read.

Output arguments: prog: The name of the program that originally created the file.
numOfElec: The number of electrodes for which data is provided.
elecName: A cell containing the name of these electrodes.
val: The number of different types of values in the file.
valName: A cell containing the names of those types.
data: A matrix containing the actual data. Columns contain data of the same type.

Syntax: [prog, numOfElec, elecName, val, valName, data] =
PARSELOG(filename)

PLOTLOG creates plots of data that exist in a log file.

Function name: PLOTLOG

Input arguments: filename: The name of the .log file to be read.

x-axis: The number of the data type to appear on the x-axis. This is the number that is shown by the DISPLOG function.

y-axis: The number of the data type to appear on the y-axis. This is the number that is shown by the DISPLOG function.

style: The style of the line to be used for the plot. See PLOT function for the supported styles.

xmult: Multiplication factor for the values on the x-axis.

ymult: Multiplication factor for the values on the y-axis.

Output arguments: none

Syntax: PLOTLOG(filename, x-axis, y-axis, style, xmult, ymult)

EV2UM , *UM2EV* and *E2NJ* are also written to implement unit transformations for supporting the above files.

THIS PAGE INTENTIONALLY LEFT BLANK

VII. MATERIAL PROPERTIES

The next portion of thesis study contains the research related to how various materials and their physical and electrical properties are modeled. This was a challenging task as most of the materials used in advanced solar cell technology are exotic and little published research exists.

A. CURRENT STATUS

Analytical modeling relies on the use of equations to approximate the actual behavior of – in our case – solar cells. As such, they require a detailed description of the device to be simulated and the materials that are used in its construction. It will become apparent in later chapters that the selection of the appropriate material type and composition as well as its electrical properties are very important to the efficiency of both real and simulated cells.

According to the existing literature, the materials mostly used are the single element semiconductors Si and Ge and the binary compounds GaAs and InP. In addition to those, many ternary and quaternary compounds are also used in most cases. These are alloys of three or four of the Al, As, Be, Cd, Ga, Hg, In, N, P, Pb, S, Sb, Sc, Se, Te, Zn and other, less common, elements. The large number of these combinations provides electronic device researchers with a valuable abundance of choices.

However, the electrical and physical properties of each material cannot be theoretically calculated with enough accuracy. Instead, they need to be measured in very precise and expensive experiments. Therefore, the material abundance, mentioned earlier, creates a huge task for physicists. The single element semiconductors and the binary GaAs have been studied exhaustively. However, for the rest of the binaries, only their major and most important properties are published. For the ternaries and quaternaries, very little is available and most of the times, the only solution is provided by interpolating the properties of their binary components.

B. SILVACO LIBRARY

Silvaco maintains a property library of many materials common to electronic devices. However, in an effort to push solar cell efficiency to higher levels, researchers tend to use many exotic materials. For them, Silvaco's library is under development and mostly incomplete.

The models used in this thesis are heavily dependent on the following properties:

- Bandgap E_g
- Electron and hole density of states N_C and N_V
- Electron and hole mobilities μ_n and μ_p
- Lattice constant a
- Permittivity
- Electron and hole lifetimes τ_n and τ_p
- Electron affinity
- Radiative recombination rate C_{R0}
- Electron and hole Auger coefficients A_{GN} and A_{GP}
- Optical parameters n and k

Values for most of these have been provided by various publications. As another part of this thesis, a large number of such publications has been researched. This collection of information has been identified, categorized and compared. Finally, the best have been selected and used in the simulations described in this thesis. Parameters, for materials not found in publications, have been mathematically approximated. In addition, several well-studied cells were also used as references to provide calibration for these unknown values.

Furthermore, a very large number of additional parameters can still be specified. However, they mostly represent secondary phenomena. These will be approximated by values of well-known materials like Si, Ge or GaAs. Due to the secondary significance of the properties, bad approximations will only lead to errors within acceptable noise margins.

C. LATTICE MATCHING AND ALLOY PROPERTIES

An alloy is created with a combination of binary compounds under certain proportions. Thus, one part of the ternary GaInP is actually x parts GaP plus $1-x$ parts InP. A way to represent this is $(\text{GaP})_x(\text{InP})_{1-x}$ or simpler $\text{Ga}_x\text{In}_{1-x}\text{P}$.

The properties of the alloy have values between those of the properties of its components. This is rarely a linear 1: x relationship, as shown in Figure 7.1, but most of the times it can be approximated as such. For example, GaAs has a lattice constant $\alpha=5.65\text{\AA}$, GaP has $\alpha=5.45\text{\AA}$ and InP has $\alpha=5.87\text{\AA}$. In order to lattice match $\text{Ga}_x\text{In}_{1-x}\text{P}$ to GaAs we need

$$a_{\text{GaAs}} = a_{\text{GaP}} \cdot x + a_{\text{InP}} \cdot (1-x) \Leftrightarrow x = \frac{a_{\text{GaAs}} - a_{\text{InP}}}{a_{\text{GaP}} - a_{\text{InP}}}$$

which returns $x \approx 0.52$ ($\text{Ga}_{0.52}\text{In}_{0.48}\text{P}$). GaP has $E_g=2.35\text{eV}$ and InP has $E_g=1.42\text{eV}$ so, in this case, its bandgap will be

$$E_g^{\text{GaInP}} = x E_g^{\text{GaP}} + (1-x) E_g^{\text{InP}}$$

which returns $E_g \approx 1.9\text{eV}$. Other properties can also be calculated the same way for ternaries and quaternaries.

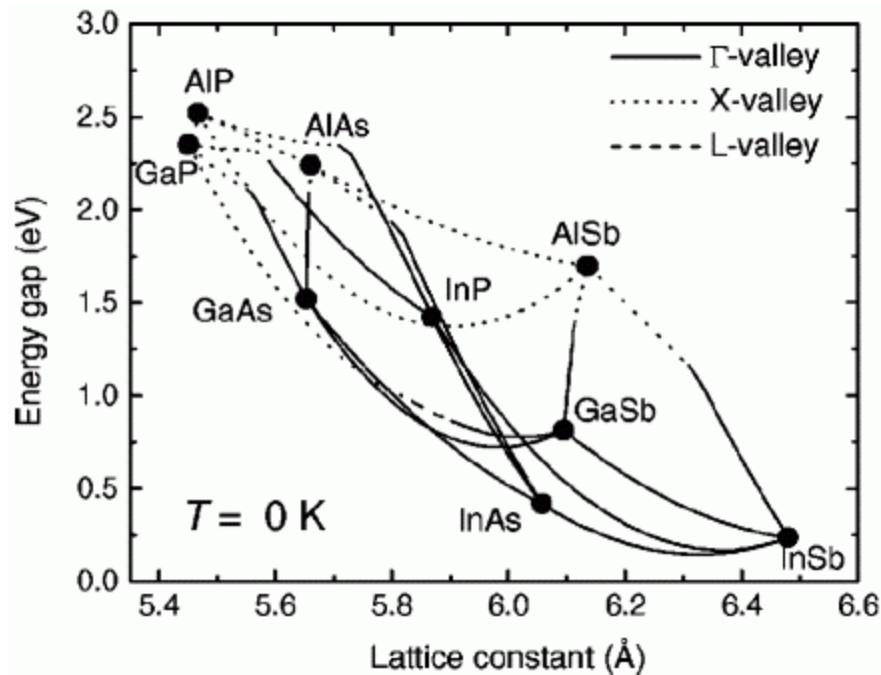


Figure 7.1. Bandgap vs. lattice constant for binary compounds [Ref. 33].

When higher accuracy is required, sets of *bowing parameters* have been published to produce a better approximation to this non-linearity. For ternaries the quadratic form

$$E_g^{GaInP} = x \cdot E_g^{GaP} + (1-x) \cdot E_g^{InP} - x(1-x) \cdot B_{GaInP} \quad [\text{Ref. 33}]$$

is used where B_{GaInP} is the bowing parameter for GaInP. For quaternaries like the $Al_xGa_{1-x}In_yP_{1-y}$ the expression

$$E_g^{AlGaInP} = \frac{x \cdot (1-x) [(1-y) \cdot E_g^{AlGaP} + y \cdot E_g^{AlGaIn}] + y \cdot (1-y) [x \cdot E_g^{AlInP} + (1-x) \cdot E_g^{GaInP}]}{x \cdot (1-x) + y \cdot (1-y)}$$

[Ref. 33]

can be used where E_g^{AlGaP} and E_g^{AlGaIn} are the bandgaps for $Al_xGa_{1-x}P$ and $Al_xGa_{1-x}In$ respectively and E_g^{AlInP} and E_g^{GaInP} are the bandgaps for $AlIn_yP_{1-y}$ and $GaIn_yP_{1-y}$ respectively as calculated above.

D. OTHER CALCULATIONS

Temperature compensation for the bandgap can be calculated by using the following equation:

$$E_g(T) = E_g(0) - \frac{\alpha T^2}{T + \beta}$$

where α , β and either $E_g(T)$ or $E_g(0)$ can easily be found in existing research.

The effective density of states of electrons N_C and holes N_V can be found using

$$N_C = 2 \cdot \left(\frac{600 \cdot \mathbf{p} \cdot m_e^* \cdot k}{h^2} \right)^{\frac{3}{2}} \quad \text{and} \quad N_V = 2 \cdot \left(\frac{600 \cdot \mathbf{p} \cdot m_h^* \cdot k}{h^2} \right)^{\frac{3}{2}} \quad [\text{after Ref. 10:p. 3.5}]$$

where m^* is the effective mass of the carrier in question, h is Plank's constant and k is Boltzmann's constant.

E. RESULTS

A detailed set of major material parameters has been produced by literature research and calculations as well as calibration from well-known cells. Tables 7.1 to 7.5 show the values that were finally produced and used for the purposes of this research. All Nitrides are zinc blende. Numbers in blue color indicate that the values were found in existing literature, while numbers in green have been calculated. All properties are at 300°K unless other wise indicated. Values indicated with a “NR” were not found anywhere in published research. The optical parameters n and k are different for every wavelength. Due to the large quantity of numbers, they are not shown here.

Material	Bandgap E_g^G [eV] @0°K	a(G) [meV/K]	b(G) [K]	Bandgap E_g^X [eV] @0°K	a(G) [meV/K]	b(G) [K]	Bandgap E_g^L [eV] @0°K	a(G) [meV/K]	b(G) [K]	Bandgap E_g [eV] @300°K
Si										1.12
Ge										0.67
GaAs	1.519	0.5405	204	1.981	0.46	204	1.815	0.605	204	1.42
AlAs	3.099	0.885	530	2.24	0.7	530	2.46	0.605	204	2.16
AlN	4.9	0.593	600	6	0.593	600	9.3	0.593	600	6.28
AlP	3.63	0.577	372	2.52	0.318	588	3.57	0.318	588	2.45
GaN	3.299	0.593	600	4.52	0.593	600	5.59	0.593	600	3.45
GaP	*	NR	NR	2.35	0.577	372	2.72	0.577	372	2.27
InAs	0.417	0.276	93	1.433	0.276	93	1.133	0.276	93	0.35
InN	1.94	0.245	624	2.51	0.245	624	5.82	0.245	624	2
InP	1.424	0.363	162	**	NR	NR	2.014	0.363	162	1.35
* $2.886 + 0.1081 [1 - \coth(164 / T)]$ ** $2.384 - 3.7 \cdot 10^{-4} \cdot T$										

Table 7.1. Bandgap parameters for unary and binary materials.

Material	Lattice const a [Å]	Permittivity ϵ_s/ϵ_0	Affinity ? [eV]	Heavy e^- effective mass [m_e/m_0]	Heavy h^+ effective mass [m_h/m_0]	e^- mobility MUN [$\text{cm}^2/\text{V}\cdot\text{s}$]	h^+ mobility MUP [$\text{cm}^2/\text{V}\cdot\text{s}$]	e^- density of states NC [cm^{-3}]	h^+ density of states NV [cm^{-3}]
Si	5.43	11.9	4.17	0.92	0.54	1500	500	2.8e19	1.04e19
Ge	5.66	16	4	1.57	0.28	3900	1800	1.04e19	6e18
GaAs	5.65	13.1	4.07	0.063	0.5	8800	400	4.7e17	7e18
AlAs	5.66	10.1	2.62	1.1	0.41	1200	420	3.5e19	6.6e18
AlN	4.38	NR	NR	NR	NR	NR	14	NR	NR
AIP	5.45	9	NR	3.61	0.51	60	450	2.1e20	9.2e18
GaN	4.5	12.2	NR	0.22	0.96	380	130	3.1e18	2.4e19
GaP	5.45	11.1	4	4.8	0.67	160	135	3.2e20	1.4e19
InAs	6.06	14.6	4.54	0.021	0.43	33000	450	9.2e16	7.1e18
InN	4.98	NR	NR	0.12	0.5	250	–	1.3e18	8.9e18
InP	5.87	12.4	4.4	0.325	0.6	4600	150	5.6e18	1.2e19

Table 7.2. Major parameters for unary and binary materials.

Material	Bowing parameter E_g^G [eV] @0°K	Bowing parameter E_g^X [eV] @0°K	Bowing parameter E_g^L [eV] @0°K
AlGaAs	-0.127+1.31x	0.055	0
AlGaP	0	0.13	NR
AlInAs	0.7	0	NR
AlInP	-0.48	0.38	NR
GaAsP	0.19	0.24	0.16
GaInAs	0.477	1.4	0.33
GaInP	0.65	0.2	1.03

Table 7.3. Bowing parameters for ternary materials.

Material	Bowing parameter E_g [eV] @0°K (only for the bandgap)	Bowing parameter E_g^x [eV] @0°K (for quantities other than the bandgap)	Bowing parameter E_g^L [eV] @0°K (for quantities other than the bandgap)
AlGaIn	0	0.61	0.8
AlInN	16–9.1x	NR	NR
GaAsN	120.4–100x	NR	NR
GaInN	3	0.38	NR
InAsN	4.22	NR	NR

Table 7.4. Bowing parameters for ternary Nitrides.

Material	Bandgap E_g [eV] @300°K	Lattice const a [Å]	Permittivity ϵ_s/ϵ_0	Affinity ? [eV]	Heavy e^- effective mass [m_e^*/m_0]	Heavy h^+ effective mass [m_h^*/m_0]	e^- mobility MUN [$cm^2/V\cdot s$]	h^+ mobility MUP [$cm^2/V\cdot s$]	e^- density of states NC [cm^{-3}]	h^+ density of states NV [cm^{-3}]
AlGaInP	2.3	5.65	11.7	4.2	2.85	0.64	2150	141	1.2e20	1.28e19
AlInP	2.4	5.65	11.7	4.2	2.65	0.64	2291	142	1.08e20	1.28e19
GaInP	1.9	5.65	11.6	4.16	3	0.64	1945	141	1.3e20	1.28e19

Table 7.5. Major parameters for the ternary ($Al_{0.52}In_{0.48}P$, $Ga_{0.51}In_{0.49}P$) and quaternary ($Al_{0.25}Ga_{0.25}In_{0.5}P$) lattice matched to GaAs materials used.

F. MOBILITY VS DOPING

The mobility values mentioned above are for undoped materials. However, mobility changes very much with doping. The values for GaAs are in Table 7.6 and Figure 7.2. For the purposes of this thesis, the GaAs mobility values used are interpolated from this table. For other materials mobility values are derived using this table as a guideline.

Doping concentration [cm^{-3}]	e^- mobility MUN [$\text{cm}^2/\text{V}\cdot\text{s}$]	h^+ mobility MUP [$\text{cm}^2/\text{V}\cdot\text{s}$]
1.0e14	8000.0	390.0
2.0e14	7718.0	380.0
4.0e14	7445.0	375.0
6.0e14	7290.0	360.0
8.0e14	7182.0	350.0
1.0e15	7300.0	340.0
2.0e15	6847.0	335.0
4.0e15	6422.0	320.0
6.0e15	6185.0	315.0
8.0e15	6023.0	305.0
1.0e16	5900.0	302.0
2.0e16	5474.0	300.0
4.0e16	5079.0	285.0
6.0e16	4861.0	270.0
8.0e16	4712.0	245.0
1.0e17	4600.0	240.0
2.0e17	3874.0	210.0
4.0e17	3263.0	205.0
6.0e17	2950.0	200.0
8.0e17	2747.0	186.9
1.0e18	2600.0	170.0
2.0e18	2060.0	130.0
4.0e18	1632.0	90.0
6.0e18	1424.0	74.5
8.0e18	1293.0	66.6
1.0e20	1200.0	61.0

Table 7.6. Mobility vs doping concentration [data after Ref. 10].

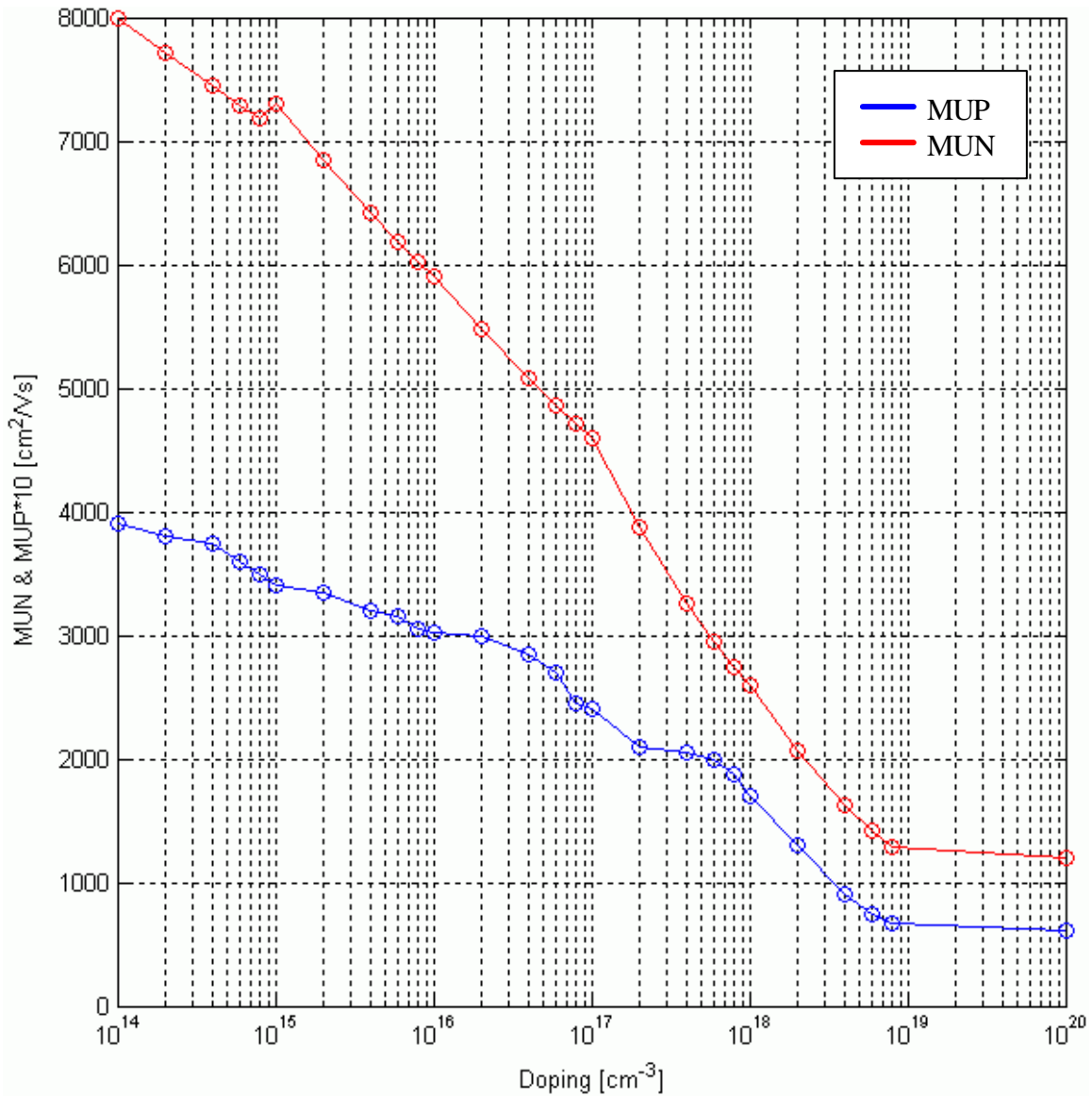


Figure 7.2. Mobility vs doping concentration [data after Ref. 10].

G. OPTICAL PARAMETERS

The meaning of optical parameters was explained in chapter 4. The values required for the purposes of this research are the n and k for wavelengths in the range of 0.2nm to 6nm. Atlas can receive this input, separately for each material, from an ASCII file of specific format. Non-existent values are automatically interpolated.

This data can only be derived by experiments and measurements performed on the each material, under very strict conditions. These have been publicized among others in

Ref. 5. The materials covered in those are most of the unaries and binaries, but only a small number of ternaries and quaternaries. Hence, the only way to produce the necessary numbers is interpolation.

In Figure 7.3, the k parameter for $\text{In}_{0.5}\text{Ga}_{0.5}\text{P}$ (red) has been interpolated from GaP (blue) and InP (violet) using a simple algorithm. Photons are absorbed by the material when k is greater than zero. Therefore, the wavelength where k first becomes non-zero, corresponds to energy approximately equal to the bandgap E_g . This can easily be verified for GaP and InP from Table 7.1. However, the result for InGaP does not seem correct. For this reason, a more sophisticated and enhanced algorithm (OPTINTERP) was implemented in Matlab and used throughout the simulations. Figure 7.4 shows the correct results. The full source code can be seen in Appendix G.

Function name: OPTINTERP

Input arguments: f1: The name of the first .mat file to be used in the interpolation.
f2: The name of the second .mat file to be used in the interpolation.

r: The ratio f1:f2 of the interpolation.

Output arguments: wavel: An array with the wavelengths of the resulting parameters.

n: An array with the n optical parameter.

k: An array with the k optical parameter.

Syntax: [wavel n k] = OPTINTERP(f1, f2, r)

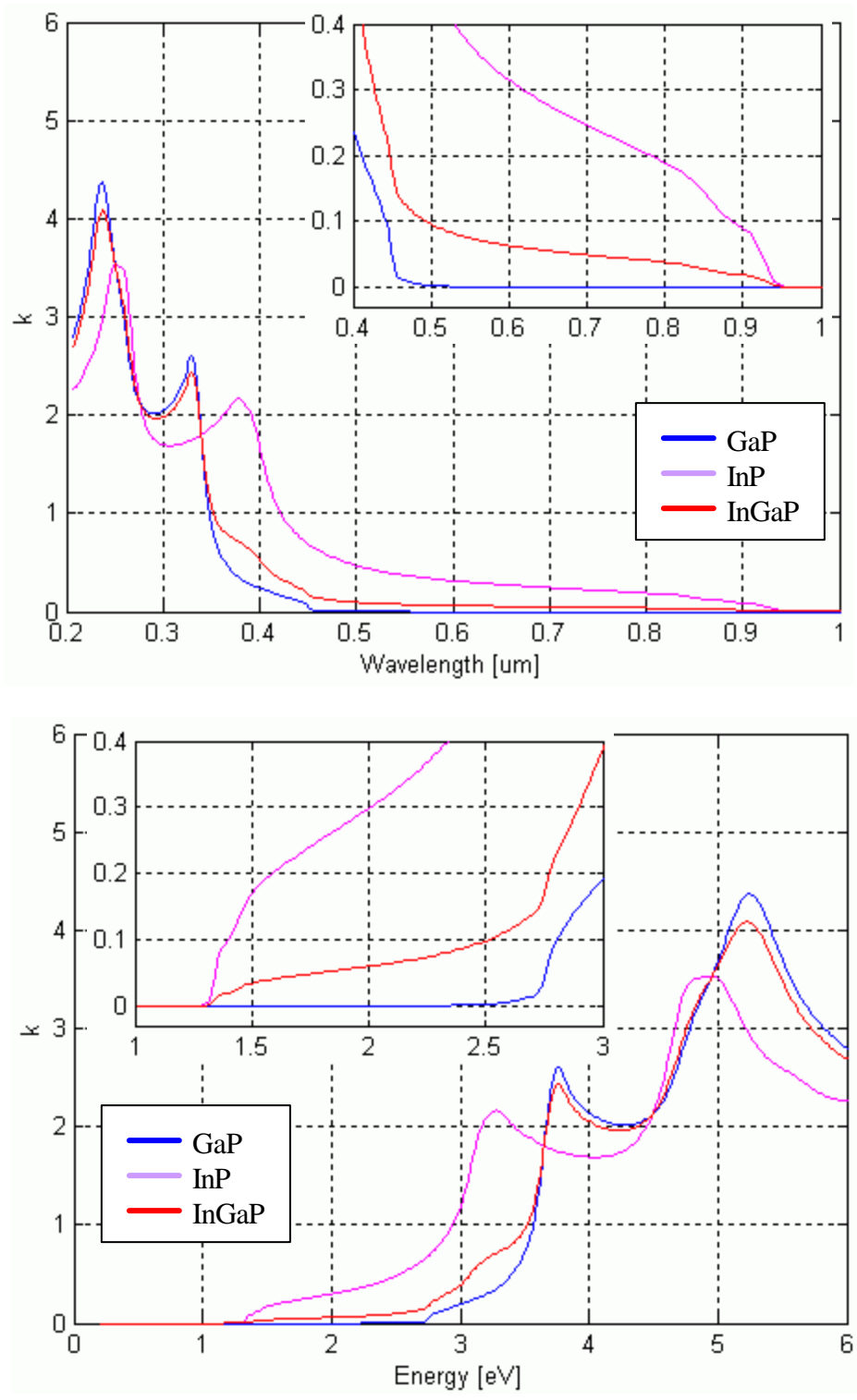


Figure 7.3. Optical parameter k vs wavelength and energy (simple interpolation).

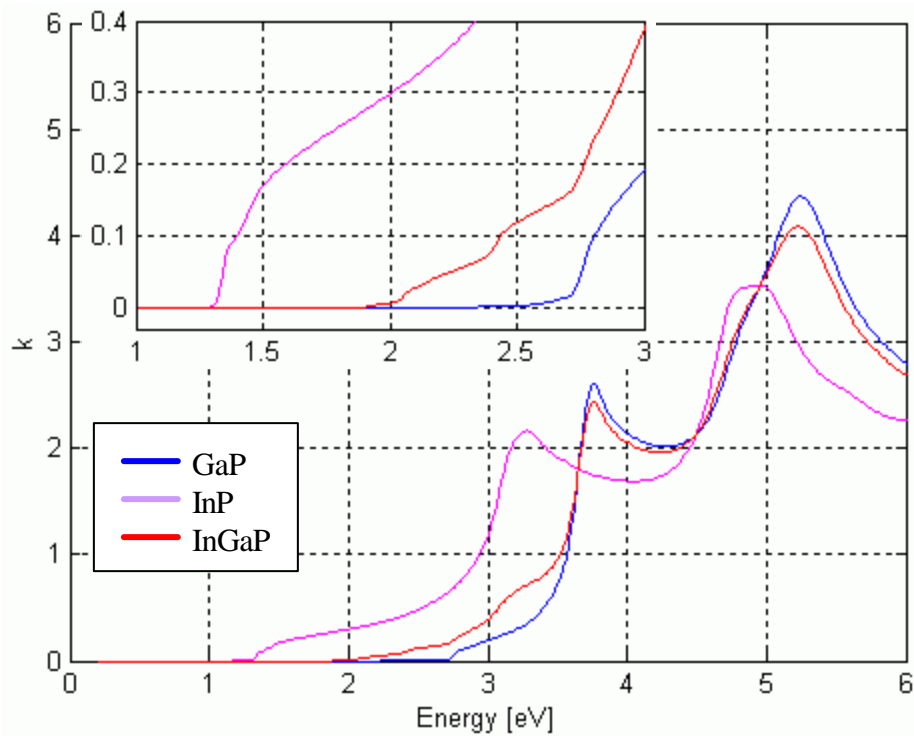
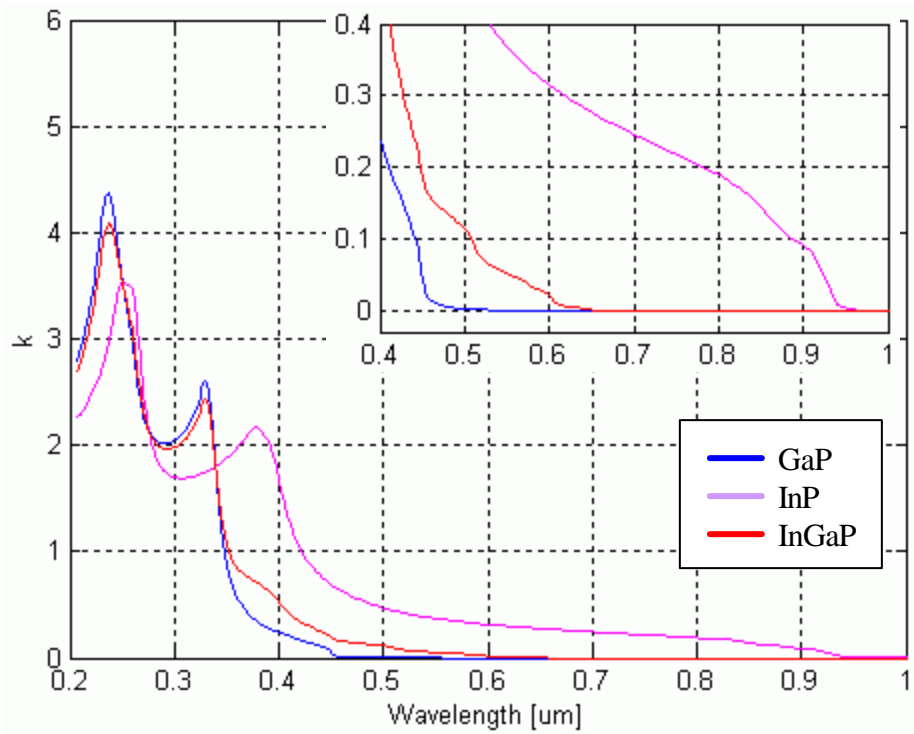


Figure 7.4. Optical parameter k vs wavelength and energy (enhanced interpolation).

VIII. BUILDING A MULTIJUNCTION CELL

This chapter uses the methodology introduced in chapter 6 and the results on material properties of chapter 7 to provide a complete simulation of an actual solar cell. This particular cell is studied very much by researchers and a large number of publications provide valuable experimental data. This data is used to verify the simulation results and thus validate the process.

A. THE PROCESS

Even though TCAD is a tool with many features and varied functionality, the fact that it has not been used to model advanced solar cells might raise doubts about the validity of its output when it is used for such a purpose. The plethora of still unexplored material and optical parameters involved, are also a cause of valid concern about the accuracy of the produced results. For the third and major part of this thesis, these issues have been addressed and resolved.

The development of a complete model starts with the building of a p–n junction which is the simplest possible device. This involves a thorough verification process. The device is fully simulated and the results are compared to published experimental results of similar devices. Various parameters and characteristics of the model are then tweaked, to approximate the results in those publications more closely. The whole process is repeated, as in a spiral (Figure 8.1), until a satisfactory level of accuracy is reached. For the sake of simplicity and brevity, only the results of this process are presented here.

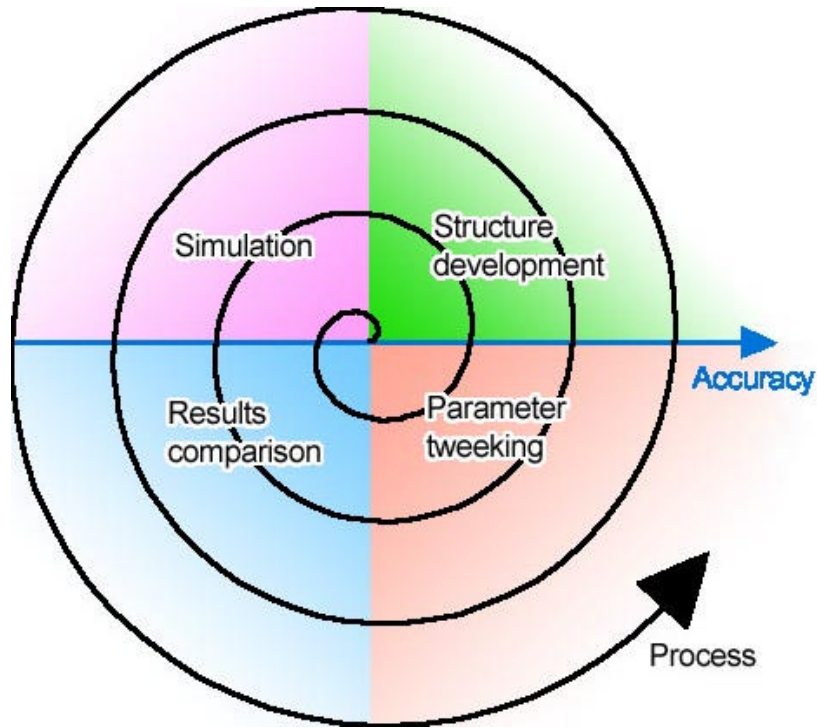


Figure 8.1. Verification process.

After the device is fully developed and its behaviour is verified, additional layers are added to it. The new structure then goes through the same verification process described earlier, thus allowing for starting with a simple model and incrementally adding and accessing successive layers of complexity. Many of these devices are later combined to create an advanced solar cell (Figure 8.2).

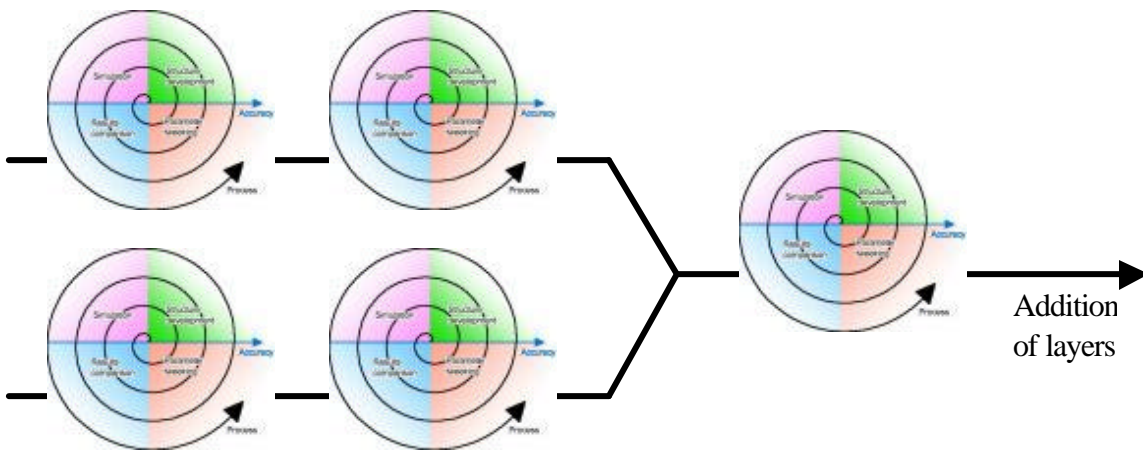


Figure 8.2. Cell development process.

B. THE SIMPLE GaAs CELL

A very common material used in solar cells is GaAs. It produces relatively high current ($I_{SC} \cong 25\text{mA/cm}^2$) and a voltage of $V_{OC} \cong 0.9\text{V}$. On this first attempt, the cell will have the basic n-on-p structure shown in Figure 8.3:

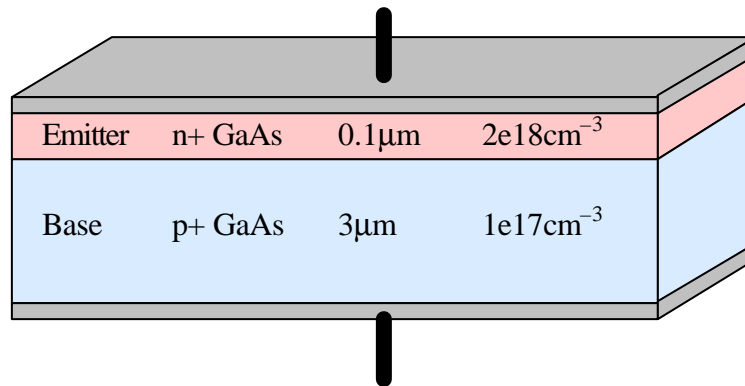


Figure 8.3. Simple GaAs cell.

In the beginning, the mesh (Figure 8.4) is created, taking special care to make it denser near the junction and to have enough divisions per layer.

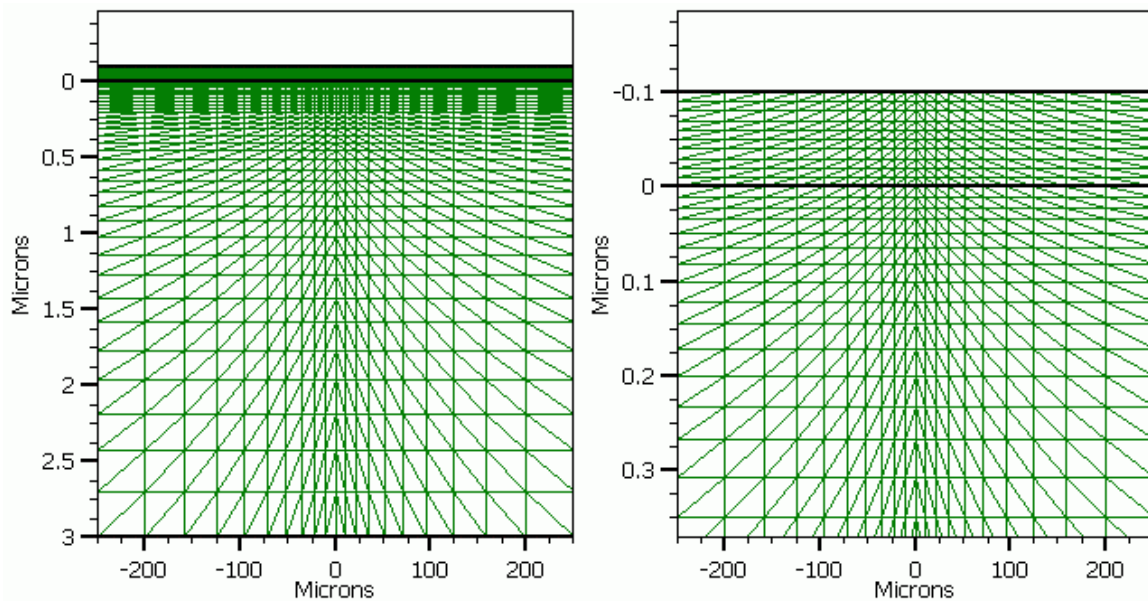


Figure 8.4. The mesh.

After the material regions and the doping levels are specified, a full set of material properties is defined. For simplicity, at this step, the electrodes are considered to be ideal and transparent. Finally, several types of results are programmed to be calculated. One of them is the potential build-up, as well as the electrostatic field of the depletion region at the junction, both of which can be seen in Figure 8.5.

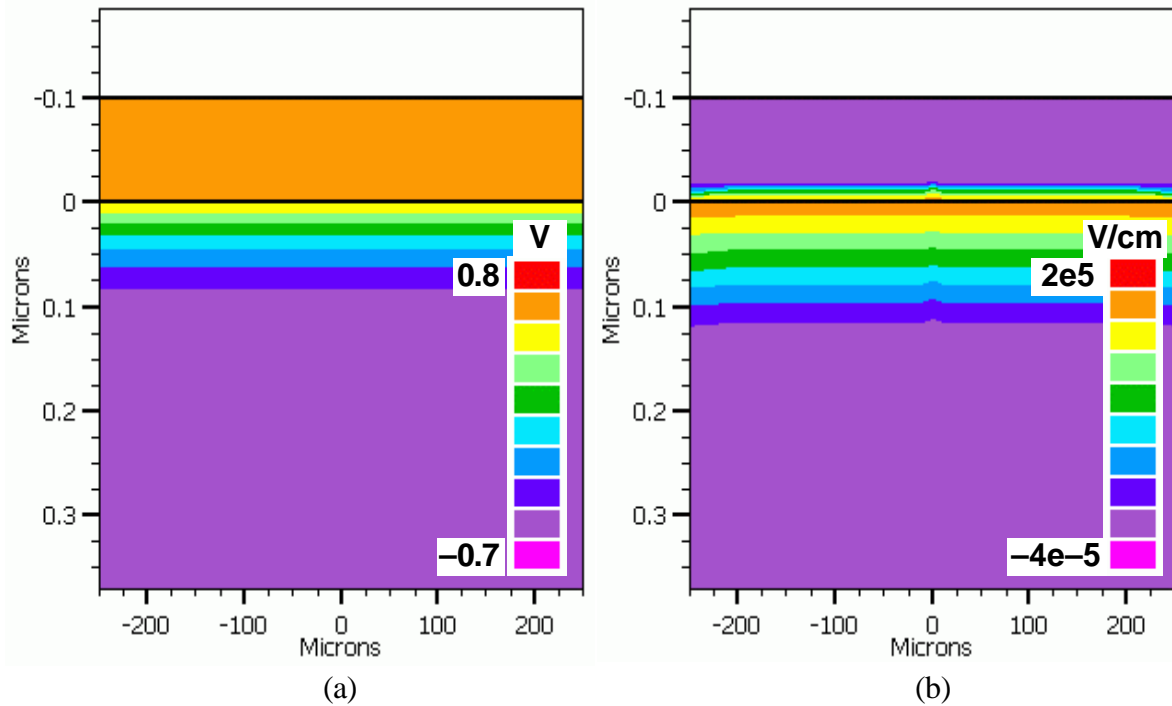


Figure 8.5. (a) Potential and (b) Electrostatic field.

At this stage of development the cell has a $V_{OC} = 0.93V$ and an $I_{SC} = 25.2mA/cm^2$ which are very close to the expected values. Furthermore, the I-V characteristic can be plotted (Figure 8.6) to aid in the determination of the cell's operating point, fill factor, efficiency etc.

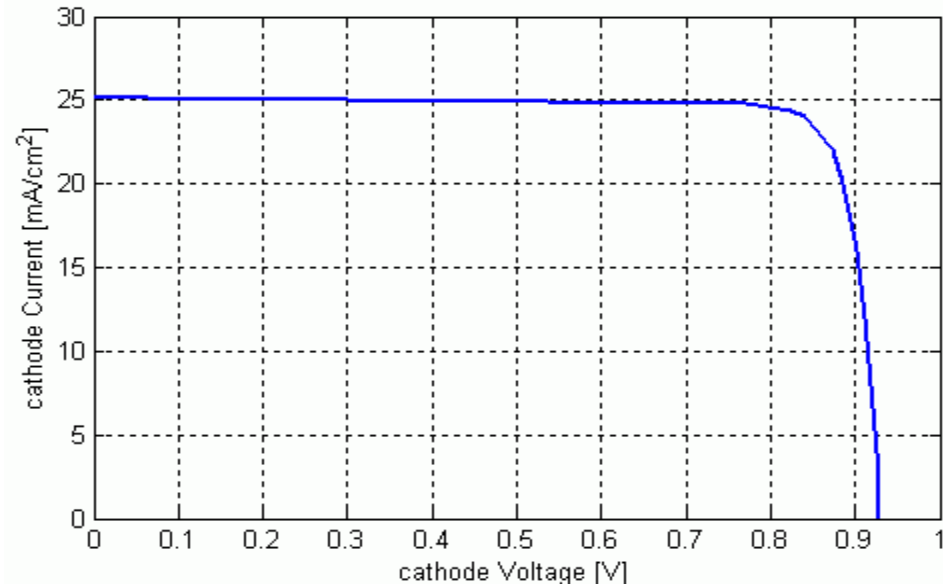


Figure 8.6. IV characteristic.

The frequency response (Figure 8.7) can be used in researching ways to improve performance. The goal is to expand the frequency range in which the multijunction cell is active and thus produces current. To succeed in this, cells that respond to different frequency ranges must be identified and used. The normalized current - used here and throughout this thesis - is actually the short-circuit current produced by the cell, for a single optical wavelength of the AM0 light shined upon it. This is normalized to its maximum value, in order to facilitate comparison.

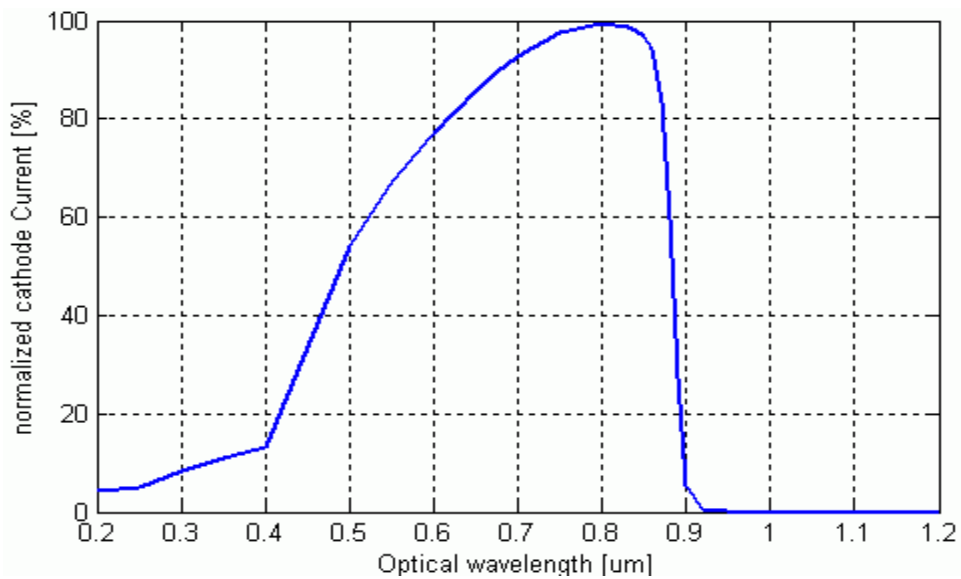


Figure 8.7. Frequency response.

Another impressive graph allows the viewing of the current as it is created by the various wavelengths (Figure 8.8).

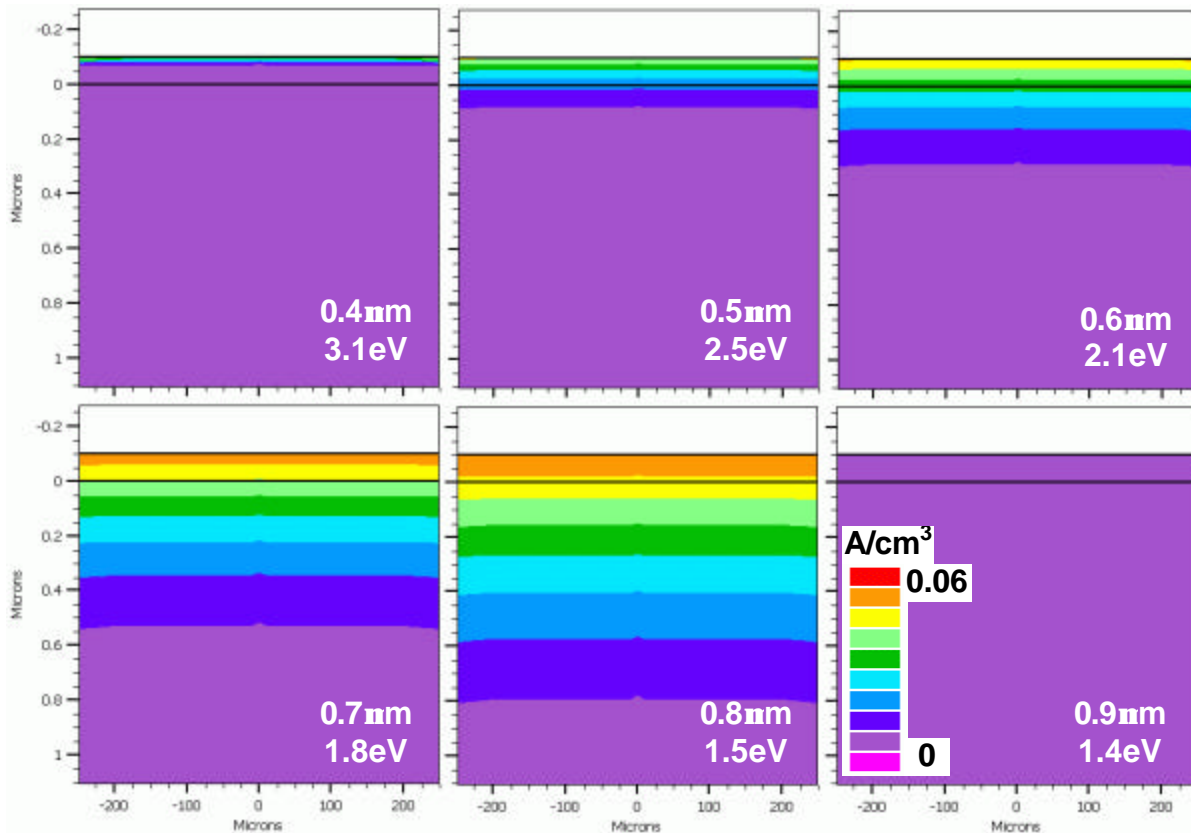


Figure 8.8. Electron current density per wavelength.

C. IMPROVING THE CELL

As discussed in chapter 8, the addition of a BSF below the cell is one of the most important improvements. It should slightly increase I_{SC} and voltage to $V_{OC} \cong 1V$. The material selected is InGaP lattice matched to GaAs.

For purposes of mechanical strength, the cell should also be built on a much thicker ($\cong 0.3mm$) substrate. GaAs is a good material to use. However, the junction of the substrate and the BSF should not create a field that opposes the movement of carriers towards the electrodes. For this reason, a heavily doped GaAs buffer layer is grown between them. Together with its window layer the cell becomes like in Figure 8.9 and 8.10:

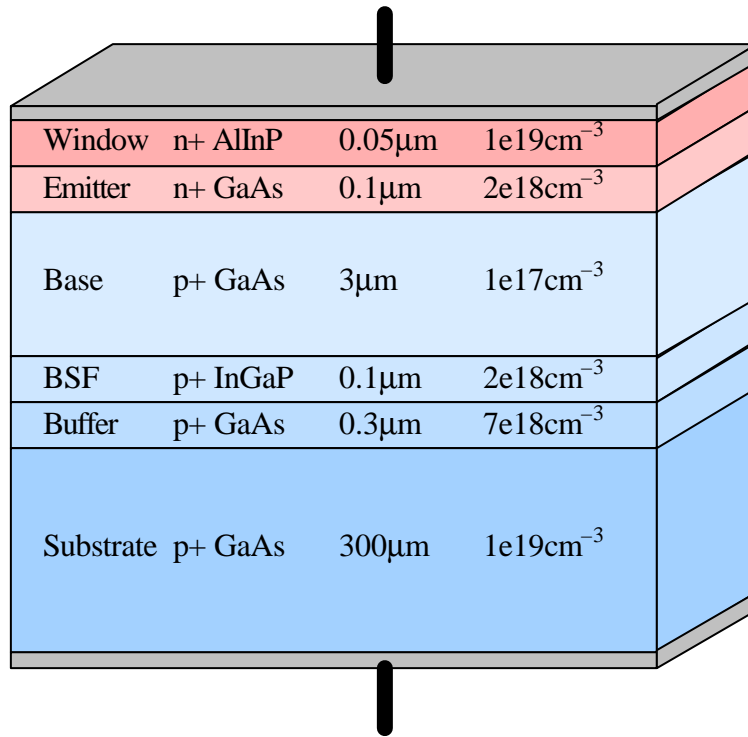


Figure 8.9. Improved GaAs cell.

The mesh of the cell now becomes:

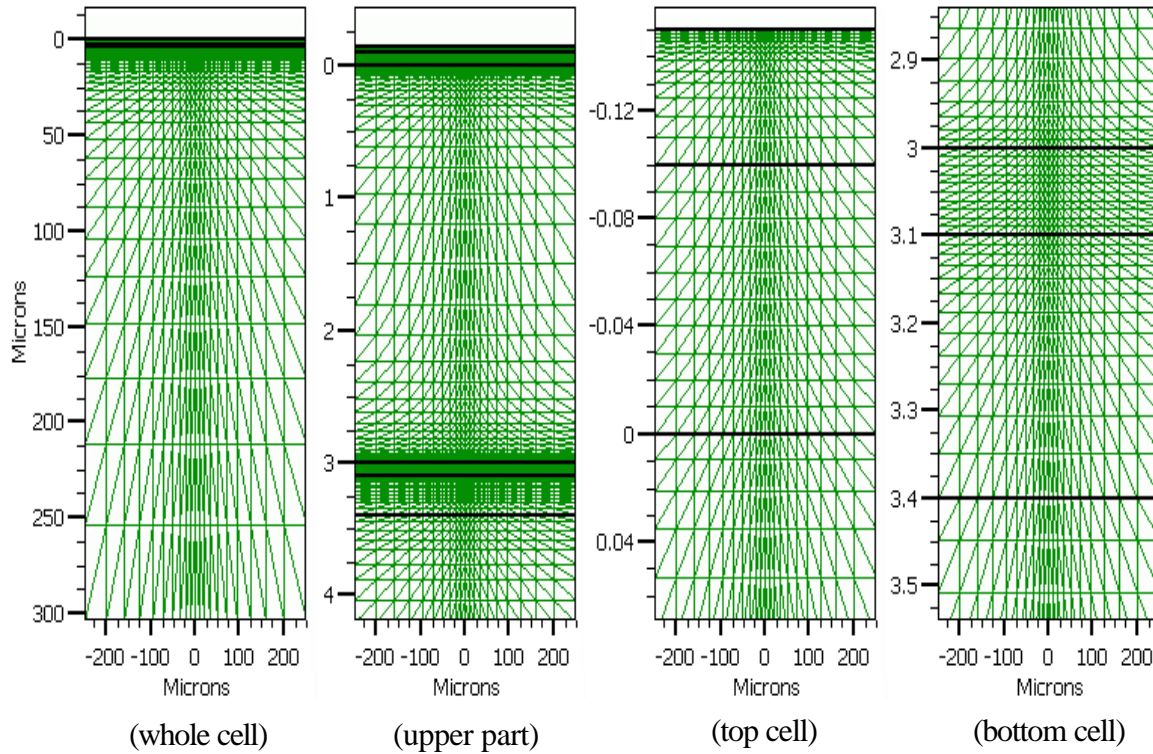


Figure 8.10. The mesh of the improved cell.

The additional electrostatic field of the BSF can also be seen in Figure 8.11:

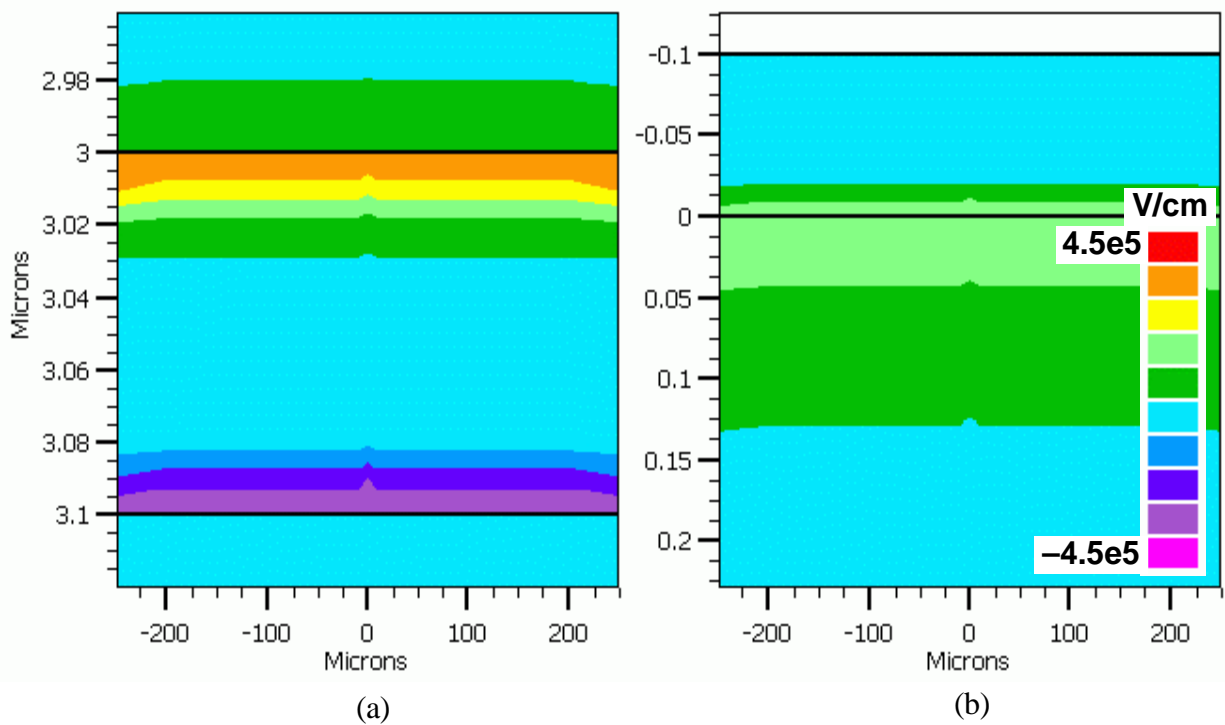


Figure 8.11. (a) The BSF and (b) the depletion region electrostatic fields.

Now the cell has a $V_{OC} = 1V$ and an $I_{SC} = 27.6mA/cm^2$. These values are almost the same as those publicized of actual GaAs cells in Ref. 15–18.

D. THE COMPLETE InGaP CELL

A similar cell can be built using InGaP. This material, when lattice-matched to GaAs, has higher bandgap ($E_g = 1.9eV$). Therefore, its V_{OC} is also expected to be larger. This also agrees with Figure 5.2. According to the same figure, I_{SC} is expected to be lower. Using the same process utilized before, the cell is simulated and is found to produce $V_{OC} = 1.3V$ and $I_{SC} = 11mA/cm^2$.

With its own BSF, buffer and window layers the cell looks like in Figure 8.12:

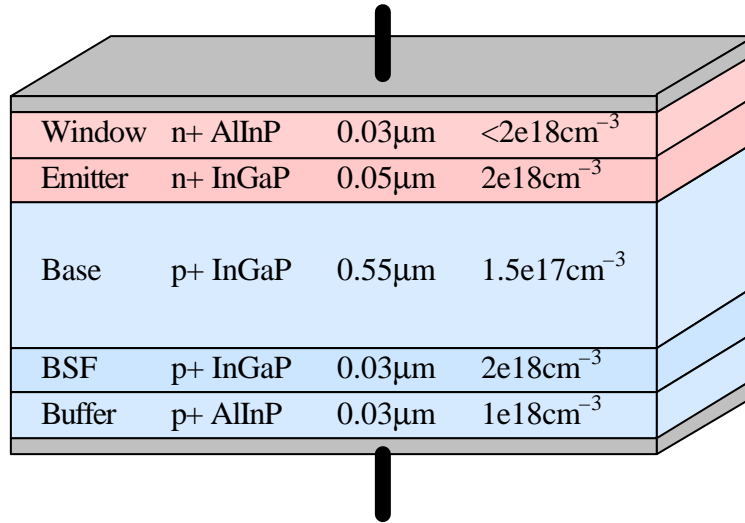


Figure 8.12. The complete InGaP cell.

The complete cell now has $V_{OC} = 1.4\text{V}$ and $I_{SC} = 19.1\text{mA}/\text{cm}^2$. Taking into account that shadow losses, caused by an actual opaque contact, are not considered at this point, the results are very similar to those in Ref. 15–18. The IV characteristic and the frequency response of the cell can be compared to the ones of the GaAs cell as follows in Figure 8.13.

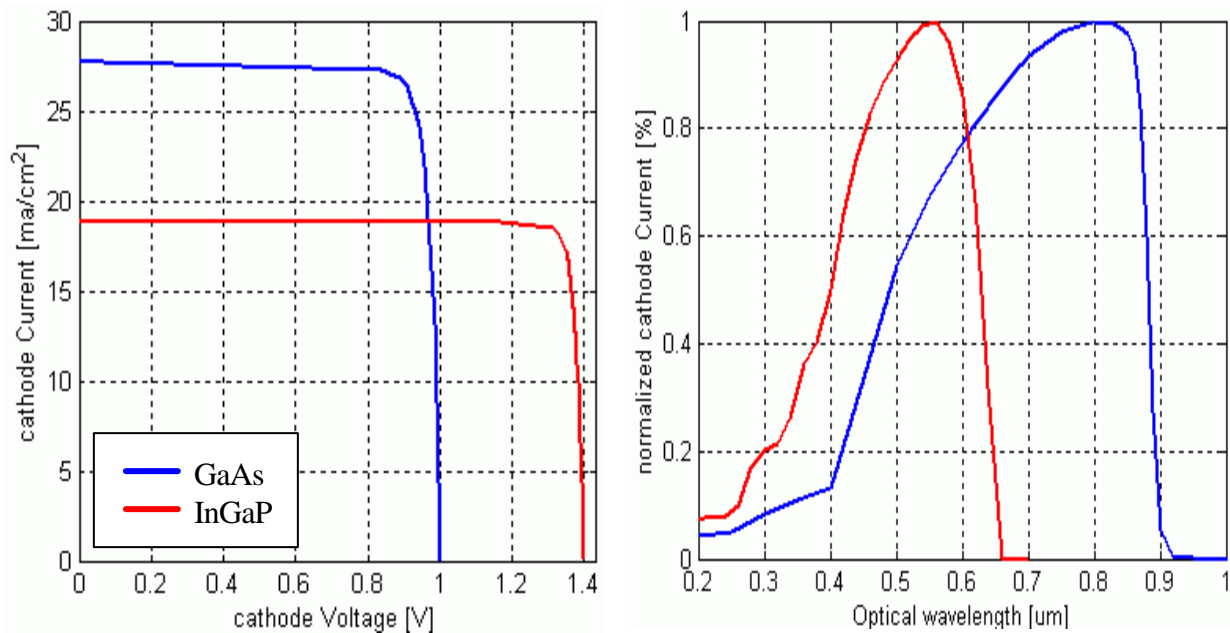


Figure 8.13. The IVs of the complete individual InGaP and GaAs cells.

E. THE TUNNEL JUNCTION

As seen in earlier chapters a tunnel junction (Figure 8.12) is actually a very thin and heavily doped p-n junction.

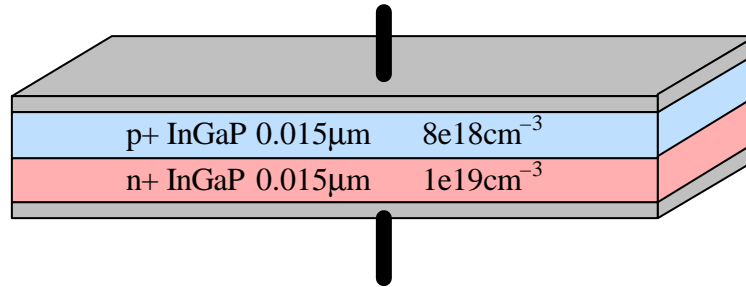


Figure 8.12. A tunnel junction.

When simulated, it produces the dark IV characteristic of Figure 8.14. Obviously the created junction can easily handle the current produced by the above cells.

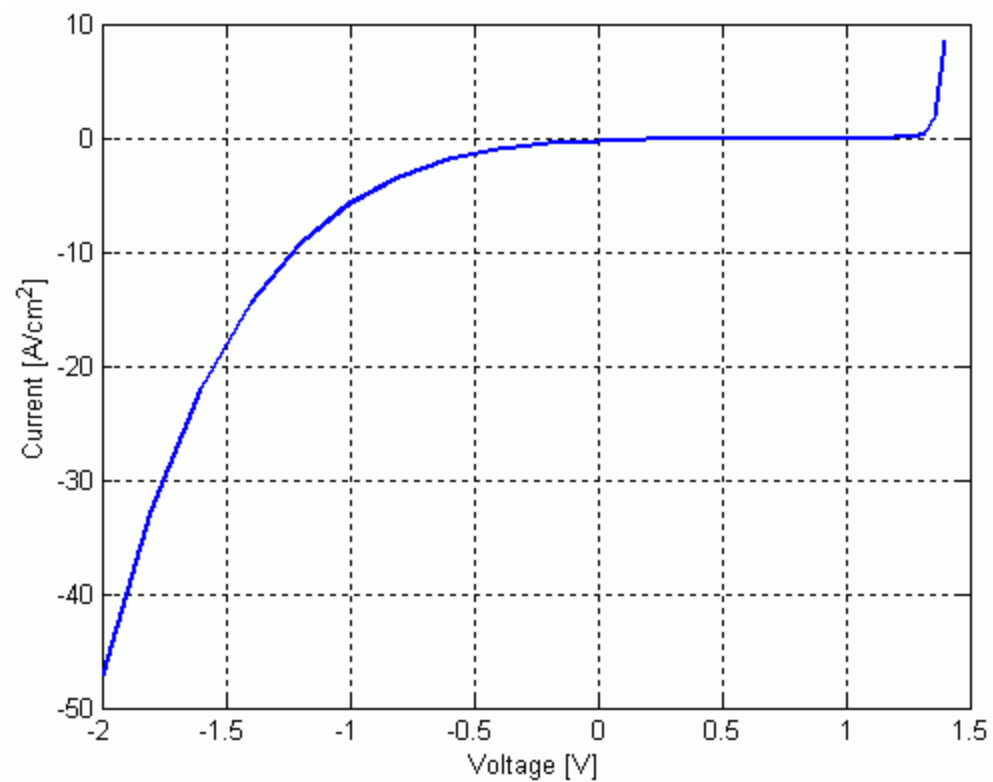


Figure 8.14. I-V characteristic of the tunnel junction.

F. THE InGaP / GaAs MECHANICALLY STACKED TANDEM CELL

In a first attempt to create a tandem cell, the mechanically stacked structure (Figure 8.15) was used for simplicity. This is the placement of the InGaP over the GaAs cell. The two cells are not in contact. Instead, they are separated by a thin layer of vacuum. Vacuum is a very good insulator for the voltage levels used here. Also it does not absorb or alter light as it goes through it. Each cell has its own ideal and transparent contacts.

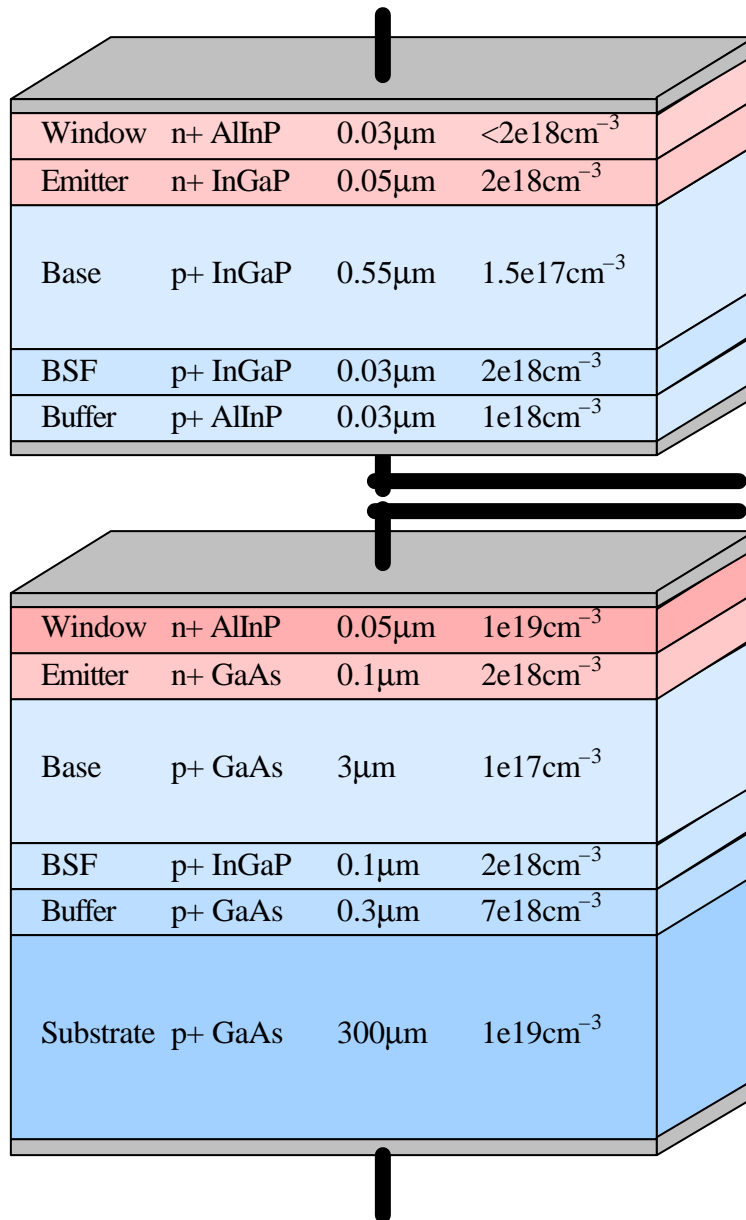


Figure 8.15. The mechanically stacked tandem cell.

The actual structure is illustrated in Figure 8.16:

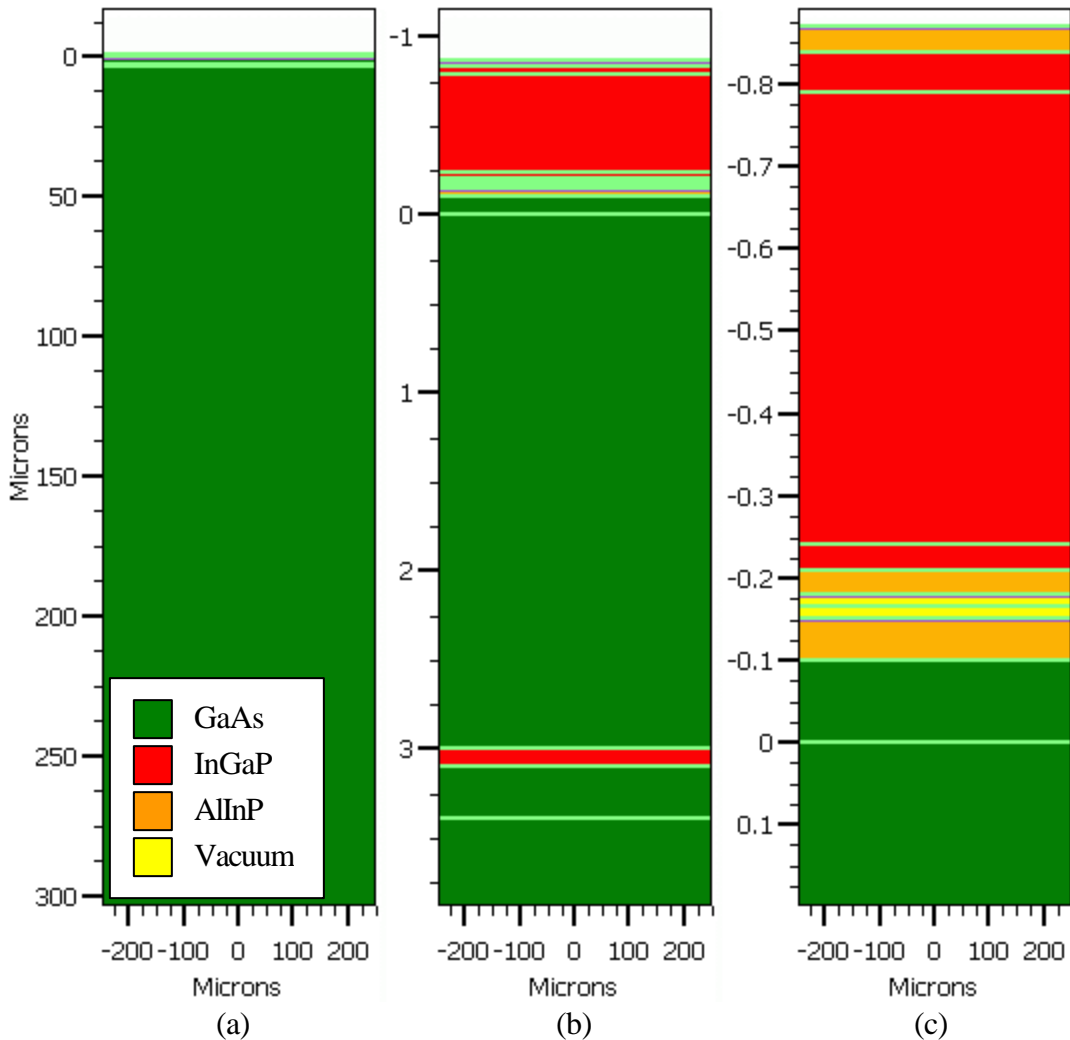


Figure 8.16. The mechanically stacked tandem cell in Silvaco:

- (a) The whole structure,
- (b) expanded view of the two cells,
- (c) expanded view of the two cell junctions.

As expected, both cells produce the same voltage as before. The top cell is totally unaffected. On the contrary, the bottom one produces less current, due to the fact that higher energy photons have been absorbed by all the layers over it. This current becomes almost equal to the current produced by the top cell (*current matching*). This can be seen in the new frequency response (Figure 8.17). The electrical characteristics of the top cell are the same, so $V_{OC} = 1.4V$ and $I_{SC} = 19.1mA/cm^2$. The bottom cell is changed and now has $V_{OC} = 1V$ and $I_{SC} = 19mA/cm^2$.

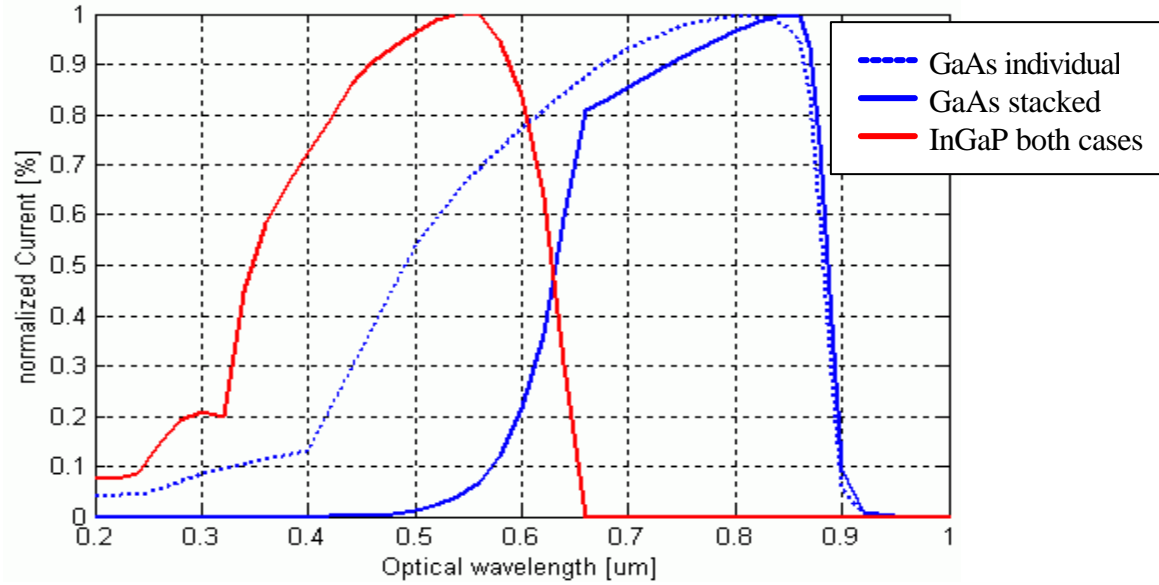


Figure 8.17. Frequency response of the stacked cells compared to that of the individual cells.

The potential build-up can be seen in Figure 8.18.

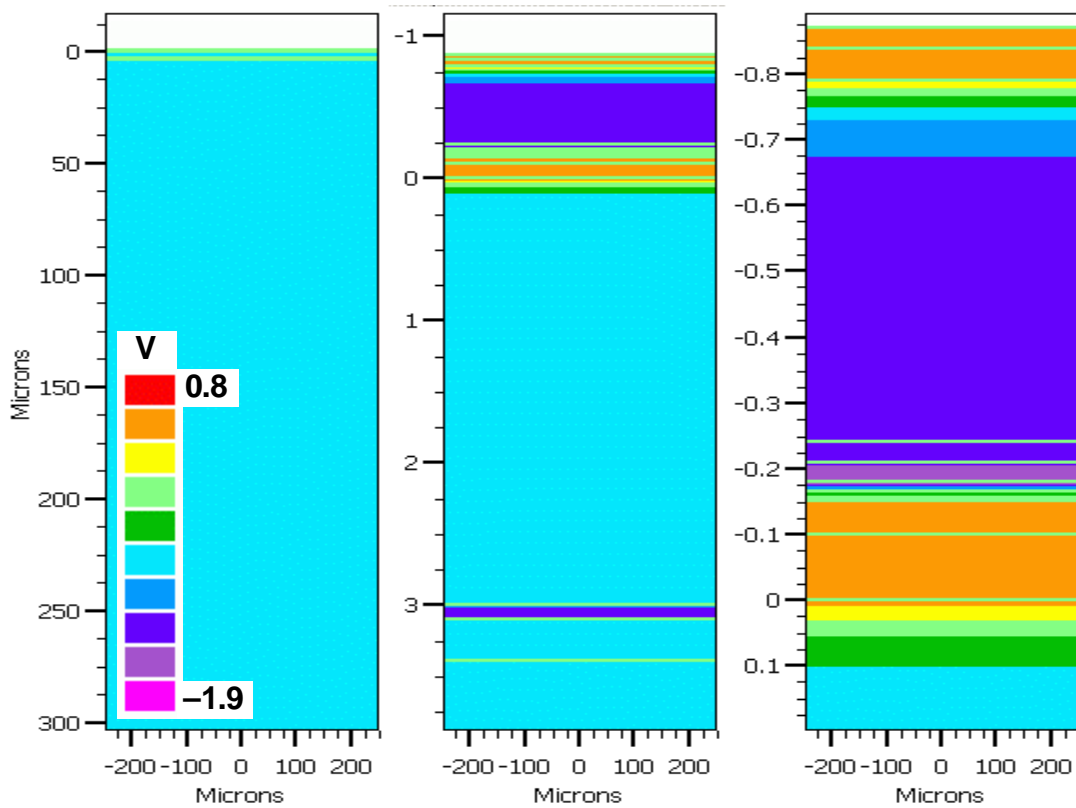


Figure 8.18. The potential build-up.

G. THE InGaP / GaAs DUAL MULTIJUNCTION CELL

The next step is to connect the two cells using the tunnel diode developed earlier. The simulated cell produced $V_{OC} = 2.49V$ and $I_{SC} = 19mA/cm^2$.

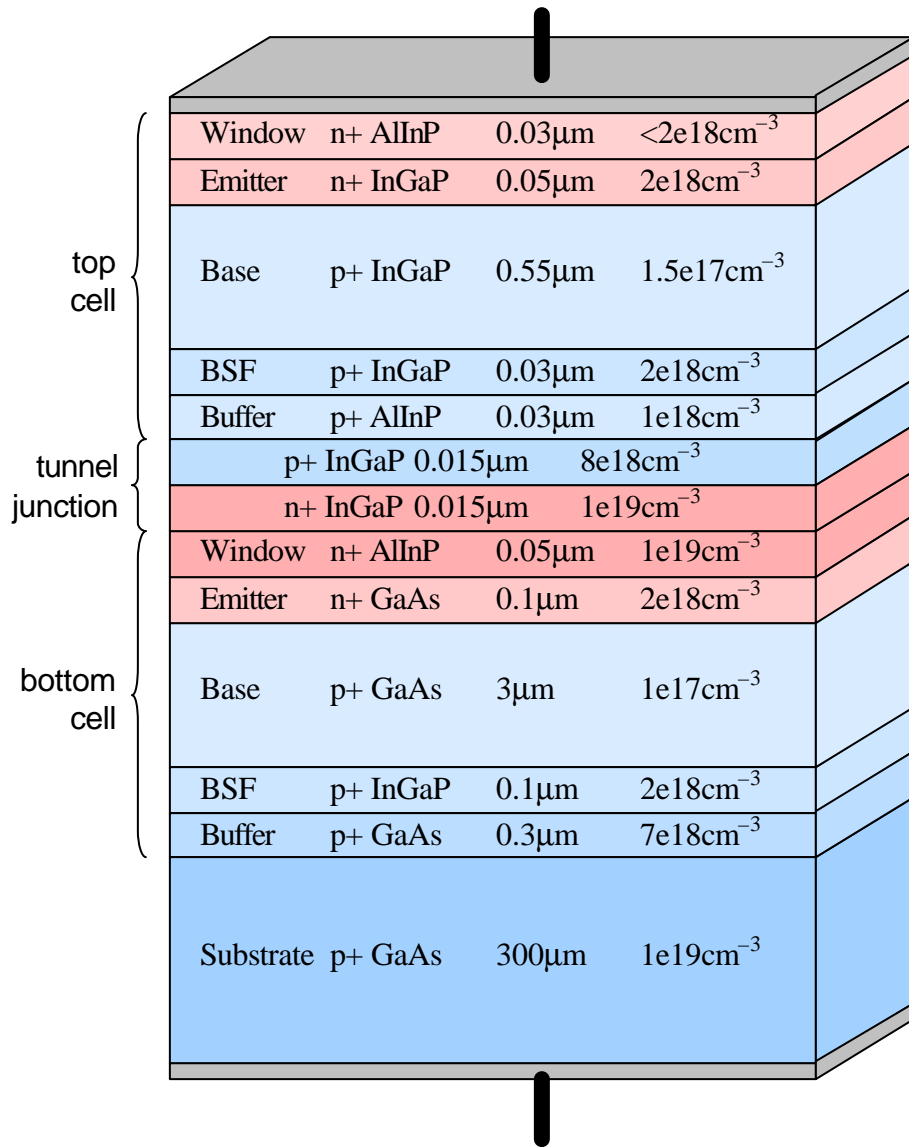


Figure 8.19. The multijunction cell.

The IV characteristic (Figure 8.20) is changed as expected and the frequency response (Figure 8.21) is actually the sum of the responses of each cell. Both are in agreement with experimental data found in Ref. 15–18.

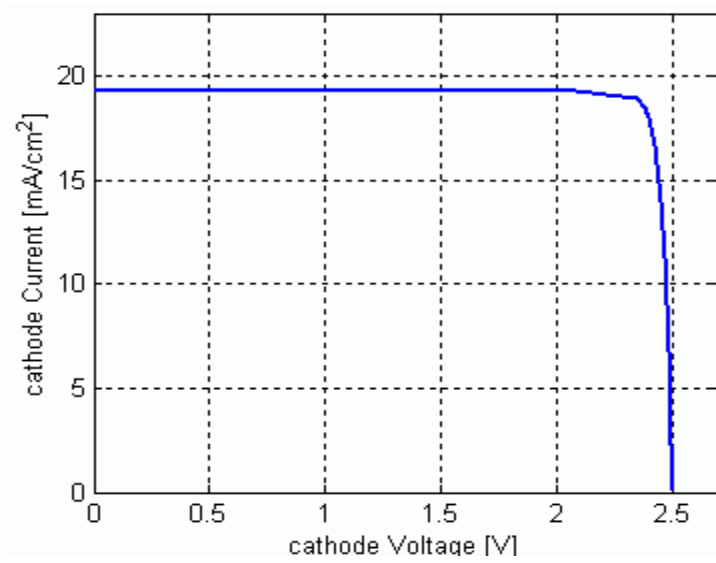


Figure 8.20. IV characteristic of the multijunction cell.

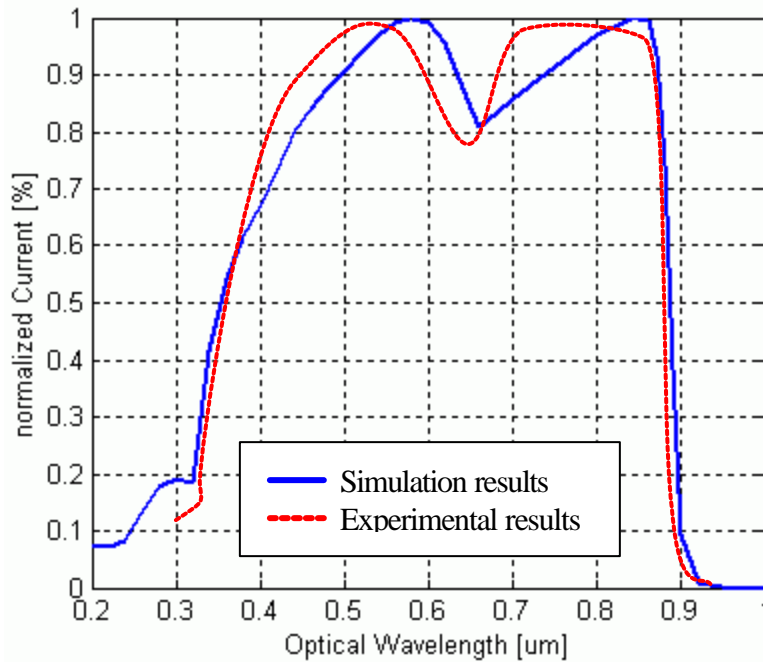


Figure 8.21. Frequency response of the multijunction cell.

(experimental data after Ref. 15–18)

Even though this cell is still not exactly the same as the one presented in Ref. 15–18, the close agreement of simulated and experimental results observed here is a strong indication that the methodology used is correct. Encouraged by this, further additions and

improvements to the cell can be modeled to improve the design. This is done in the following sections where the modeled cell becomes almost identical to those referenced.

H. THE COMPLETE InGaP / GaAs CELL

The final step (Figure 8.22) is to add an ARC layer on top to minimize reflections. A cap layer and real golden contacts are also added. The bottom contact is shined and becomes a back surface reflector (BSR) to reflect photons back into the cell.

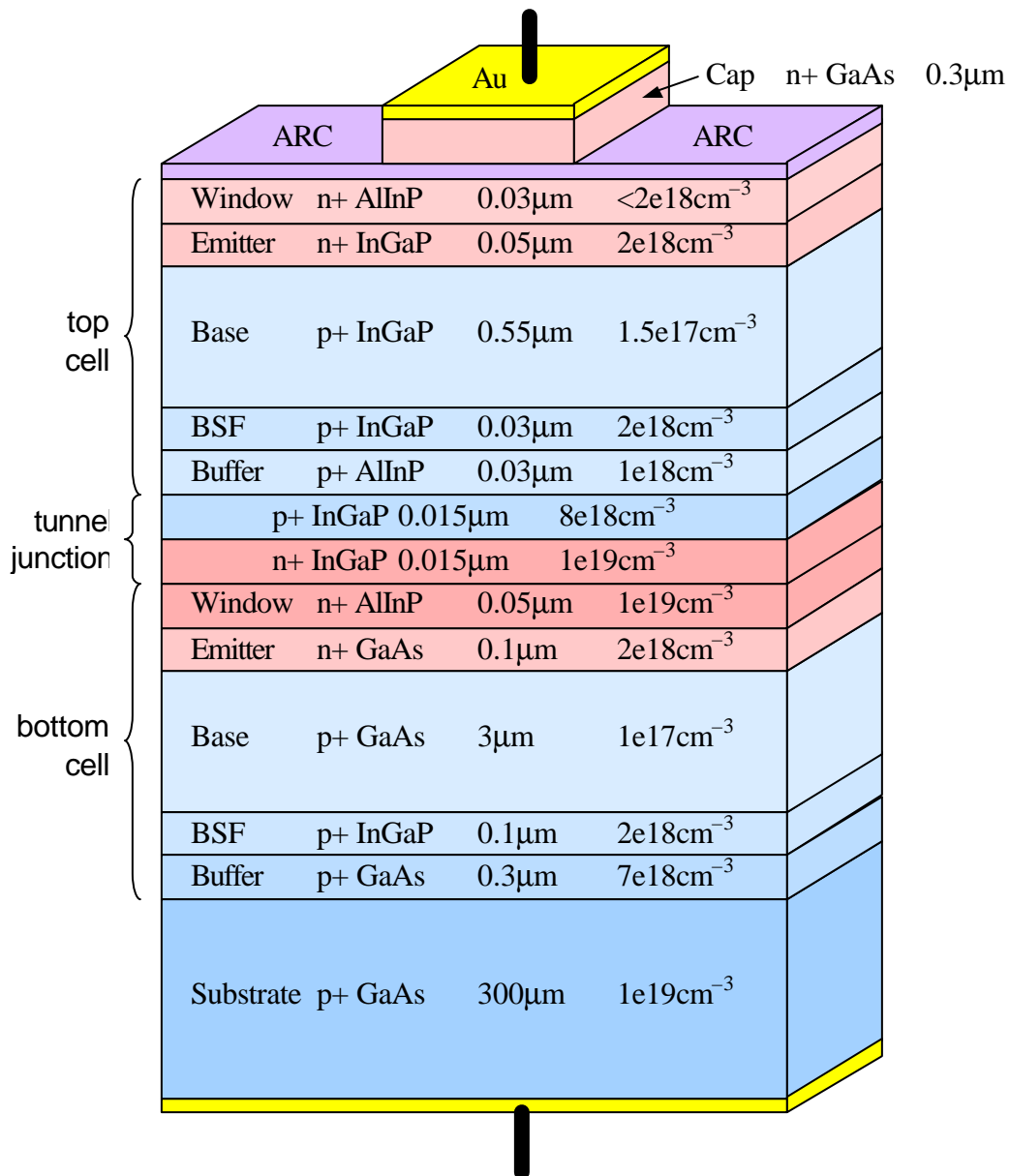


Figure 8.22. Final version of the multijunction cell.

The final IV characteristic (Figure 8.23) reflects those improvements.

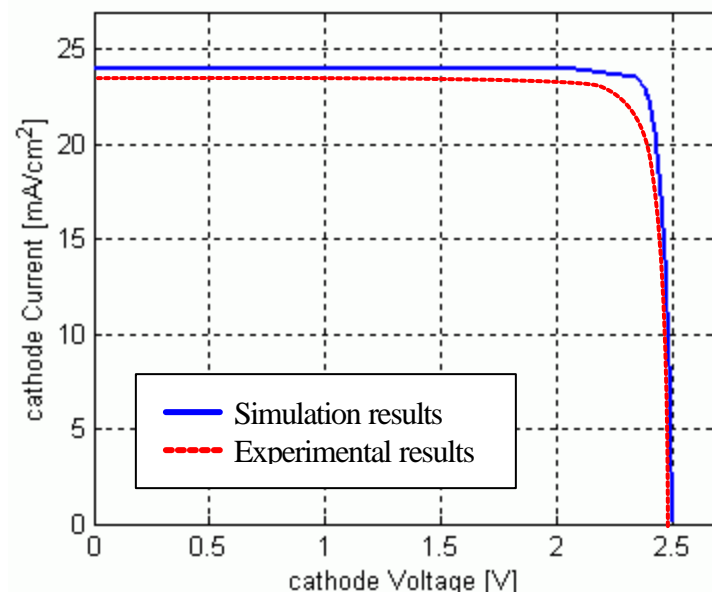


Figure 8.23. Final IV characteristic of the multijunction cell.
(experimental data after Ref. 15–18)

The simulated cell produced $V_{OC} = 2.49V$ and $I_{SC} = 24mA/cm^2$. This result is very similar to the $V_{OC} = 2.488V$ and $I_{SC} \cong 23mA/cm^2$ found in Ref. 15–18. The I–V characteristic and the frequency response are also in agreement.

Another interesting graph shows the photogeneration rate (Figure 8.25 and 8.26) vs. the wavelength of the light (Figure 8.24). Note how the top and the bottom cells are active and produce current in different wavelengths, according to their frequency response.

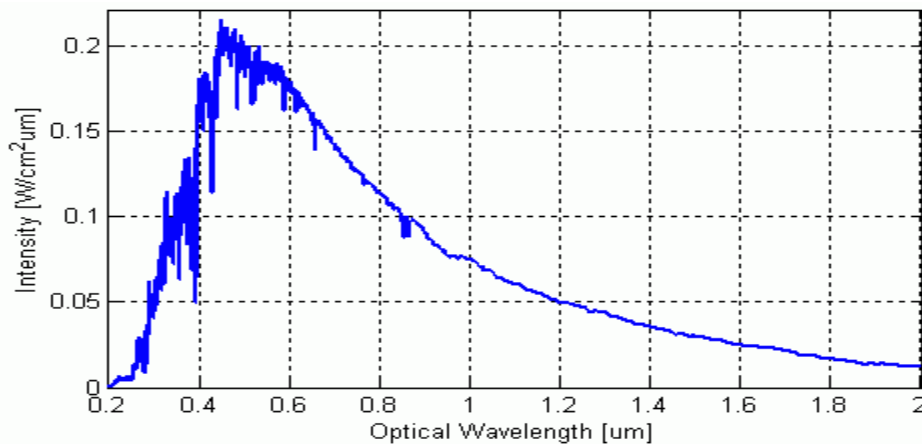


Figure 8.24. AM0 solar spectrum distribution.

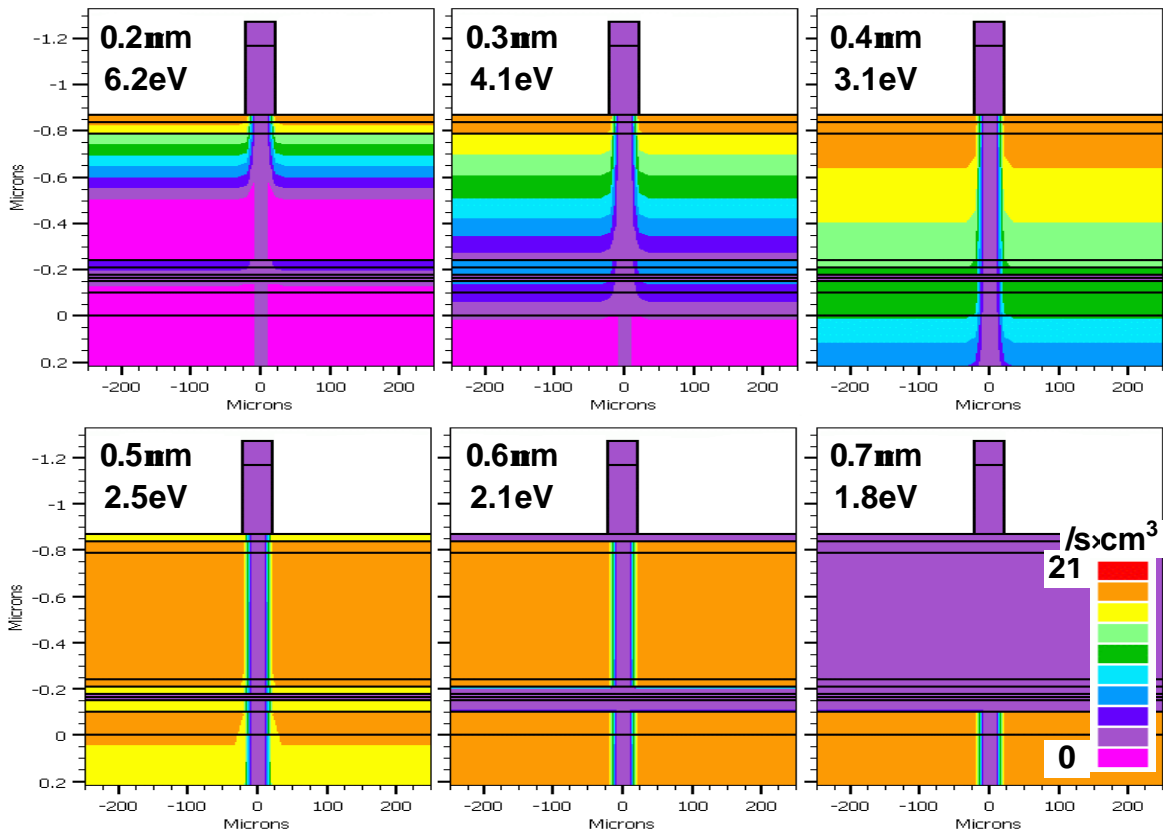


Figure 8.25. Photogeneration in the MJ cell (expanded view of the top cell).

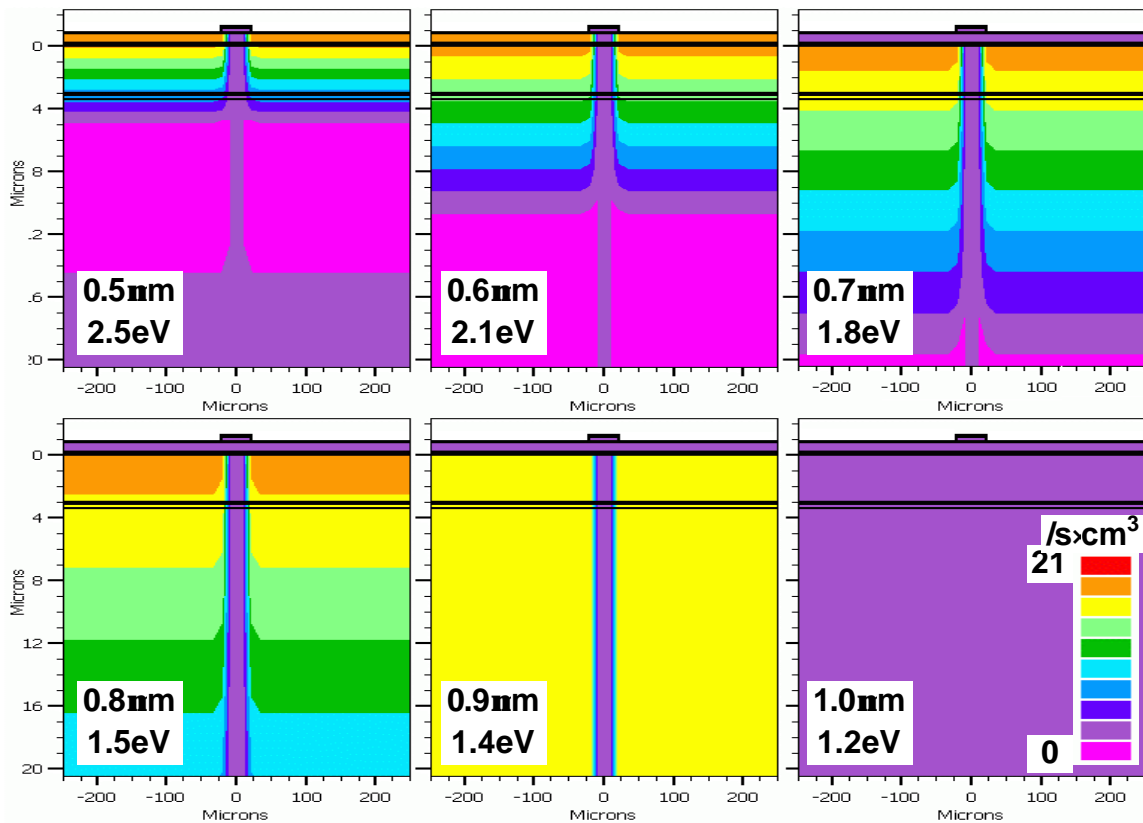


Figure 8.26. Photogeneration in the MJ cell (expanded view of the bottom cell).

IX. DEVELOPING AND OPTIMIZING A STATE-OF-THE-ART MULTIJUNCTION CELL

This final chapter has two major parts. The first part is the modeling of a state-of-the-art triple multijunction solar cell. It is a successful attempt to simulate a device currently on the cutting edge of technology. This way, the demonstrated methodology is used as a high-end research tool. On the second part, parametric analysis is used, to optimize the cell, adding to the value of the proposed process.

A. FIRST STAGE OF DEVELOPMENT

The cell with the highest efficiency ever published has been built by Spectrolab Inc and is described in Ref. 19. Under AM0, this cell is measured to produce $V_{OC} = 2.651V$, $I_{SC} = 17.73mA/cm^2$, to have efficiency = 29.3% and FF = 84.3%. Unlike the cell studied in the previous chapter, all recent publications on advanced cells treat structural details as proprietary information. Therefore, layer thicknesses and doping levels are not revealed.

Using the process explained earlier and experience gained from the research of cell development, a set of probable values has been produced in order to simulate this cell. This was used as a first estimation.

Ge is a material with very low bandgap ($E_g = 0.67eV$). This means that it can produce energy even with very low-energy photons. As upper cells absorb most of the high-energy photons, Ge is ideal for a bottom cell in a multijunction configuration. As seen in figure 5.2, Ge cells can produce very high current. Unfortunately, this advantage will largely remain unused, as this current will be choked by the above cells in the stack. Its V_{OC} is quite small (only 0.3V) and does not seem to be very important. However, the cell developed in the previous chapter produced only a total $V_{OC} = 2.49V$. An increase of 0.3V would lead to the significant power increase by 12%.

The double cell studied in the previous chapter is used again and a Ge cell is simply attached below it. Small changes have been implemented to match the design of Ref. 19. Hence, the tunnel junctions are now created using GaAs, all the buffer layers

have been removed and some materials used for the window layers are changed. The new structure can be seen in Figure 9.1:

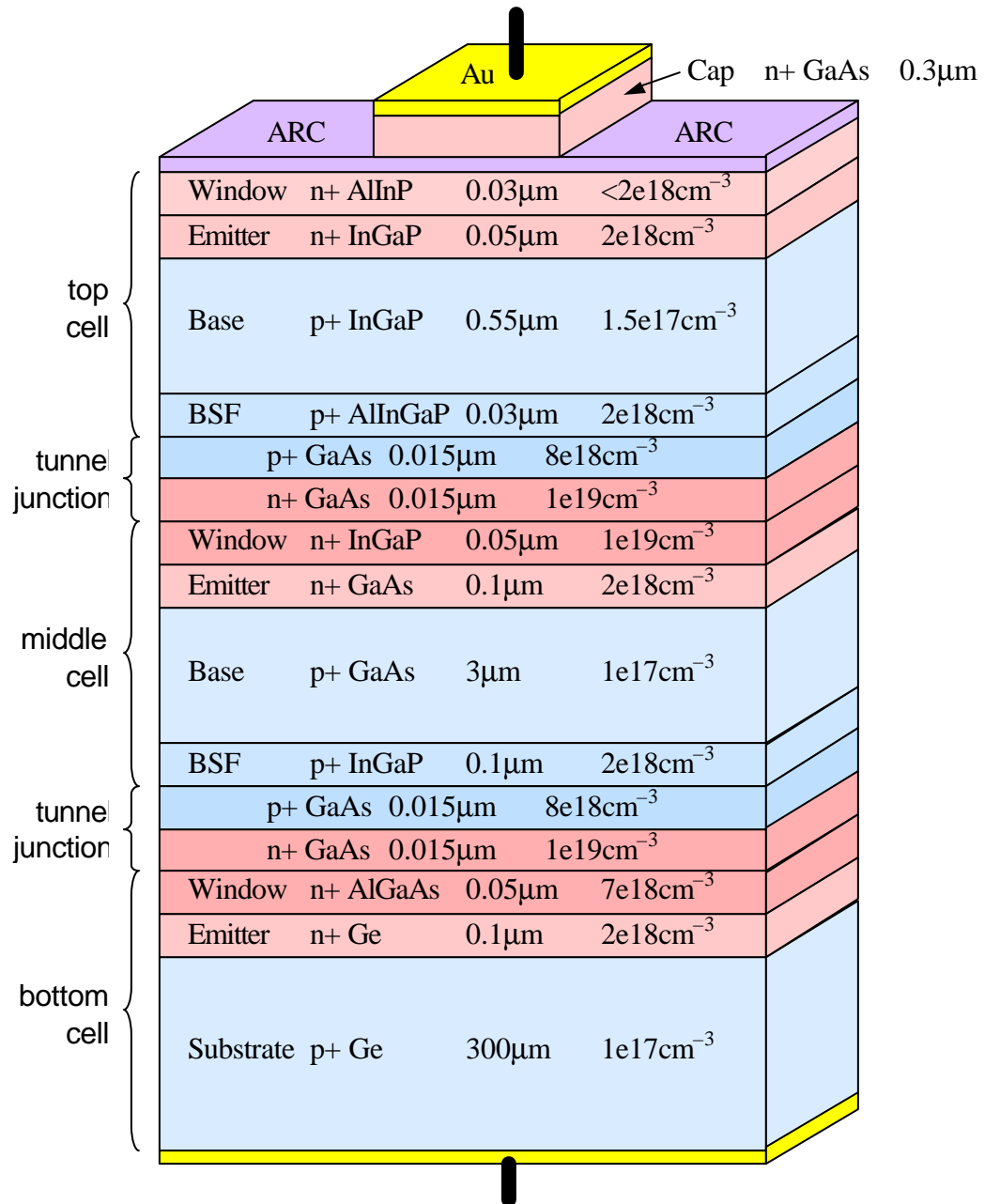


Figure 9.1. Triple MJ cell prototype.

The simulation returned $V_{OC} = 2.655V$ and $I_{SC} = 17.6mA/cm^2$ which are obviously very close to the results published in Ref. 19. Great similarity also exists in the

IV characteristic (Figure 9.2) and in the frequency response shown below. This leads to the belief that the configuration simulated is very close to the actual configuration built and published by Spectrolab.

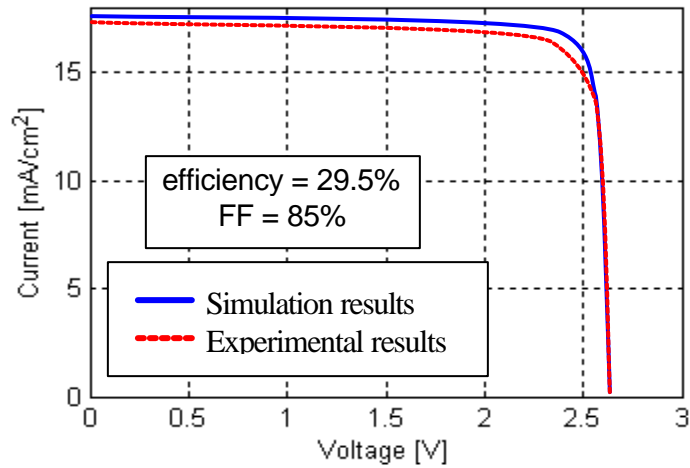


Figure 9.2. IV characteristic of the prototype triple MJ cell.
(experimental data after Ref. 19)

Like before, the frequency responses of both the individual and stacked cells have been produced and can be seen in Figures 9.3 and 9.4. Also the response of the total multijunction cell is provided and compared to the experimental results.

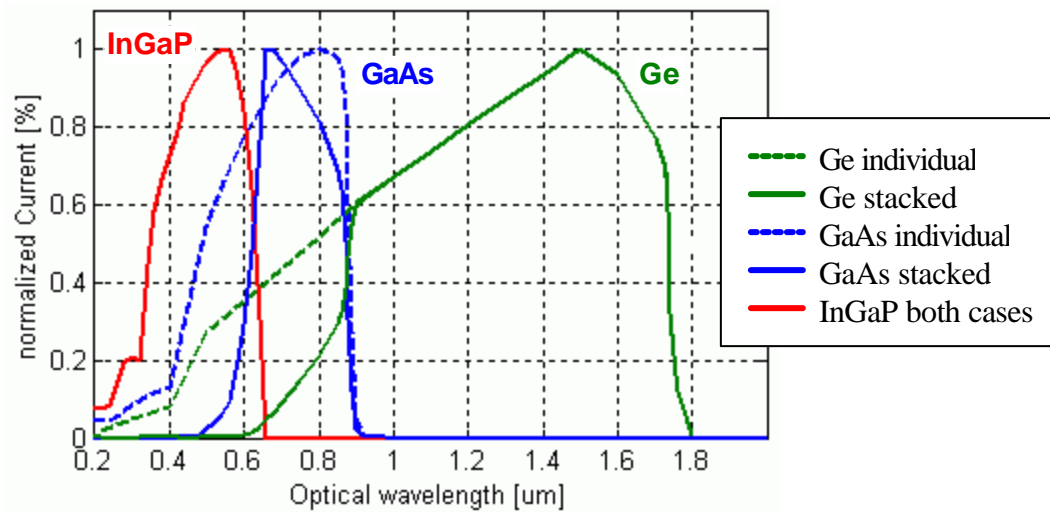


Figure 9.3. Frequency response of all cells.

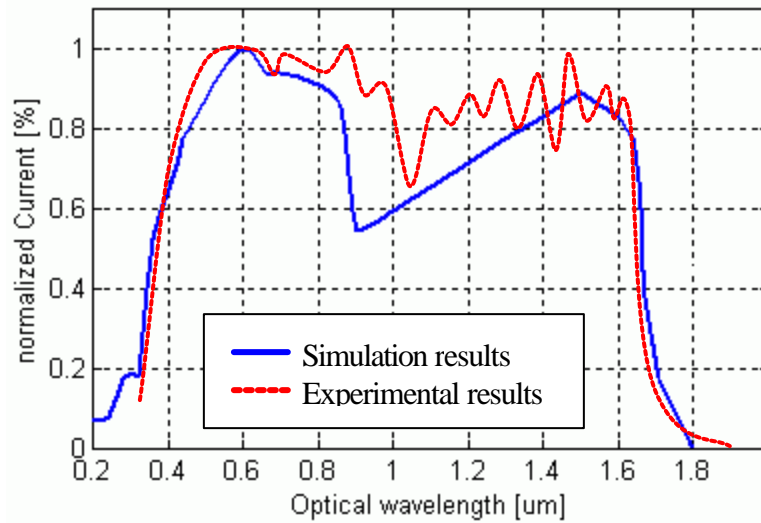


Figure 9.4. Frequency response of the total MJ cell.
(experimental data after Ref. 19)

Even though – unlike in chapter 8 – the cell is not described in detail in Ref. 19 or in any other publications, the close agreement of simulated and experimental results suggests that the structure developed here is not far from the structure originally built and tested by Spectrolab in the reference.

The photogeneration rate (Figure 9.6) for various wavelengths of the AM0 spectrum (Figure 9.5), seen in the previous chapter, is also created here.

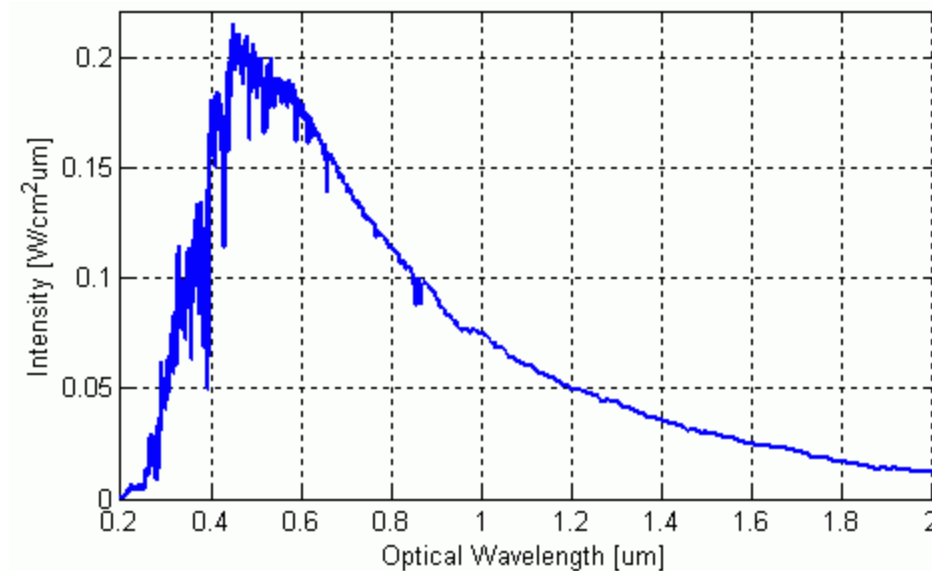


Figure 9.5. AM0 solar spectrum distribution.

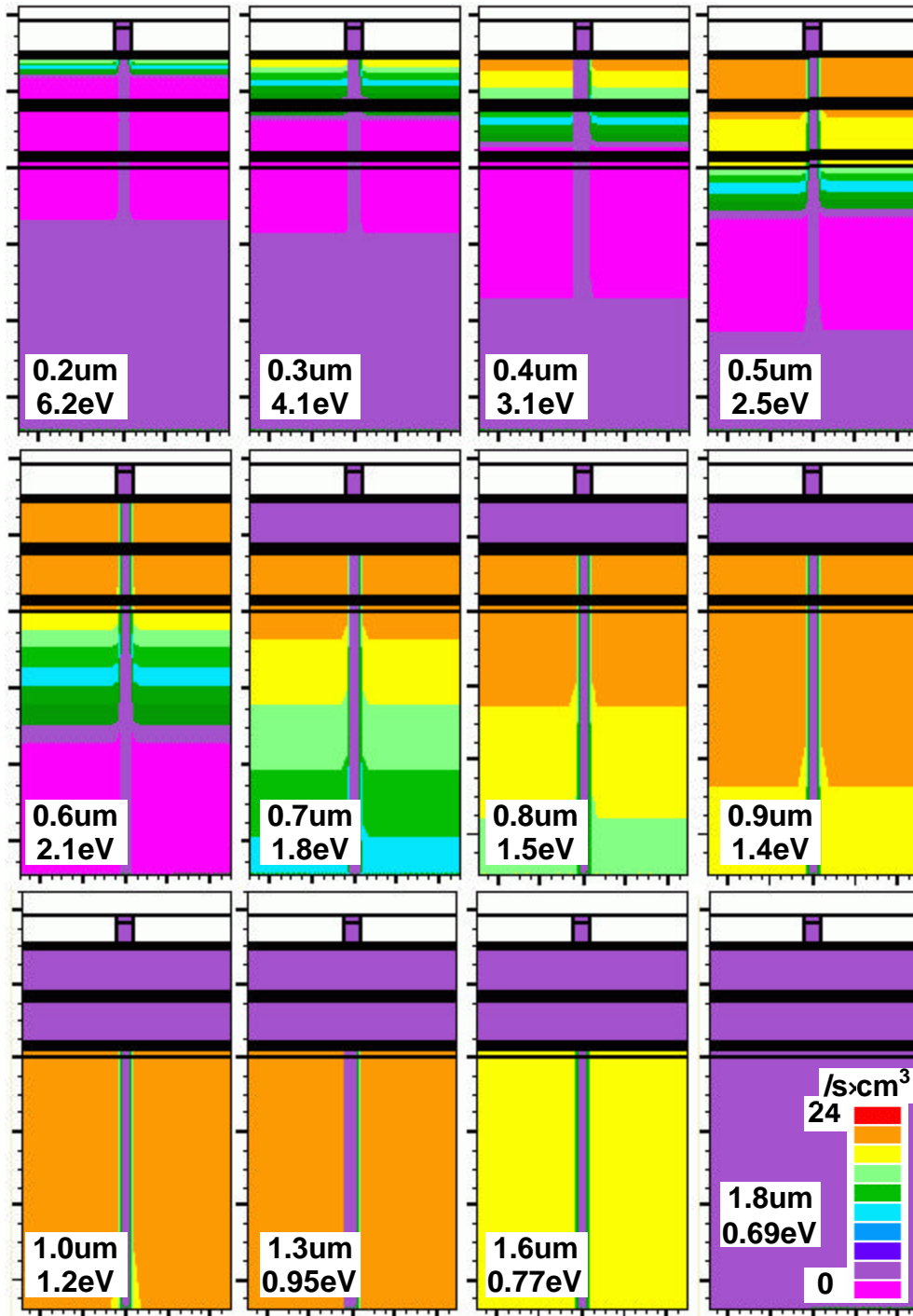


Figure 9.6. Photogeneration rate vs. optical wavelength.

B. PARAMETRIC ANALYSIS AND OPTIMIZATION

The current produced by a single cell is in direct analogy with its thickness and more specifically with the thickness of its base. As the base becomes thicker, the current produced becomes larger. In multijunction cells this principle is also true. However, the thicker a cell is, the more photons it absorbs and thus, less photons are allowed to pass through to the other cells below it. This “shadowing” affects greatly the lower cells and may lead them to photon starvation. Therefore, a thick top cell will cause the current produced by lower cells to decrease. The various thicknesses have little effect on the open-circuit voltages of the cells, thus, the selection of the open-circuit current alone can be used as a factor for overall power optimization.

In a multijunction configuration, each cell behaves like a current source. All these current sources are connected in series (Figure 9.7). Consequently, the total current produced by the structure is equal to the smallest current produced by the individual cells. Hence, a cell that is too thin or too shadowed will result in lower overall performance, creating a bottleneck for the others.

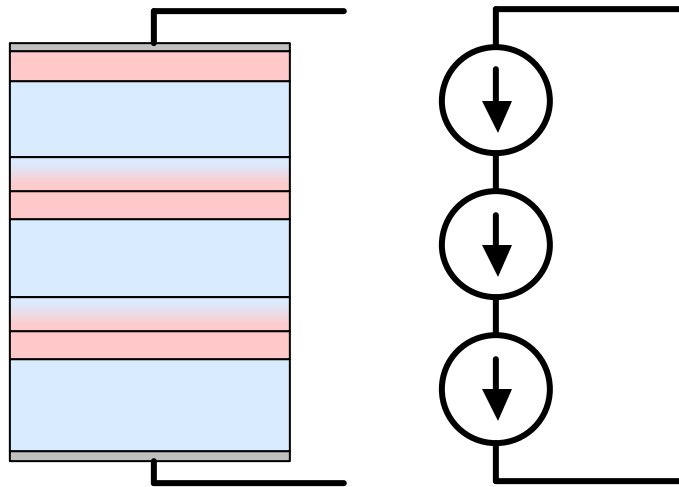


Figure 9.7. A multijunction solar cell as a set of current sources connected in series.

The top cell, obviously, cannot be shadowed and absorbs almost all photons in the range of 0.2 to 0.6 μm . The remaining photons enter the middle cell where wavelengths

from 0.6 to 0.9 μm are absorbed. Finally, the remaining photons in the range of 0.9 to 1.6 μm are absorbed by the bottom cell (Figure 9.8).

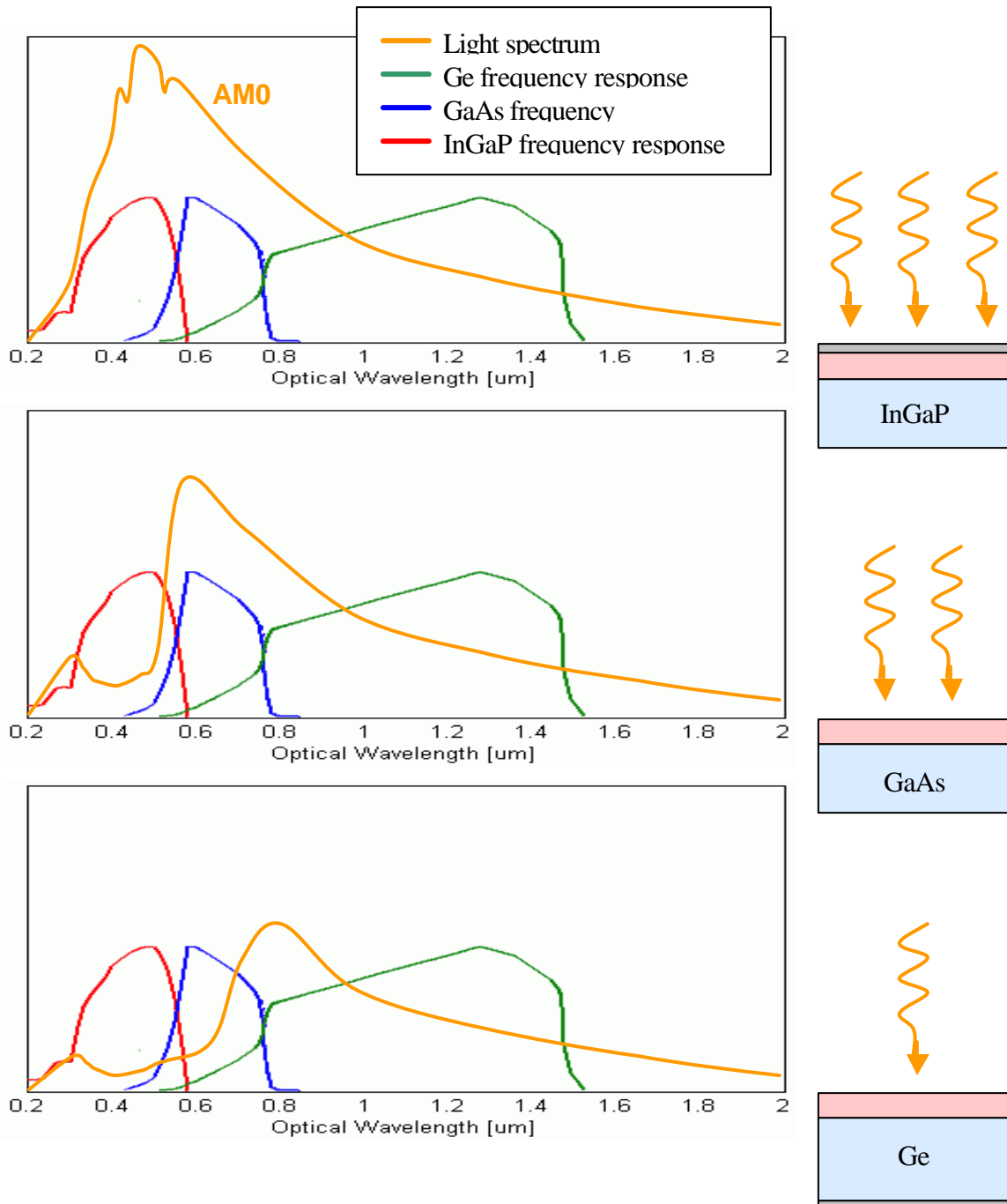


Figure 9.8. Light propagation through cells.

From published research, it is known that top cells usually have thicknesses in the range of 0.5 to 0.7 μm , while middle cells have around 2 to 4 μm . A number of

simulations have been executed and the thicknesses of those cells have been varied in a bit wider ranges. The first result shown is the short-circuit current of the top cell vs. its thickness (Figure 9.9). Note that no other parameter affects this cell.

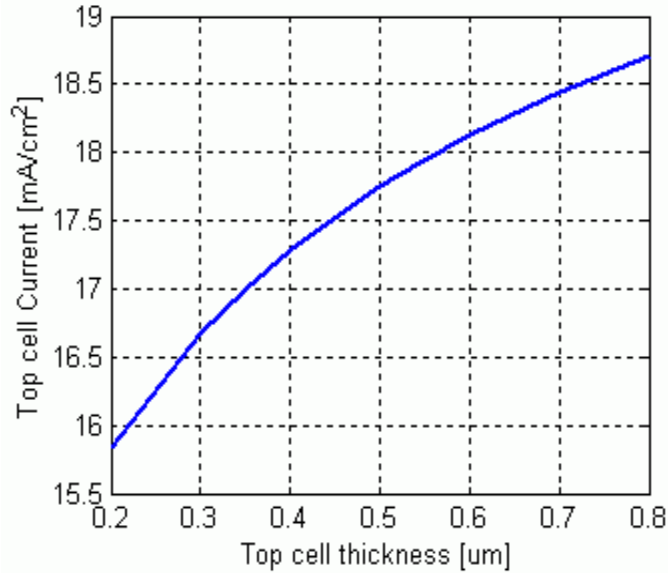


Figure 9.9. Top cell short-circuit current vs. top cell thickness.

Because of its position, the shadow casted by the bottom cell does not affect any parts of the structure. Therefore, its thickness will be chosen to be as high as possible to increase the current produced. However, the thickness of the middle cell will greatly affect it as shown in Figure 9.10.

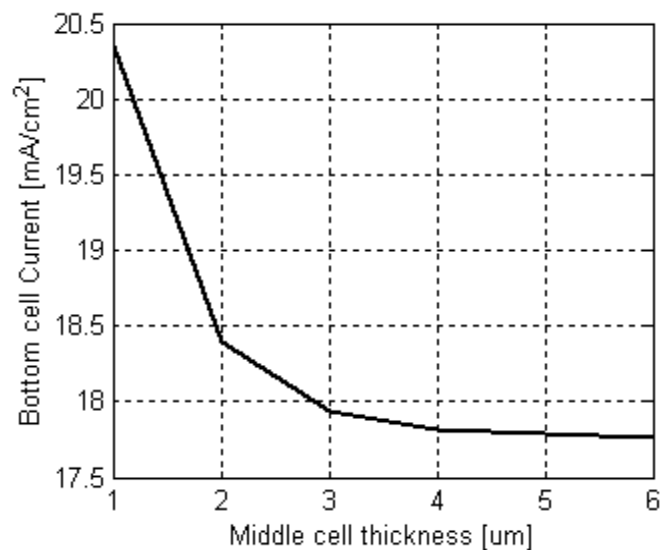


Figure 9.10. Bottom cell short-circuit current vs. middle cell thickness.

Finally, for designing the middle cell, both its thickness (due to the shadowing on the bottom cell) and the thickness of the top cell need to be considered. For this reason, the family of curves of Figure 9.11 is produced.

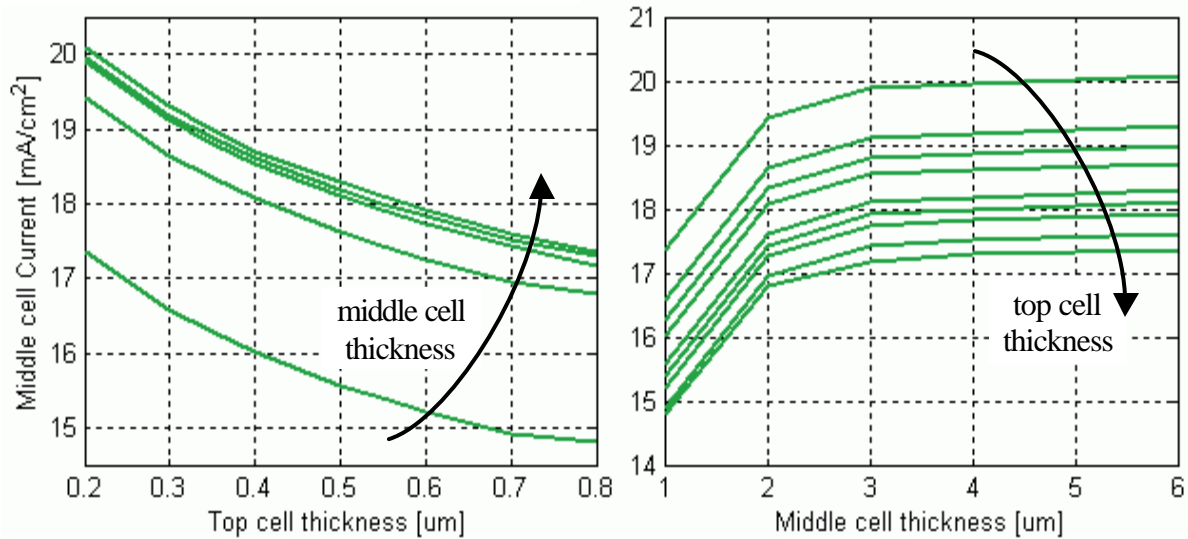


Figure 9.11. Middle cell short-circuit current vs. top and middle cell thickness.

In order to derive a conclusion, the above graphs are combined. The total current is the minimum current of the three cell currents. This is also the actual current produced by the multijunction combination of the three cells, due to their in-series connection. Therefore, the total short-circuit current is the best indication of the output power and the efficiency of the whole cell and that is why it is also plotted. First, a set of graphs of all the currents vs. the thickness of the top cell can be seen in Figure 9.12. There, all the above-mentioned theory becomes evident. In this set, the optimum point seems to be for top cell thickness equal to $0.55\mu\text{m}$ and middle cell thickness equal to $3\mu\text{m}$. A similar set of graphs, but this time, vs. middle cell thickness, follows in Figure 9.13. The optimum point is also found at the same combination of cell thicknesses. Another way to locate the optimum point is by using the contour plot of the total current seen in Figure 9.14 or the 3D surface plot in Figure 9.15.

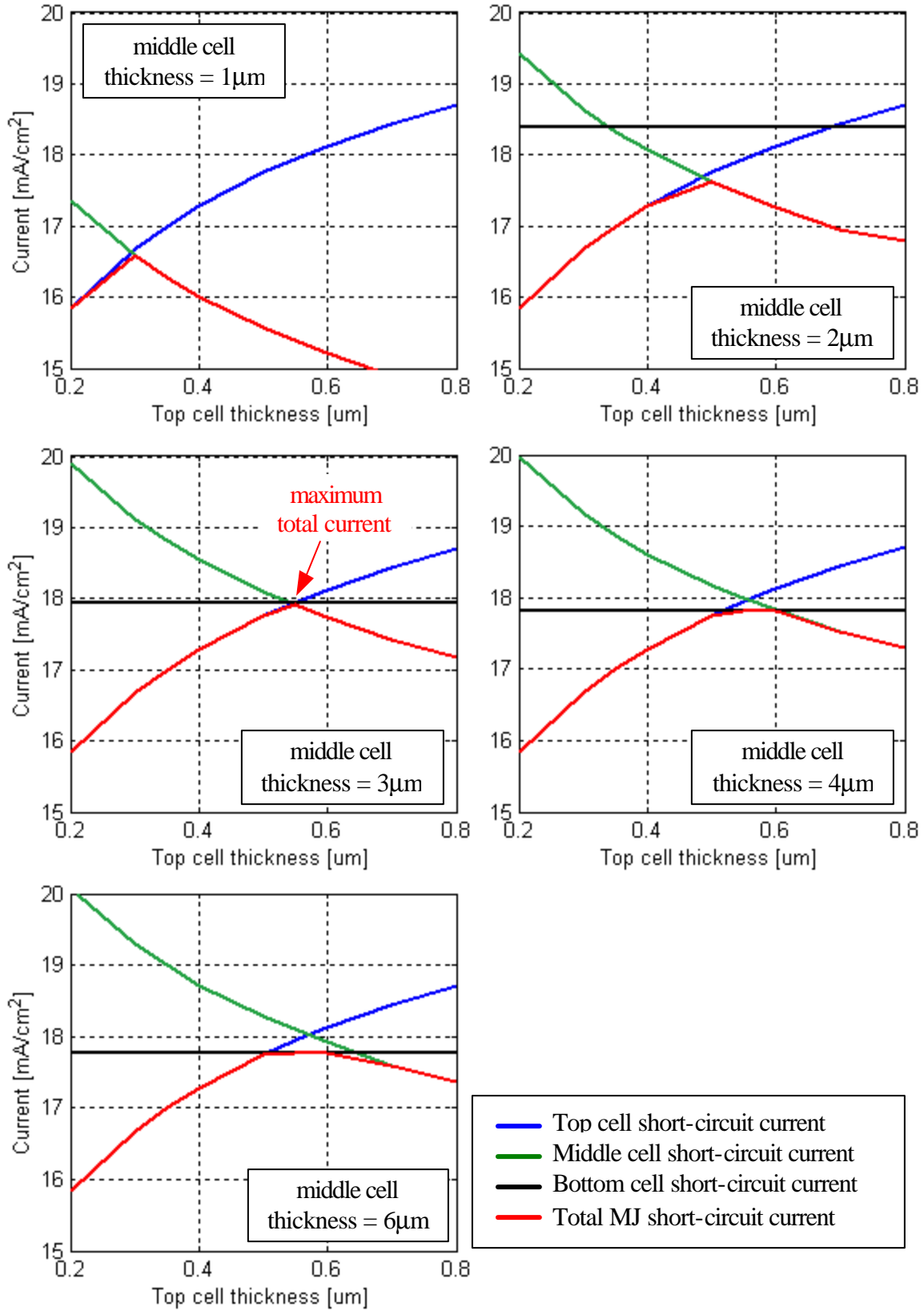
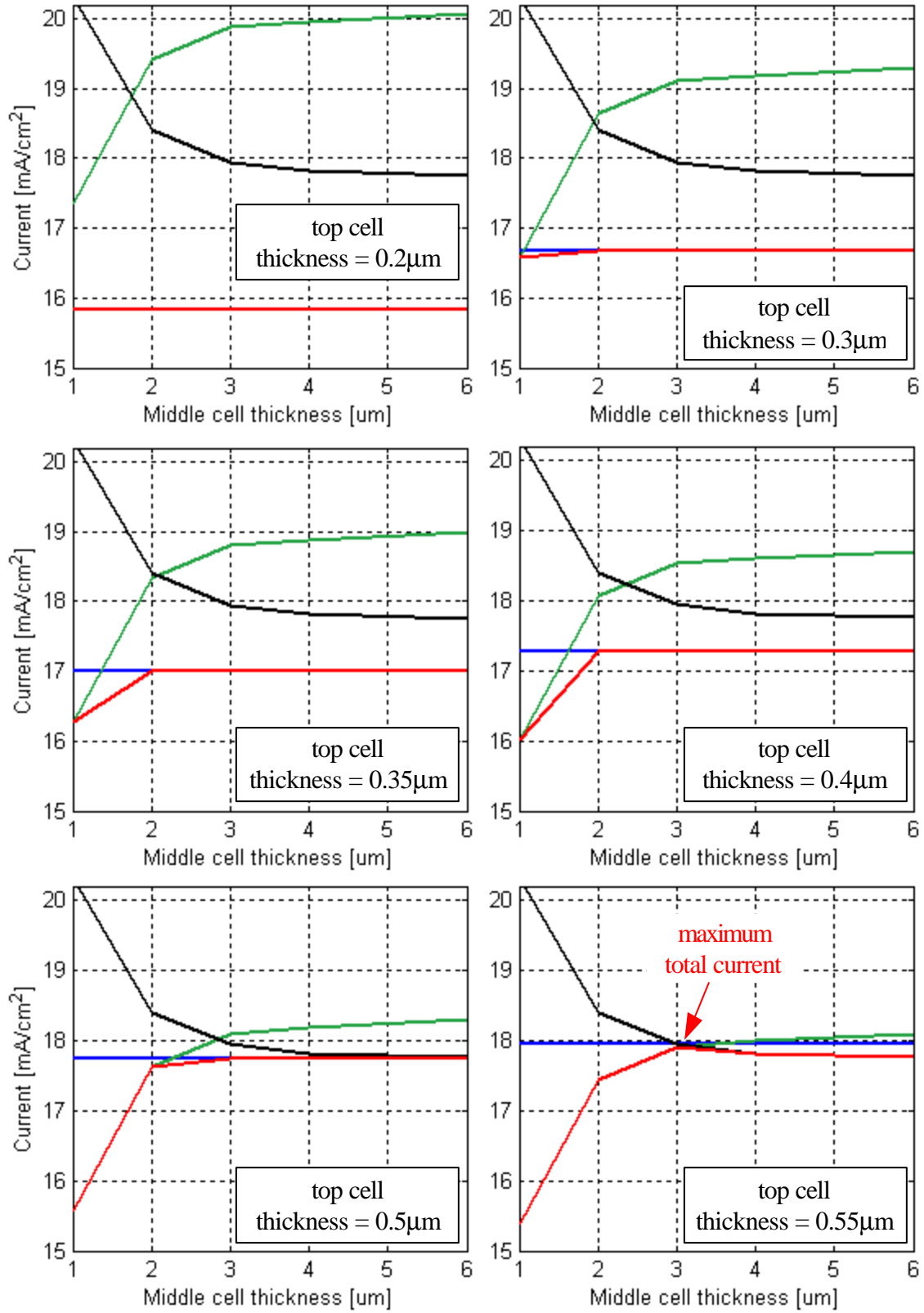


Figure 9.12. All short-circuit currents vs. top cell thickness.



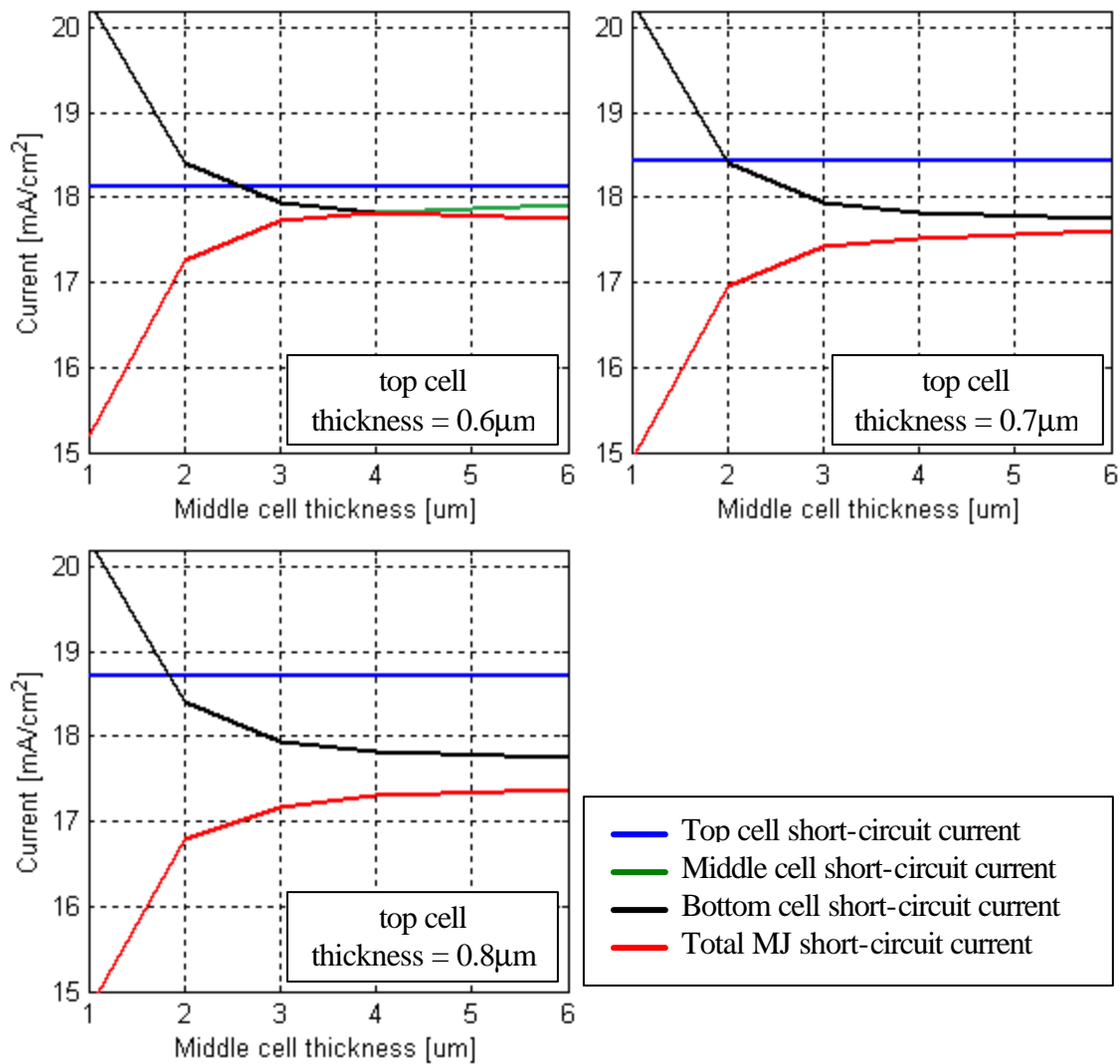


Figure 9.13. All short-circuit currents vs. middle cell thickness.

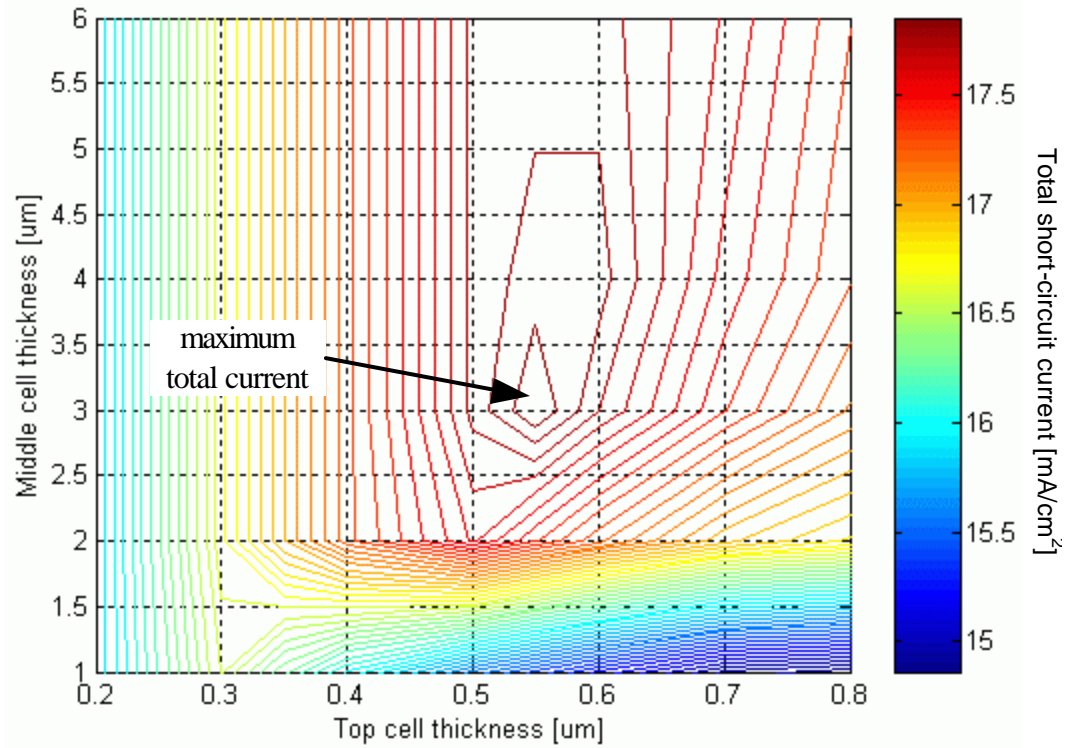


Figure 9.14. Total short-circuit current vs. top and middle cell thicknesses.

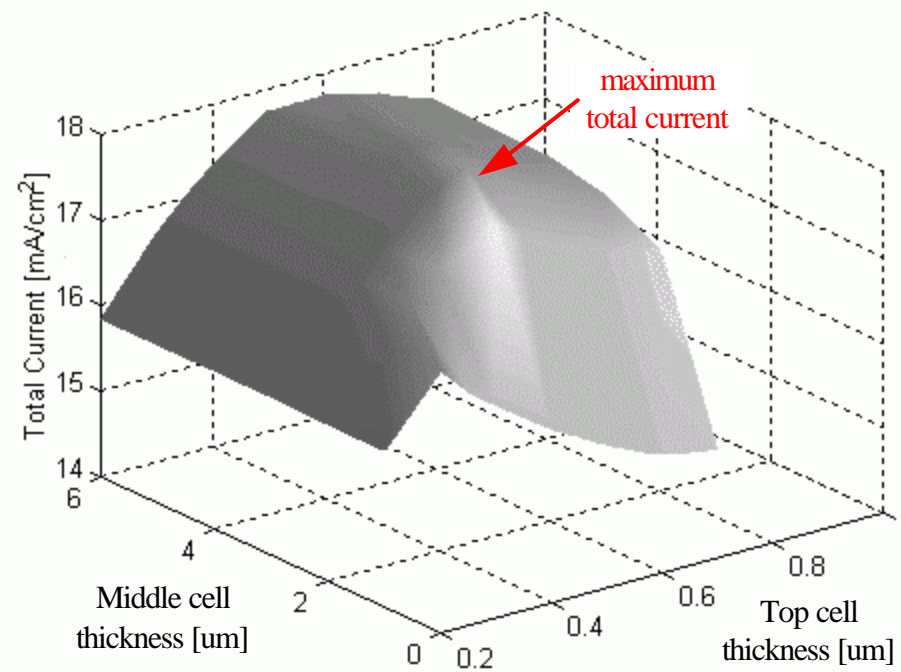


Figure 9.15. Total short-circuit current vs. top and middle cell thicknesses.

An interesting observation is that, even though the thickness of the middle cell has a major effect on the bottom cell current (as seen in Figure 9.10), the multijunction combination of cells is little affected by it. This conclusion is very reasonable and is due to the fact that the bottom cell rarely becomes the limiting current source in the structure. Therefore, the thickness of the middle cell has little effect on the total current produced. The bottom cell is a Ge one and due to its small bandgap, will absorb more photons and will produce more current than all other cells (see Figure 5.2). Additionally, its frequency response shows that it will mainly work in a region of optical wavelengths very different and larger than the GaAs or InGaP cells (see Figure 9.3). Therefore, the shadowing of the upper cells will not reduce its current enough to make it a limiting factor in the design.

The results of the optimization process point towards the results obtained in the previous section and are very similar to the ones in Ref. 19. This indicates that the structure tested earlier was already optimized. This choice is not attributed to luck. As it was explained in the beginning of this chapter, the two upper cells were almost identical to the dual cell tested in chapter 8. That cell was experimentally optimized by its creators and all the details of its structure were fully described in their publication. These parameters were also used in this simulation. The addition of the bottom cell did not change the optimum point of the triple-cell structure due to the reasons mentioned in the previous paragraph.

X. CONCLUSIONS AND RECOMMENDATIONS

A. RESULTS AND CONCLUSIONS

A novel methodology was presented for modeling and developing state-of-the-art solar cells. It is believed that it will be of great value to the photovoltaic industry and the developers of spacecrafts. Since almost all research on advanced solar cells is currently conducted via expensive and complex experimentation, the proposed simulation method is expected to help reduce that cost, simplify the design process, and allow the designer to focus on the final result.

In this thesis, as a first step, the exotic materials used in such designs were identified and all their major electrical and optical parameters were researched or derived. In addition, software code was developed to adjust and calibrate ATLAS for the task of simulating solar cells. More software was also developed to exchange data between ATLAS and MatLab, thus enhancing the abilities of the package.

An InGaP/GaAs dual multijunction cell was built and was fully simulated. The whole process was done in stages and detailed explanations were provided. Every result was also compared with published experimental results to verify the close agreement and accuracy of this methodology. This has formed a paper that has been submitted for publication in the 9th IEEE International Conference on Electronics, Circuits and Systems - ICECS 2002 September 15-18, 2002, in Dubrovnik Croatia.

A state-of-the-art InGaP/GaAs/Ge triple multijunction cell was also built and simulated. Although the structural details of the cell were not available, the cell was tweaked according to the experience gained on solar cells and the results matched the experiments very closely. Another paper was written and has already been accepted for publication in the 6th WSEAS International Conference on CIRCUITS – July 7-14, 2002 in Rethymna Beach, Rethymnon, Crete, Greece.

Additional optimization was finally done on the triple cell attempting to further improve its efficiency. The modeling, simulation and optimization of the triple cell has been submitted, as a paper, for publication in the 29th IEEE Photovoltaic Specialists Conference (PVSC) – May 20-24, 2002 in New Orleans, Louisiana USA.

B. FURTHER OPTIMIZATIONS AND RECOMMENDATIONS

There are several elements that might improve the performance of the configuration tested. One of these is the addition of buffer layers below each cell, to achieve better lattice matching of cells and tunnel junctions. Another very important improvement could be the addition of a BSF layer for the Ge cell. An attempt was made to incorporate both enhancements and the result was an increase in the V_{OC} by 0.15V (5.6%) and a total efficiency of 30.5%. This is a proposal to researchers for further development. However, due to the time limitations of this thesis, detailed results were not presented here. They may be researched in future work.

Another topic, that may be the subject of further research, is the investigation of various doping concentration effects on the electrical and optical properties of materials, with the aim of attaining higher levels of accuracy.

Additionally, in this thesis, the layer boundaries are treated as being strictly defined and their doping is assumed to be uniform. However, during any fabrication process, material diffusion and gradually varying doping are the dominant characteristics in a device. Their study will allow the simulation and modeling of both the basic cell structure and the actual fabricated implementation.

The possibility of radiation effects on solar cells and whether these can be simulated using VWF may be investigated in the future. This is a very important field for space applications.

Shining laser beams on cells may also be researched. Lasers can be used for providing additional photons to the cell, but also for countering some of the radiation effects.

Finally, modeling of secondary phenomena could also increase the accuracy of the results produced.

APPENDIX A. LIST OF SYMBOLS

Symbol	Description	Unit
a	Angle	deg
α	Absorption coefficient	m^{-1}
α	Lattice constant	\AA
AUGN / AUGP	Electron / hole Auger coefficients	cm^6/s
C	Capacitance	F
c	Speed of light	m/s
COPT	Radiative recombination rate	cm^3/s
E	Energy	eV
ϵ	Dielectric function	–
$\epsilon_1, \epsilon_2, n, k$	Optical constants	–
ϵ_S	Permittivity	F/cm
E_C	Bottom of conduction band	eV
E_F	Fermi energy level	eV
E_g	Energy bandgap	eV
E_V	Top of valence band	eV
f	Frequency	Hz
$f(E)$	Fermi–Dirac distribution function	–
h	Plank’s constant	J·s
hv	Photon energy	eV
I	Current	A
I_D / I_S	Diffusion / drift current	A
I_{SC}	Short circuit current	A
k	Boltzmann’s constant	J/K
kT	Thermal energy	eV
m^*	Effective mass	m_e

μ_n (MUN) / μ_p (MUP)	Electron / hole mobility	$\text{cm}^2/\text{V}\cdot\text{s}$
η	Power conversion efficiency	–
ν	Photon frequency	Hz
N_C / N_V	Electron / hole density of states	cm^{-3}
N_D / N_A	Donor / acceptor impurity atom concentration	cm^{-3}
n_i^2	Majority · minority carrier concentration product	cm^{-3}
n_{n0} / p_{p0}	Majority carrier (electrons / holes) concentration	cm^{-3}
n_{p0} / p_{n0}	Minority carrier (electrons / holes) concentration	cm^{-3}
n_r / n_r^*	Refraction / complex refraction index	–
P	Power	W
R	Reflectivity	–
ρ	Resistivity	$\Omega\cdot\text{m}$
σ	Conductivity	S/m
T	Absolute temperature	$^\circ\text{K}$
TAUN / TAUP	Electron / hole lifetimes	s
V	Voltage	V
V_{OC}	Open circuit current	V
χ	Absorption index	–
χ	Affinity	eV

APPENDIX B. GREEK ALPHABET

Letter	Pronunciation	Uppercase	Lowercase
Alpha	‘alpha	A	α
Beta	‘veeta	B	β
Gamma	‘yama	Γ	γ
Delta	‘delta	Δ	δ
Epsilon	‘epsilon	E	ε
Zeta	‘zeeta	Z	ζ
Eta	‘eeta	H	η
Theta	‘theeta	Θ	θ
Iota	‘yota	I	ι
Kappa	‘kapa	K	κ
Lambda	‘lamda	Λ	λ
Mu	mee	M	μ
Nu	nee	N	ν
Xi	ksee	Ξ	ξ
Omicron	‘omikron	O	ο
Pi	pee	Π	π
Rho	rho	P	ρ
Sigma	‘siyma	Σ	σ
Tau	taf	T	τ
Upsilon	‘ipseelon	Υ	υ
Phi	fee	Φ	φ
Chi	hee	X	χ
Psi	psee	Ψ	ψ
Omega	om’eya	Ω	ω

-
- * The phonetic ‘y’ is pronounced like in ‘y–es’ or ‘y–ellow’.
 The phonetic ‘d’ is pronounced like in ‘th–is’ or ‘th–ere’
 The phonetic ‘th’ is pronounced like in ‘th–ank’ or ‘th–ink’

THIS PAGE INTENTIONALLY LEFT BLANK

APPENDIX C. SOME PHYSICAL CONSTANTS

Quantity	Symbol	Value
Boltzmann's constant	k	$1.38066 \cdot 10^{-23}$ J/K
Electron charge	q_e	$1.60218 \cdot 10^{-19}$ Cb
Electronvolt	eV	$1.60218 \cdot 10^{-19}$ J
Electron mass at rest	m_e	$0.91093897 \cdot 10^{-30}$ Kg
Proton mass at rest	m_p	$1.6726231 \cdot 10^{-27}$ Kg
Plank's constant	h	$6.6260755 \cdot 10^{-34}$ J·s
Light speed in vacuum	c	$2.99792458 \cdot 10^8$ m/s

APPENDIX D. UNITS

Fundamental Units

Quantity	Unit	Symbol
Length	meter	m
Mass	kilogram	Kgr
Time	second	s
Current	ampere	A
Temperature	degree Kelvin	K
Light intensity	candela	Cd

Additional Units

Quantity	Unit	Symbol
Angle	radian	rad
Solid angle	steradian	sr
Matter quantity	mole	mol

Produced Units

Quantity	Unit	Symbol	Equivalence
Surface	square meter	m ²	m ²
Volume	cube meter	m ³	m ³
Velocity	–	m/s	m/s
Acceleration	–	m/s ²	m/s ²
Density	–	Kg/m ³	Kg/m ³
Momentum	–	Kg·m/s	Kg·m/s
Force	Newton	N	Kg·m/s ²
Frequency	Hertz	Hz	1/s
Pressure	Pascal	Pa	N/m ²
Viscosity	–	N·s/m ²	N·s/m ²
Energy	Joule	J	Kg·m ² /s ²
Heat	–	J	Kg·m ² /s ²
Power	Watt	W	N·m/s
Electric charge	Coulomb	Cb	A·s
Electric potential	Volt	V	Kg·m ² / A·s ³
Electric resistance	Ohm	Ω	Kg·m ² / A ² ·s ³
Electric conductivity	Siemens	S	m ² ·A ² ·s ⁴ / Kg
Electric capacitance	Farad	F	A ² ·s ⁴ / Kg·m ²
Electric inductance	Henry	H	Kg·m ² / A ² ·s ²
Magnetic flux	Weber	Wb	Kg·m ² /A·s ²
Magnetic induction	Tesla	T	Kg / A ² ·s ²
Light flux	Lumen	Φ	cd·sr
Illumination	Lux	lx	cd / m ²

APPENDIX E. MAGNITUDE PREFIXES

Magnitude prefix	Symbol	Multiple factor
yotta	Y	$1 \times 10^{+24}$
zetta	Z	$1 \times 10^{+21}$
exa	E	$1 \times 10^{+18}$
peta	P	$1 \times 10^{+15}$
tera	T	$1 \times 10^{+12}$
giga	G	$1 \times 10^{+9}$
mega	M	$1 \times 10^{+6}$
kilo	K	$1 \times 10^{+3}$
hecto	h	$1 \times 10^{+2}$
deka	da	$1 \times 10^{+1}$
-	-	1×10^0
deci	d	1×10^{-1}
centi	c	1×10^{-2}
milli	m	1×10^{-3}
micro	μ	1×10^{-6}
nano	n	1×10^{-9}
pico	p	1×10^{-12}
femto	f	1×10^{-15}
atto	a	1×10^{-18}
zepto	z	1×10^{-21}
yocto	y	1×10^{-24}

THIS PAGE INTENTIONALLY LEFT BLANK

APPENDIX F. ATLAS SOURCE CODE

A. MAIN STRUCTURE

```
go atlas
# Definition of constants
# Mesh
# X-Mesh
# Y-Mesh
# Regions
# Electrodes
# Doping
# Material properties
# Models
# Light beams
# Solving
```

B. COMMON SECTIONS

1. Mesh and X-Mesh

```
mesh space.mult=1
# X-Mesh: surface=500 um2 = 1/200,000 cm2
x.mesh loc=-250 spac=50
x.mesh loc=0 spac=10
x.mesh loc=250 spac=50
```

2. Material Properties

```
material TAUN=1e-7 TAUP=1e-7 COPT=1.5e-10 AUGN=8.3e-32 AUGP=1.8e-31

# Vacuum
material material=Vacuum real.index=3.3 imag.index=0

# Ge
material material=Ge EG300=0.67 PERMITTIVITY=16 AFFINITY=4
material material=Ge MUN=3900 MUP=1800
material material=Ge NC300=1.04e19 NV300=6e18
material material=Ge index.file=Ge.opt

# GaAs
material material=GaAs EG300=1.42 PERMITTIVITY=13.1 AFFINITY=4.07
material material=GaAs MUN=8800 MUP=400
material material=GaAs NC300=4.7e17 NV300=7e18
material material=GaAs index.file=GaAs.opt

# InGaP
material material=InGaP EG300=1.9 PERMITTIVITY=11.62 AFFINITY=4.16
material material=InGaP MUN=1945 MUP=141
material material=InGaP NC300=1.3e20 NV300=1.28e19
material material=InGaP index.file=InGaP-1.9.opt
```

```

# AlInP (=InAsP)
material material=InAsP EG300=2.4 PERMITTIVITY=11.7 AFFINITY=4.2
material material=InAsP MUN=2291 MUP=142
material material=InAsP NC300=1.08e20 NV300=1.28e19
material material=InAsP index.file=AlInP.opt

# AlInGaP (=InAlAsP)
material material=InAlAsP EG300=2.4 PERMITTIVITY=11.7 AFFINITY=4.2
material material=InAlAsP MUN=2150 MUP=141
material material=InAlAsP NC300=1.2e20 NV300=1.28e19
material material=InAlAsP index.file=AlInP.opt

```

3. Models

models BBT.KL TATUN TRAP.TUNNEL

4. Light Beams

```

beam num=1 x.origin=0 y.origin=-5 angle=90 \
power.file=AM0sily.spec wavel.start=0.21 wavel.end=4 wavel.num=50

```

B. InGaAs / GaAs CELL

1. Bottom Cell

a. Y-Mesh

```

# Vacuum
y.mesh loc=-0.15 spac=0.001
# Window (0.05 um)
y.mesh loc=-0.1 spac=0.01
# Emitter (0.1 um)
y.mesh loc=0 spac=0.01
# Base (3 um)
y.mesh loc=1.5 spac=0.3
y.mesh loc=3 spac=0.01
# BSF (0.1 um)
y.mesh loc=3.1 spac=0.01
# Buffer (0.3 um)
y.mesh loc=3.4 spac=0.05
# Substrate (300 um)
y.mesh loc=303.4 spac=50

```

b. Regions

```

# Window AlInP (=InAsP)
region num=1 material=InAsP x.min=-250 x.max=250 y.min=-0.15 y.max=-0.1
# Emitter
region num=2 material=GaAs x.min=-250 x.max=250 y.min=-0.1 y.max=0
# Base
region num=3 material=GaAs x.min=-250 x.max=250 y.min=0 y.max=3
# BSF
region num=4 material=InGaP x.min=-250 x.max=250 y.min=3 y.max=3.1
# Buffer
region num=5 material=GaAs x.min=-250 x.max=250 y.min=3.1 y.max=3.4

```

```
# Substrate
region num=6 material=GaAs x.min=-250 x.max=250 y.min=3.4 y.max=303.4
```

c. Electrodes

```
electrode name=cathode x.min=-250 x.max=250 y.min=-0.15 y.max=-0.15
electrode name=anode x.min=-250 x.max=250 y.min=303.4 y.max=303.4
```

d. Doping

```
# Window
doping uniform region=1 n.type conc=1e19
# Emitter
doping uniform region=2 n.type conc=2e18
# Base
doping uniform region=3 p.type conc=1e17
# BSF
doping uniform region=4 p.type conc=2e18
# Buffer
doping uniform region=5 p.type conc=7e18
# Substrate
doping uniform region=6 p.type conc=1e19
```

e. Solving

(1) I_{SC} and V_{OC}

```
# Get Isc and Voc
solve init
method gummel maxtraps=10 itlimit=25
solve b1=0.9
method newton maxtraps=10 itlimit=100
solve b1=1
```

```
contact name=cathode current
method newton maxtraps=10 itlimit=100
solve icathode=17.404e-8 b1=1
solve icathode=0 b1=1
```

(2) Frequency response

```
# Get frequency response
solve init
log outfile=freq-bot.log
solve b1=0.1 lambda=0.2
solve b1=0.1 lambda=0.25
solve b1=0.1 lambda=0.3
solve b1=0.1 lambda=0.35
solve b1=0.1 lambda=0.4
solve b1=0.1 lambda=0.45
solve b1=0.1 lambda=0.5
solve b1=0.1 lambda=0.6
solve b1=0.1 lambda=0.65
solve b1=0.1 lambda=0.675
solve b1=0.1 lambda=0.7
solve b1=0.1 lambda=0.75
solve b1=0.1 lambda=0.8
```

```

solve b1=0.1 lambda=0.83
solve b1=0.1 lambda=0.84
solve b1=0.1 lambda=0.85
solve b1=0.1 lambda=0.9
solve b1=0.1 lambda=0.95
solve b1=0.1 lambda=1
solve b1=0.1 lambda=1.2

```

2. Top Cell

a. *Y-Mesh*

```

# Vacuum
y.mesh loc=-0.87 spac=0.003
# Window (0.03 um)
y.mesh loc=-0.84 spac=0.003
# Emitter (0.05 um)
y.mesh loc=-0.79 spac=0.003
# Base (0.55 um)
y.mesh loc=-0.5 spac=0.1
y.mesh loc=-0.24 spac=0.003
# BSF (0.03 um)
y.mesh loc=-0.21 spac=0.003
# Buffer (0.03 um)
y.mesh loc=-0.18 spac=0.002

```

b. *Regions*

```

# Window AlInP (=InAsP)
region num=1 material=InAsP x.min=-250 x.max=250 y.min=-0.87 y.max=-
0.84
# Emitter
region num=2 material=InGaP x.min=-250 x.max=250 y.min=-0.84 y.max=-
0.79
# Base
region num=3 material=InGaP x.min=-250 x.max=250 y.min=-0.79 y.max=-
0.24
# BSF
region num=4 material=InGaP x.min=-250 x.max=250 y.min=-0.24 y.max=-
0.21
# Buffer AlInP (=InAsP)
region num=5 material=InAsP x.min=-250 x.max=250 y.min=-0.21 y.max=-
0.18

```

c. *Electrodes*

```

electrode name=cathode x.min=-250 x.max=250 y.min=-0.87 y.max=-0.87
electrode name=anode x.min=-250 x.max=250 y.min=-0.18 y.max=-0.18

```

d. *Doping*

```

# Window
doping uniform region=1 n.type conc=1.95e18
# Emitter
doping uniform region=2 n.type conc=2e18
# Base
doping uniform region=3 p.type conc=1.5e17

```

```
# BSF
doping uniform region=4 p.type conc=2e18
# Buffer
doping uniform region=5 p.type conc=0.95e18
```

e. Solving

(1) I_{sc} and V_{oc}

```
# Get  $I_{sc}$  and  $V_{oc}$ 
solve init
method gummel maxtraps=10 itlimit=25
solve b1=0.9
method newton maxtraps=10 itlimit=100
solve b1=1

contact name=cathode current
method newton maxtraps=10 itlimit=100
solve icathode=14.364e-8 b1=1
solve icathode=0 b1=1
```

(2) Frequency response

```
# Get frequency response
solve init
log outfile=freq-top.log
solve b1=0.1 lambda=0.2
solve b1=0.1 lambda=0.25
solve b1=0.1 lambda=0.3
solve b1=0.1 lambda=0.35
solve b1=0.1 lambda=0.4
solve b1=0.1 lambda=0.45
solve b1=0.1 lambda=0.5
solve b1=0.1 lambda=0.6
solve b1=0.1 lambda=0.65
solve b1=0.1 lambda=0.675
solve b1=0.1 lambda=0.7
solve b1=0.1 lambda=0.75
solve b1=0.1 lambda=0.8
solve b1=0.1 lambda=0.83
solve b1=0.1 lambda=0.84
solve b1=0.1 lambda=0.85
solve b1=0.1 lambda=0.9
solve b1=0.1 lambda=0.95
solve b1=0.1 lambda=1
solve b1=0.1 lambda=1.2
```

3. Stacked Cell

a. Y-Mesh

```
# Vacuum
y.mesh loc=-0.87 spac=0.003
# Window (0.03  $\mu\text{m}$ )
y.mesh loc=-0.84 spac=0.003
# Emitter (0.05  $\mu\text{m}$ )
y.mesh loc=-0.79 spac=0.003
```

```

# Base (0.55 um)
y.mesh loc=-0.5 spac=0.1
y.mesh loc=-0.24 spac=0.003
# BSF (0.03 um)
y.mesh loc=-0.21 spac=0.003
# Buffer (0.03 um)
y.mesh loc=-0.18 spac=0.002
# Vacuum (0.015 um)
y.mesh loc=-0.165 spac=0.002
# Vacuum (0.015 um)
y.mesh loc=-0.15 spac=0.001
# Window (0.05 um)
y.mesh loc=-0.1 spac=0.01
# Emitter (0.1 um)
y.mesh loc=0 spac=0.01
# Base (3 um)
y.mesh loc=1.5 spac=0.3
y.mesh loc=3 spac=0.01
# BSF (0.1 um)
y.mesh loc=3.1 spac=0.01
# Buffer (0.3 um)
y.mesh loc=3.4 spac=0.05
# Substrate (300 um)
y.mesh loc=303.4 spac=50

```

b. Regions

```

# Window AlInP (=InAsP)
region num=1 material=InAsP x.min=-250 x.max=250 y.min=-0.87 y.max=-
0.84
# Emitter
region num=2 material=InGaP x.min=-250 x.max=250 y.min=-0.84 y.max=-
0.79
# Base
region num=3 material=InGaP x.min=-250 x.max=250 y.min=-0.79 y.max=-
0.24
# BSF
region num=4 material=InGaP x.min=-250 x.max=250 y.min=-0.24 y.max=-
0.21
# Buffer AlInP (=InAsP)
region num=5 material=InAsP x.min=-250 x.max=250 y.min=-0.21 y.max=-
0.18
# Vacuum
region num=6 material=Vacuum x.min=-250 x.max=250 y.min=-0.18 y.max=-
0.165
region num=7 material=Vacuum x.min=-250 x.max=250 y.min=-0.165 y.max=-
0.15
# Window AlInP (=InAsP)
region num=8 material=InAsP x.min=-250 x.max=250 y.min=-0.15 y.max=-0.1
# Emitter
region num=9 material=GaAs x.min=-250 x.max=250 y.min=-0.1 y.max=0
# Base
region num=10 material=GaAs x.min=-250 x.max=250 y.min=0 y.max=3
# BSF
region num=11 material=InGaP x.min=-250 x.max=250 y.min=3 y.max=3.1
# Buffer
region num=12 material=GaAs x.min=-250 x.max=250 y.min=3.1 y.max=3.4

```

```
# Substrate
region num=13 material=GaAs x.min=-250 x.max=250 y.min=3.4 y.max=303.4
```

c. Electrodes

```
electrode name=cathode x.min=-250 x.max=250 y.min=-0.87 y.max=-0.87
electrode name=cc x.min=-250 x.max=250 y.min=-0.18 y.max=-0.18
electrode name=ee x.min=-250 x.max=250 y.min=-0.15 y.max=-0.15
electrode name=anode x.min=-250 x.max=250 y.min=303.4 y.max=303.4
```

d. Doping

```
# Window
doping uniform region=1 n.type conc=1.95e18
# Emitter
doping uniform region=2 n.type conc=2e18
# Base
doping uniform region=3 p.type conc=1.5e17
# BSF
doping uniform region=4 p.type conc=2e18
# Buffer
doping uniform region=5 p.type conc=0.95e18
# Window
doping uniform region=8 n.type conc=1e19
# Emitter
doping uniform region=9 n.type conc=2e18
# Base
doping uniform region=10 p.type conc=1e17
# BSF
doping uniform region=11 p.type conc=2e18
# Buffer
doping uniform region=12 p.type conc=7e18
# Substrate
doping uniform region=13 p.type conc=1e19
```

e. Solving

(1) I_{sc} and V_{oc}

```
# Get  $I_{sc}$  and  $V_{oc}$ 
solve init
method gummel maxtraps=10 itlimit=25
solve b1=0.9
method newton maxtraps=10 itlimit=100
solve b1=1

contact name=emitter current
method newton maxtraps=10 itlimit=100
#solve iemitter=3.67113e-8 icathode=14.3731e-8 b1=1
solve iemitter=3.67113e-8 b1=1
solve iemitter=0 b1=1
```

(2) Frequency response

```
# Get frequency response
solve init
```

```

log outfile=InGaP-GaAs-stack-freq.log
solve b1=0.1 lambda=0.2
solve b1=0.1 lambda=0.22
solve b1=0.1 lambda=0.24
solve b1=0.1 lambda=0.26
solve b1=0.1 lambda=0.28
solve b1=0.1 lambda=0.3
solve b1=0.1 lambda=0.32
solve b1=0.1 lambda=0.34
solve b1=0.1 lambda=0.36
solve b1=0.1 lambda=0.38
solve b1=0.1 lambda=0.4
solve b1=0.1 lambda=0.42
solve b1=0.1 lambda=0.44
solve b1=0.1 lambda=0.46
solve b1=0.1 lambda=0.48
solve b1=0.1 lambda=0.5
solve b1=0.1 lambda=0.52
solve b1=0.1 lambda=0.54
solve b1=0.1 lambda=0.56
solve b1=0.1 lambda=0.58
solve b1=0.1 lambda=0.6
solve b1=0.1 lambda=0.62
solve b1=0.1 lambda=0.64
solve b1=0.1 lambda=0.66
solve b1=0.1 lambda=0.68
solve b1=0.1 lambda=0.7
solve b1=0.1 lambda=0.75
solve b1=0.1 lambda=0.8
solve b1=0.1 lambda=0.83
solve b1=0.1 lambda=0.84
solve b1=0.1 lambda=0.85
solve b1=0.1 lambda=0.86
solve b1=0.1 lambda=0.87
solve b1=0.1 lambda=0.88
solve b1=0.1 lambda=0.89
solve b1=0.1 lambda=0.9
solve b1=0.1 lambda=0.92
solve b1=0.1 lambda=0.95
solve b1=0.1 lambda=1
solve b1=0.1 lambda=1.2

```

4. Tunnel Junction

a. Y-Mesh

```

y.mesh loc=-0.18 spac=0.002
# Tunnel emitter (0.015 um)
y.mesh loc=-0.165 spac=0.002
# Tunnel base (0.015 um)
y.mesh loc=-0.15 spac=0.001

```

b. Regions

```

region num=1 material=InGaP x.min=-250 x.max=250 y.min=-0.18 y.max=-
0.165

```

```
region num=2 material=InGaP x.min=-250 x.max=250 y.min=-0.165 y.max=-0.15
```

c. Electrodes

```
electrode name=cathode x.min=-250 x.max=250 y.min=-0.18 y.max=-0.18  
electrode name=anode x.min=-250 x.max=250 y.min=-0.15 y.max=-0.15
```

d. Doping

```
doping uniform region=1 p.type conc=8e18  
doping uniform region=2 n.type conc=1e19
```

e. Solving

(1) IV characteristic

```
solve init  
solve vcathode=0  
solve vcathode=-0.5  
solve vcathode=-1  
solve vcathode=-1.5  
  
log outfile=InGaP-td-IV.log  
solve vcathode=-2  
solve vcathode=-1.75  
solve vcathode=-1.5  
solve vcathode=-1.25  
solve vcathode=-1  
solve vcathode=-0.75  
solve vcathode=-0.5  
solve vcathode=-0.3  
solve vcathode=-0.2  
solve vcathode=-0.1  
solve vcathode=0  
solve vcathode=0.1  
solve vcathode=0.2  
solve vcathode=0.3  
solve vcathode=0.4  
solve vcathode=0.5  
solve vcathode=0.6  
solve vcathode=0.7  
solve vcathode=0.8  
solve vcathode=0.9
```

5. MJ Cell

a. Y-Mesh

```
# Vacuum  
y.mesh loc=-0.87 spac=0.003  
# Window (0.03 um)  
y.mesh loc=-0.84 spac=0.003  
# Emitter (0.05 um)  
y.mesh loc=-0.79 spac=0.003  
# Base (0.55 um)  
y.mesh loc=-0.5 spac=0.1
```

```

y.mesh loc=-0.24 spac=0.003
# BSF (0.03 um)
y.mesh loc=-0.21 spac=0.003
# Buffer (0.03 um)
y.mesh loc=-0.18 spac=0.002
# Tunnel emitter (0.015 um)
y.mesh loc=-0.165 spac=0.002
# Tunnel base (0.015 um)
y.mesh loc=-0.15 spac=0.001
# Window (0.05 um)
y.mesh loc=-0.1 spac=0.01
# Emitter (0.1 um)
y.mesh loc=0 spac=0.01
# Base (3 um)
y.mesh loc=1.5 spac=0.3
y.mesh loc=3 spac=0.01
# BSF (0.1 um)
y.mesh loc=3.1 spac=0.01
# Buffer (0.3 um)
y.mesh loc=3.4 spac=0.05
# Substrate (300 um)
y.mesh loc=303.4 spac=50

```

b. Regions

```

# Window AlInP (=InAsP)
region num=1 material=InAsP x.min=-250 x.max=250 y.min=-0.87 y.max=-
0.84
# Emitter
region num=2 material=InGaP x.min=-250 x.max=250 y.min=-0.84 y.max=-
0.79
# Base
region num=3 material=InGaP x.min=-250 x.max=250 y.min=-0.79 y.max=-
0.24
# BSF
region num=4 material=InGaP x.min=-250 x.max=250 y.min=-0.24 y.max=-
0.21
# Buffer AlInP (=InAsP)
region num=5 material=InAsP x.min=-250 x.max=250 y.min=-0.21 y.max=-
0.18

# Tunnel emitter
region num=6 material=InGaP x.min=-250 x.max=250 y.min=-0.18 y.max=-
0.165
# Tunnel base
region num=7 material=InGaP x.min=-250 x.max=250 y.min=-0.165 y.max=-
0.15

# Window AlInP (=InAsP)
region num=8 material=InAsP x.min=-250 x.max=250 y.min=-0.15 y.max=-0.1
# Emitter
region num=9 material=GaAs x.min=-250 x.max=250 y.min=-0.1 y.max=0
# Base
region num=10 material=GaAs x.min=-250 x.max=250 y.min=0 y.max=3
# BSF
region num=11 material=InGaP x.min=-250 x.max=250 y.min=3 y.max=3.1
# Buffer

```

```
region num=12 material=GaAs x.min=-250 x.max=250 y.min=3.1 y.max=3.4
# Substrate
region num=13 material=GaAs x.min=-250 x.max=250 y.min=3.4 y.max=303.4
```

c. Electrodes

```
electrode name=cathode x.min=-250 x.max=250 y.min=-0.87 y.max=-0.87
electrode name=anode x.min=-250 x.max=250 y.min=303.4 y.max=303.4
```

d. Doping

```
# Window
doping uniform region=1 n.type conc=1.95e18
# Emitter
doping uniform region=2 n.type conc=2e18
# Base
doping uniform region=3 p.type conc=1.5e17
# BSF
doping uniform region=4 p.type conc=2e18
# Buffer
doping uniform region=5 p.type conc=0.95e18
# Tunnel
doping uniform region=6 p.type conc=8e18
# Tunnel
doping uniform region=7 n.type conc=1e19
# Window
doping uniform region=8 n.type conc=1e19
# Emitter
doping uniform region=9 n.type conc=2e18
# Base
doping uniform region=10 p.type conc=1e17
# BSF
doping uniform region=11 p.type conc=2e18
# Buffer
doping uniform region=12 p.type conc=7e18
# Substrate
doping uniform region=13 p.type conc=1e19
```

e. Solving

(1) I_{SC} and V_{OC}

```
# Get Isc and Voc
solve init
method gummel maxtraps=10 itlimit=25
solve b1=0.9
method newton maxtraps=10 itlimit=100
solve b1=1

contact name=cathode current
method newton maxtraps=10 itlimit=100
solve icathode=8.17e-8 b1=1
solve icathode=0 b1=1
```

B. InGaAs / GaAs / Ge CELL

1. Bottom Cell

a. Definition of Constants

```
set botLo=0
set botWindowThick=0.05
set botEmitterThick=0.1
set botBaseThick=300
set botBaseLo=$botLo
set botBaseMid=$botBaseLo-$botBaseThick/2
set botEmitterLo=$botBaseLo-$botBaseThick
set botWindowLo=$botEmitterLo-$botEmitterThick
set botHi=$botWindowLo-$botWindowThick
set botBaseDiv=$botBaseThick/20
set botEmitterDiv=$botEmitterThick/20
set botWindowDiv=$botWindowThick/20
set lightY=$botHi-5
```

b. Y-Mesh

```
# Vacuum
y.mesh loc=$botHi spac=$botWindowDiv
# Window
y.mesh loc=$botWindowLo spac=$botWindowDiv
# Emitter
y.mesh loc=$botEmitterLo spac=$botEmitterDiv
# Base
y.mesh loc=$botBaseMid spac=$botBaseDiv
y.mesh loc=$botBaseLo spac=$botEmitterDiv
```

c. Regions

```
# Window
region num=1 material=GaAs x.min=-250 x.max=250 y.min=$botHi
y.max=$botWindowLo
# Emitter
region num=2 material=Ge x.min=-250 x.max=250 y.min=$botWindowLo
y.max=$botEmitterLo
# Base
region num=3 material=Ge x.min=-250 x.max=250 y.min=$botEmitterLo
y.max=$botBaseLo
```

d. Electrodes

```
electrode name=cathode x.min=-250 x.max=250 y.min=$botHi y.max=$botHi
electrode name=anode x.min=-250 x.max=250 y.min=$botLo y.max=$botLo
```

e. Doping

```
# Window
doping uniform region=1 n.type conc=1e19
# Emitter
doping uniform region=2 n.type conc=2e18
# Base
doping uniform region=3 p.type conc=1e17
```

f. Light Beams

```
beam num=1 x.origin=0 y.origin=$lightY angle=90 \  
power.file=AM0silv.spec wavel.start=0.21 wavel.end=4 wavel.num=50
```

g. Solving

(1) I_{sc} and V_{oc}

```
# Get  $I_{sc}$  and  $V_{oc}$   
solve init  
method gummel maxtraps=10 itlimit=25  
solve b1=0.9  
method newton maxtraps=10 itlimit=100  
solve b1=1
```

```
contact name=cathode current  
method newton maxtraps=10 itlimit=100  
solve icathode=3.1654e-7 b1=1  
solve icathode=0 b1=1
```

(2) Frequency response

```
solve init  
log outfile=InGaP-GaAs-Ge-bot-freq.log  
solve b1=0.1 lambda=0.22  
solve b1=0.1 lambda=0.3  
solve b1=0.1 lambda=0.4  
solve b1=0.1 lambda=0.5  
solve b1=0.1 lambda=0.6  
solve b1=0.1 lambda=0.7  
solve b1=0.1 lambda=0.8  
solve b1=0.1 lambda=0.9  
solve b1=0.1 lambda=1  
solve b1=0.1 lambda=1.1  
solve b1=0.1 lambda=1.2  
solve b1=0.1 lambda=1.3  
solve b1=0.1 lambda=1.4  
solve b1=0.1 lambda=1.5  
solve b1=0.1 lambda=1.6  
solve b1=0.1 lambda=1.7  
solve b1=0.1 lambda=1.8  
solve b1=0.1 lambda=1.9  
solve b1=0.1 lambda=2.1  
solve b1=0.1 lambda=2.2  
solve b1=0.1 lambda=2.3  
solve b1=0.1 lambda=2.4  
solve b1=0.1 lambda=2.5  
solve b1=0.1 lambda=2.6  
solve b1=0.1 lambda=2.7  
solve b1=0.1 lambda=2.8  
solve b1=0.1 lambda=2.9  
solve b1=0.1 lambda=3  
solve b1=0.1 lambda=3.1  
solve b1=0.1 lambda=3.2  
solve b1=0.1 lambda=3.3
```

```

solve b1=0.1 lambda=3.4
solve b1=0.1 lambda=3.5
solve b1=0.1 lambda=3.6
solve b1=0.1 lambda=3.7
solve b1=0.1 lambda=3.8
solve b1=0.1 lambda=3.9

```

2. Middle Cell

a. Definition of Constants

```

set midLo=0
set midWindowThick=0.03
set midEmitterThick=0.05
set midBaseThick=0.55
set midBsfThick=0.03
set midBsfLo=$midLo
set midBaseLo=$midBsfLo-$midBsfThick
set midBaseMid=$midBaseLo-$midBaseThick/2
set midEmitterLo=$midBaseLo-$midBaseThick
set midWindowLo=$midEmitterLo-$midEmitterThick
set midHi=$midWindowLo-$midWindowThick
set midBsfDiv=$midBsfThick/20
set midBaseDiv=$midBaseThick/20
set midEmitterDiv=$midEmitterThick/20
set midWindowDiv=$midWindowThick/20

```

b. Y-Mesh

```

# Vacuum
y.mesh loc=$midHi spac=$midWindowDiv
# Window
y.mesh loc=$midWindowLo spac=$midWindowDiv
# Emitter
y.mesh loc=$midEmitterLo spac=$midEmitterDiv
# Base
y.mesh loc=$midBaseMid spac=$midBaseDiv
y.mesh loc=$midBaseLo spac=$midBsfDiv
# BSF
y.mesh loc=$midBsfLo spac=$midBsfDiv

```

c. Regions

```

# Window
region num=1 material=InGaP x.min=-250 x.max=250 y.min=$midHi
y.max=$midWindowLo
# Emitter
region num=2 material=GaAs x.min=-250 x.max=250 y.min=$midWindowLo
y.max=$midEmitterLo
# Base
region num=3 material=GaAs x.min=-250 x.max=250 y.min=$midEmitterLo
y.max=$midBaseLo
# BSF
region num=4 material=InGaP x.min=-250 x.max=250 y.min=$midBaseLo
y.max=$midBsfLo

```

d. Electrodes

```
electrode name=cathode x.min=-250 x.max=250 y.min=$midHi y.max=$midHi
electrode name=anode x.min=-250 x.max=250 y.min=$midLo y.max=$midLo
```

e. Doping

```
# Window
doping uniform region=1 n.type conc=1.95e18
# Emitter
doping uniform region=2 n.type conc=2e18
# Base
doping uniform region=3 p.type conc=1.5e17
# BSF
doping uniform region=4 p.type conc=2e18
```

f. Solving

(1) I_{SC} and V_{OC}

```
# Get Isc and Voc
solve init
method gummel maxtraps=10 itlimit=25
solve b1=0.9
method newton maxtraps=10 itlimit=100
solve b1=1

contact name=cathode current
method newton maxtraps=10 itlimit=100
solve icathode=1.376e-7 b1=1
solve icathode=0 b1=1
```

3. Top Cell

a. Definition of Constants

```
set topLo=0
set topWindowThick=0.03
set topEmitterThick=0.05
set topBaseThick=0.55
set topBsfThick=0.03
set topBsfLo=$topLo
set topBaseLo=$topBsfLo-$topBsfThick
set topBaseMid=$topBaseLo-$topBaseThick/2
set topEmitterLo=$topBaseLo-$topBaseThick
set topWindowLo=$topEmitterLo-$topEmitterThick
set topHi=$topWindowLo-$topWindowThick
set topBsfDiv=$topBsfThick/20
set topBaseDiv=$topBaseThick/20
set topEmitterDiv=$topEmitterThick/20
set topWindowDiv=$topWindowThick/20
```

b. Y-Mesh

```
# Vacuum
y.mesh loc=$topHi spac=$topWindowDiv
# Window
```

```

y.mesh loc=$stopWindowLo spac=$stopWindowDiv
# Emitter
y.mesh loc=$stopEmitterLo spac=$stopEmitterDiv
# Base
y.mesh loc=$stopBaseMid spac=$stopBaseDiv
y.mesh loc=$stopBaseLo spac=$stopBsfDiv
# BSF
y.mesh loc=$stopBsfLo spac=$stopBsfDiv

```

c. Regions

```

# Window AlInP (=InAsP)
region num=1 material=InAsP x.min=-250 x.max=250 y.min=$stopHi
y.max=$stopWindowLo
# Emitter
region num=2 material=InGaP x.min=-250 x.max=250 y.min=$stopWindowLo
y.max=$stopEmitterLo
# Base
region num=3 material=InGaP x.min=-250 x.max=250 y.min=$stopEmitterLo
y.max=$stopBaseLo
# BSF AlInGaP (=InAlAsP)
region num=4 material=InAlAsP x.min=-250 x.max=250 y.min=$stopBaseLo
y.max=$stopBsfLo

```

d. Electrodes

```

electrode name=cathode x.min=-250 x.max=250 y.min=$stopHi y.max=$stopHi
electrode name=anode x.min=-250 x.max=250 y.min=$stopLo y.max=$stopLo

```

e. Doping

```

# Window
doping uniform region=1 n.type conc=1.95e18
# Emitter
doping uniform region=2 n.type conc=2e18
# Base
doping uniform region=3 p.type conc=1.5e17
# BSF
doping uniform region=4 p.type conc=2e18

```

f. Solving

(1) I_{SC} and V_{OC}

```

# Get Isc and Voc
solve init
method gummel maxtraps=10 itlimit=25
solve b1=0.9
method newton maxtraps=10 itlimit=100
solve b1=1

contact name=cathode current
method newton maxtraps=10 itlimit=100
solve icathode=8.4714e-8 b1=1
solve icathode=0 b1=1

```

3. Stacked Cell

a. Definition of Constants

```
set divs=10
set topBaseThick=0.55
set midBaseThick=0.55
set topWindowThick=0.03
set topEmitterThick=$topBaseThick/10
set topBsfThick=0.03
set midWindowThick=0.03
set midEmitterThick=$midBaseThick/10
set midBsfThick=0.03
set botWindowThick=0.05
set botEmitterThick=0.1
set botBaseThick=300
set tunnelThick=0.015
# Bottom
set botLo=0
set botBaseLo=$botLo
set botBaseMid=$botBaseLo-$botBaseThick/2
set botEmitterLo=$botBaseLo-$botBaseThick
set botWindowLo=$botEmitterLo-$botEmitterThick
set botHi=$botWindowLo-$botWindowThick
set botBaseDiv=$botBaseThick/$divs
set botEmitterDiv=$botEmitterThick/$divs
set botWindowDiv=$botWindowThick/$divs
# Bot Tunnel
set botTunnelLo=$botHi
set botTunnelMid=$botTunnelLo-$tunnelThick
set botTunnelHi=$botTunnelMid-$tunnelThick
set tunnelDiv=$tunnelThick/$divs
# Middle
set midLo=$botTunnelHi
set midBsfLo=$midLo
set midBaseLo=$midBsfLo-$midBsfThick
set midBaseMid=$midBaseLo-$midBaseThick/2
set midEmitterLo=$midBaseLo-$midBaseThick
set midWindowLo=$midEmitterLo-$midEmitterThick
set midHi=$midWindowLo-$midWindowThick
set midBsfDiv=$midBsfThick/$divs
set midBaseDiv=$midBaseThick/$divs
set midEmitterDiv=$midEmitterThick/$divs
set midWindowDiv=$midWindowThick/$divs
# Top Tunnel
set topTunnelLo=$midHi
set topTunnelMid=$topTunnelLo-$tunnelThick
set topTunnelHi=$topTunnelMid-$tunnelThick
# Top
set topLo=$topTunnelHi
set topBsfLo=$topLo
set topBaseLo=$topBsfLo-$topBsfThick
set topBaseMid=$topBaseLo-$topBaseThick/2
set topEmitterLo=$topBaseLo-$topBaseThick
set topWindowLo=$topEmitterLo-$topEmitterThick
set topHi=$topWindowLo-$topWindowThick
set topBsfDiv=$topBsfThick/$divs
```

```

set topBaseDiv=$stopBaseThick/$divs
set topEmitterDiv=$stopEmitterThick/$divs
set topWindowDiv=$stopWindowThick/$divs
# Light
set lightY=$stopHi-5

```

b. Y-Mesh

```

# Vacuum
y.mesh loc=$stopHi spac=$stopWindowDiv
# Window
y.mesh loc=$stopWindowLo spac=$stopWindowDiv
# Emitter
y.mesh loc=$stopEmitterLo spac=$stopEmitterDiv
# Base
y.mesh loc=$stopBaseMid spac=$stopBaseDiv
y.mesh loc=$stopBaseLo spac=$stopBsfDiv
# BSF
y.mesh loc=$stopBsfLo spac=$tunnelDiv
# Vacuum
y.mesh loc=$stopTunnelMid spac=$tunnelDiv
# Vacuum
y.mesh loc=$midHi spac=$tunnelDiv
# Window
y.mesh loc=$midWindowLo spac=$midWindowDiv
# Emitter
y.mesh loc=$midEmitterLo spac=$midEmitterDiv
# Base
y.mesh loc=$midBaseMid spac=$midBaseDiv
y.mesh loc=$midBaseLo spac=$midBsfDiv
# BSF
y.mesh loc=$midBsfLo spac=$tunnelDiv
# Vacuum
y.mesh loc=$botTunnelMid spac=$tunnelDiv
# Vacuum
y.mesh loc=$botHi spac=$tunnelDiv
# Window
y.mesh loc=$botWindowLo spac=$botWindowDiv
# Emitter
y.mesh loc=$botEmitterLo spac=$botEmitterDiv
# Base
y.mesh loc=$botBaseMid spac=$botBaseDiv
y.mesh loc=$botBaseLo spac=$botEmitterDiv

```

c. Regions

```

# Window AlInP (=InAsP)
region num=1 material=InAsP x.min=-250 x.max=250 y.min=$stopHi
y.max=$stopWindowLo
# Emitter
region num=2 material=InGaP x.min=-250 x.max=250 y.min=$stopWindowLo
y.max=$stopEmitterLo
# Base
region num=3 material=InGaP x.min=-250 x.max=250 y.min=$stopEmitterLo
y.max=$stopBaseLo
# BSF AlInGaP (=InAlAsP)

```

```

region num=4 material=InAlAsP x.min=-250 x.max=250 y.min=$stopBaseLo
y.max=$stopBsflLo

# Vacuum
region num=5 material=Vacuum x.min=-250 x.max=250 y.min=$stopTunnelHi
y.max=$stopTunnelMid
#Vacuum
region num=6 material=Vacuum x.min=-250 x.max=250 y.min=$stopTunnelMid
y.max=$stopTunnelLo

# Window
region num=7 material=InGaP x.min=-250 x.max=250 y.min=$midHi
y.max=$midWindowLo
# Emitter
region num=8 material=GaAs x.min=-250 x.max=250 y.min=$midWindowLo
y.max=$midEmitterLo
# Base
region num=9 material=GaAs x.min=-250 x.max=250 y.min=$midEmitterLo
y.max=$midBaseLo
# BSF
region num=10 material=InGaP x.min=-250 x.max=250 y.min=$midBaseLo
y.max=$midBsflLo

# Vacuum
region num=11 material=Vacuum x.min=-250 x.max=250 y.min=$botTunnelHi
y.max=$botTunnelMid
#Vacuum
region num=12 material=Vacuum x.min=-250 x.max=250 y.min=$botTunnelMid
y.max=$botTunnelLo

# Window
region num=13 material=GaAs x.min=-250 x.max=250 y.min=$botHi
y.max=$botWindowLo
# Emitter
region num=14 material=Ge x.min=-250 x.max=250 y.min=$botWindowLo
y.max=$botEmitterLo
# Base
region num=15 material=Ge x.min=-250 x.max=250 y.min=$botEmitterLo
y.max=$botBaseLo

```

d. Electrodes

```

electrode name=gate x.min=-250 x.max=250 y.min=$stopHi y.max=$stopHi
electrode name=drain x.min=-250 x.max=250 y.min=$stopLo y.max=$stopLo

electrode name=collector x.min=-250 x.max=250 y.min=$midHi y.max=$midHi
electrode name=emitter x.min=-250 x.max=250 y.min=$midLo y.max=$midLo

electrode name=cathode x.min=-250 x.max=250 y.min=$botHi y.max=$botHi
electrode name=anode x.min=-250 x.max=250 y.min=$botLo y.max=$botLo

```

e. Doping

```

# Window
doping uniform region=1 n.type conc=1.95e18
# Emitter
doping uniform region=2 n.type conc=2e18

```

```
# Base
doping uniform region=3 p.type conc=1.5e17
# BSF
doping uniform region=4 p.type conc=2e18

# Window
doping uniform region=7 n.type conc=1.95e18
# Emitter
doping uniform region=8 n.type conc=2e18
# Base
doping uniform region=9 p.type conc=1.5e17
# BSF
doping uniform region=10 p.type conc=2e18

# Window
doping uniform region=13 n.type conc=1e19
# Emitter
doping uniform region=14 n.type conc=2e18
# Base
doping uniform region=15 p.type conc=1e17
```

f. Light Beams

```
beam num=1 x.origin=0 y.origin=$lightY angle=90 \  
power.file=AM0silv.spec wavel.start=0.21 wavel.end=4 wavel.num=50
```

APPENDIX G. MATLAB SOURCE CODE

A. VEC2SPEC

```
% VEC2SPEC Converts spectrum data to a Silvaco spec file.
% VEC2SPEC(wavel, int, filename) creates the file filename.spec
% and stores the wavel and int information of the spectrum.

% (c)2001 by P. Michalopoulos

function vec2spec(wavel, int, filename)

% Error checking
len = length(wavel);
if (len ~= length(int))
    disp('ERROR! Vector lengths must agree.')
    break;
end

% Initialize output file
file = fopen([filename '.spec'], 'w');
fprintf(file, '%d', len);

% Save data to file
for i = 1:len,
    fprintf(file, '\n%e %e', wavel(i), int(i));
end

fclose(file);
```

B. OPT2SILV

```
OPT2SILV Convert an optical parameter mat file into a Silvaco
file.
% OPT2SILV(filename, t) Creates the Silvaco optical parameter file
filename.opt
% from the filename.mat file.
% If t='e' then filename.mat must contain eV-e1-e2 data
% If t='n' then filename.mat must contain wavel-n-k data

% (c)2001 by P. Michalopoulos

function opt2silv(filename, t)

% Load data
load(['Data\' filename '.mat'])

% Convert to common units
if t == 'e'
    wavel = ev2um(eV);
```

```

    [n k] = e2nk(e1, e2);
end

% Initialize file
file = fopen(['Data\' filename '.opt'], 'w');
len = length(wavel);
fprintf(file, '%d\n', len);

% Save data to file
for i = 1:len
    fprintf(file, '%d %d %d\n', wavel(i), n(i), k(i));
end

fclose(file);

```

C. DISPLOG

```

% DISPLOG Displays the properties of a Silvaco log file.
% DISPLOG(filename) prints the major properties of a Silvaco log file.

% (c)2001 by P.Michalopoulos

function displog(filename)

[program, numOfElectrodes, electrodeName, values, valueName, data] =
parselog(filename);

disp(program)
disp('Electrodes:')
for i = 1:numOfElectrodes,
    disp([' ' num2str(i) '. ' electrodeName{i}])
end
disp('Values:')
for i = 1:values,
    disp([' ' num2str(i) '. ' valueName{i}])
end

```

D. PARSELOG

```

% PARSELOG Parses a Silvaco log file.
% [prog, numOfElec, elecName, val, valName, data]=PARSELOG(filename)
% parses filename.log and returns:
% prog      : the program that generated the log file
% numOfElec : the number of electrodes
% elecName  : a cell with the names of the electrodes
% val       : the number of different types of values contained
% valName   : a cell with the names of those values
% data      : a matrix with the actual data (each column is a value)

% (c)2001 by P. Michalopoulos

function [program, numOfElectrodes, electrodeName, values, valueName,
data] = parselog(filename)

data = [];

```

```

% Read log file
file = fopen([filename '.log']);
while 1
    line = fgetl(file);
    if ~ischar(line), break, end

    % Translate data codes and parse data
    switch line(1)
    case 'v'      % program used
        [token, line] = strtok(line);
        [token, line] = strtok(line);
        program = token;
    case '#'     % comments
    case 'y'
    case 'z'
    case 'f'     % electrode names
        [token, line] = strtok(line);
        [token, line] = strtok(line);
        numofElectrodes = str2num(token);
        electrodeName = cell(numofElectrodes,1);
        for i = 1:numofElectrodes,
            [token, line] = strtok(line);
            electrodeName{i} = token;
        end
    case 'p'     % data properties
        [token, line] = strtok(line);
        [token, line] = strtok(line);
        values = str2num(token);
        valueName = cell(values,1);
        for i = 1:values,
            [token, line] = strtok(line);
            token = str2num(token);
            switch token
            case 2
                valueName{i} = [electrodeName{1} ' Voltage'];
            case 3
                valueName{i} = [electrodeName{2} ' Voltage'];
            case 4
                valueName{i} = [electrodeName{3} ' Voltage'];
            case 5
                valueName{i} = [electrodeName{4} ' Voltage'];
            case 6
                valueName{i} = [electrodeName{5} ' Voltage'];
            case 7
                valueName{i} = [electrodeName{6} ' Voltage'];
            case 20
                valueName{i} = [electrodeName{1} ' Current'];
            case 21
                valueName{i} = [electrodeName{2} ' Current'];
            case 22
                valueName{i} = [electrodeName{3} ' Current'];
            case 23
                valueName{i} = [electrodeName{4} ' Current'];
            case 24
                valueName{i} = [electrodeName{5} ' Current'];
            case 25

```

```

        valueName{i} = [electrodeName{6} ' Current'];
    case 85
        valueName{i} = 'Available photo current';
    case 86
        valueName{i} = 'Source photo current';
    case 87
        valueName{i} = 'Optical wavelength';
    case 91
        valueName{i} = 'Light Intensity beam 1';
    case 601
        valueName{i} = [electrodeName{1} ' Int. Voltage'];
    case 602
        valueName{i} = [electrodeName{2} ' Int. Voltage'];
    case 603
        valueName{i} = [electrodeName{3} ' Int. Voltage'];
    case 604
        valueName{i} = [electrodeName{4} ' Int. Voltage'];
    case 605
        valueName{i} = [electrodeName{5} ' Int. Voltage'];
    case 606
        valueName{i} = [electrodeName{6} ' Int. Voltage'];
    otherwise
        disp('Unknown value name')
    end
end
end
case 'd' % data values
    dataLine = [];
    [token, line] = strtok(line);
    for i = 1:values,
        [token, line] = strtok(line);
        value = str2double(token);
        dataLine = [dataLine value];
    end
    data = [data; dataLine];
otherwise
    disp('Unknown command')
end
end
end
fclose(file);

```

E. PLOTLOG

```

% PLOTLOG Plots a Silvaco log file.
% PLOTLOG(filename, x-axis, y-axis, style, xmult, ymult) Creates
% a plot of the value in y-axis vs the value in x-axis with values
% and data derived from filename.log. The line style used is specified
% after that. The x and y values are scaled according to xmult and
% ymult accordingly.

% (c)2001 by P.Michalopoulos

function plotlog(filename, x, y, p, mx, my)

[program, numofElectrodes, electrodeName, values, valueName, data] =
parselog(filename);

```

```

sx = sign(x);
sy = sign(y);
x = abs(x);
y = abs(y);

if (x > values) | (y > values),
    disp('ERROR! Axis parameter can not be found.')
else
    plot(sx*data(:,x)'*mx, sy*data(:,y)'*my, p), grid on
    title([filename '.log from ' program]);
    xlabel(valueName{x});
    ylabel(valueName{y});
end

```

F. OPTINTERP

```

% OPTINTERP Interpolates optical parameters.
% OPTINTERP(f1, f2, r) Interpolates the optical parameters found in
% f1.mat and f2.mat with a ratio of r and returns the wavel, n
% and k of the result.

```

```

% (c)2002 by P. Michalopoulos

```

```

function [wavel, n, k] = optinterp(file2, file1, ratio)

```

```

% Load optical parameters for material 1
load(['Data\' file1 '.mat'])
wavelComp1 = ev2um(eV);
[nComp1 kComp1] = e2nk(e1, e2);

```

```

% Load optical parameters for material 2
load(['Data\' file2 '.mat'])
wavelComp2 = ev2um(eV);
[nComp2 kComp2] = e2nk(e1, e2);

```

```

% Perform simple interpolation
wavelResult1 = wavelComp1;
nResult = nComp1*(1-ratio) + nComp2*ratio;
kResult = kComp1*(1-ratio) + kComp2*ratio;
kResultlen = length(kResult);
wavelResult = wavelComp1;

```

```

% Locate the area where only k1 or k2 is zero
kComp2ch = (kComp2 ~= 0);
kComp1ch = (kComp1 ~= 0);
kResultch = xor(kComp2ch, kComp1ch);
area = find(kResultch);
arealen = length(area);

```

```

% Implement correction in material 2
kComp2ch = kComp2;
index = find(~kComp2ch);

```

```

kComp2ch(index) = [];
kComp2chlen = length(kComp2ch);
kComp2ch = kComp2ch(kComp2chlen - arealen + 1 : kComp2chlen);
wavelComp2ch = wavelComp2;
wavelComp2ch(index) = [];
wavelComp2chlen = length(wavelComp2ch);
wavelComp2ch = wavelComp2(wavelComp2chlen - arealen + 1 :
wavelComp2chlen);

% Implement correction in material 1
kComp1ch = kComp1;
index = find(~kComp1ch);
kComp1ch(index) = [];
kComp1chlen = length(kComp1ch);
kComp1ch = kComp1ch(kComp1chlen - arealen + 1 : kComp1chlen);
wavelComp1ch = wavelComp1;
wavelComp1ch(index) = [];
wavelComp1chlen = length(wavelComp1ch);
wavelComp1ch = wavelComp1(wavelComp1chlen - arealen + 1 :
wavelComp1chlen);

% Combine corrections
kResultch = kComp1ch*(1-ratio) + kComp2ch*ratio;

% Smooth-out result
kResultch1 = kResultch(1);
[h index] = min(abs(kResult - kResultch1));
ratio = linspace(0, 1, arealen);
kResult(index + 1 : index + arealen) = kResultch.*ratio + kResult(index
+ 1 : index + arealen).*(1-ratio);
kResult(index + arealen + 1 : kResultlen) = kResult(index + arealen + 1
: kResultlen)*0;

wavel = wavelResult;
n = nResult;
k = kResult;

```

F. EV2UM

```

% EV2UM Converts photon energy (eV) into wavelength (um).

% (c)2001 by P. Michalopoulos

function um = ev2um(ev)

h = 6.6260755e-34;
eV = 1.60218e-19;
c = 2.99792458e8;

ev = ev * eV;
f = ev / h;
wavel = c ./ f;
um = wavel / 1e-6;

```

G. UM2EV

```
% UM2EV Converts photon wavelength (um) into energy (eV).  
  
% (c)2001 by P. Michalopoulos  
  
function ev = um2ev(um)  
  
h = 6.6260755e-34;  
eV = 1.60218e-19;  
c = 2.99792458e8;  
  
wavel = um * 1e-6;  
f = c ./ wavel;  
ev = h * f;  
ev = ev ./ eV;
```

H. E2NK

```
% E2NK Convert the e1, e2 pairs into n, k pairs.  
% [n k] = E2NK(e1, e2)  
  
% (c)2001 by P. Michalopoulos  
  
function [n,k] = e2nk(e1, e2)  
  
ap = (e1 + sqrt(e1.^2 + e2.^2)) / 2;  
an = (e1 - sqrt(e1.^2 + e2.^2)) / 2;  
  
app = ap >= 0;  
anp = an >= 0;  
err = (app < 0) & (anp < 0);  
err = sum(err);  
if err ~= 0  
    disp('ERROR!')  
end  
  
a = ap .* app + an .* anp;  
  
n = sqrt(a);  
  
k = e2 ./ (2 * n);
```

THIS PAGE INTENTIONALLY LEFT BLANK

LIST OF REFERENCES

1. Sze, S. M., *Semiconductor Devices*, 2nd edition, John Wiley & Sons, Inc, 2001.
2. Sze, S. M., *Physics of Semiconductor Devices*, 2nd edition, John Wiley & Sons, Inc, 1981.
3. Shur, M., *Physics of Semiconductor Devices*, Prentice–Hall, Inc, 1990.
4. Messenger, G. C., Ash, M. S., *The Effects of Radiation on Electronic Systems*, Van Nostrand Reinhold Company Inc, 1986.
5. Palik, E. D., *Handbook of Optical Constants of Solids*, Academic Press, Inc, 1985.
6. Palik, E. D., Gorachand, G., *Electronic Handbook of Optical Constants of Solids*, Academic Press, Inc, 1999.
7. Sze, S. M., *Modern Semiconductor Device Physics*, John Wiley & Sons, Inc, 1998.
8. Fraser, D. A., *The Physics of Semiconductor Devices*, Clarendon Press – Oxford, 1986.
9. Bolz, R. E., Tuve, G. L., *CRC Handbook of Tables for Applied Engineering Science*, The Chemical Rubber Co, 1973.
10. *ATLAS User's Manual*, vols 1–2, SILVACO International, 2000.
11. *ATHENA User's Manual*, SILVACO International, 2000.
12. *DEVEDIT User's Manual*, SILVACO International, 2000.
13. *PC Interactive Tools User's Manual*, SILVACO International, 1999.
14. SILVACO International, www.silvaco.com
15. T. Agui, T. Takamoto, E. Ikeda, H. Kurita, “High-efficient dual-junction InGaP/GaAs solar cells with improved tunnel interconnect”, Indium Phosphide and Related Materials, 1998 International Conference on, pp 203-206, 1998
16. T. Takamoto, E. Ikeda, H. Kurita, M. Ohmori, “High efficiency InGaP solar cells for InGaP/GaAs tandem cell application”, Photovoltaic Energy Conversion, 1994., Conference Record of the Twenty Fourth. IEEE Photovoltaic Specialists Conference - 1994, 1994 IEEE First World Conference on , Volume: 2, pp 1729 -1732 vol.2, 1994

17. H. Kurita, T. Takamoto, E. Ikeda, M. Ohmori, "High-efficiency monolithic InGaP/GaAs tandem solar cells with improved top-cell back-surface-field layers", *Indium Phosphide and Related Materials, 1995. Conference Proceedings., Seventh International Conference on*, pp 516-519 , 1995
18. B.T. Cavicchi, D.D. Krut, D.R. Lillington, S.R. Kurtz, J.M. Olson, "The design and evaluation of dual-junction GaInP/sub 2//GaAs solar cells for space applications", *Photovoltaic Specialists Conference, 1991., Conference Record of the Twenty Second IEEE*, pp 63-67 vol. 1 , 1991
19. R.R. King, N.H. Karam, J.H. Ermer, N. Haddad, P. Colter, T. Isshiki, H. Yoon, H.L. Cotal, D.E. Joslin, D.D. Krut, R. Sudharsanan, K. Edmondson, B.T. Cavicchi, D.R. Lillington, "Next-generation, high-efficiency III-V multijunction solar cells", *Photovoltaic Specialists Conference, 2000. Conference Record of the Twenty-Eighth IEEE , 2000*, pp. 998 -1001
20. D. Lillington, H. Cotal, J. Ermer, D. Friedman, T. Moriarty, A. Duda, "32.3% efficient triple junction GaInP/sub 2//GaAs/Ge concentrator solar cells", *Energy Conversion Engineering Conference and Exhibit, 2000. (IECEC) 35th Intersociety , Volume: 1 , 2000*, pp. 516 -521
21. J.E. Granata, J.H. Ermer, P. Hebert, M. Haddad, R.R. King, D.D. Krut, J. Lovelady, M.S. Gillanders, N.H. Karam, B.T. Cavicchi, "Triple-junction GaInP/GaAs/Ge solar cells-production status, qualification results and operational benefits", *Photovoltaic Specialists Conference, 2000. Conference Record of the Twenty-Eighth IEEE , 2000*, pp. 1181 -1184
22. N.H. Karam, R.R. King, B.T. Cavicchi, D.D. Krut, J.H. Ermer, M. Haddad, Li Cai, D.E. Joslin, M. Takahashi, J.W. Eldredge, W.T. Nishikawa, D.R. Lillington, B.M. Keyes, R.K. Ahrenkiel, "Development and characterization of high-efficiency Ga/sub 0.5/In/sub 0.5/P/GaAs/Ge dual- and triple-junction solar cells", *Electron Devices, IEEE Transactions on , Volume: 46 Issue: 10 , Oct. 1999*, pp. 2116 -2125
23. Reinhardt K.C, Mayberry C.S, Lewis B.P, Kreifels T.L, "Multijunction solar cell iso-junction dark current study", *Photovoltaic Specialists Conference, 2000, Conference Record of the Twenty-Eighth IEEE , 2000*, pp 1118-1121
24. King R.R, Karam N.H, Ermer J.H, Haddad N, Colter P, Isshiki T, Yoon H, Cotal H.L, Joslin D.E, Krut D.D, Sudharsanan R, Edmondson K, Cavicchi B.T, Lillington D.R., "Next-generation, high-efficiency III-V multijunction solar cells", *Photovoltaic Specialists Conference, 2000, Conference Record of the Twenty-Eighth IEEE , 2000*, pp 998-1001

25. Van Kerschaver E, Nijs J, Mertens R, Ghannam M, "Twodimensional solar cell simulations by means of circuit modelling", Photovoltaic Specialists Conference, 1997., Conference Record of the Twenty-Sixth IEEE , 1997, pp 175-178
26. Jain R.K, Flood D.J, "Simulation of high-efficiency n/sup +/p indium phosphide solar cell results and future improvements", Electron Devices, IEEE Transactions on , Volume: 41 Issue: 12 , Dec. 1994, pp 2473-2475
27. Kurtz S, Geisz J.F, Friedman D.J, Olson J.M, Duda A, Karam N.H, King R.R, Ermer J.H, Joslin D.E, "Modeling of electron diffusion length in GaInAsN solar cells", Photovoltaic Specialists Conference, 2000, Conference Record of the Twenty-Eighth IEEE , 2000, pp 1210-1213
28. Walters R.J, Summers G.P, Messenger S.R, "Analysis and modeling of the radiation response of multijunction space solar cells", Photovoltaic Specialists Conference, 2000, Conference Record of the Twenty-Eighth IEEE , 2000, pp 1092 -1097
29. Panse P, Sankaranarayanan H, Narayanaswamy R, Shankaradas M, Ying Y, Ferekides C.S, Morel D.L, "Evaluation and modeling of junction parameters in Cu(In,Ga)Se/sub 2/ solar cells", Photovoltaic Specialists Conference, 2000, Conference Record of the Twenty-Eighth IEEE , 2000, pp 599 -602
30. Lewis, B. P., Dark current analysis and computer simulation of triple-junction solar cells, Naval Postgraduate School, 1999.
31. Renewable Resource Data Center (rredc.nrel.gov)
32. US Department of Energy – Photovoltaics Program (<http://www.eren.doe.gov/pv>)
33. I. Vurgaftman, J.R. Meyer, L.R. Ram-Mohan, "Band parameters for III-V compound semiconductors and their alloys", Applied Physics Review, Journal of Applied Physics, vol 89, number 11, 1 June 2001, pp. 5815–5875
34. McCloy, D. J., High efficiency solar cells: a model in Silvaco, Naval Postgraduate School, 1999.

THIS PAGE INTENTIONALLY LEFT BLANK

INITIAL DISTRIBUTION LIST

1. Defense Technical Information Center
Ft. Belvoir, Virginia
2. Dudley Knox Library
Naval Postgraduate School
Monterey, California
3. Chairman, Department of Electrical of Computer Engineering
Naval Postgraduate School
Monterey, CA
4. Chairman, Department of Computer Science
Naval Postgraduate School
Monterey, CA
5. Dr. Sherif Michael, Code EC/Mi
Department of Electrical and Computer Engineering
Naval Postgraduate School
Monterey, CA
6. Dr. Bret Michael, Code CS/Mj
Department of Computer Science
Naval Postgraduate School
Monterey, CA
7. Dr. Todd Weatherford, Code EC/Wt
Department of Electrical and Computer Engineering
Naval Postgraduate School
Monterey, CA
8. Embassy of Greece, Naval Attaché
Washington, DC
9. LT Panayiotis Michalopoulos H.N.
Ekfantidou 46, Vyronas, Athens, 16232,
Greece

THIS PAGE INTENTIONALLY LEFT BLANK